

MAGNETISM IN SOME
SULPHUR SPINELS.

by

M.R. Spender.

A thesis submitted to the Faculty of Graduate
Studies of the University of Manitoba in partial
fulfilment of the requirements for the degree
of Doctor of Philosophy.

Winnipeg, February 19th 1973.



With love to my parents.

Preface

The investigations described in this thesis began in the winter of 1967 and were brought to their present state by about the end of November 1972. We were late getting into the field of magnetism in chalcogenide spinels and somewhat lacking in expertise. The first two years tended to be more frustrating than absorbing partly, I think, because of a lack of purpose but mainly because there were more experiments that seemed to go wrong than achieved even partial success.

The study of magnetism in sulphides is made difficult in two ways. First the compounds themselves are quite unpredictable, second, no real consensus of opinion yet exists to explain why this should be. Qualitatively we appreciate that it has to do with the properties of sulphur and in particular, its low electronegativity. How this precept should be applied to the explanation of sulphides is still apparently a matter of controversy. We hope the work described here goes a little way towards a solution.

The organization of the work is as

follows. In Chapter I, we give an introduction to the studies, covering rather briefly the spinel structure, and a comparison of sulphur and oxygen in an attempt to see why sulphides and oxides should have more differences than similarities. There is also a rather cavalier treatment of chemical bonding and some remarks about d-electrons. Chapter II is concerned with the basic theory needed to do, and understand in principle, the sort of experiments described. We also talk about the equipment available to us and the experimental techniques used. Chapter III is the first of two on our experimental work and gives accounts of investigations of Fe_3S_4 , FeCr_2S_4 , CdCr_2S_4 and FeRh_2S_4 . Chapter IV concerns itself with experiments on the mixed crystals $\text{Cd}_{1-x}\text{Fe}_x\text{Cr}_2\text{S}_4$ $0 < x < 1$. Chapter V states where we stand regarding the existing explanations of the magnetic properties of thiospinels and offers our reasons. We also summarise the more interesting of our findings.

There are a number of people to thank for their various contributions. It is a pleasure to acknowledge my friend and erstwhile colleague J.M.D. Coey, with whom I worked on the Fe_3S_4 study. Thanks are also due to G.A. Sawatzky whose example and attitudes so greatly influenced me when I first came

to this university. Our last post doctoral fellow, D.C. Price was more than helpful on several occasions. Many faculty members have, at various times, given me advice and help, in particular, Professors C.W. Searle, P.D. Loly, P. Gaunt, W.H. Kleiner and W.N.R. Stevens, to all of them I express my gratitude.

I have always enjoyed most excellent relations with the technical staff of our department. They have always been most understanding and special word of thanks goes to Mr. R.H. Batten, Mr. G. Knote, Mr. P. Lindsay and Mr. J. Sewell. The ladies who have at times typed letters and papers for me have always done an excellent job, for which they really deserve more than a mention. My wife, Michele, typed and indexed this thesis for me, an effort marked by unflagging enthusiasm, attention to detail and not a little patience.

During the course of my studies I have received monies from the University of Manitoba for minor teaching duties but the bulk of my financial support came from the grant my supervisor received from the Defence Research Board of Canada. The work was supervised by Professor A.H. Morrish and to him I owe my greatest debt of thanks. He has always treated me well, encouraged my efforts and discussed my work. He suggested many of the experiments and contributed to them in many ways.

Abstract

Experimental studies of several sulphide spinels are presented. The techniques used were magnetization and electrical resistivity measurements and Mössbauer Effect spectroscopy. All the work was performed on polycrystalline powders; the crystal structures being determined by means of Debye-Sherrer x-ray powder diffraction methods. A variety of magnetic and electrical properties were observed but it is concluded that a good understanding of all the compounds can be had in terms of the qualitative ideas set out by Goodenough [1]. Several qualitative reasons are offered to support this opinion and a more quantitative test is also suggested. Specific results for the various compounds are as follows.

The spinel form of Fe_3S_4 is a ferrimagnet with $T_{\text{FN}}=606^\circ\text{K}$, the low temperature moment, $2.2 \mu_{\text{B}}$ /molecule, is far smaller than expected from any spin only value consistent with the Mössbauer studies and electrical measurements indicate semi-metallic conductivity suggesting the presence of partially localized and partially delocalized charge

carriers. The samples we studied appear to be typical of synthetic Fe_3S_4 ; in common with other investigations, we find large central peaks in the Mössbauer spectra which we account for partly through superparamagnetic relaxation but largely through spin state changes resulting from local differences in chemical bonding.

FeCr_2S_4 is a semiconductor and orders with a simple Néel spin arrangement at 170°K . The Mössbauer spectra show a magnetic hyperfine splitting and a quadrupole interaction below this temperature. The quantity $\frac{1}{2}e^2qQ$ is positive and V_{zz} makes an angle of $11 \pm 1^\circ$ with H_{hf} until $T \sim 20^\circ\text{K}$ when θ begins to decrease towards zero and then changes abruptly to 90° . This is accompanied by a change in sign of the E.F.G. so that below 9°K $\frac{1}{2}e^2qQ$ is negative and there is also a small asymmetry parameter. We attribute this to a J-T stabilization of the $^5\text{E}(\text{Fe}^{2+})$ ground state and suppose that the E.F.G. above 10°K is a result of dynamic stabilization.

Attempts to synthesize FeRh_2S_4 met with partial success and samples containing about 10% impurity phase were studied. The spinel phase is stabilized by annealing at 500°C after quenching from temperatures above 900°K ; however, the quenching induces strains, apparently on a local basis, so that

~10% of the iron sites exhibit a large quadrupole splitting at room temperature while the others show a small or zero splitting. Magnetization and Mössbauer measurements indicate antiferromagnetic order with $T_N = 215 \pm 5^\circ\text{K}$ $\theta = -240^\circ\text{K}$. The Curie constant $C_M = 3.2$ is in keeping with the expectation of only Fe^{2+} in the compound, a view confirmed by the total spectrum shift.

The compounds $\text{Cd}_{1-x}\text{Fe}_x\text{Cr}_2\text{S}_4$ $0 < x < 1$ are all ferrimagnets with T_{FN} ranging from 96°K ($x=0.05$) to 165°K ($x=0.9$) in a smooth fashion. The Curie-Weiss parameter θ changes from 130°K ($x=0.05$) to -223°K ($x=0.9$) but the variation is not continuous, there being an abrupt change from positive to negative values between $x=0.4$ and $x=0.5$. Resistivity measurements show that all the compounds are semiconductors indicating localized electron behaviour and a simple model is offered to explain why the Curie constants are not always in keeping with those expected from spin only considerations. The Mössbauer spectra of these compounds are extremely complicated, all but the members with $x=0.9$ and 0.05 show quadrupole splitting above the ordering temperatures. This quadrupole splitting is temperature dependent. Once below the ordering temperature all spectra show evidence of quadrupole interactions

and all spectra have temperature dependent line widths. We suggest that this results from a combination of effects. On the one hand there is a time dependent E.F.G. resulting from dynamic J-T stabilization and on the other, proximity effects resulting from a variety of environments with different elastic anisotropy.

1. J.B. Goodenough, J. Phys. Chem. Solids, 30, 261, 1969.

Contents

| | |
|--|-----|
| Preface | iii |
| Abstract | vi |
| List of Figures | xiv |
| List of Tables | xx |
| I. INTRODUCTION | |
| 1. The Spinel Structure | 1 |
| 2. Sulphur as an Anion | 7 |
| 3. Chemical Bonding | 13 |
| 4. Descriptions of d-electrons | 19 |
| 5. Preparation of Sulphide Spinel | 30 |
| Literature Cited | 36 |
| II. BASIC THEORY, EQUIPMENT AND TECHNIQUES | |
| 1. Magnetization Measurements | |
| 1.1 Theoretical Background | 39 |
| 1.2 The Magnetometer | 53 |
| 1.3 Ancillary Equipment | 59 |
| 1.4 Experimental Details | 67 |
| 2. Electrical Measurements | |
| 2.1 Basic Theoretical Results | 73 |
| 2.2 Equipment | 77 |
| 2.3 Experimental Procedure | 78 |
| 3. Mössbauer Effect Studies | |
| 3.1 Review of Theory | 81 |

| | | |
|-----|-----------------------------|-----|
| 3.2 | Hyperfine Interactions | 85 |
| 3.3 | The Mössbauer Spectrometer | 99 |
| 3.4 | Ancillary Equipment | 101 |
| 3.5 | Experimental Procedure | 111 |
| 3.6 | Data Analysis | 118 |
| | Literature Cited | 119 |
| | Manufacturers and Suppliers | 122 |

III. EXPERIMENTAL WORK ON FOUR COMPOUNDS

| | | |
|-----|---|-----|
| 1. | A Study of $\text{Fe}[\text{Fe}_2]\text{S}_4$ | |
| 1.1 | Introduction | 125 |
| 1.2 | Preparation of Samples | 127 |
| 1.3 | Magnetization Studies | 131 |
| 1.4 | Electrical Measurements | 135 |
| 1.5 | Mössbauer Effect Spectroscopy | 135 |
| 1.6 | Discussion of Bulk Properties | 144 |
| 1.7 | Discussion of Sample Peculiarities | 151 |
| 1.8 | Conclusions | 160 |
| 2. | A Study of $\text{Fe}[\text{Cr}_2]\text{S}_4$ | |
| 2.1 | Introduction | 161 |
| 2.2 | Theoretical Considerations | 164 |
| 2.3 | Preparation of Samples | 170 |
| 2.4 | Magnetization Measurements | 172 |
| 2.5 | Electrical Measurements | 175 |

| | | |
|-----|--|-----|
| 2.6 | Mössbauer Effect Studies | 177 |
| 2.7 | Discussion | 192 |
| 2.8 | Conclusions | 205 |
| 3. | A Comment on CdCr_2S_4 | |
| 3.1 | Introduction | 206 |
| 3.2 | Magnetization Measurements | 209 |
| 3.3 | Discussion | 213 |
| 3.4 | Conclusions | 218 |
| 4. | Experiments on FeRh_2S_4 | |
| 4.1 | Introduction | 218 |
| 4.2 | Preparation of Samples | 220 |
| 4.3 | Magnetization Measurements | 225 |
| 4.4 | Electrical Measurements | 226 |
| 4.5 | Mössbauer Effect Studies | 228 |
| 4.6 | Discussion | 233 |
| 4.7 | Conclusions | 242 |
| | Literature Cited | 244 |

IV. EXPERIMENTAL WORK ON A MIXED SYSTEM

| | | |
|-----|--|-----|
| 1. | The Family of Compounds $\text{Cd}_{1-x}\text{Fe}_x\text{Cr}_2\text{S}_4$ | |
| 1.1 | Introduction | 252 |
| 1.2 | Preparation | 253 |
| 1.3 | Magnetization Measurements | 259 |
| 1.4 | Electrical Measurements | 265 |

| | | |
|-------|--------------------------------|-----|
| 1.5 | Mössbauer Effect Investigation | 269 |
| 1.5.1 | The cadmium rich region | 270 |
| 1.5.2 | The iron rich end | 275 |
| 1.5.3 | The central region | 280 |
| 1.5.4 | Total spectrum shift | 283 |
| 1.6 | Discussion | 287 |
| 1.7 | Conclusions | 300 |
| | Literature Cited | 302 |

V. CONCLUDING REMARKS

| | | |
|----|------------------------------|-----|
| 1. | Summary | 304 |
| 2. | Suggestions for Further Work | 311 |
| | Literature Cited | 313 |

| | |
|------------|------|
| Appendix A | xxii |
| Appendix B | xxx |
| Appendix C | xxxv |
| Appendix D | xlv |
| Appendix E | liii |

List of Figure Captions

| | Page |
|--|------|
| Chapter I | |
| 1. To illustrate the f.c.c. anion stacking | 2 |
| 2. Positions of atoms in the primitive cell | 4 |
| 3. Illustrating the 6 magnetic sublattices | 6 |
| 4. The hydrogen molecule problem | 13 |
| 5. To illustrate various molecular orbitals | 17 |
| 6. Illustrating d-orbitals | 21 |
| 7. Bonding of hypothetical FeS_6 complex | 22 |
| 8. Illustrating the effect of firing | 34 |
| Chapter II | |
| 9. Transducer assembly in the magnetometer | 56 |
| 10. To illustrate the operation of the pick-up coils | 56 |
| 11. Diagram of the magnetometer cryostat | 61 |
| 12. Diagram of the magnetometer furnace | 63 |
| 13. Magnetometer support rod | 65 |
| 14. A schematic magnetization curve | 68 |
| 15. Nature of background correction in magnetometer furnace | 72 |
| 16. Circuit for electrical measurements | 77 |
| 17. To illustrate the ohmicity of the electrical contacts | 80 |
| 18. The decay scheme of ^{57}Co | 84 |
| 19. Splitting of the two lowest states of the ^{57}Fe nucleus | 93 |
| 20. To illustrate the core polarization mechanism for H_s | 96 |

| | | |
|-----|--|-----|
| 21. | Block diagram of the Mössbauer spectrometer | 100 |
| 22. | Line diagram of flow-through liquid nitrogen cryostat | 103 |
| 23. | (a) Line diagram of oxford cryostat | 105 |
| | (b) Sample rod for the oxford cryostat | 106 |
| 24. | Effect of stray fields on velocity calibration | 114 |
| 25. | To illustrate collimation geometry | 115 |
| 26. | Line widths as a function of collimation angle for various line positions | 116 |
| 27. | Illustrating the effect of collimation on α -Fe ₂ O ₃ line widths and positions | 117 |

Chapter III

| | | |
|-----|---|-----|
| 28. | Infra-red absorption spectra | 132 |
| 29. | H_c versus T, $D(7)=137 \text{ \AA}$, $D(24)=91 \text{ \AA}$ | 133 |
| 30. | M_R/M_∞ versus T, $D(7)=137 \text{ \AA}$, $D(24)=91 \text{ \AA}$ | 133 |
| 31. | M_∞ versus T, $D(7)=137 \text{ \AA}$, $D(24)=91 \text{ \AA}$ | 133 |
| 32. | Thermal scans of magnetization in Fe ₃ S ₄ | 134 |
| 33. | Mössbauer spectra at 296°K for various samples of synthetic Fe ₃ S ₄ | 137 |
| 34. | Mössbauer spectra 296°K | 138 |
| 35. | Mössbauer spectra of sample 24 | 140 |
| 36. | Mössbauer spectra of sample 7 | 140 |
| 37. | Variation of H_{eff} with H_{app} for the two sublattices | 141 |
| 38. | To illustrate the effect of H_{app} on H_{hf} | 142 |
| 39. | Proposed one-electron energy band schemes for (a) Fe ₃ O ₄ and (b) Fe ₃ S ₄ | 150 |
| 40. | Alternative energy band scheme for Fe ₃ S ₄ | 151 |

| | | |
|-----|--|-----|
| 41. | To illustrate the potential well for the vibronic problem | 166 |
| 42. | To illustrate the nature of the two degenerate modes associated with a tetrahedral site | 168 |
| 43. | Temperature dependence of H_c | 173 |
| 44. | Temperature dependence of magnetic moment and inverse molar susceptibility for FeCr_2S_4 | 174 |
| 45. | Magnetic moment at various temperatures as a function of applied field | 175 |
| 46. | Temperature dependence of the resistivity | 176 |
| 47. | Variation of resistance with applied field at various temperatures | 178 |
| 48. | Magneto-resistance in 10 kOe field as a function of temperature | 178 |
| 49. | Typical spectra at various temperatures | 180 |
| 50. | Mössbauer spectra of FeCr_2S_4 | 181 |
| 51. | Mössbauer spectra from powdered absorbers | 182 |
| 52. | The temperature dependence of ϵ | 184 |
| 53. | The temperature dependence of the hyperfine field | 184 |
| 54. | The total spectrum shift in FeCr_2S_4 as a function of temperature | 185 |
| 55. | The temperature dependence of the quantity $\frac{1}{2}e^2qQ$, $T \gg 20^\circ\text{K}$ | 186 |
| 56. | The temperature dependence of (a) the hyperfine field (b) the quantity $\frac{1}{2}e^2qQ$ (c) the total spectrum shift | 188 |
| 57. | Spectra obtained in applied fields | 190 |
| 58. | The variation of ϵ with applied field at various temperatures | 191 |
| 59. | The variation of effective field with applied field at various temperatures | 191 |

| | | |
|-----|---|-----|
| 60. | Suggested band scheme for FeCr_2S_4 | 198 |
| 61. | Dependence of average line width on the quadrupole shift in the spectra | 202 |
| 62. | Temperature dependence of M_s and χ_M^{-1} for CdCr_2S_4 | 211 |
| 63. | Magnetization as a function of applied field at various temperatures for CdCr_2S_4 | 212 |
| 64. | Suggested energy band scheme for CdCr_2S_4 in terms of multi-electron crystal field states | 217 |
| 65. | Magnetization of FeRh_2S_4 as a function of applied field for various temperatures | 224 |
| 66. | Inverse molar susceptibility of FeRh_2S_4 as a function of temperature | 225 |
| 67. | The temperature dependence of the resistivity and magneto-resistance of FeRh_2S_4 | 227 |
| 68. | Mössbauer spectra of FeRh_2S_4 | 230 |
| 69. | Mössbauer spectra from FeRh_2S_4 below T_N | 231 |
| 70. | Temperature dependence of (a) H_{hf} and (b) $\frac{1}{2}e^2qQ$ for FeRh_2S_4 | 232 |
| 71. | The temperature dependence of the total spectrum shift of the major part of the spectrum of FeRh_2S_4 | 234 |
| 72. | Mössbauer spectra of FeRh_2S_4 after quenching from 1100°K | 238 |
| 73. | Suggested band scheme for FeRh_2S_4 | 241 |

Chapter IV

| | | |
|-----|---|-----|
| 74. | Compositional dependence of the lattice parameters of members of the family $\text{Cd}_{1-x}\text{Fe}_x\text{Cr}_2\text{S}_4$ | 256 |
| 75. | Magnetic moments of (a) CD95 (b) CD90 (c) CD80 (d) CD60 as a function of temperature | 260 |
| 76. | Magnetic moments of (a) CD50 (b) CD20 (c) CD10 as a function of temperature | 261 |

77. Inverse molar susceptibility (a) CD95 and CD90 (b) CD80, CD60, CD50 and (c) CD20, CD10 as a function of temperature 262
78. Compositional dependence of (a) Ordering temperatures (b) Curie-Weiss parameters (c) Magnetic moments and (d) Curie constants for members of the family $\text{Cd}_{1-x}\text{Fe}_x\text{Cr}_2\text{S}_4$ 264
79. Temperature dependence of the resistivity of (a) CD90 (b) CD80 (c) CD60 (d) CD50 (f) CD20 (e) CD10 266
80. Magneto-resistance of several members of the family $\text{Cd}_{1-x}\text{Fe}_x\text{Cr}_2\text{S}_4$ in a 10 kOe field 268
81. Mössbauer spectra of (a) CD95 and (b) CD90 at various temperatures 271
82. Temperature dependence of $\frac{1}{2}e^2qQ$ in CD95 and CD90 274
83. Temperature dependence of H_{hf} in CD95 and CD90 274
84. Mössbauer spectra of (a) CD20 and (b) CD10 at various temperatures 276
85. The temperature dependence of H_{hf} in CD10 278
86. Quadrupole interactions in CD10 and CD20 278
87. Mössbauer spectra of CD50 at various temperatures 281
88. The temperature dependence of the splitting of paramagnetic doublets in CD50 284
89. To illustrate the use of (II.25) to find the Debye temperatures 286
90. Temperature dependence of total spectrum shift in CD90 286
91. Temperature dependence of total spectrum shift in CD95 assuming spectra associated with different environments 286

92. Extrapolation of M_s and M_∞ to zero iron content for CD95 and CD90 291
93. Qualitative representation of the temperature dependencies of some magnetic exchange interactions in $\text{Cd}_{1-x}\text{Fe}_x\text{Cr}_2\text{S}_4$ 291
94. Correlation of properties of the two isomorphous systems $\text{Cd}_{1-x}\text{Fe}_x\text{Cr}_2\text{S}_4$ and $\text{Fe}_{1-x}\text{Cu}_x\text{Cr}_2\text{S}_4$ 298

Chapter V

95. Illustrating a correlation between T_{FN} and the total spectrum shift 308

List of Table Headings

| | Page |
|---|------|
| Chapter I | |
| 1. Atomic positions in the spinel structure | 3 |
| 2. Some properties of oxygen and sulphur | 8 |
| 3. Relationship between ground state term and decomposition into I.R. | 25 |
| Chapter II | |
| 4. Calibration constants for the magnetometer | 73 |
| 5. Nuclear parameters for ^{57}Fe | 84 |
| 6. Calibration data for Mössbauer spectrometer | 113 |
| Chapter III | |
| 7. Part of the powder pattern from synthetic Fe_3S_4 samples | 129 |
| 8. Crystallographic and magnetic data for synthetic Fe_3S_4 | 131 |
| 9. Intensity ratio of outer, inner and middle pairs of lines | 138 |
| 10. Hyperfine parameters for sample 24 deduced from zero field spectra | 139 |
| 11. Hyperfine interaction parameters in some iron sulphides | 144 |
| 12. Magnetization data for FeCr_2S_4 | 162 |
| 13. X-ray powder diffraction data for FeCr_2S_4 | 171 |
| 14. Magnetic crystallographic and electrical resistivity data for FeCr_2S_4 | 173 |
| 15. Hyperfine parameters of FeCr_2S_4 Mössbauer spectra, powder absorbers | 189 |

| | | |
|-----|--|-----|
| 16. | X-ray powder diffraction pattern for CdCr_2S_4 | 210 |
| 17. | Magnetic and crystallographic data from CdCr_2S_4 | 212 |
| 18. | X-ray powder diffraction pattern for FeRh_2S_4 | 222 |
| 19. | Magnetic and crystallographic data for FeRh_2S_4 | 226 |
| 20. | Comparison of the paramagnetic susceptibilities of (A) $(\text{Cu}_{0.5}\text{Fe}_{0.5}[\text{Rh}_2]\text{S}_4$ and (B) $\text{Fe}[\text{Rh}_2]\text{S}_4$ | 237 |

Chapter IV

| | | |
|-----|--|-----|
| 21. | Magnetization data from reference {1} | 252 |
| 22. | Magnetic and crystallographic data for members of the family $(\text{Cd}_{1-x}\text{Fe}_x)\text{Cr}_2\text{S}_4$ | 255 |
| 23. | X-ray powder diffraction patterns for four members of the family $\text{Cd}_{1-x}\text{Fe}_x\text{Cr}_2\text{S}_4$ | 257 |
| 24. | X-ray diffraction patterns for three members of the family $\text{Cd}_{1-x}\text{Fe}_x\text{Cr}_2\text{S}_4$ | 258 |
| 25. | Resistivity data from some members of the family $\text{Cd}_{1-x}\text{Fe}_x\text{Cr}_2\text{S}_4$ | 267 |
| 26. | Probability $P(N)$ of N nearest neighbour magnetic A-site ions for various x , assuming random distributions | 273 |
| 27. | Total spectrum shift data for some members of the family $\text{Cd}_{1-x}\text{Fe}_x\text{Cr}_2\text{S}_4$ | 285 |

Chapter V

| | | |
|-----|-----------------------------|-----|
| 28. | Data used to plot figure 95 | 309 |
|-----|-----------------------------|-----|

I INTRODUCTION

There are five sections in this introductory chapter, which are intended to lay the ground work for this description of our study of some transition metal sulphides with the spinel structure. The first section describes the spinel structure. Section 2 is devoted to sulphur, and an attempt is made to indicate why we should expect sulphides to exhibit rather different properties from their related oxides. Section 3 consists of a few notes on chemical bonding. In section 4 we indicate the nature of arguments leading to the concepts of localized and collective behaviour of electrons, ending with a hint of the variety of properties that are encountered in sulphide spinels. Section 5 describes how spinel sulphides, or at least some of them, can be synthesized.

1. THE SPINEL STRUCTURE.

Descriptions of the spinel structure can be found in {1,2}. In what follows we shall try to give as clear a summary as possible.

We start by considering the anion sublattice. This is sketched in part in figure 1. In the figure, the

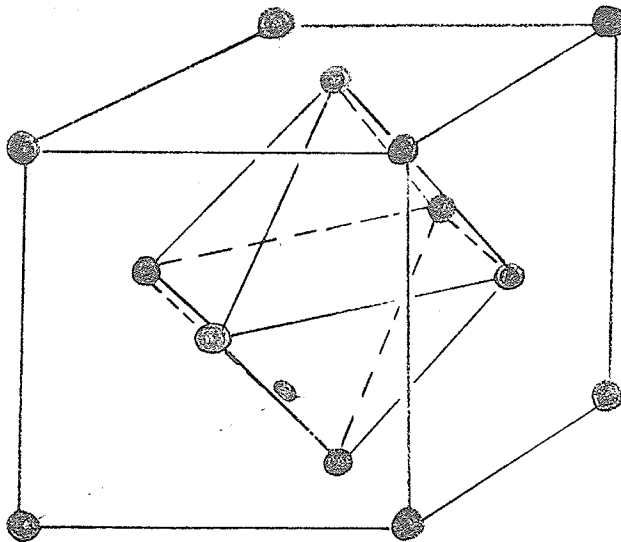


Figure 1. To illustrate the f.c.c. anion stacking.

6 face centred atoms circumscribe an octahedral or B-site. Sites such as these are situated at body centres and cube edges. Between a face of the octahedron and the nearest cube vertex atom is a tetrahedral or A-site. There are twice as many tetrahedral as octahedral interstices.

In order to see where the cations are positioned we note that the space group is $O_h^7 \cong Fm\bar{3}m$ the crystal structure being first determined for Fe_2O_3 and $MgAl_2O_4$. Figure 2 illustrates the atomic positions in the primitive unit cell which is $\frac{1}{8}$ the size of the unit cell and has two of the anion units shown in figure 1. Anions are denoted X and occupied octahedral sites are denoted B. The anion positions are identical in each octant and each is co-ordinated by four cations 3B and 1A. In figure 2, the line joining X_1 and X_2 is in a $\langle 111 \rangle$

direction and on this line lie the two occupied A-sites in the primitive cell, between these A-sites is an unoccupied B-site and it is characteristic of the A-sites that the nearest octahedra are empty. If we start at B_1 and look along the $\langle \bar{1}10 \rangle$ every available B-site is occupied. A translation from B_1 $\langle \bar{1}01 \rangle$ takes us to the plane of B-sites above B_1 and looking in a $\langle 110 \rangle$ from B_2 all the available octahedral sites are full. Similar (001) planes repeat every fourth layer and since cubic symmetry is preserved the f.c.c. cell of figure 1 is doubled in all three directions. Table 1 summarises the unit cell atomic positions and the four translations needed to generate the rest of the unit cell.

Table 1. Atomic Positions In The Spinel Structure.

| Co-ordinates relative to a_0 | | |
|--|-----------------|--|
| A | B | X |
| $0,0,0$ | $5/8, 5/8, 5/8$ | u, u, u |
| $\frac{1}{4}, \frac{1}{4}, \frac{1}{4}$ | $7/8, 7/8, 5/8$ | u, \bar{u}, \bar{u} |
| | $5/8, 7/8, 7/8$ | $\bar{u}, \bar{u}, \bar{u}$ |
| | $7/8, 5/8, 7/8$ | \bar{u}, \bar{u}, u |
| Plus four translations among the octants | | $\frac{1}{4}+u, \frac{1}{4}+u, \frac{1}{4}-u$ $\frac{1}{4}-u, \frac{1}{4}-u, \frac{1}{4}-u$ $\frac{1}{4}+u, \frac{1}{4}-u, \frac{1}{4}+u$ $\frac{1}{4}-u, \frac{1}{4}-u, \frac{1}{4}+u$ |
| $(0, 0, 0; 0, \frac{1}{2}, \frac{1}{2}; \frac{1}{2}, 0, \frac{1}{2}; \frac{1}{2}, \frac{1}{2}, 0)$ | | |

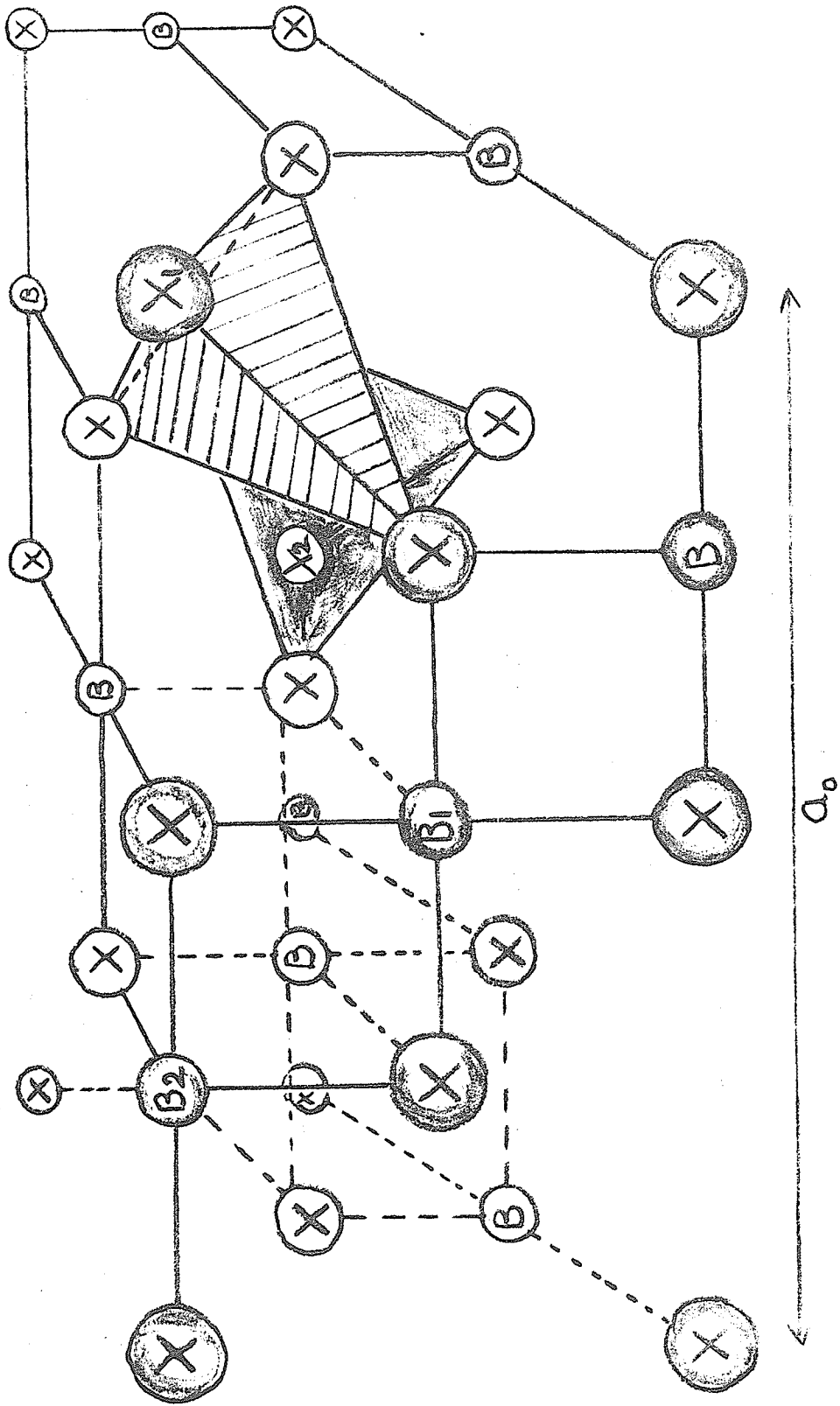


Figure 2. Positions of atoms in the primitive cell.

The primitive cell thus contains 16 anions 4 B-site and 2 A-site cations and the unit cell twice these numbers. The lattice parameter a_0 of table 1 is defined in figure 2 and the parameter u is defined in terms of the anion cation separations i.e.

$$AX = a_0(u - 1/4)\sqrt{3}$$

$$BX = a_0(5/8 - u)$$

$$\text{while } BB = 1/4(a_0\sqrt{2})$$

$$\text{and } AA = 1/4(a_0\sqrt{3})$$

In the ideal f.c.c. lattice $u = 3/8$ but this generally makes the A-sites too small for cation occupancy so that most spinels have $u > 3/8$. The anions are displaced along one of $\{<111>\}$ away from the nearest A-site cation. This movement results in trigonal fields at the B-sites but they are in different $<111>$ directions for each of the B-cations in the primitive cell. Thus overall cubic symmetry is preserved. This trigonal component is superposed on a component arising from the B-cation lattice in any case. At any B-site the two trigonal fields are oppositely directed. The A-site symmetry is perfectly cubic.

As we have seen, the primitive cell contains six cations, meaning that, in total, there must be six magnetic sublattices. The B-site array is complicated, if we number the lattices B_1 - B_4 and choose any cation for example one belonging to B_1 then it is co-ordinated by six other cations, two from each of B_2 , B_3 , and B_4 . In figure 3a

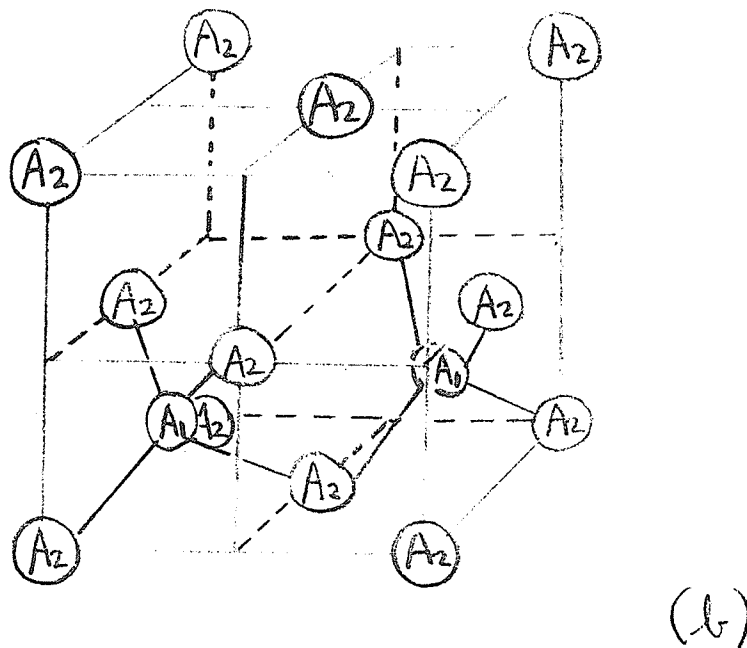
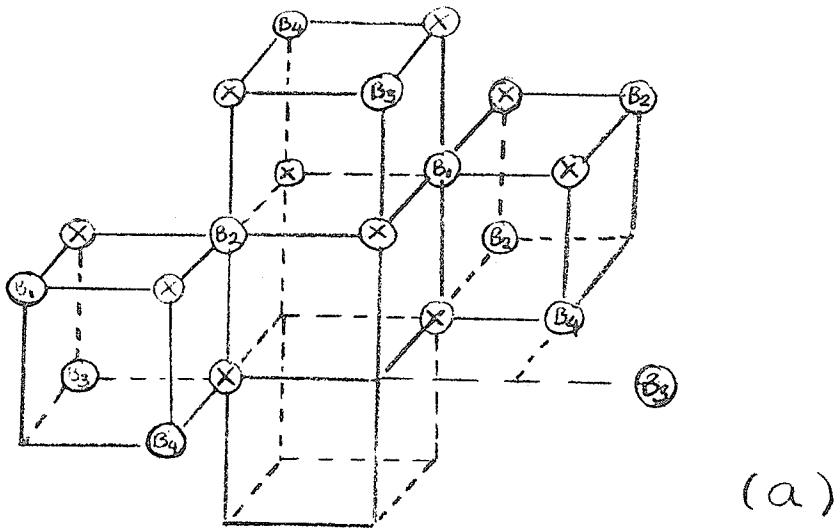


Figure 3. Illustrating the 6 Magnetic Sublattices (a) the 4 B sublattices (b) the 2 A sublattices.

we have tried to illustrate the arrangement. Because there is no obvious way that the B sublattices can be arranged into interpenetrating lattices, there is a possibility of complex spin arrangements among the cations. The A-site cations are more straightforwardly arranged into two interpenetrating f.c.c. lattices such that a cation belonging to A_1 is tetrahedrally co-ordinated by four A-site cations belonging to A_2 . This arrangement is illustrated in figure 3b.

2. SULPHUR AS AN ANION.

As we shall see later, sulphide spinels exhibit a very wide variety of properties, much greater than the diversity among comparable oxidic spinels. The reasons why this should be so are not particularly clear, but it is certain that the nature of sulphur, or rather its character as an anion, must play an important role. In table 2 some physical quantities associated with sulphur and oxygen are given. It seems natural to compare the two elements since later we shall often try to relate the properties of an oxide with those of a similar sulphide.

First we note that sulphur is a bigger atom than oxygen. This means that the outer electrons ($3s^2 3p^4$) will be better shielded from the nuclear charge than the ($2s^2 2p^4$) electrons in oxygen and it follows that the sulphur ion S^{2-} will be able to sustain greater deviations from

charge symmetry in its surroundings than will O^{2-} . As a result, there is the possibility of forming a larger number of sulphides than oxides with a given crystal structure. This follows from the way in which the crystal structure is determined by the Madelung and polarization energies. The Madelung energy is lowest when the anion is co-ordinated symmetrically by cations of opposite charge. In the event that the cations are not all similar, the position of the anion will be displaced towards the cation with the highest polarizing power. The larger the anion, the more polarization it can sustain and the less exacting the demands of the polarization energy. It follows quite naturally that a crystallographic distortion that occurs in an oxide may not occur in the corresponding sulphide or, if it does, then it will likely be at a much lower temperature.

Table 2. Some Properties of Oxygen and Sulphur.

| PROPERTY | SULPHUR | OXYGEN |
|----------------------------------|------------------|------------------|
| Atomic Number | 16 | 8 |
| Atomic Weight | 32.07 | 16 |
| Electron Configuration | (Ne) $3s^2 3p^4$ | (He) $2s^2 2p^4$ |
| Atomic Radius (Å) | 1.27 | - |
| Ionic Radius (X^{2-}) (Å) | 1.84 | 1.40 |
| Covalent Radius (Å) | 1.02 | 0.73 |
| Pauling Electronegativity Number | 2.5 | 3.5 |

Leaf blank to correct numbering.

Next we note that sulphur is much less electronegative than oxygen. On the Pauling scale {4} oxygen is assigned an electronegativity of 3.5 and is the most electronegative element known. Sulphur, on the other hand, is assigned 2.5 and is only slightly more electronegative than elements that generally behave as cations in chemical compounds. e.g. Fe is 1.8, Rh is 2.2. Two important results arise from this fact, regardless of the absolute accuracy of the Pauling scale {5}. In the first place, a sulphur lattice will find it difficult to sustain any but the lowest ionization states of the cations in it. Thus, although there is plenty of evidence for the simultaneous presence of Fe^{2+} and S^{2-} , e.g. FeS and hexagonal Fe_3S_4 , the evidence for the existence of Fe_2S_3 is at best dubious {6}, which suggests that Fe^{3+} is unstable in the sulphur lattice. Secondly, bonds between metal atoms and sulphur will be considerably less ionic in character than bonds between the same metal and oxygen. While there is no absolute difference between an ionic and a covalent bond, the fact that the bonding electrons are distributed differently between the bonded atoms makes a considerable difference to the physical character of the compound formed {7}. We shall make some further remarks about chemical bonding in the next section. Suffice for the moment to say that, where the bonding is strictly ionic, the forces between ions are non-directional whereas in the covalent bond, the bonds are highly directional. In the former

case, crystals can be pictured as arrays of close packed highly co-ordinated hard spheres but in the latter, the directionality and symmetry requirements of the bonds place severe limitations on the geometric arrangement of atoms.

The hard sphere model can be tested in the case of two isomorphous compounds, for example $(\text{Fe})\{\text{Cr}_2\}\text{O}_4$ and $(\text{Fe})\{\text{Cr}_2\}\text{S}_4$. In the spinel $(\text{Fe})\{\text{Cr}_2\}\text{O}_4$, the lattice parameter is 8.37 \AA at room temperature {8,9} whereas from table 2, we would have expected $\sim 7.94 \text{ \AA}$ for a close packed O^{2-} lattice, the indication being that the cation lattice has caused an expansion of the oxygen lattice. The $\text{Cr}^{3+}-\text{O}^{2-}$ distance is 2.09 \AA which compares favourably with the distance predicted by the ionic radii, i.e. 2.09 \AA . For the spinel $(\text{Fe})\{\text{Cr}_2\}\text{S}_4$, $a_0 = 9.996 \text{ \AA}$ {10,11} whereas, we calculate 10.05 \AA for a close stacked f.c.c. S^{2-} lattice, consideration of the $\text{Cr}^{3+}-\text{S}^{2-}$ distance leads to 2.35 \AA compared with a predicted value of 2.53 \AA . Obviously it is wrong to take the ionic radius of S^{2-} as a gauge for finding the lattice spacing, we should take a smaller number and this suggests at least some covalency in the cation anion bonds. Consideration of the A-site situation leads to $\text{Fe}^{2+}-\text{S}^{2-} = 2.43 \text{ \AA}$ which is considerably less than the hard sphere model value of 2.60 \AA .

One further feature of sulphur is its ability to form molecular ions $(\text{S}_2)^{=}$ even in the solid state.

Thus, the compound pyrite $\text{Fe}(\text{S}_2)^{\ominus}$ is extremely common as a natural mineral but its partner oxide $\text{Fe}(\text{O}_2)^{\ominus}$ is unknown. It is also noteworthy that sulphur compounds often demonstrate a strong tendency to support non-stoichiometric structures, usually in the form of vacancy ordered, cation deficient, compounds, the pyrrhotites for example. Such non stoichiometry greatly depletes the anion p orbitals since charge conservation demands holes in the valence band to compensate for the cation deficiency. Under the circumstances it is interesting to enquire why the complex anion $(\text{S}_2)^{\ominus}$ is not formed in such compounds. In the equilibrium situation two holes are localized on the anion, their energy is given by:

$$\frac{1}{4\pi\epsilon_0} \frac{e^2}{r} \quad \text{where } r \text{ is the separation of} \\ \text{of the Ne cores.}$$

The $(\text{S}_2)^{\ominus}$ bond energy is $\sim 102 \text{ kcal/mole}$ {12} hence we must have

$$r \sim \frac{e^2}{4\pi\epsilon_0} \frac{N_0}{5 \times 10^5} \sim 3.3 \text{ \AA}$$

In the pyrrhotites the $\text{S}^{2-} - \text{S}^{2-}$ separation is $\sim 3.54 \text{ \AA}$ {13}, somewhat larger than the result above. A perfect spinel with the lattice parameter of 9.35 \AA would have a $\text{S}^{2-} - \text{S}^{2-}$ separation $\sim 3.3 \text{ \AA}$. This is somewhat smaller than normally found. It seems plausible however, that in local defect structure regions, there may be a tendency towards $(\text{S}_2)^{\ominus}$

formation.

In summary, many of the differences between oxides and sulphides can be traced back to the different electronegativities of the two elements. For, although sulphur is similar chemically to oxygen, it will only form simple ionic structures with the most electropositive metals, otherwise the bonding is predominantly covalent and this fact must be taken into account when attempting to explain the observed properties of sulphide compounds.

3. CHEMICAL BONDING.

No new ground will be broken in this section, it is included in order to introduce various terms and concepts that will be useful later. The ideas are explained in a variety of text books of which {14,15,16} are as helpful as any.

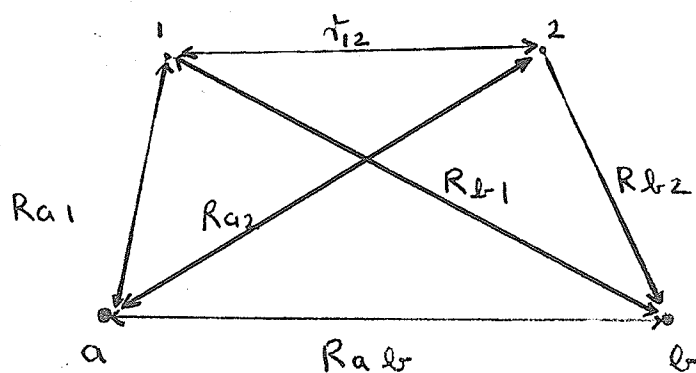


Figure 4. The hydrogen molecule problem.

Perhaps the best way to start is with an example and the simplest is that of the hydrogen molecule. We follow Tinkham [14] and, referring to figure 4, write the Hamiltonian as:

$$H = -1/2 \Delta_1^2 - 1/2 \Delta_2^2 - 1/R_{a_1} - 1/R_{a_2} - 1/R_{b_1} - 1/R_{b_2} + 1/r_{12} + 1/R_{ab}$$

There are no exact solutions to the problem so we need to approximate and the usual approach is to suppose that the electrons 1 and 2 will have hydrogenic wavefunctions associated with each of the nuclei a and b and that the overall wavefunction of the molecule will be a linear combination of such wavefunctions. We may consider two possibilities:

$$\psi_1 = N(a(1)+b(1))(a(2)+b(2))\{\alpha(1)\beta(2)-\beta(1)\alpha(2)\}2^{1/2}$$

$$\psi_2 = N(a(1)-b(1))(a(2)-b(2))\{\alpha(1)\beta(2)-\beta(1)\alpha(2)\}2^{1/2}$$

Where N is a normalization factor and α and β are spin functions necessary to give ψ_1 and ψ_2 the antisymmetrical properties required for fermions. If we just look at the space parts we have:

$$\psi_1 \sim a(1)a(2)+b(1)b(2)+a(1)b(2)+b(1)a(2)$$

$$\psi_2 \sim a(1)a(2)+b(1)b(2)-a(1)b(2)-b(1)a(2)$$

The "correct" wavefunction will presumably be some combination like:

$$\phi = C_1 \psi_1 + C_2 \psi_2$$

where C_1 and C_2 are varied until $\langle \phi | H | \phi \rangle$ is at a minimum.

What we shall do however, is just examine the terms in the spatial parts of ψ_1 and ψ_2 to see what they mean.

There are two sorts of terms. The first, like $a(1)a(2)$, clearly concentrates the electrons on the nuclei. The second, like $a(1)a(2)$ concentrates the charges between the nuclei, a situation which would appear to be most favourable since the electrons then experience attractive potentials from both nuclei. Terms like $a(1)a(2)$ are ionic, whereas $a(1)b(2)$ is a covalent term. The variational procedure determines the relative weights of each of the two types of term necessary to obtain the correct binding energy of the molecule. Consequently, we see that there is no physical difference between the terms ionic and covalent bonding they are parts of the same problem. Any confusion that may arise does so because of the approximate models used to describe the bonding in a given crystal.

Thus, in electrostatic Crystal Field Theory (C.F.T.), zero weight is placed on the covalent terms. In this model, charge is transferred completely from the outer orbitals of the more electropositive atom and placed in the empty orbitals of the more electronegative atom. The atoms become ions carrying formal charges and they are bound together electrostatically.

In the Valence Bond Theory (V.B.T.) {4}, zero weight is given to the ionic terms. Instead, appropriate

combinations of atomic orbitals are combined into a new set of hybrid orbitals and these are filled with electrons that belonged to the metal and the non-metal components. The bonds predicated are the most stable that can be formed between the metal and the ligand.

Molecular Orbital Theory (M.O.T.) {17,18} takes both aspects into account and it is basically a better approximation than either C.F.T. or V.B.T. The mechanics of the method have really been illustrated by the hydrogen molecule problem. What we have in ψ_1 and ψ_2 are two linear combinations of atomic orbitals (A.O.), (hydrogen s wave-functions). In one of them, the overlap region is added in, whereas it is subtracted out for the other. Two "molecular orbitals" are formed, the one having the overlap included is at a lower energy than the other because of the favourable potential for electrons between the nuclei. This is called a bonding orbital (denoted σ) whereas, the other is called an antibonding orbital (denoted σ^*).

At this point a diagram becomes necessary, and we refer to figure 5. In figure 5a, we show the situation just described. Note that the energy difference $\sigma^*-\sigma$ depends on the size of the overlap. If the overlap were zero, then the atomic orbitals would be unchanged in energy from that in the free atom, such orbitals are

A.O.

M.O. 17.

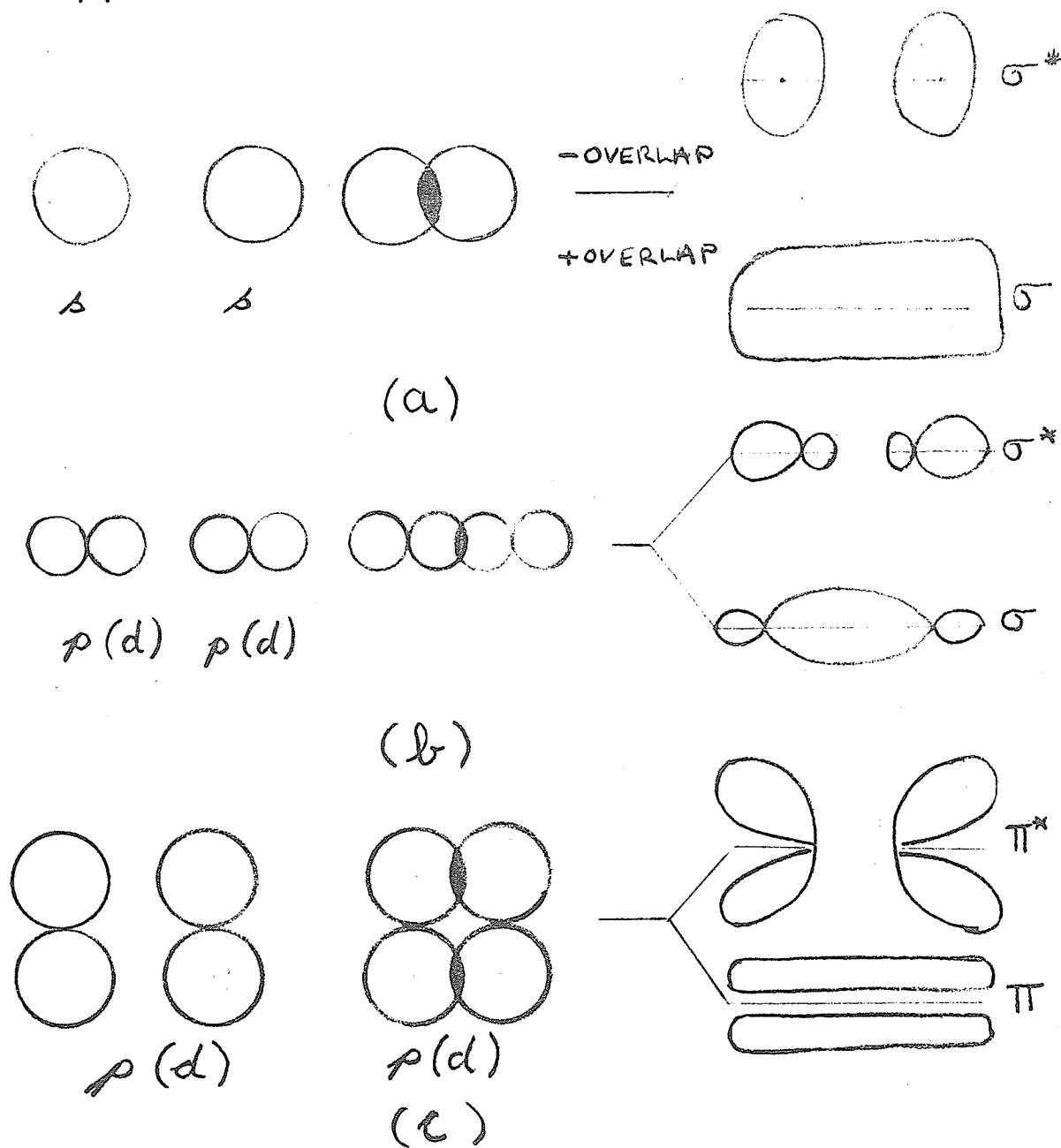


Figure 5. To illustrate various molecular orbitals formed from:

- (a) overlap of atomic s orbitals
- (b) overlap of atomic p or d orbitals in σ configuration
- (c) overlap of atomic p or d orbitals in π configuration.

then called non bonding. Figure 5b shows the same exercise but for p or d orbitals. Figure 5c shows another type of overlap possible for p and d orbitals because of the fact that these atomic orbitals have zero amplitude at the nucleus. The M.O. formed are denoted π and π^* . Charge resides above and below, but not on, the bond axis. A simple measure of bond strength is the numerical value of the angular function along the bond axis; hence, since in π bonding there is a plane along the bond axis where there is zero probability of finding an electron, π bonding is always weaker than σ bonding.

As we mentioned in section 2, the bigger the electronegativity difference in the atoms entering the bond the more ionic is the bond. In the M.O. picture, electronegativity enters via the energy difference of the A.O.'s used in forming each bonding and antibonding orbital. Thus the greater the electronegativity difference, the greater is the energy difference of like A.O.'s and the greater the ionic character of the bond formed.

To summarise then the following points are important;

- (i) The greater is the overlap of the A.O. from which the M.O. are formed, the greater is the energy difference between the bonding and anti-

bonding orbitals.

- (ii) The greater is the electronegativity difference of the two elements entering a bonding process, the greater is the energy difference of their corresponding A.O. and the more ionic is the bond formed.
- (iii) For A.O. with spherical symmetry only σ bonds can be formed, all other A.O. form both π and σ bonds. This fact is important in determining a parameter called crystal field splitting.
- (iv) Bonds formed from π overlaps are weaker than bonds formed from σ overlaps.

4. DESCRIPTIONS OF d-ELECTRONS.

There exist two extreme ways of describing electrons in solids viz. localized and collective. The explanations of the behaviour characteristic of the territory between these extremes is a subject of continuing theoretical investigation. There are however, several basic ideas that can be used to give at least a qualitative understanding of the situation and what follows is a very brief outline of these ideas. Useful references are {15,19}.

We start fairly far back and mention that from the solutions to the hydrogen atom problem, it is possible

to obtain zero order d-electron wavefunctions i.e. the solutions when the angular momentum quantum number $l=2$.

These have the angular dependencies:

$$\begin{aligned}\psi_{\pm 2} &\sim \sin^2\theta \exp\{\pm i2\phi\} \\ \psi_{\pm 1} &\sim \sin\theta \cos\theta \exp\{\pm i\phi\} \\ \psi_0 &\sim 3\cos^2\theta - 1\end{aligned}$$

(A co-ordinate system is defined in figure 6a)

Linear combinations of these angular functions are taken to form the real functions that are sketched in figures 6b, c, and d. The linear combinations used are:

$$\begin{aligned}\phi_1 &= \psi_0 \sim (2z^2 - x^2 - y^2) / r^2 \\ \phi_2 &= (\psi_2 + \psi_{-2}) / \sqrt{2} \sim (x^2 - y^2) / r^2 \\ \phi_3 &= (\psi_2 - \psi_{-2}) / \sqrt{2} \sim (xy) / r^2 \\ \phi_4 &= (\psi_1 + \psi_{-1}) / \sqrt{2} \sim (zx) / r^2 \\ \phi_5 &= (\psi_1 - \psi_{-1}) / \sqrt{2} \sim (yz) / r^2\end{aligned}$$

The first thing to note about the orbitals is that there are two types, a group of two that have lobes along the cartesian axes and a group of three that have lobes pointing between the axes. The first group ϕ_1 and ϕ_2 are denoted e_g the second group ϕ_3 , ϕ_4 , ϕ_5 are denoted t_{2g} . In the light of our previous remarks on the M.O. approach to bonding, we see that this division has some interesting consequences when the cation is co-ordinated by a set of ligands. Consider octahedral co-ordination, the e_g group are directed towards the ligands whereas the t_{2g} group are

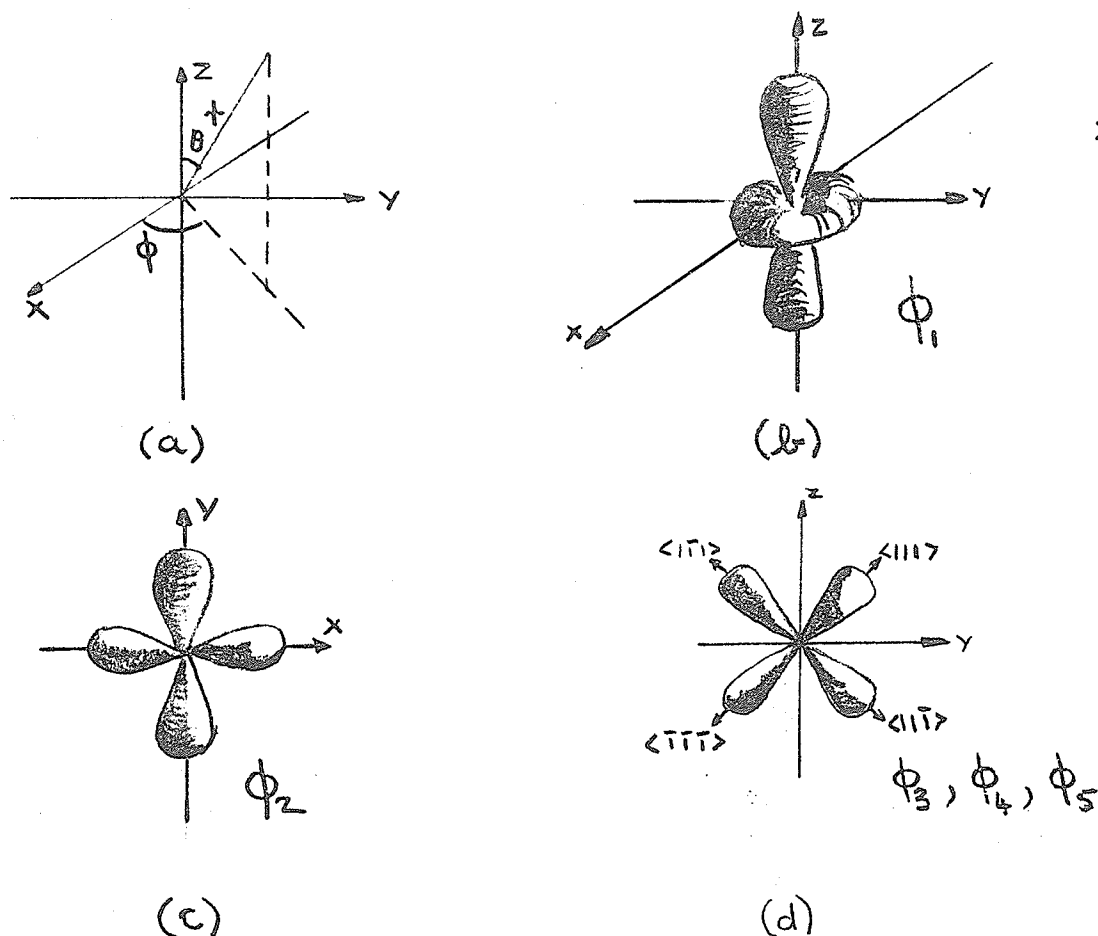


Figure 6. Illustrating d-orbitals.

directed between them. Hence the e_g group overlap with the anion orbitals and are therefore involved in σ type bonding and antibonding whereas, to a first approximation, the t_{2g} group are non-bonding. Consider then, the hypothetical $\{FeS_6\}$ complex shown in figure 7. All told, the cation s and p, and the anion σ orbitals combine to give 4 bonding M.O. and 4 antibonding M.O. The cation e_g group provide 2 more bonding and 2 more antibonding M.O. whereas the t_{2g} group are non-bonding. We expect the σ_d^* to fall within the band of $\sigma(s-p)$ orbitals but σ_d to fall below $\sigma^*(s-p)$ and above the non-bonding t_{2g} . Hence, with the

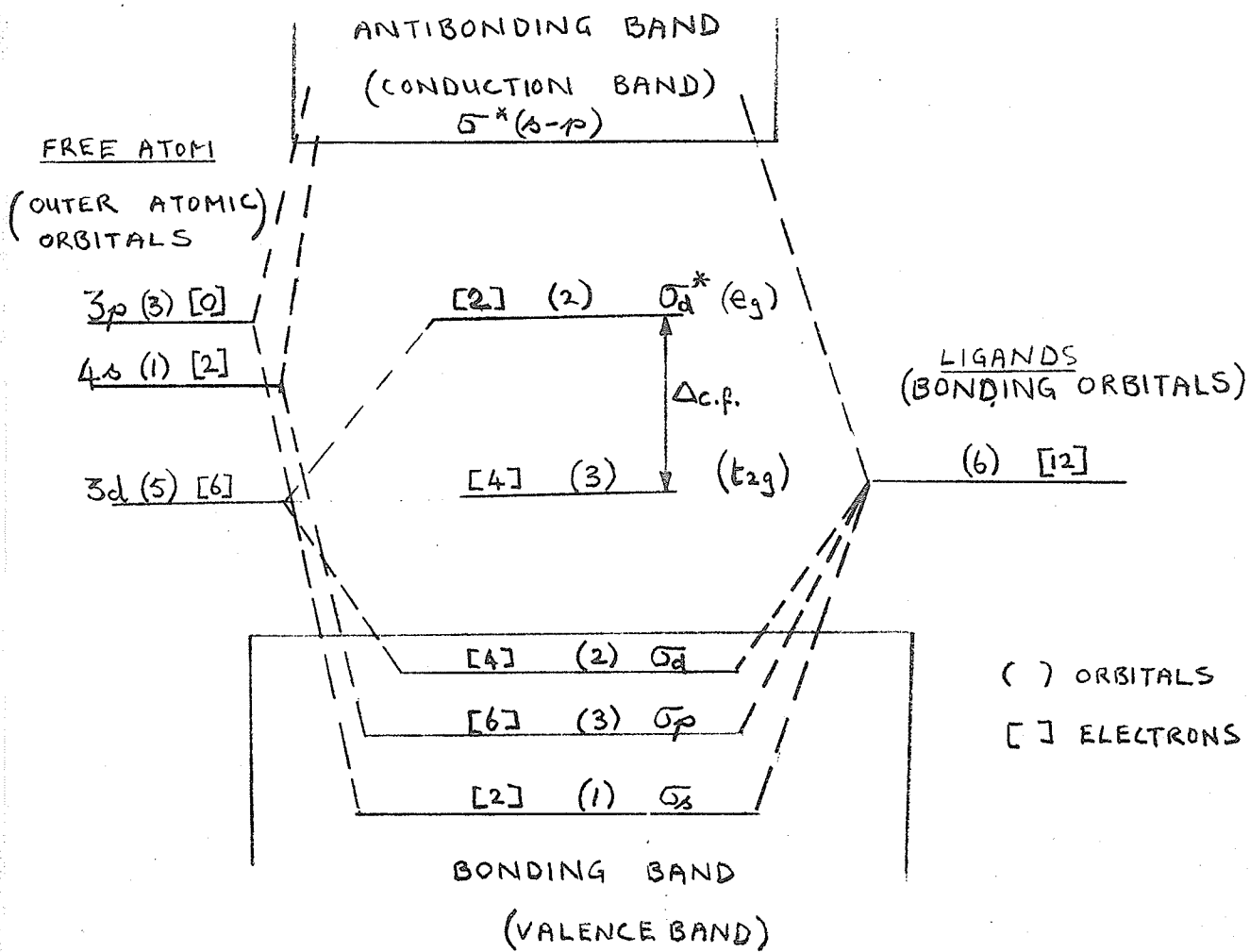


Figure 7. Bonding of a hypothetical FeS_6 complex.

available electrons, all the σ states are filled, all the $\sigma^*(s-p)$ orbitals are empty, between them is a gap in which lie the t_{2g} and the σ_d^* and there are six electrons to place in these 5 orbitals. Apparently, we could put all six in the t_{2g} or four in t_{2g} and two in σ_d^* . One of the consequences of the symmetry of the d-orbitals is that in a crystal, the degeneracy, normally 5 fold, is partially removed and a 3 fold plus a 2 fold degeneracy remains. Another is that problems about what to assign as the ground state arise. Of interest is the energy difference between t_{2g} and σ_d^* . In C.F.T., this is called the crystal field splitting, we shall retain that name but sometimes this splitting is called the ligand field splitting. Had we chosen to look at a tetrahedral site (4 co-ordination) we would have obtained a similar result but the roles of the e_g and t_{2g} groups would be reversed.

The ground state problem is tackled using Hund's rules and some intuition. Hund's first rule {20} states

Of the terms given by equivalent electrons,
those with greatest $(2S+1)$ are favoured and
of these, the most favourable is that with
the greatest L.

Here L and S are the total orbital and total spin angular momentum numbers. The word term here is a reference to a spectroscopic notation denoting different angular momentum states.

As an illustration, take a free Fe^{2+} ion.

There are 6 d-electrons so, making use of the Pauli Exclusion Principle, the maximum $(2S+1)$ is $(2(5/2-1/2)+1)=5$. For 6 d-electrons, we have $L=0,1,2$, there are therefore, S, P and D terms. From these terms, 5S , 5P , 5D we pick 5D as the ground state since this has the greatest L associated with it.

Hund's rule tells us that as far as possible electrons prefer to line up with their spins parallel. This is partly because in this fashion double occupancy of spatial orbitals is minimised and so, therefore, is electron-electron repulsion, but it is also because the magnetic exchange interaction among the electrons favour the largest possible $(2S+1)$. If we apply these considerations to the hypothetical complex of figure 7, we see that the first three electrons readily enter t_{2g} but the next two can only be placed in σ_d^* if:

$$\Delta_{ex} > \Delta_{c.f.}$$

where Δ_{ex} is the intra-atomic exchange energy. If this is the case, then we have the electron configuration

$^5T_{2g}(t_{2g}^4, \sigma_d^*2)$, if the reverse is true, then we will get $^1A_{1g}(t_{2g}^6, \sigma_d^*0)$. The short notations of the electron configurations $^5T_{2g}$, $^1A_{1g}$ are derived from the irreducible representations of cubic symmetry for the $(2L+1)$ dimensional representation of the continuous notation group. Table 3

below, shows how they are derived from the ground state term 5D . How the choice is made between the two high spin states ${}^5T_{2g}$ and 5E_g belonging to 5D is a matter of considering the degeneracy of the state formed. If the sixth electron is placed in t_{2g} then there are 3 ways of doing it and we require a ground state that is triply degenerate i.e. ${}^5T_{2g}$. The ${}^1A_{1g}$ state is called a low spin state, we have 3 doubly occupied orbitals, therefore, $L=0$, S is clearly zero, so the representation must be chosen from the terms consistent with 1S .

Table 3. Relationship Between Ground State Term and Decomposition into I.R.

| TERM | L | DECOMPOSITION | | | T_{1g} | T_{2g} | (Mulliken) (Bethe) (Degeneracy) | NUMBER OF TERMS |
|------|---|---------------|------------|------------|------------|------------|---------------------------------------|-----------------------|
| | | A_{1g} | A_{2g} | E_g | | | | |
| | | Γ_1 | Γ_2 | Γ_3 | Γ_4 | Γ_5 | | |
| | | 1 | 1 | 2 | 3 | 3 | | |
| S | 0 | 1 | 0 | 0 | 0 | 0 | 1 | |
| P | 1 | 0 | 0 | 0 | 1 | 0 | 1 | |
| D | 2 | 0 | 0 | 1 | 0 | 1 | 2 | |
| F | 3 | 0 | 1 | 0 | 1 | 1 | 3 | |
| G | 4 | 1 | 0 | 1 | 1 | 1 | 4 | |
| H | 5 | 0 | 0 | 1 | 2 | 1 | 4 | |
| I | 6 | 1 | 1 | 1 | 1 | 2 | 6 | |

It may be thought that because there are electrons in a partially filled M.O. σ_d^* , these electrons must behave like those in a metal. Consider now a whole collection of complexes such as that in figure 7, σ_d^* certainly does extend throughout the whole crystal but because it is antibonding, electrons in it belong to the cation sublattice. As long as the coulomb potential U^1 , that normally traps the free atom's electrons in the potential well of the nucleus, remains large enough in the crystal to split σ_d^* into up spin and down spin states, then it is still reasonable to describe the cations in terms of the crystal field states like ${}^5T_{2g}$ etc. {21}. This brings us rather abruptly to the nub of this section.

Consider a cation in a crystal and suppose that the d-electrons are associated with it in much the same way as they would be were it a free atom, ie. the cation has some well defined crystal field state corresponding to an ionization state M^{n+} . Consider removing an electron from this ion so that M^{n+} becomes $M^{(n+1)+}$. This requires the energy U_1 by which the two states are separated. In a crystal however, we must arrange for the electron to become trapped somewhere else, presumably on a like, neighbouring cation whose state changes from M^{n+} to $M^{(n-1)+}$. Suppose the net amount of energy required for transfer is U , and assume that a transfer energy b is available. So long as $U > b$ then clearly, a localized electron picture holds

but if $U \ll b$ then a collective electron description is necessary and the assignment of crystal field states and formal valencies becomes meaningless.

A little more detail will perhaps clarify the situation. We have already hinted that U_1 is not the same as the free atom potential U^1 . Consider for example the d-orbitals, they are no longer equivalent so that if there are more than 3 d-electrons, some will be less stable than others. Hence U^1 is lowered by the surrounding atoms. Electrons in orbitals closest to surrounding atoms feel their parent nucleus' potential less strongly so it appears that the influence of the surroundings is in the nature of a screening effect. As the screening becomes larger and larger, so the electrons become less and less tightly bound, so that the net transfer energy U is of the form:

$$U \sim \frac{e^2}{r_{12}} \exp(-\xi r_{12})$$

where r_{12} is the separation of the cations and ξ is a screening parameter. To increase the screening effect, it appears from the arguments concerning the stability of the d-orbitals, that we must increase the overlap with the anion orbitals. For these two cations we must, by analogy, decrease r_{12} , but this would tend to increase U so we conclude that ξ must be a function that increases with increasing overlap.

The transfer energy available from the overlap

integral is of the form:

$$b \sim \int \psi_2^* h \psi_1 d\tau$$

where h represents the change in local potential at cation 1 as a result of the presence of cation 2. It is therefore clear that b increases as the overlap increases, and since U decreases at the same time, there must be a critical value of b where the localized picture goes over to a collective picture for the d-electrons [21].

The wavefunctions ψ_1 and ψ_2 are d-electron wavefunctions but they cannot be the simple zero order functions ϕ_1, ϕ_2 etc; because of the overlap with the anions, at least in compounds that we shall be considering. Some account must be taken of the covalent, mixing of the anion functions. Therefore, for octahedral sites, we might for example write:

$$\psi_e = N_\sigma (\phi_e + \lambda_\sigma \phi_\sigma) \text{ and } \psi_t = N_\pi (\phi_t + \lambda_\pi \phi_\pi)$$

Where ϕ_e and ϕ_t represent the functions associated with the groups of e_g and t_{2g} orbitals, λ_σ and λ_π are covalent mixing parameters, ϕ_σ and ϕ_π are site symmetrized s, p_σ and p_π orbitals and N_σ and N_π are normalizing constants. On tetrahedral sites, it is the t_{2g} orbitals that σ bond and the e_g that π bond and we might write:

$$\psi_e = N_\pi (\phi_e + \lambda_\pi \phi_\pi) \text{ and } \psi_t = N_\sigma (\phi_t + \lambda_\sigma \phi_\sigma)$$

although the $\lambda_{\pi}, \lambda_{\sigma}, \phi_{\pi}, \phi_{\sigma}$ will be different for the two sites.

Naturally, direct experimental measurement of any one of the parameters involved, is fraught with difficulty because of their interdependence. A study of compounds can however, be justified because it is possible to at least draw inferences about the ways in which various factors must be influencing the observations. For example, in sulphide spinels, direct d-electron overlap is unlikely because the cation separations are determined by the stacking of the larger anions. Therefore, drastic changes in observed properties in comparable compounds indicate the role of cation-anion covalency.

To sum up then, we can say that the character of d-electrons in a compound will be determined by several factors. In the localized regime, the initial ionization state and the extent to which covalent overlap with anionic p orbitals de-stabilizes the d-orbitals are probably the most important. The properties of compounds that give evidence of this character are activated electrical conduction, paramagnetic Curie constants that are consistent with well defined ionization states, and low temperature saturation magnetizations consistent with localized spins. In the collective regime, metallic behaviour is expected, the inference being that the proximity of other atoms so

completely shields electrons from the nuclear charges that there is no question of electrons belonging to any particular nucleus. In the intermediate regime there are no obvious guide lines but intuitively we expect low activation energy conduction with rather low resistivity indicating broad bands separated by small energy gaps, the inference being that b is close to but smaller than some critical value b_c ; or semi-metallic conductivity i.e. little or no temperature dependence, the inference being that $b \gtrsim b_c$.

5. PREPARATION OF SULPHIDE SPINELS.

The method used to prepare most of the compounds studied is that described in {10}. There are however, several technicalities that are worth emphasizing because it is rarely that complete details of experimental preparations are found.

Stoichiometric quantities of the required elements are weighed and mixed together thoroughly. Mixing may be effected in a ball mill or by hand with a pestle and mortar. Ball milling is most satisfactory when large quantities of the initial mix are required, hand grinding is satisfactory for small quantities. Whether large or small quantities are prepared depends mainly on the price of the reagents involved, a factor that is determined by the purity and rarity.

For samples used in magnetization measurements we generally used reagent grade elements (99.9% assay), so large quantities ~100g could be made and the initial mixing was done in a glass ball mill. Some of our Mössbauer samples needed to be enriched in the isotope ^{57}Fe for good Mössbauer absorption. This isotope comes 99.999% pure so generally we used spectrographically pure reagents for the rest of the elements. We, therefore, made only small quantities ~1g and hand ground the elements in an agate mortar and pestle. We also used spectrographically pure starting elements when conductivity specimens were prepared.

After grinding, the mix was introduced into quartz or vycor ampuls, evacuated and sealed. These ampuls were made in the form of test tubes with a necked portion about 1 inch long, 3 inches from the closed end, the open end being roughly 2 inches from the necked region. The ampuls were thoroughly cleaned before use by soaking them in an 80:20 $\text{HCl}/\text{H}_2\text{O}$ mixture and washing with distilled water. They were vacuum dried prior to use. The evacuation of the ampul with the compound took ~12 hours, the nominal pressure was 10^{-5} mmHg and sealing was accomplished with an oxy-acetylene torch.

After sealing it was necessary to carefully remove all traces of grease from the outside of the ampul. This can be done with water and detergent or a high grade

acetone but lower grade solvents must be avoided since they are full of grease themselves. If grease is left on the ampul, it will react and etch the surface, thus, weakening it so that explosions occur or oxidation of the specimen results.

The actual firing must be approached with caution on account of the high vapour pressure of sulphur. Three precautionary measures may be adopted. First, the quantity of mix contained in the ampul can be kept to a minimum, in an ampul 3 inches long $\frac{3}{4}$ inch diameter and 1-2 mm wall thickness; we found 3g was a safe quantity. Second, some of the free sulphur can be eliminated by using stable sulphides instead of elements eg CdS instead of Cd, transition metal sulphides were not used however, on account of their tendency towards non-stoichiometry. Third, the firing can be done in stages. Thus, we held the temperature below 400°C for the first 5 hours so that some degree of reaction occurred and reduced the free sulphur concentration. The temperature was then raised slowly to $850 - 900^{\circ}\text{C}$ for the next 45 hours after which time the ampul was allowed to cool slowly in the furnace. After this treatment, the sample was in the form of a grey/black sintered lump. This product was thoroughly reground, pelleted, resealed and fired for a further 48 hours at 850°C . At the end of this time, the furnace temperature was briefly raised to 1100°C and then the ampul was

allowed to cool in the furnace. We have tried to give an indication of the improvement in quality that results after two firings by showing in figure 8 part of the FeK α x-ray powder diffraction pattern of one of our samples (a) after 1 firing (b) after the second firing. Notice how much sharper are the high angle reflections in (b) compared with (a) also note that in (b) the x-ray doublet is clearly resolved whereas in (a), the diffuse nature of the reflections makes doublet resolution impossible. This clarity indicated good homogeneity and strain free crystallites of good size. Diffuse lines result from inhomogeneity, excessive random strain, or a small particle size.

The product after the second firing was not in a form suitable for conductivity measurements, partly because pieces tended to break off the pellets leaving them irregularly shaped, but mainly because the density was low. We, therefore, inserted another stage in the preparation when conductivity samples were required. After the first firing and grinding, we pressure sintered 0.5g lots into rectangular section pellets $\sim 1/4 \times 1/4 \times 1/8$ inches. This pressure sintering was accomplished by pressing the reacted powder in a tool steel die at 70,000 psi and 500° C for 8 hours in a nitrogen atmosphere. After this treatment, the pellets were hard enough for their surfaces to be cleaned by mechanical grinding on

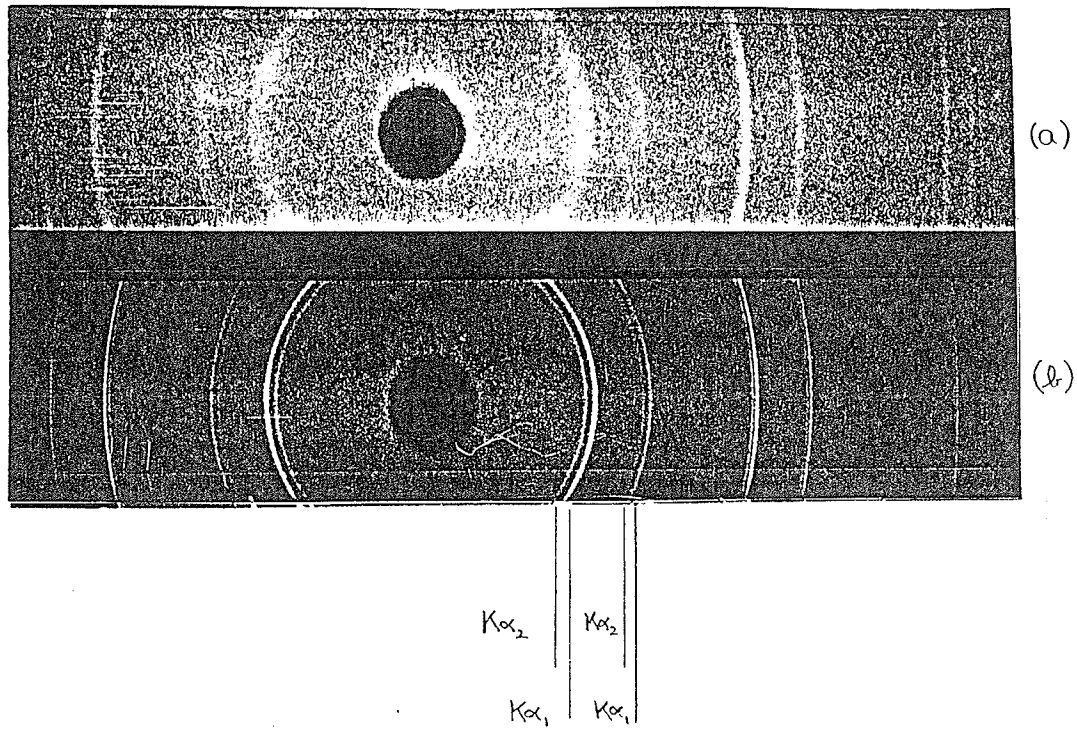


Figure 8. Illustrating the effect of firing:

- (a) Fired 48 h. 850° C furnace cooled;
- (b) Fired 96 h. 850° C with intermediate regrinding after 48 h. furnace cooled.

fine corundum paper. These pellets were then fired and the resulting product was a regularly shaped piece with density close to the theoretical x-ray density, to be specific, we obtained between 95 and 97% theoretical density.

One of the problems encountered in magnetic measurements on compounds containing more than one cation is that of cation distribution if there is more than one type of crystallographic site. To avoid this problem, we decided to use cations with well defined site preferences, and to do the heat treatments carefully so that full advantage could be taken of the site preferences. While this tends to be somewhat restrictive, it is worthwhile because the problem of deciding whether cation distribution is seriously affecting results does not arise. Thus, good B-site cations are Cr^{3+} and Rh^{3+} . The site preference of Cr^{3+} is a result of the two empty e_g orbitals that form both σ and π bonds on the octahedral site {22}. Similar considerations are probably applicable to Rh^{3+} which is low spin ($^1A_{1g}$) on octahedral sites. Good A-site cations are Cd and Zn. Iron has no particular preference for either site but it has little compatibility with Cr^{3+} on octahedral sites, from {23}, it is apparent that perhaps 10% of the octahedral sites can be doped with Fe when Cr occupies the rest. The situation is different in oxides {24}.

Literature Cited in Chapter I

1. E.W. Gorter, Philips. Res. Rept., 2, 295, 1954.
2. J.B. Goodenough, Magnetism Vol. III, Edited by G. T. Rado and H. Suhl, Academic Press, New York, 1963.
3. W.H. Bragg, Nature, 95, 561, 1915, Phil. Mag. 30, 305, 1915.
4. L. Pauling, The Nature of the Chemical Bond, Cornell University Press, 1960.
5. J.C. Philips, Rev. Mod. Phys., 42, 317, 1970.
6. J.C. Ward, Rev. Pure and Appl. Chem., 20, 175, 1970.
7. R.C. Evans, An Introduction to Crystal Chemistry, Cambridge University Press, 1966.
8. F.K. Lotgering, Philips, Res. Rept., 11, 190, 1956.
9. E.R. Whipple and A. Wold, J. Inorg. Nucl. Chem., 24, 23, 1962.
10. R.J. Bouchard, P.A. Russo, and A. Wold, J. Inorg. Chem., 4, 685, 1965.
11. M.R. Spender and A.H. Morrish, Can. J. Phys., 49, 2659, 1972.
12. Handbook of Chemistry and Physics, Edited by R.C. Weast, Chemical Rubber Company, Cleaveland, Ohio, 1968.
13. H. Haraldsen, Z. Anorg. Allg. Chem., 231, 78, 1937.
14. M. Tinkham, Group Theory and Quantum Mechanics, McGraw Hill, 1964.
15. J.B. Goodenough, Magnetism and the Chemical Bond, John Wiley, New York, 1966.
16. F. Basolo and R. Johnson, Co-ordination Chemistry, W.A. Benjamin, New York, 1964.
17. R.S. Mulliken, Phys. Rev., 32, 186, 761, 1928; 33, 730, 1928.

18. F. Hund, Z. Physik., 51, 759, 1928; 63, 719, 1930.
19. N.F. Mott and H. Jones, Metals and Alloys, Dover Press, New York, 1958.
20. See for Example A.H. Morrish in The Physical Principles of Magnetism, Page 36, John Wiley, New York, 1965.
21. J.B. Goodenough, J. Phys. Chem. Solids, 30, 261, 1969.
22. J.B. Goodenough, J. Phys. Chem. Solids, 25, 151, 1964.
23. M. Robbins, R. Wolfe, A.J. Kurtzig, R.C. Sherwood, and M.A. Miksovsky, J. Appl. Phys., 41, 1086, 1970.
24. M.H. Francombe, J. Phys Chem. Solids, 3, 37, 1957.

II BASIC THEORY, EQUIPMENT AND TECHNIQUES.

This chapter has three sections. These sections are subdivided into various parts. Thus section 1 relates to the magnetization measurements, section 2 to the electrical measurements and section 3 to the Mössbauer Effect spectroscopy. The first part of each section reviews mostly well known theory relating to the type of experiment performed, the second part describes experimental equipment and the third part indicates the experimental procedures adopted. Section 3 deviates somewhat from this recipe but not in a manner that is likely to be confusing.

In preparing the parts on basic theory we have made use of a number of standard text books. Thus, we found {1,2,3} useful in preparing the notes in section 1.1 and in section 2.1 we have been guided by {4,5}. There are many good descriptions of the Mössbauer Effect and the observable hyperfine interactions, we found {6,7,8} usefull. We do not wish to

imply that other works were ignored, there are references to various papers and reviews but sometimes we are forgetful of our sources of common knowledge.

1. MAGNETIZATION MEASUREMENTS.

1.1 Theoretical Background.

There are several topics that ought to be introduced in this section for these days, magnetism covers a wide range of phenomena, but only a few of them can be briefly dealt with here. All materials exhibit the phenomenon of diamagnetism when a field is applied, by virtue of the motion of the electrons and Lenz's Law. Paramagnetism is the magnetism associated with ions that have well localized electrons in partially filled d-subshells. If a field H_{app} is applied to an array of such ions subject to the condition that:

$$g\mu_B H_{app} \ll kT \ll \Delta$$

where g is the gyromagnetic factor μ_B is the Bohr magneton Δ is the multiplet separation and T is the absolute temperature, then a magnetization arises because the field tends to align the electronic angular momenta associated with each ion. The results of an experiment where H_{app} and T are varied show that, the magnetization at constant temperature is proportional

to the applied field and the molar susceptibility

$$\chi_M = M(T)/H_{app}$$

is proportional to the inverse temperature. Thus,

$$\chi_M = C_M/T$$

where C_M is the molar Curie constant given by:

$$C_M = N_O g^2 \mu_B^2 J(J+1)/3k \quad (II.1)$$

The quantity $g J(J+1)^{1/2}$ is called the effective magnetic moment μ_{eff} and is clearly given by:

$$\mu_{eff} = \left[\frac{3kC_M}{N_O \mu_B^2} \right]^{1/2} = \sqrt{8C_M} \quad (II.2)$$

If the orbital angular momentum is zero then $g=2$ and S is used instead of J where S is as defined in Chapter 1 section 4 and $J=L+S$ or $L-S$ as the d -sub-shell has more or less than 5 electrons. If there is more than one sort of ion present, then each contributes its own μ_{eff} and a term like (II.1) must be added for each type of ion in the array.

The topic of superparamagnetism is one that is gaining popularity lately and, although we shall not deal with it here, a short section is devoted to the subject in Chapter III section 1.

The phenomena discussed so far have a common feature; they are not associated with any long range magnetic ordering. If this parameter is introduced then there exists several ways in

which the ground state of the spin system may be described. There are, however, four broad categories that may be distinguished:

- (i) Ferromagnetic,
- (ii) Antiferromagnetic,
- (iii) Ferrimagnetic,
- (iv) Noncollinear.

In order to decide which of these possibilities pertains to a given compound, consideration must be given to a number of factors. A rather thorough account of the procedures involved is given in {9}. This aspect of long range order will not particularly concern us, what we shall do is define what is meant by each of the terms.

A ferromagnetic ground state implies a parallel array of equivalent spins on equivalent crystallographic sites. Such ordering leads to spontaneous magnetism below some critical temperature T_c called the Curie Temperature. At low temperatures $\ll T_c$ a saturation magnetization is measured, corresponding to complete alignment of all the spins. At higher temperatures the magnetization is smaller as thermal energy tends to randomize the spin system. The spontaneous magnetization, associated with long range order, disappears at T_c although a magnetization associated with short range order may persist up to

perhaps $2T_c$. Far enough above T_c the magnetic susceptibility follows a relationship:

$$\chi_M = C_M / (T - \theta) \quad (\text{II.3})$$

called the Curie-Weiss Law and θ is the positive intercept on the temperature axis when χ_M^{-1} is plotted against T . The parameter θ is the Weiss parameter.

An antiferromagnetic ground state implies the existence of at least two magnetic sublattices arranged so that an ion on sublattice 1 has nearest neighbours that belong to sublattice 2 only (and vice-versa). The ions on the two sublattices are identical and their spins are aligned antiparallel. The temperature at which this type of long range order occurs is called the Néel point, T_N . Below T_N the sublattices have magnetizations of equal magnitude oppositely directed. Crystalline anisotropy determines the common axis of the magnetizations and the magnetic susceptibility is different as a field is applied \parallel or \perp to this axis. Thus, \perp to the easy axis the susceptibility is roughly constant with temperature whereas \parallel to the easy axis the susceptibility increases with increasing temperature up to T_N . There is no spontaneous magnetization, i.e. $\underline{M} \rightarrow 0$ as $\underline{H}_{\text{app}} \rightarrow 0$. The Néel point is often illdefined in magnetization

measurements and may only be detectable because the susceptibility follows a Curie-Weiss Law above T_N i.e.

$$\chi_M = C_M / (T + \theta) \quad (\text{II.4})$$

Here, θ is the Weiss parameter and is the negative intercept on the temperature axis of a χ_M^{-1} -T plot

A ferrimagnetic ground state has some of the characteristics of both the previous arrangements. Thus, there are at least two magnetic sublattices that may have ions of different types associated with them. It is easier to consider a specific example and we shall consider the spinel structure and for simplicity, we shall lump the B-sites together and all the A-sites together and call them the B-sublattice and the A-sublattice. Thus, even if the ions on A and B are identical, ferrimagnetism arises when \underline{M}_A is oppositely directed to \underline{M}_B since $|\underline{M}_A| = \frac{1}{2} |\underline{M}_B|$. Hence, a ferrimagnet shows a spontaneous magnetization below some critical temperature called the Ferrimagnetic Néel point, T_{FN} . In this definition, \underline{M}_A is always collinear with \underline{M}_B so the low temperature saturation magnetization depends on the number and magnitude of the spins associated with A and B. The temperature dependence of the spontaneous magnetization depends on the individual temperature dependencies of \underline{M}_A and \underline{M}_B in accordance with theoretical predictions by Néel {10}

for which a large body of experimental evidence exists {11,12}. Just above T_{FN} the susceptibility is extremely complex but far enough above T_{FN} the susceptibility follows a Curie-Weiss Law:

$$\chi_M = C_M / (T + \theta) \quad (II.5)$$

similar to an antiferromagnet. The constant C_M however, is complicated because of the presence of different ions:

$$C_M = C_A + C_B = \sum_i N_i g_i^2 \mu_B^2 J_i (J_i + 1) / 3k + \sum_j N_j g_j^2 \mu_B^2 J_j (J_j + 1) / 3k \quad (II.6)$$

where N_i is the number of ions per mole of compound with angular momentum J_i on sublattice A etc.

Non-Collinear spin arrangements arise because of competing magnetic interactions or anisotropy axes. In {9} there is a detailed review of the theoretical basis for such spin arrangements. A good deal of work has been done on spinels. For example in {13} the relative stabilities of the Néel (Ferrimagnetic) arrangement, the triangular (Jaffet-Kittel) and the ferromagnetic spiral are considered. In {14} the relative stabilities of the antiferromagnetic and the ferromagnetic spiral arrangements are considered. A concise account of the subject with various examples is given in {2}. The existence of Helical spin arrangements was predicted by the authors of {15,16,17}. Canted

antiferromagnetism and weak ferromagnetism also represent examples of non-collinear spin arrangements. The first arises from single ion anisotropy terms and the example of NiF_2 is dealt with in {2}, the second arises from antisymmetric spin interactions first considered by the author of {18} to explain the weak ferromagnetism in Haematite.

At this point we give some consideration to the type of information that we can obtain in our lab. and see in what ways this can be used to draw inferences about the microscopic behaviour of the material. Regardless of whether there is a long range ordering temperature or not, we can measure the magnetic susceptibility and, providing the compound is not simply diamagnetic, we shall determine C_M . If the data yield a non zero θ then we ought to be able to find the long range ordering temperature. The Curie constant yields information about μ_{eff} and the sign of θ will yield up information regarding the principal magnetic interaction in the compound, (This point will be dealt with later.). If θ is positive then we shall probably be able to measure a spontaneous magnetization and find an approximate value of the long range ordering temperature. For a ferromagnet, the low temperature

magnetic moment is given by:

$$\underline{\mu} = ngJ$$

in units of μ_B /molecule where n is the number of ions per molecule. A measurement of $\underline{\mu}$ therefore, yields information that can be compared with deductions made from the value of C_M . For a ferri-magnet the low temperature magnetization must be compared to values deduced from the various possible ways of arranging the sublattice magnetizations. It is also of interest to determine whether there is any difference between θ and T_C or T_N ; how nearly saturation can be approached, and the temperature dependence of the spontaneous magnetization. To obtain useful information from measurements of θ and T_C or T_N , we need to consider rather specific models so we look at this problem next.

At the basis of the concept of a magnetic exchange interaction is the Pauli Exclusion Principle and for localized electrons in orthogonal orbitals the spin dependent contributions to the total energy of a system can often be written as the operator {2}

$$\tilde{H}_H = -2 \sum_{\langle ij \rangle} J_{ij} \underline{S}_i \cdot \underline{S}_j \quad (\text{II.7})$$

this expression is commonly known as the Heisenberg-Dirac Hamiltonian. From a classical viewpoint J_{ij} is the exchange interaction energy of two spin vectors \underline{S}_i and \underline{S}_j and a parallel or antiparallel alignment of the spins is favoured as J_{ij} is positive or negative.

In the Weiss Molecular Field Theory, we take a system of identical spins on equivalent crystal sites and consider one magnetic atom. The interaction of this atom with the rest of the system is represented by an effective field proportional to the average magnetization of the crystal, i.e.

$$\underline{H}_{\text{eff}} = N \frac{M}{W} \quad (\text{II.8})$$

where N_W is called the molecular field constant.

The single ion Heisenberg Hamiltonian is from (II.7):

$$\tilde{H} = -2J \underline{S}_i \cdot \sum_{j=1}^Z \underline{S}_j \quad (\text{II.9})$$

where Z is the number of nearest neighbours to the i^{th} ion and J_{ij} has been replaced by J since all Z interactions are identical. The magnetic energy of the ion is:

$$\underline{H} = \underline{\mu} \cdot \underline{H}_{\text{eff}} \quad (\text{II.10})$$

where $\underline{\mu}$ is the magnetic moment which we consider here to be the spin only value, i.e.

$$\underline{\mu} = -g \mu_B \underline{S} \quad (\text{II.11})$$

so from (II.10) and (II.11):

$$\tilde{H} = -g \mu_B \underline{S} \cdot \underline{H}_{\text{eff}} \quad (\text{II.12})$$

equating (II.9) and (II.12):

$$\underline{H}_{\text{eff}} = 2J/g \mu_B \sum_{j=1}^Z \underline{S}_j \quad (\text{II.13})$$

Now, with the assumption that all magnetic ions are identical, we replace the \underline{S}_j by the average value $\langle \underline{S} \rangle$ and the average magnetization is then:

$$\langle \underline{M} \rangle = Ng \mu_B \langle \underline{S}_j \rangle \quad (\text{II.14})$$

so from (II.14) and (II.13):

$$H_{\text{eff}} = \frac{2Jz}{g\mu_B} S_j = \frac{2Jz}{Ng^2\mu_B^2} \frac{M}{N} \quad (\text{II.15})$$

With these results one finds by employing well known methods {1} that:

$$\theta = T_c = \frac{2JzS(S+1)}{3k} \quad (\text{II.16})$$

for a ferromagnet and:

$$\theta = -T_N = \frac{2JzS(S+1)}{3k} \quad (\text{II.17})$$

for an antiferromagnet, with consideration of just the intersublattice exchange.

The reason why θ and T_c are identical in this model is that each spin is considered to be statistically independent of all the others.

Thus, if we write down a short range order parameter:

$$\chi = \frac{\langle S_i \cdot S_j \rangle}{S \cdot S} = \frac{\langle S_i \rangle \langle S_j \rangle}{S \cdot S}$$

because of the statistical independence.

Introducing the reduced magnetization σ as:

$$\sigma = \frac{\langle S_z \rangle}{S}$$

we have:

$$\begin{aligned} \chi &= \sigma^2 & T < T_c \\ &= 0 & T > T_c \end{aligned}$$

Thus any short range order is proportional to the square of the long range order parameter and there is no difference between θ and T_c

There are other effective field theories, perhaps the simplest to include here is that commonly called the Oguchi method. In this model the statistical correlation of the spins is included explicitly for one randomly chosen pair consisting of a central ion and one of its z nearest neighbours. The Hamiltonian becomes:

$$\tilde{H}_p = -2J \underline{S}_i \cdot \underline{S}_j - g \mu_B (S_{iz} + S_{jz}) \underline{H} \quad (\text{II.18})$$

where:

$$\underline{H} = \underline{H}_{\text{eff}} + \underline{H}_{\text{app}}$$

and H_{eff} is the effective field due to the $(z-1)$ nearest neighbours. The properties of the system can be found by seeking the simultaneous eigenstates of $\underline{S}_i \cdot \underline{S}_j$ and $(S_{iz} + S_{jz})$. The effective field is found in a method similar to that described for M.F.T. and the expression:

$$\underline{H}_{\text{eff}} = \frac{2(z-1)J}{Ng^2 \mu_B} \cdot \underline{M} \quad (\text{II.19})$$

is obtained. It differs from the Weiss Field expression only in that $z \rightarrow (z-1)$ because, of the z interactions between the central atom and its neighbours, one has been treated exactly and the other $(z-1)$ are treated in the M.F. approximation. In appendix A, various expressions are derived in the case of $z=6$ $S=3/2$. We find for example that:

$$J/kT_c = 0.0688 \quad \text{while} \quad J/k\theta = 0.0666, \quad \theta/T_c = 1.03$$

These may be compared with the M.F.T. results that:

$$J/kT_c = J/k\theta = 0.0666 \quad \theta/T_c = 1$$

In addition, the model predicts finite short range order above the Curie Temperature and for high enough temperatures the short range order parameter:

$$\chi \propto J/kT.$$

In fact, the Oguchi model does not represent a great improvement over M.F.T. but the concept of pair correlation is used with more success in model known as the Constant Coupling approximation.

In this model, the effective field is regarded as a parameter to be determined self consistently (In the previous models H_{eff} was included explicitly). Specifically, {2} the model predicts for $z=6$ $S=1/2$:

$$\theta/T_c = 1.65$$

In fact, we have greatly oversimplified the problem by considering only one of the many possible exchange interactions i.e. nearest neighbours only. Molecular Field Theory does have a rather unique advantage over most other effective field theories in that a large number of interactions may be considered. If we, for example, consider the antiferromagnet, then with just the inclusion of second nearest neighbours, several interesting results emerge, among them the fact that:

$$-3 < \theta/T_N < +1$$

from which we see that a positive value of θ can be associated with an antiferromagnet, this occurs when the ratio of first to second neighbour interaction is less than -1. We can also assert that ferromagnetism is impossible if the nearest neighbour interaction is negative, no matter how large and positive the second neighbour interaction may be. However, as a rough guide, θ gives the sign of the nearest neighbour exchange interaction and in certain simple systems, it is possible {19} to deduce the magnitude of this interaction. In general, we should not expect θ and T_C , T_N to be equal and we should expect at least some degree of short range order above the long range ordering temperature.

Finally, this section would not be complete without a note on the nature of magnetic interactions and their relationship to the chemical bonding of the crystal. We have seen the expression for the Heisenberg-Dirac Hamiltonian that is at the heart of magnetic exchange but this expression does not account properly for the strengths nor the observed systematic behaviour of interactions between cations. For example, it is possible to calculate the interaction energy of two spins assuming it to be of the dipole-dipole type. It is found {1} that the inter-

action falls off as $1/r^3$ where r is the separation of the ions. There are many systems where the strength of the exchange interaction increases with increasing r . A solution to the problem was suggested in {20} extended in {21} and more recently a set of guide lines called The Goodenough-Kanamori rules of superexchange{22,23} have been given.

We now set down these rules:

- (1) Superexchange between two empty or two half filled orbitals will be negative (antiferromagnetic);
- (2) Superexchange between a half filled and an empty orbital will be positive.

The physical explanations of these rules are as follows: Because of the Pauli Principle electron transfer between half filled orbitals can only occur without a change of spin (i.e. spin angular momentum is conserved), if the two cations involved have their net spins oppositely directed, i.e. an antiferromagnetic alignment. The Pauli Principle allows either kind of alignment in the case of transfer from a half filled or a full orbital to an empty orbital but Hund's rule stabilizes the highest possible spin states so that ferromagnetic alignment is preferred.

Superexchange as such, is a mechanism by which neighbouring, though widely separated, cations may exchange electrons virtually with the aid of an intermediary anion whose state does not change. The important parameters involved are the net transfer energy U and the transfer integral b that we already met in Chapter I section 4.

1.2 The Magnetometer.

In our laboratory, we have a vibrating sample magnetometer ⁽¹⁾. The magnetic fields used in experiments are supplied by an electromagnet to a maximum of 18kOe ⁽²⁾. The field is regulated by a precision control unit ⁽²⁾, for which the field sensor is a gaussmeter probe ⁽³⁾. The magnet is water cooled through a primary, closed system filled with distilled water and a secondary system operating through a heat exchanger off the mains water supply. Two, fail safe, relays, monitor the water temperature and pressure in the primary circuit. The current in the magnet will also cut off if the power supply to the field monitor fails.

The operation of the magnetometer has been described previously in a number of theses from this laboratory {24} and technical descriptions are contained in several manufacturers' manuals filed in the

lab: A brief outline of operation will, however, be given here. The magnetometer is based on a design described in {25}. The main features of our system are shown schematically in figure 9. The sample, 1 is attached by means of a rigid rod, 2 to the transducer, 3. The transducer causes vertical oscillations of the sample relative to a pair of sensing coils, 5 that are fixed to the pole pieces of the electromagnet. The rod is also attached to a pair of circular metal plates 6a which together with a pair of fixed plates, 6b make up a vibrating capacitor. With a field applied to the sample an a.c. signal at the vibration frequency is generated at the sensing coils and its amplitude is proportional to the magnetic moment of the sample. A signal of the same frequency appears between the fixed plates 6b with an amplitude proportional to the d.c. voltage applied to the plates 6a. The phases of both signals are determined mainly by the mechanical motion. Suitable electronics allow these two signals to be added in phase opposition. If their amplitudes are equal, then their combined out-put is zero. The signal from the plates 6b is called the reference signal, the other, the sample signal.

Two manners of operation are possible. In the first, the "Meter" switch on the control console is turned to "Reference Signal" in which case the meter

reading is proportional to the d.c. feed-back signal going to 6b to render zero the combined sample and reference signals. In this mode the sample magnetic moment is given by:

$$(\text{Calibrated Meter Reading} \times \text{Range})/100$$

where the range is determined by the setting of a six decade precision attenuator necessary to span the entire change of sample magnetization. In our lab, we generally use the second mode in which the "Meter" switch is set to "Output Balance". In this mode the meter is used as a null detector in conjunction with a 5 decade digital potentiometric divider and a direct measure of the difference between the sample and reference signals is obtained.

The magnetometer is extremely sensitive, the main reason for which lies in the design of the sample signal pickup assembly and it is worth making a few comments about it. Some preliminary remarks are in order. A sample with non-zero magnetic susceptibility, placed in a uniform magnetic field, changes the field in its vicinity so that as well as the uniform field, there now exists a non-uniform field arising from the sample. The P.A.R. magnetometer operates by detecting and measuring that part of the field due to the sample. In the neighbourhood of the sample, the ratio of the non-uniform field to

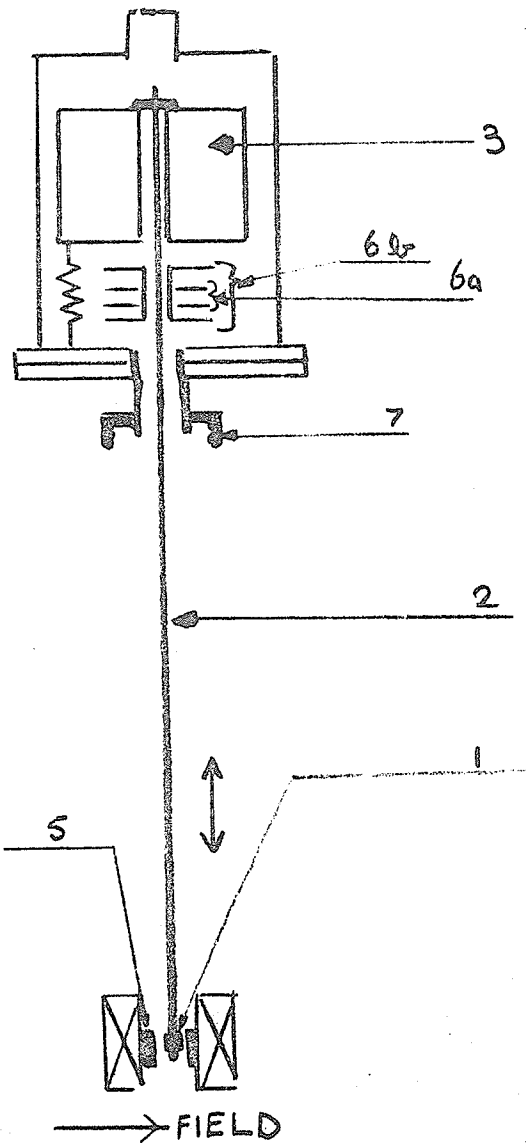
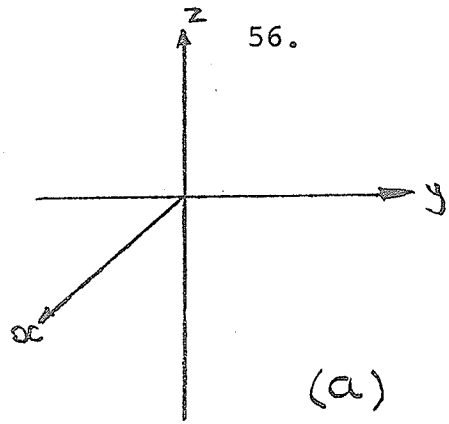
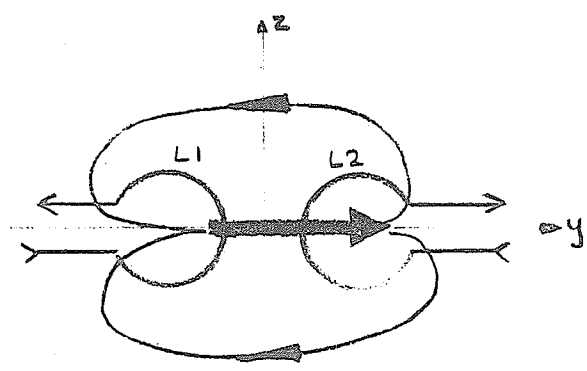


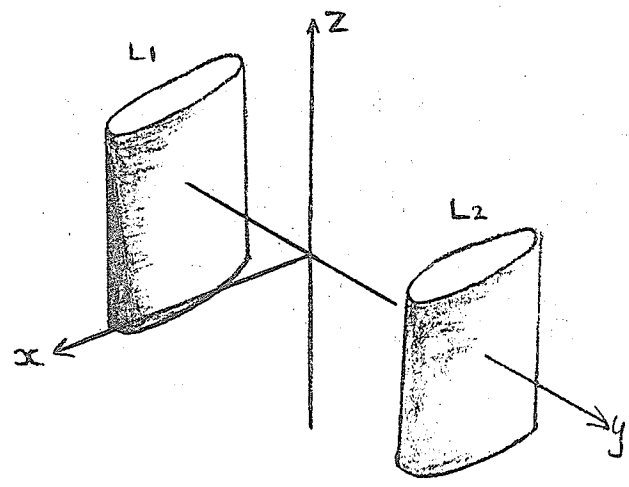
Figure 9. Transducer assembly in the magnetometer.



(a)



(b)



(c)

Figure 10. To illustrate the operation of the pick-up coils.

the applied field is of the order of the sample susceptibility and the design specifications of the magnetometer are such that susceptibility changes 5×10^{-9} e.m.u. may be detected. Put another way, we are able to detect changes of about 5 parts in 10^9 of the applied field. The pick-up assembly is designed so that fluctuations in the magnet field do not set the lower limit of detection. The system is based on a modulation technique, in describing it, we shall refer to Figure 10, a,b,c. Figure 10a shows the laboratory co-ordinate system with its origin at the centroid of the pole pieces of the magnet. The field will be in the y direction and the z axis is vertical. The sample is vibrated sinusoidally along the z axis at a nominal frequency of 82Hz. The non-uniform field, therefore, varies at 82Hz and a narrow band width detection system centred on this frequency senses the field plus any fluctuations in the lab. magnet field of the same frequency. As it turns out, most lab. magnets have negligible noise fluctuations at this frequency.

The operation of the sensing coils is indicated in figure 10b in terms of one turn loops L_1 and L_2 . For an arbitrarily shaped sample, the field will be complex, but for reasonably shaped samples, the dipole component dominates and in figure 10b

the sample magnetization indicated by the heavy arrow, really represents the y component of the dipole term. A pair of magnetic field lines are shown in figure 10b, so long as L_1 , L_2 and the sample lie in the x-y plane the net flux in L_1 and L_2 is zero but if the sample moves downwards the net flux is non-zero and currents circulate in L_1 and L_2 as shown. Note that these currents circulate in opposite senses. L_1 and L_2 are connected in series so as to add the two currents. Thus voltages induced in L_1 and L_2 that are produced by spurious, time varying fields cancel out, provided the fields are uniform over the volume of space containing the loops. Conversely, time varying fields that are not uniform over the sensing volume do contribute to the signal detected. Thus, the size of the sample is limited to typical dimensions $\sim \frac{1}{4}$ ". The actual pick-up coil arrangement is indicated in figure 10c.

It is desirable from the point of view of repeating experiments to position the sample at the origin of the co-ordinate system since this is supposedly a well defined point. To this end, the transducer assembly head is fitted with 3 adjustments. One to enable small adjustments of the sample along each co-ordinate axis. Intuitive considerations show that the output signal is a maximum at the

origin along the z-axis, a minimum at the origin along the y-axis and a maximum along the origin on the x-axis. In principle, it is a simple matter to adjust each of the controls in some fixed order z,y,x for example until the saddle point is reached. In fact, this adjustment is tedious and extremely time consuming because the controls do not operate entirely independently of each other and the set of adjustments $\{z,y,x\}$ must be made several times before the magnetometer reading after the (n+1)th set agrees with that found from the nth set to better than 0.5%. However, we usually find that three sets are enough to obtain 1% agreement between the nth and (n+1)th set. The machine is calibrated with a standard sample, usually nickel, that occupies the same physical volume as the samples to be studied.

1.3 Ancillary Equipment.

Unless the magnetometer is to be used exclusively at room temperature, at least two facilities are required; a cryostat to reach temperatures below 300° k and a furnace to reach temperatures above 300° k. Our lab. possesses both of these attachments and they are described in the following paragraphs.

Our cryostat (4) is a flow through type with a working range of 4-300° K. Figure 11 shows the basic features. In operation, the cryostat is suspended from the flange fitting, 7 in figure 9. The main feature of the cryostat is the capillary tube, 1 that connects the helium reservoir, 2 to the bottom of the sample chamber, 3. The flow of liquid through this tube is controlled by the needle valve, 4. A small 10w heater, 5 supplies enough power to the sample chamber to cover the working range quoted above. It is possible to use liquid nitrogen as the cryogenic fluid but temperature stability is noticeably poorer $\pm 1^\circ$ K compared with a figure of $\pm 0.5^\circ$ K when liquid helium is used. The temperature is measured using a calibrated carbon resistor in the range 4.2-30° K and a copper/constantan thermocouple otherwise. An important, and rather attractive feature of the cryostat is the activated charcoal getter, 6 affixed to the bottom of the liquid nitrogen radiation shield. The common vacuum space in the dewar is rather small so even small leaks and outgassing of the walls can seriously impair the vacuum. The getter, however, allows the dewar vacuum to remain hard for periods of a week or more. More important, the cryostat can be used without continuous pumping and a 3 litre fill of

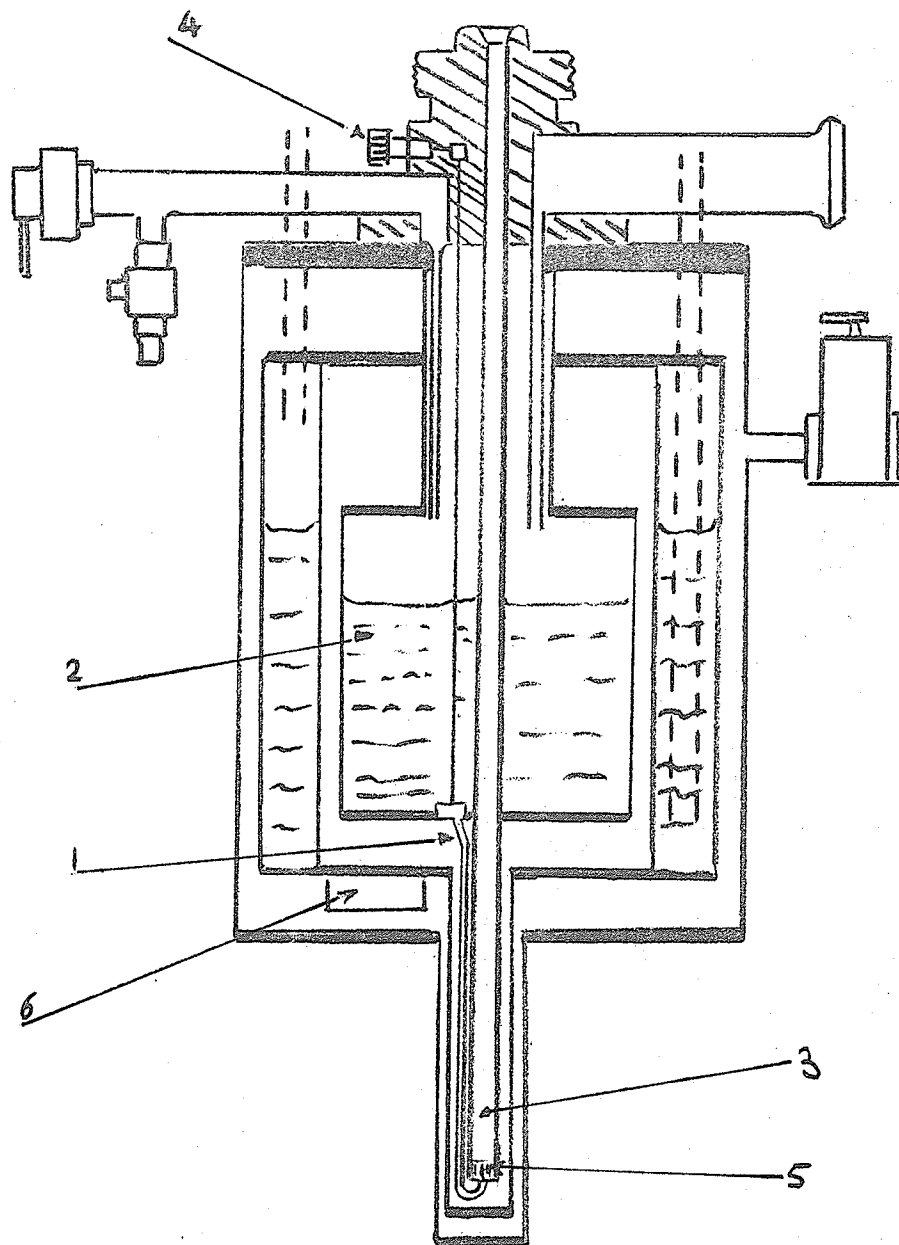


Figure 11. Diagram of the magnetometer cryostat.

helium, carefully managed, can last up to 12 hours.

Our furnace ⁽¹⁾ is sketched in figure 12. The outer case, 1 is of stainless steel and is 3/4" outer diameter. The radiation shielding, 2 consists of a sheet of tantalum rolled into a tube so that in effect, there are a large number of concentric radiation shields. The heating element, 4 is of nichrome, non-inductively wound on to a closed end corundum tube, 5. The windings are held in place by high purity alumina cement. Electrical connection to the windings is through the vacuum sealed receptical, 6. A pumping port, 7 allows the vacuum space to be evacuated. The maximum operating temperature is specified as 770° C, for this, a power input of ~0.5A, 50V d.c. is required. The furnace is straightforward in operation and temperature stability of ±2°K can be readily obtained. The sample chamber itself, is lined with a stainless steel tube, 8. In use, this tube becomes dirty, presumably because of the high temperatures involved, and must be cleaned periodically. During operation, the vacuum space in the furnace must be continuously pumped because of outgassing of the corundum and alumina cement, this represents a disadvantage because some vibration is transmitted along the pumping line and and the line itself restricts the movement of the

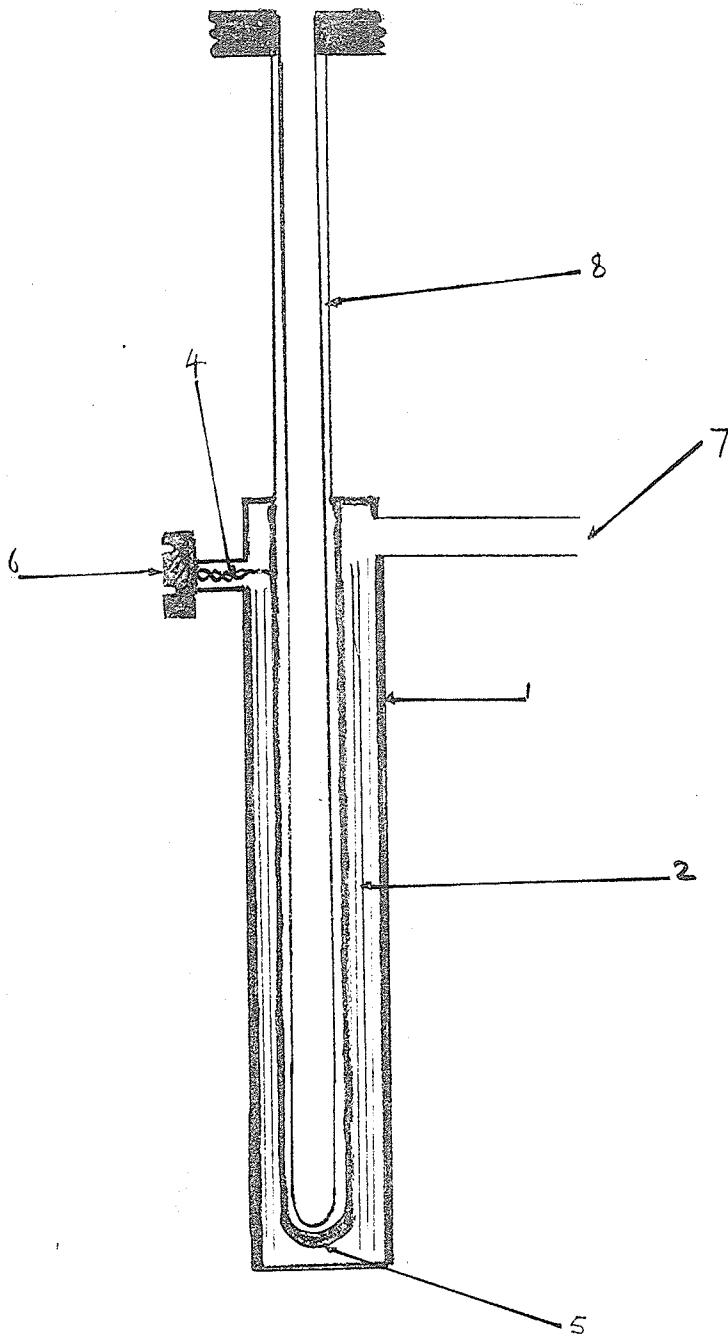


Figure 12. Diagram of the magnetometer furnace.

furnace so that care must be taken when setting up the furnace in the sensing coils. When working with paramagnetic materials, it is necessary to check and allow for the background signal, since this can be fairly large.

To complete the description of the magnetometer equipment, we describe the assemblies by which the sample is supported in the field of the magnet. The items to be discussed here are the sample support rod and the two extensions needed for use in the dewar and furnace described earlier. Figure 13 shows the details of the assemblies. The support rod, (a) is common to both the dewar extension, (b), and the furnace extension, (c). The overall length of (a) is 29 11/16". It is constructed of telescoping brass tubing soft soldered together. At the upper end is a captive knurled screw which allows mounting in the transducer unit described in section 1.2. On the shaft are two cone shaped brass bushings that carry keying slots to ensure that when the transducer head is rotated, the rod also rotates. The lower end of the rod carries a 6-32NC female thread that is used to mount the extension pieces.

The low temperature extension piece, (b)

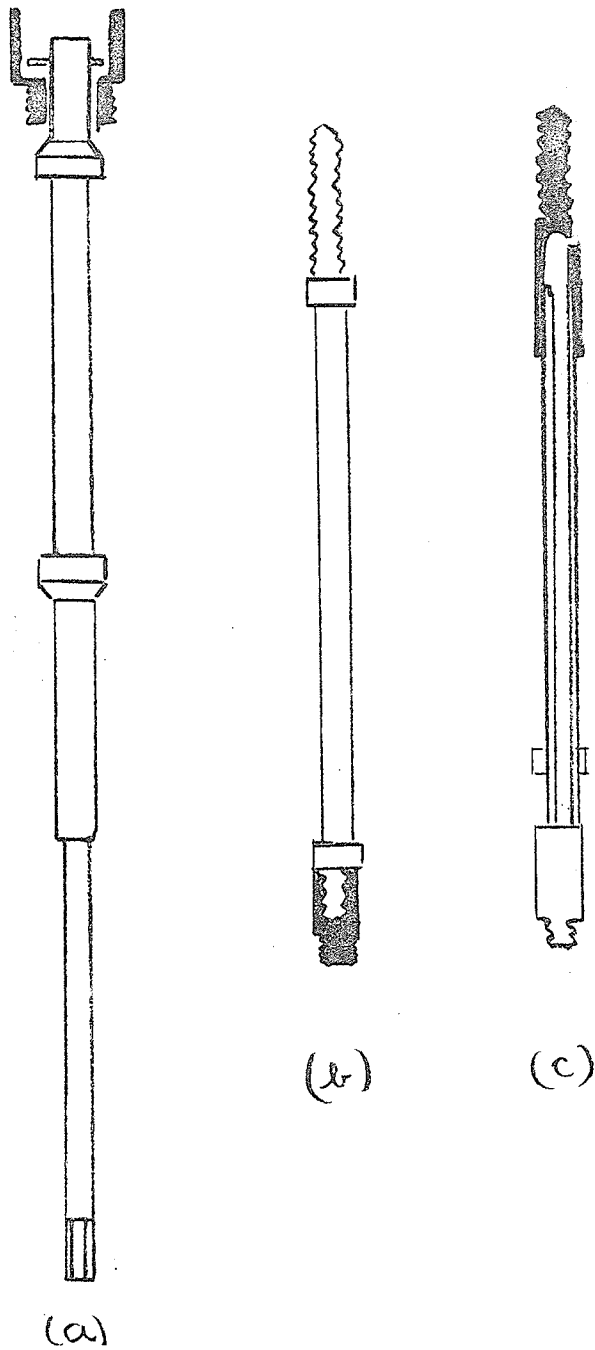


Figure 13. Magnetometer support rod (a), low (b), and high (c) temperature extension pieces.

has an overall length of $10\frac{1}{4}$ " and is made from epoxy bonded fibre glass. At its top end, it is threaded 6-32NC male to mate with the sample rod. It carries two teflon bushings that allow the sample to centre in the dewar sample tube without producing excessive resistance to the vertical vibrations. At the lower end is an aluminum sample holder support that also acts as a thermal sink for the copper constantan thermocouple.

The high temperature extension, (c) is also $10\frac{1}{4}$ " long and is constructed as follows: the main shaft is a quartz tube. At its upper end, it is sealed to a partially hollowed brass rod that is threaded to mate with the support rod. At 9" from the upper end, a boron nitride bushing is cemented and the tube is closed with a boron nitride, sample holder, support. The bushing and the support together provide the centering restrictions for the sample in the furnace tube.

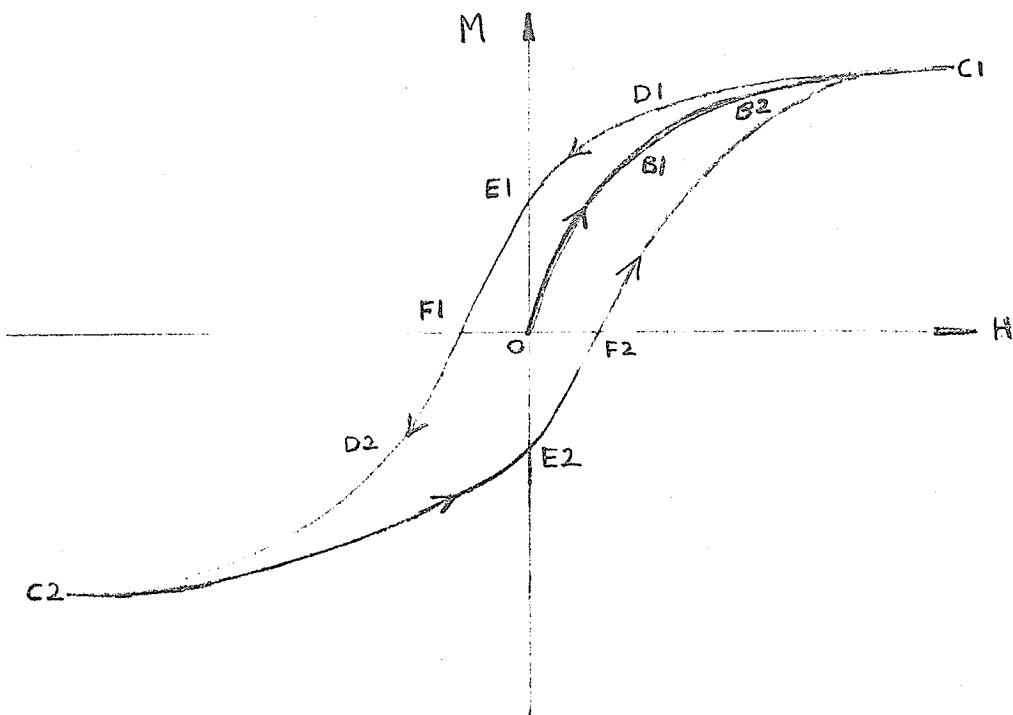
The temperature of the sample is determined by a thermocouple. In the case of the low temperature work, the thermocouple leads run down through the support rod, along a flat in the thread on the extension, are coiled around the shaft on the extension, and the junction is clamped between the lower teflon

bushing and the aluminum holder support. A similar arrangement exists for the high temperature work but the leads run down through the quartz tube and the junction is butted against the boron nitride holder support. This avoids weakening the boron nitride bushing by obviating the need to cut or drill it to afford access for the thermocouple to the sample area.

The high temperature extension described was made in the lab. The original extension, supplied by P.A.R., was constructed from a solid rod of quartz and was extremely fragile. The extension described has proved itself to be much more durable and is somewhat more convenient to use because of the ease with which a thermocouple can be introduced into the sample region.

1.4 Experimental Details.

The samples were in the form of polycrystalline powders and were contained in aluminum sample holders. The holders were machined from rod to an O.D. of $7/32$ " and length $1/2$ ". One end was recessed to a depth of $1/8$ " and threaded 10-32N.C. to mate with the lower end of either extension piece described earlier. The other end was recessed to a depth of $11/32$ " and again threaded 10-32N.C. to accommodate a plunger $1/8$ " long that had a slot cut in one of the flat faces.



68.

Figure 14. A schematic magnetization curve.

In use, the sample was placed into the larger recess and the plunger was turned in as far as possible using a screwdriver; thus, immobilizing the granules.

Before use, the sample holders were cleaned in detergent and diluted HCl, rinsed in water and acetone, and allowed to dry. Finally, the holder was weighed, filled with the sample, and re-weighed.

With the aid of figure 14, we shall explain how a full magnetization curve is obtained for a ferro- or ferrimagnetic sample. It should be stated, however, that this full curve was not measured for all the samples at all temperatures, the description is to be regarded as a model and in the later discussion of specific samples, it will be made clear which parts of the full curve were actually measured. For anti-

ferromagnetic specimens, we measured the susceptibility over the whole temperature range of interest.

First the support rod and extension piece is assembled and the sample holder attached. The sample is positioned in the sensing coils and the optimum position is located as described earlier. The field is increased from zero and the region $OB_1B_2C_1$ is obtained. The ill-defined point B_1 , the knee in the curve, is often regarded as the point at which saturation occurs. We generally take the region B_2C_1 where the curve is reasonably flat as the region of technical saturation. C_1 defines the point at which the maximum attainable field has been applied. The field is decreased in the region $C_1D_1E_1$ and E_1 defines the remanent magnetization M_R for which the applied field is zero. On reaching E_1 , the sample is rotated through 180° and the signal measured on the magnetometer reverses polarity. From E_1 to F_1 , the field is increased slowly and it is now oppositely directed to the sample magnetization. When the magnetometer signal has reduced to zero, the point F_1 has been reached and F_1 defines the coercivity of the sample H_C . The magnetometer signal again reverses polarity and the region $F_1D_2C_2$ is traced out by continuing to increase the field. The region C_2E_2 is obtained

by decreasing the field, the sample is once more rotated 180° on reaching E_2 and the rest of the curve, $E_2 F_2 C_1$, obtained by continuing to increase the field.

This description has already defined the remanence M_R and the coercivity H_C ; it remains to define the saturation magnetization M_S . Two common conventions exist in our lab., both derived from the region $B_2 C_1$ on the magnetization curve. In the first, the data are extrapolated linearly to the magnetization axis at $H=0$. This magnetization is denoted M_S . In the second, the magnetization data are plotted against $1/H$ and linearly extrapolated to $1/H=0$ corresponding to $H \rightarrow \infty$. This magnetization is denoted M_∞ .

The extension of the measurements to find the temperature dependence of all or some of the above quantities is obvious. No "critical point" determinations were made although we did estimate the long range ordering temperatures from the steeply falling regions of the M_S versus T curves.

The magnetization in the paramagnetic region was determined in a conventional manner, and, except for work in the furnace where a background signal was subtracted off, the slope of the curve of

magnetization versus applied field was taken to be the susceptibility. For the furnace work, the background signal was measured at a few temperatures as a function of field. Figure 15a indicates that the required susceptibility χ_s is given by:

$$\chi_s = \frac{(A_o - A_b) - (B_o - B_b)}{H_2 - H_1} = \frac{(A_o - B_o) - (A_b - B_b)}{(H_2 - H_1) (H_2 - H_1)}$$

where the subscripts o and b refer to the observed signal with a sample and the background signal in the absence of a sample. Thus, the required susceptibility is the difference of the two slopes. Figure 15b was obtained experimentally and it may be seen that the background is linear in H. The background is diamagnetic in character (negative slope) indicating that the major contribution is from the aluminum sample holder and its boron nitride support. There must also be some contribution from the vibration of the furnace induced by the pumping line.

After obtaining all the χ_s as indicated, the data from the furnace work was normalized to that from the dewar at the common temperature of 296° K.

The magnetometer was calibrated using spectrographically pure nickel for which the magnetization was taken to be 54.8 e.m.u./g {26}, a more recent set of measurements {27} gives $M_S = 55.07$ e.m.u./g

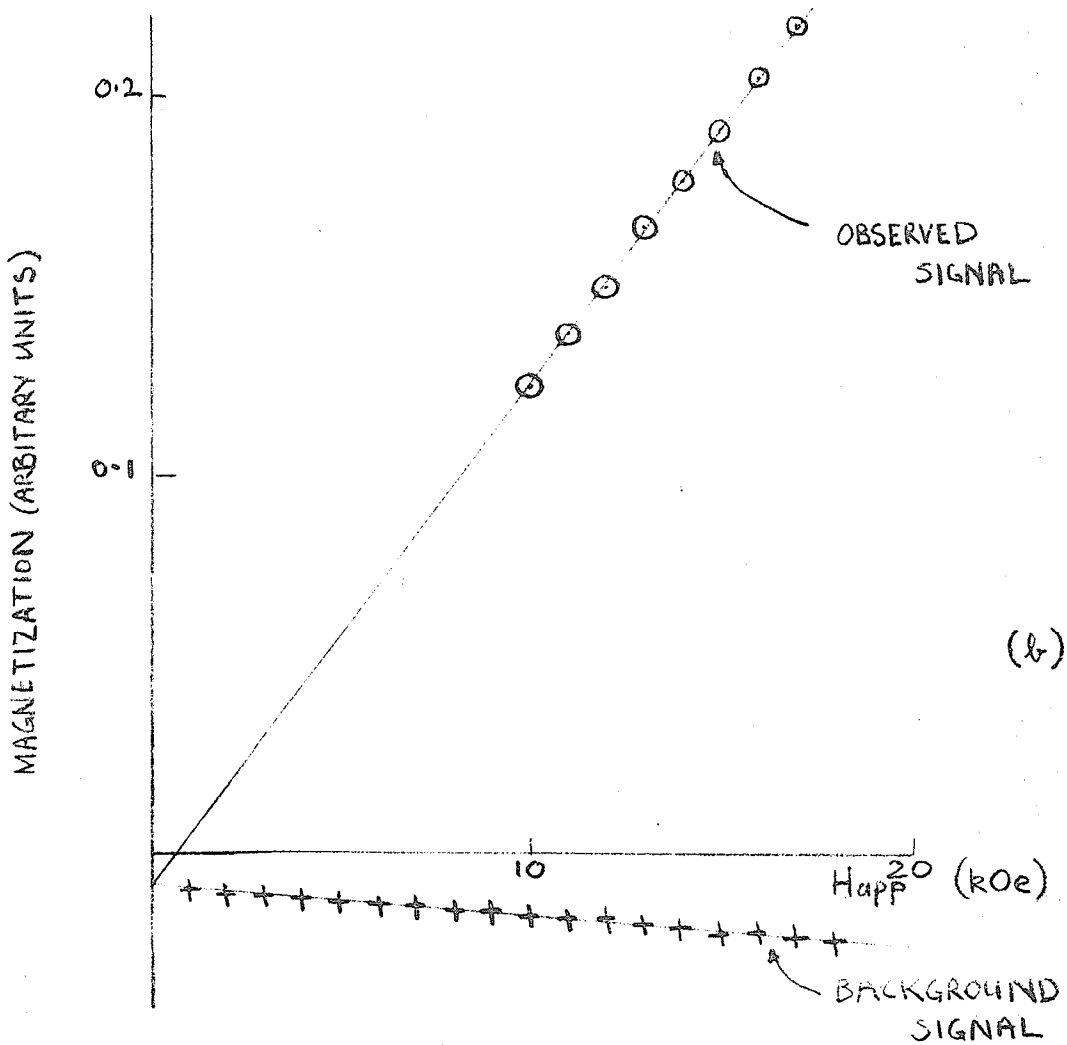
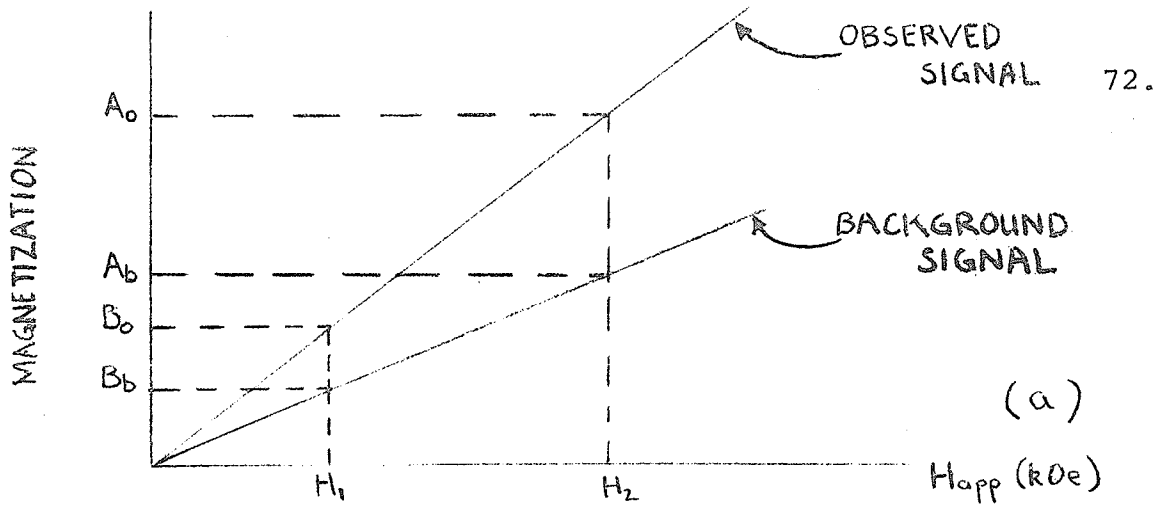


Figure 15. Nature of background correction in magnetometer furnace (a) schematic, (b) experimental result.

for nickel. In table 4 we show the results of calibrations obtained by various experimenters in the lab. over the last year. These group around a mean value of 7.289×10^{-4} e.m.u./division with a maximum deviation of 0.8%.

Table 4. Calibration constants for the magnetometer.

| Experimenter | Date | Sample Weight (g) | Value e.m.u./Division |
|--------------|-------------|-------------------|------------------------|
| I. Maartense | May 1971 | 0.011 | 7.350×10^{-4} |
| C. Boumford | August " | 0.225 | 7.289×10^{-4} |
| M.R. Spender | August 1972 | 0.225 | 7.257×10^{-4} |
| G.G. Hembree | October " | 0.372 | 7.258×10^{-4} |

2. ELECTRICAL MEASUREMENTS.

2.1 Basic Theoretical Results.

All the compounds that we investigated showed semiconducting type behaviour. We made two sorts of measurements, conductivity and magnetoresistance. In appendix B, we show how the well-known formula:

$$\rho = \rho_0 \exp[E/kT] \quad (\text{II.20})$$

may be derived. This relates the resistivity ρ to the energy gap $2E$ between the highest occupied state

and the conduction band as a function of temperature. The agreement between this prediction and the observations will be tested. We also mention the effect of magnetic ordering on the energy gap. This is a topic that has been dealt with recently {28}. Basically, a break in the curve $\ln \epsilon$ versus T^{-1} is expected at, or just below, the magnetic ordering temperature because of the spin splitting of the valence and conduction band induced by the (s,p)-d exchange interaction.

Perhaps of more interest are the microscopic scattering mechanisms that contribute to ϵ_0 . In the particular approximation used to find ϵ_0 in appendix B, we obtained an expression for the mobility μ which was:

$$\mu = \frac{\lambda}{(m^*T)^{3/2}}$$

Here, λ is the mean free path between scattering events and m^* is the effective mass of the carriers.

It is worth listing some of the processes that contribute to λ . First we consider scattering by lattice phonons for this is consistent with the approximation made for the relaxation time τ in Appendix B i.e. $\tau = \lambda c^{-1}$ where c was the total velocity. As it turns out, a simple analysis of electron phonon scattering in the Debye model {4} yields:

$$\tau \propto T^{-1} \epsilon^{-1/2} m^{*-3/2}$$

where ϵ is the energy of the electron, so that:

$$\lambda \propto T^{-1} \propto \gamma$$

Hence $\mu \propto T^{-3/2}$ for lattice scattering. Next important is impurity scattering. In a simple approach, we ignore the screening effect of the collective electrons and consider the scattering of a conduction electron using the approach suggested by Rutherford for α -particle scattering. It is found that approximately {4}:

$$\gamma \propto C^3$$

where C is the velocity of the electron. With this approximation for γ in the formalism of Appendix B we find:

$$\mu \propto T^{3/2}$$

This effect dominates the mobility at low temperatures whereas lattice phonon scattering is the dominant factor at high temperatures.

There are many other scattering mechanisms and there is certainly insufficient room to discuss them all but one other that we shall discuss briefly since it may have application to sulphide spinels is magnetic polaron formation. This mechanism has been considered by the authors of {29,30,31}. In this

process a conduction electron in a magnetic semiconductor can become self trapped by polarizing the 3d spins of nearby cations. A narrow conduction band is required also a large s-d exchange and it is necessary that the susceptibility of the cations be large for the polaron to be stable; hence, $T \gg T_c$. Under these conditions, the mobility is found, in a first approximation, to be independent of temperature. The analogy between these polarons and conventional lattice polarons is seen by noting that:

"s-d exchange corresponds to lattice deformation potential and magnetic susceptibility corresponds to lattice compressibility."

We have some good guides {28} as to results expected in magneto-resistance measurements on magnetic semi-conductors. If the magnetic polaron effect is viable or even if spin-spin scattering is important, then in a compound that is essentially ferromagnetic, we may expect that a decrease in resistivity would occur on applying a magnetic field. For an anti-ferromagnet, it is shown in {29} that increasing s-d exchange increases the effective mass of the magnetic polaron so we might expect an increase in resistivity as a result of applying a magnetic field.

2.2 Equipment.

The equipment used in these experiments was fairly simple. A description of the specimen preparation will be given in the next section, for the present we shall state that the specimens were prepared as small bars $1/4" \times 1/8" \times 1/32"$ and 4 leads were soldered to them using In15%Sn solder. Figure 16 then, shows the electrical circuitry used to make the measurements. A dry cell battery provides the current through the circuit, and a digital voltmeter ⁽⁵⁾ with a maximum sensitivity of $1\mu\text{V}$ was used to measure the voltages dropped across the specimen and a standard $100\ \Omega$ resistor. The input impedance of the D.V.M. is $\sim 10^8 - 10^{12}\ \Omega$ depending on the range used. Generally, we measured voltages $\sim 10^{-3}\ \text{V}$ and currents $\sim 10^{-5}\ \text{A}$ in the specimen so that the power dissipated was small $\sim 10^{-8}\ \text{W}$.

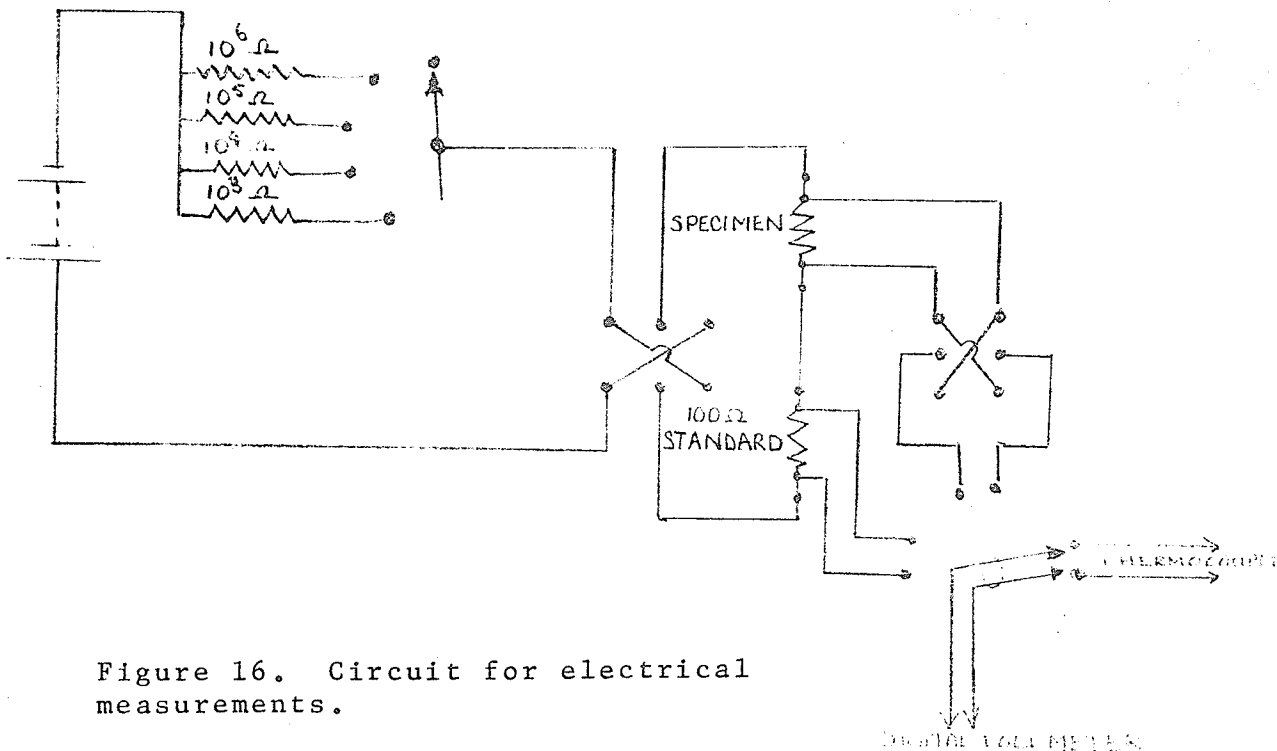


Figure 16. Circuit for electrical measurements.

We attempted measurements in the temperature range 4.2-300°K by making use of the dewar described in section 1.3. The lower temperature limit of the measurements was in fact, set by the actual value of the resistance of the specimen, our equipment failed to function for resistance values $\geq 10^5 \Omega$. Presumably stray currents become comparable with the steady circuit currents and the measuring equipment is unable to distinguish between them {32}.

2.3. Experimental Procedure.

In section 5 of chapter I, we described how sulphide samples with densities approaching theoretical x-ray values could be prepared. It is from these samples that specimens for the electrical measurements were cut. We used a diamond saw to slice bars that were typically 1/4" x 1/8" x 1/32". A micrometer screwgauge was used to determine the actual dimensions. After slicing, the bars were soaked in acetone for about 12 hours and then degreased by suspending them over hot toluene for about 4 hours. After this, the specimens were readily wetted by the In15%Sn solder that was used to make contacts to them. The specimens were fixed to aluminum holders from which they were electrically insulated by a 0.002" thick mylar sheet. The thermal contact between the specimen and holder

seems to be reasonably good since the thermal e.m.f. found during the experiments was generally $\lesssim 2$ parts in 500. The ohmicity of the contacts was excellent; we checked this at room temperature and at some other much lower temperature. Figure 17 is typical of the results we found; the tests are made by measuring the V,I characteristic of the specimen for forward and reversed current flow. The V,I characteristic should be linear and pass through the origin, departures from this expectation may be interpreted in terms of "diode" type contact behaviour.

In use, the specimen holder is screwed onto a replica of the extension piece and support rod described in section 1.3. The dewar was suspended from the magnetometer drive head and the specimen was introduced into the field space of the magnet in the same fashion as for magnetization measurements. We were, therefore, able to make both resistivity and magneto-resistance measurements. Standard current and voltage reversal techniques were used throughout. At one time, we also made some Hall Effect measurements, but because of the large magneto-resistance effects, the data proved to be altogether too confusing and are neither discussed nor presented in the reports on the compounds.

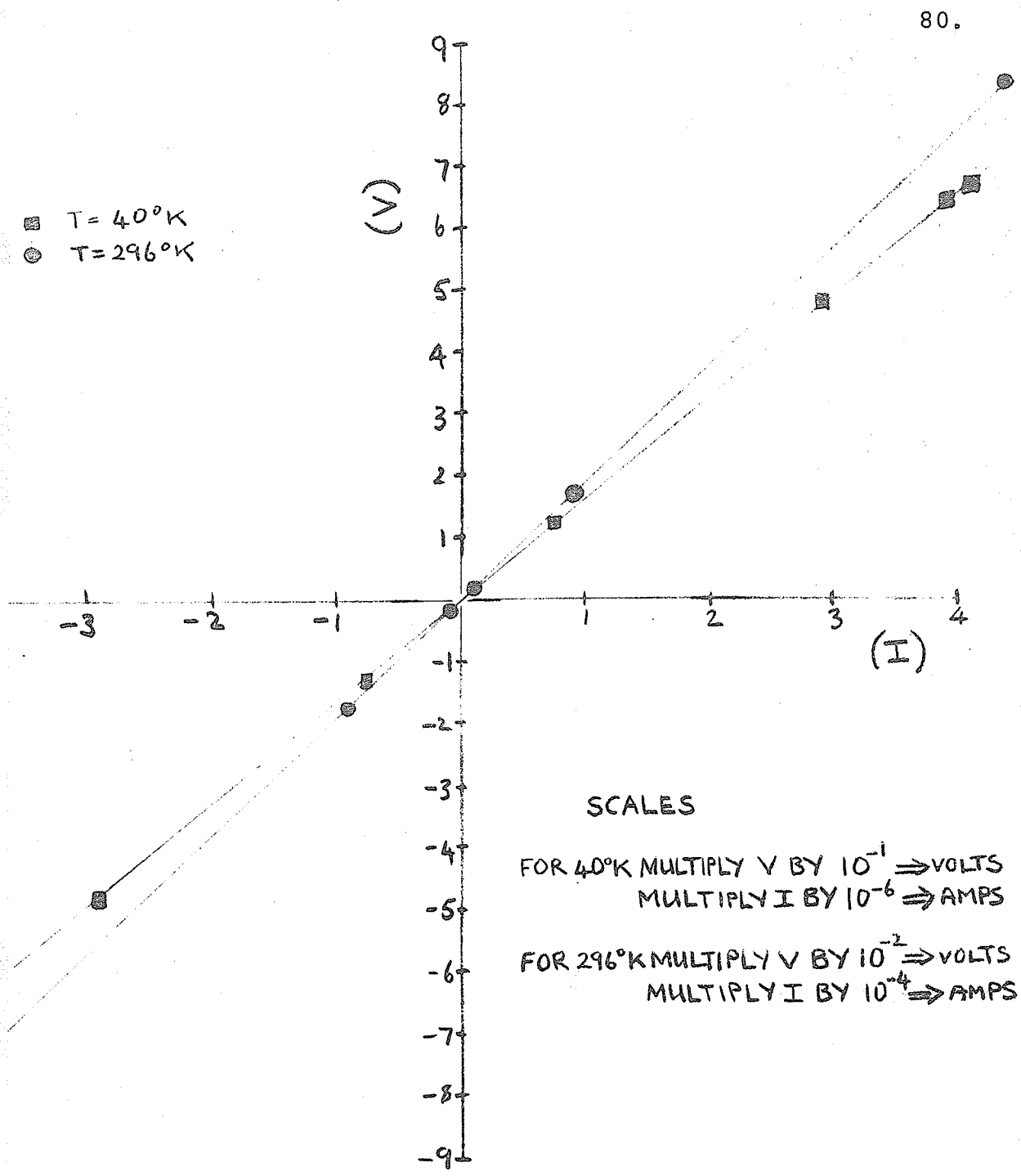


Figure 17. To illustrate the ohmicity of the electrical contacts.

3. MÖSSBAUER EFFECT STUDIES

3.1 Review of Theory.

When a nucleus is bound into a solid and excited in some fashion, it will naturally decay to its ground state. At the heart of the Mössbauer Effect is the fact that this decay can result in the emission of a γ -ray whose energy is well defined in the event that no phonons are excited in the process. The experimental evidence was obtained by Mössbauer during an investigation of the nuclear resonance absorption of γ -rays in ^{191}Ir {33}. The point is, that normally, the recoil energy of the nucleus as it emits the photon, is enough to excite one or more lattice phonons so that the energy of the emitted γ -ray is ill-defined. However, it was shown by Lamb {34} that this is not the only possibility for there was a finite probability of the recoil momentum being taken up by the crystal as a whole without changing the vibrational state of the crystal. Mössbauer envisaged his discovery as a method for investigating low lying nuclear energy levels but, as it turns out, the effect has had its greatest application in the field of solid state physics. As such, the Mössbauer nuclei are used to probe the immediate environment produced by the surrounding solid. The important characteristics of this

environment are the charge density, the electric field gradient and the magnetic field. These quantities are sampled by the nuclear properties; radius, quadrupole moment and magnetic moment in the ground and excited states. Each of the observable Mössbauer parameters; isomer shift, quadrupole interaction, and hyperfine field consists of a product of a solid state and a nuclear property so that a knowledge of the nuclear parameters is required before the solid state properties can be deduced.

Not all nuclei exhibit the Mössbauer effect. In fact, of all the elements, only about 40 have suitable isotopes and of these 70 isotopes, only a few have found wide application in solid state physics. In our lab. for example, the effect has been exploited in ^{57}Fe and ^{119}Sn . To see what the limiting conditions are, we examine the expression giving the number of nuclei that absorb or emit a γ -ray recoillessly. This is called the recoilless fraction, f where:

$$f = \exp \left[-E_{\gamma}^2 \langle x^2 \rangle / \hbar^2 c^2 \right] \quad (\text{II.21})$$

in which E_{γ} is the energy of the emitted γ -ray and $\langle x^2 \rangle$ is the component of the mean square vibrational amplitude of the nucleus in the γ -ray direction. For large E_{γ} , E_{γ} and $\langle x^2 \rangle$ must be small. In fact if sources are to be used at room temperature $E_{\gamma} < 50\text{keV}$. It is clear that $f=1$ for $\langle x^2 \rangle = 0$, the case of a nucleus

in a completely rigid lattice and $f \rightarrow 0$ for $\langle x^2 \rangle \rightarrow \infty$, the case of a completely free nucleus. In addition, since the recoil energy imparted to the emitting nucleus is:

$$E_R = E_\gamma^2 / 2M_L c^2$$

where M_L is the mass of the whole lattice, there is a lower limit to the size of particles that may be utilized because we must have E_R less than the natural line width. There are two other conditions to be satisfied. First, we need to have the half life of the excited state about an order of magnitude less than the various hyperfine interactions and secondly, internal conversion in the solid must be small so that a γ -ray is detected rather than an electron.

Of all Mössbauer nuclei, the $3/2 \leftrightarrow 1/2$ transition in ^{57}Fe best satisfies all the conditions and the decay scheme for $^{57}\text{Co} \rightarrow ^{57}\text{Fe}$, together with the various γ -rays emitted, is shown in figure 18. The stable isotope ^{57}Fe represents 2.17% of natural iron, quite enough for most iron compounds to be used as Mössbauer absorbers. The important nuclear parameters for ^{57}Fe are listed in table 5. The minimum possible observable line width is twice the natural width because experimentally, we use a source and an absorber and the line width of the source photon

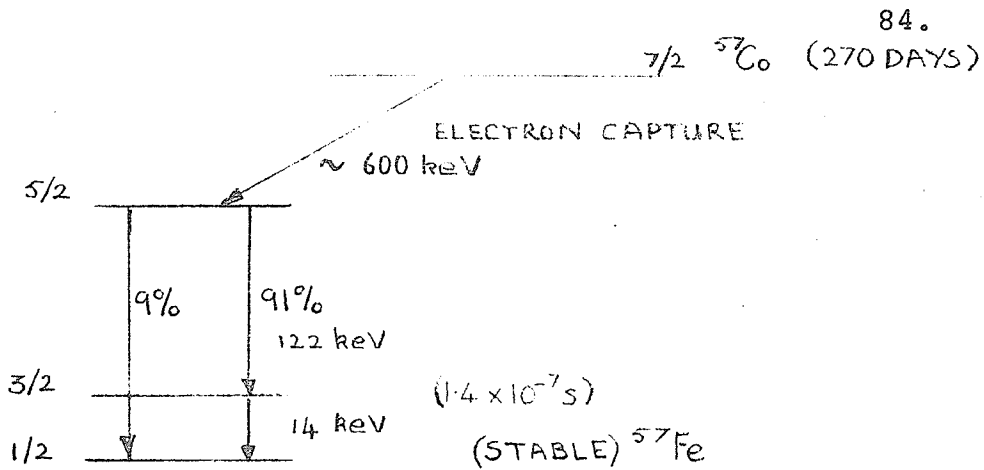


Figure 18. The decay scheme of ^{57}Co .

Table 5. Nuclear parameters for ^{57}Fe .

| | |
|---|---------------------------------|
| Quadrupole Moment ground state $Q_{1/2}$ | 0b |
| Quadrupole Moment excited state $Q_{3/2}$ | 0.2-0.29b |
| Nuclear g-factor ground state $g_{1/2}$ | 0.1805 |
| Nuclear g-factor excited state $g_{3/2}$ | -0.1031 |
| Half life of excited state $\tau_{3/2}$ | $0.98 \times 10^8 \text{ s}$ |
| Line width of emitted photon Γ | $4.67 \times 10^9 \text{ eV}$ |
| Minimum possible absorption line width $W_0 (=2\Gamma)$ | 0.194mm/s |
| Energy of emitted photon E_γ | $14.413 \times 10^3 \text{ eV}$ |

is folded with that emitted from the absorber. The units of W_0 are given in the natural Mössbauer energy units, the relationship between mm/s and other energy units can be obtained by considering the energy E of

a photon emitted from a moving source viz.

$$E = E_\gamma (v/c) + E_\gamma$$

$$\text{or } (E - E_\gamma) / E_\gamma = \delta E / E_\gamma = v/c \quad (\text{II.22})$$

where v is the source velocity and E_γ the unshifted photon energy. Thus, for the 14.4 keV γ -ray from ^{57}Fe a source velocity of 1.298×10^{19} mm/s corresponds to an energy shift δE_γ of 1 erg or, alternatively a source velocity of 1 mm/s corresponds to a shift of 4.804×10^{-7} eV.

3.2 Hyperfine Interactions.

We shall describe briefly the three hyperfine interactions of interest to us, namely:

- (i) The Isomer Shift;
- (ii) The Quadrupole Interaction;
- (iii) The Magnetic Hyperfine Interaction.

The isomer or chemical shift arises because the radius of the nucleus in the ground state is different to its radius in the excited state. Experimentally, it is related to the difference between the centre of gravity of the observed Mössbauer spectrum and the zero of velocity in the spectrometer. We say related, because in fact that difference is the sum of two effects. One being the isomer shift δ_i which is usually independent of temperature, the other, which is strongly temperature dependent, is the second

order Doppler shift δ_D . The experimentally determined shift δ_t is called the total spectrum shift i.e.

$$\delta_t = \delta_i + \delta_D \quad (\text{II.23})$$

A first calculation of δ_i {6} involves the charge densities resulting from s-electrons since this type of electron has a large probability of being located at the nucleus. Thus,

$$\delta_i = \frac{2\pi}{5} Ze^2 \left[|\psi_a(0)|^2 - |\psi_s(0)|^2 \right] \left[R_{ex}^2 - R_{gd}^2 \right]$$

where Z is the atomic number e^2 is the square of the electronic charge, R_{ex} is the nuclear radius in the excited state, R_{gd} is the nuclear radius in the ground state, $-e|\psi_a(0)|^2$ and $-e|\psi_s(0)|^2$ are the s-electron charge densities at the nucleus in absorber and source respectively. Notice that δ_i is, therefore, read relative to some standard. In our work, this standard is ^{57}Co in chromium, although there is now some international feeling that isomer shifts should be quoted relative to sodium nitroprusside.

This picture however, does not show up all the details and δ_i depends rather sensitively on two other important features. First, the chemical nature of the compound in which the nucleus is bound. To be specific, let us consider the two isomorphous

compounds $(\text{Fe})\{\text{Fe}_2\}\text{O}_4$ and $(\text{Fe})\{\text{Fe}_2\}\text{S}_4$ magnetite and greigite respectively. Both compounds have the spinel structure and in both, the iron shown thus, $\{\text{Fe}\}$, is octahedrally co-ordinated by 6 anions. The isomer shifts however, are 0.82 and 0.70 mm/s respectively. At least part of the difference results from the ways in which the cations and anions bond together. We have already discussed the chemical distinction between ionic and covalent bonding in chapter I section 3. Thus, in the moderately ionic oxide, the valence electrons from the cations reside mainly in anion orbitals and the Mössbauer nucleus experiences little or no contribution to δ_i from 4s like electrons. In the sulphide, the low cation-anion electronegativity difference results in more covalent bonds so some charge is shared between cations and anions, enhancing the electron density at the nucleus. The reason why the extra charge results in a smaller δ_i is that δ_i is intrinsically a negative number since $R_{\text{ex}} < R_{\text{gd}}$ in $^{57}\text{Fe}\{35\}$.

The second point to be made can also be illustrated by an example. Consider the two compounds $(\text{Fe})\{\text{Cr}_2\}\text{S}_4$ and $(\text{Fe})\{\text{Fe}_2\}\text{S}_4$. Again both are spinels, the iron shown (Fe) is tetrahedrally co-ordinated by the sulphur anions. The isomer shifts are 0.78 and

0.41 mm/s respectively. At least part of the difference is caused by the different valence states of the iron thus, in FeCr_2S_4 , the (Fe) iron is ferrous, whereas, in FeFe_2S_4 , the (Fe) iron appears to be essentially ferric. It may seem rather surprising that the removal of one d-electron that does not itself have a significant charge density at the nucleus should change δ_i so noticeably. To discover the reason, it is necessary to consider the spatial distributions of the 3d and 3s electrons. The 3d electrons spend an appreciable time closer to the nucleus than the 3s electrons. As such, the 3d electrons help to screen the 3s electrons from the nuclear charge. Therefore, the more 3d electrons there are, the better are the 3s electrons screened and the smaller is their density at the nucleus. Recalling the negative character of δ_i , it is clear that $\text{Fe}^{2+}(3s^23d^6)$ will have a larger δ_i than $\text{Fe}^{3+}(3s^23d^5)$.

We mentioned the second order Doppler shift earlier; here we consider briefly the way in which it arises and give an expression for its magnitude. The shift δ_D is relativistic in origin and is associated with lattice phonons {36,37}. If E_γ is the energy of the unshifted photon and E the energy of the Doppler shifted photon, V_E the velocity of the emitting nucleus in the direction of the emitted

photon then:

$$E = E_0 (1 - (V_E/c)) \cdot (1 - (V_E^2/c^2))^{-1/2}$$

Phonon frequencies are much higher than the frequency associated with the nuclear excited state lifetime, 10^{12} compared with 10^8 s^{-1} so that:

$$\langle V_E/c \rangle \rightarrow 0$$

but $\langle V_E^2/c^2 \rangle \neq 0$ so that

$$E = E_0 (1 - (V_E^2/c^2))^{-1/2}$$

and since $V_E^2 \ll c^2$

$$\text{we have } \Delta E_0/E_0 = -\langle V_E^2 \rangle / 2c^2$$

The next step requires the use of a specific model usually a monatomic solid with an energy U per atom of mass M and in this approximation:

$$\mathcal{E}_D = -E_0 U / 2c^2 M$$

U is calculated by assuming one of the models for the frequency distribution of the lattice vibrations, often the Debye model and the expression for \mathcal{E}_D

becomes:

$$\mathcal{E}_D = -\frac{9kTE_0}{4Mc^2} \left\{ \frac{\theta_D}{4T} + 2 \left(\frac{T}{\theta_D} \right)^3 \int_0^{\theta_D/T} \frac{x^3}{e^x - 1} dx \right\} \quad (\text{II.24})$$

At this point, we recall that:

$$f = \exp[-E_0^2 \langle x^2 \rangle / \hbar^2 c^2]$$

and note that in the Debye approximation, the expression

for f becomes:

$$f = \exp \left[\left(-3E_{\gamma}^2 / Mc^2 k \theta_D^2 \right) \left(\frac{1}{2} + (T/\theta_D) \int_0^{\theta_D/T} \frac{x}{e^x - 1} dx \right) \right]$$

which can be approximated for $T > \theta_D/2$ as:

$$f = \exp \left[-3E_{\gamma}^2 T / Mc^2 k \theta_D^2 \right]$$

or $\ln f = -KT$

(II.25)

with $K = 3E_{\gamma}^2 / Mc^2 k \theta_D^2$

Thus, a plot of the area under the absorption curve for various temperatures can be used to determine θ_D and so \mathcal{S}_D can be calculated assuming θ_D is the same over the whole temperature range. It is therefore, possible to subtract \mathcal{S}_D from \mathcal{S}_t and discover whether there is any temperature dependence of \mathcal{S}_i . Care must be taken however, because θ_D may itself, depend on temperature, either directly or as a result of magnetic order {38}. In addition, it has been suggested that in a polyatomic solid, the value of M maybe different in the high and low temperature limits {39}. Thus, at high temperatures, where phonon frequencies are high $M = M(^{57}\text{Fe})$ because the wavelengths involved do not involve much more of the lattice than the Mössbauer nucleus itself. However, at low temperatures $T \ll \theta_D$ phonon wavelenths may involve much larger portions of the lattice so that $M \rightarrow \bar{M}$ the average mass of the atoms in the lattice.

The isomer shift may depend on temperature via a number of effects for example, if a crystallographic transition occurs, if there is a change in band structure, if magnetic ordering is accompanied by magnetostriction, and it has been shown {40} that a small, probably immeasurable, change occurs when magnetic order sets in, regardless of any other considerations.

The next hyperfine interaction of interest arises from the coupling of the nuclear quadrupole moment with the electric field gradient produced by the surrounding crystal and the electrons belonging to the nucleus itself. This is called the quadrupole interaction. There is no quadrupole moment associated with nuclei in spherically symmetric states ($I=0, \frac{1}{2}$), where I is the nuclear spin quantum number. Thus, in ^{57}Fe , there is no quadrupole coupling with the ground state, $I=\frac{1}{2}$, but there is coupling with the first excited state for which $I=3/2$.

The electric field gradient (E.F.G.) is found by taking the gradient of the electric field at the nuclear site and is therefore, a 3 x 3 tensor that reduces to diagonal form with the proper choice of co-ordinate system. The three diagonal components $\partial^2 V / \partial x_i \partial x_i$ are generally abbreviated as V_{xx} , V_{yy} , V_{zz}

and by convention $|V_{zz}| \geq |V_{xx}| \geq |V_{yy}|$. Now at the nuclear site the charge density is almost entirely due to s-electrons but since these electrons are spherically symmetric, their charge does not contribute to the E.F.G. and therefore, Laplace's equation must be satisfied by the components of the E.F.G. at the nuclear site. Thus, the requirement that $\nabla^2 V \equiv 0$ leads to $V_{zz} + V_{yy} + V_{xx} \equiv 0$. Hence, only two independent components of the E.F.G. remain. By convention, one of these is $V_{zz} = eq$ (see appendix C), the other is called the asymmetry parameter η defined as:

$$\eta = \left| \frac{V_{xx} - V_{yy}}{V_{zz}} \right| \text{ whence } 0 \leq \eta \leq 1$$

The Hamiltonian for the interaction is:

$$\tilde{H} = Q \cdot \nabla E$$

In the paramagnetic state V_{zz} defines the axis of quantization. The Hamiltonian is therefore, written:

$$H = \frac{eQ}{4I(2I-1)} \left\{ V_{zz} [3I_z^2 - I(I+1)] + (V_{xx} - V_{yy}) (I_x^2 - I_y^2) \right\}$$

Then using the definition of V_{zz} and η , we have the eigenvalues:

$$E_Q = \frac{e^2 q Q}{4I(2I-1)} \cdot \left[3m_I^2 - I(I+1) \right], \quad (1 + \frac{\eta^2}{3})^{\frac{1}{2}}$$

$$m_I = I, (I-1) \dots -I$$

where m_I is the nuclear magnetic quantum number.

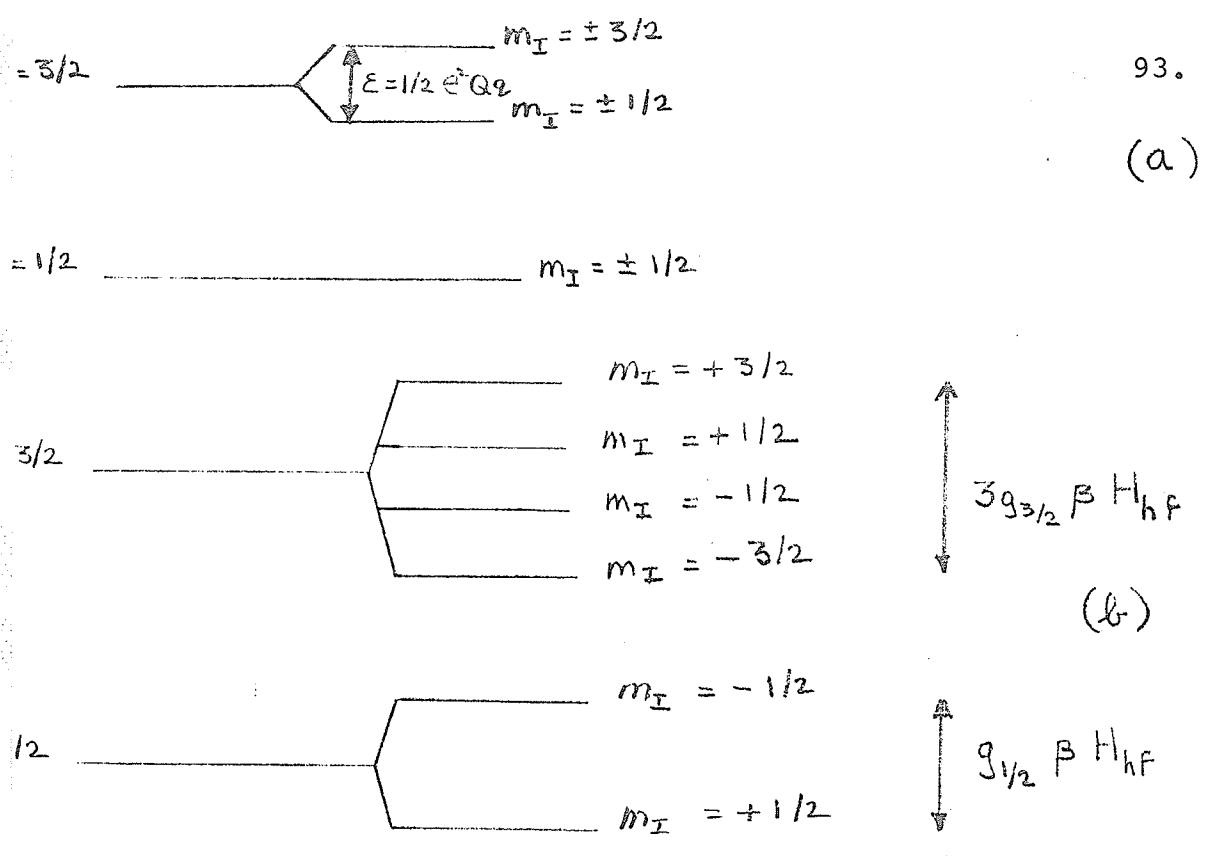


Figure 19. Splitting of the two lowest states of the ⁵⁷Fe nucleus as a result of:

- (a) An electric quadrupole interaction;
- (b) The magnetic hyperfine interaction.

Since the expression contains only m_I^2 , states that differ only in sign are degenerate. Hence, in the particular case of ⁵⁷Fe, in an axially symmetric E.F.G. ($\eta=0$) the $I=3/2$ state splits into $\pm 3/2$, $\pm 1/2$ with the splitting given by:

$$\epsilon = \frac{e^2 q Q}{2}$$

The situation is illustrated in figure 19a.

Of particular interest in solid state

physics is the mechanism by which the E.F.G. arises. In appendix C, a few specific mechanisms are considered. These divide into, mechanisms that are related to the behaviour of electrons in incomplete shells of the parent atom, especially in the case of ferrous iron, and the mechanism by which charges on distant ions in the lattice produce on E.F.G. which is of interest in the case of ferric iron.

The third hyperfine interaction results from the coupling of the nuclear magnetic dipole moment with the magnetic field arising from the electrons associated with the parent atom. It is called the magnetic hyperfine interaction. The Hamiltonian is:

$$\tilde{H} = -\underline{\mu} \cdot \underline{H}_{hf} = -g \beta \underline{I} \cdot \underline{H}_{hf}$$

and the eigenvalues are:

$$E_m = -\mu H_{hf} \frac{m_I}{I}$$

with $m_I = I, I-1, \dots, -I$ and H_{hf} the axis of quantization. Here, β is the nuclear Bohr magneton and g , the nuclear gyromagnetic ratio. Thus, the magnetic hyperfine interaction lifts the $(2I+1)$ fold degeneracy of the nuclear states completely, and the situation for ^{57}Fe is illustrated in figure 19b.

Of interest are the contributions to the field H_{hf} , first we list them and then consider the

origin of each term:

- (i) The Fermi Contact field (H_S)
- (ii) The Orbital field (H_{orb})
- (iii) The Dipolar field (H_{dip})
- (iv) The Local field (H_1)
- (v) The field resulting from
Conduction Electron Polarization (H_{cep})
- (vi) The Supertransferred Hyper-
fine field (H_{sthf})

Numbers (v) and (vi) are included for completeness and will not concern us.

The term H_S is usually the largest contribution to H_{hf} and it arises from the direct coupling of the nucleus and the s-electrons. An expression can be written for H_S in terms of the up and down spin densities $S\uparrow$, $S\downarrow$ of s-electrons at the nucleus:

$$H_S = -(16\pi/3)\mu_B \langle \sum (S\uparrow - S\downarrow) \rangle$$

but the expression for H_S is not particularly transparent especially when ions with completely filled s-shells can show large contact fields. In figure 20, we attempt to illustrate how a difference in spin up spin down densities can appear at the nucleus even for filled s-shells as a result of the exchange interaction between the s-electrons and d-electrons in an incomplete shell. Thus, the exchange between $d\uparrow$ and $s\uparrow$ is attractive and between $d\uparrow$ and $s\downarrow$

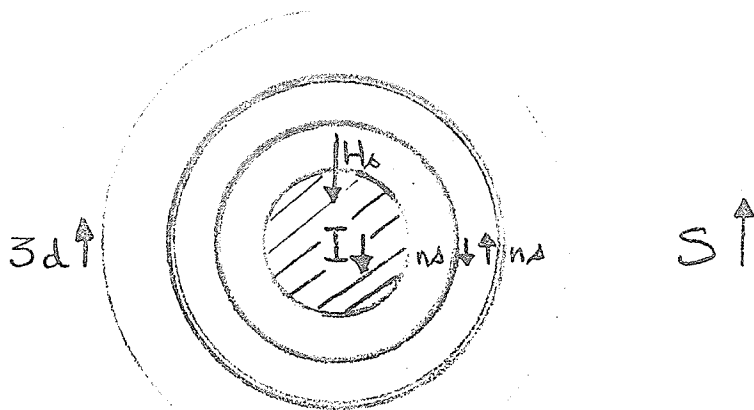


Figure 20. To illustrate the core polarization mechanism for H_S .

repulsive. Hence, $s\uparrow$ electrons are pulled away from the nucleus and vice-versa. Therefore, the spin densities $S\uparrow$ and $S\downarrow$ no longer cancel and $H_S \neq 0$. Notice that H_S is parallel to the magnetic moment of the parent ion, antiparallel to the spin of the parent ion.

In order for the term H_{orb} to appear, two conditions must be met. First, the ion must be in a state where the orbital angular momentum is non-zero second, there must be at least partial lifting of the orbital degeneracy of the ground state. Hence, for ions in S states where $L=0$, $H_{orb}=0$ and for ions in cubic environments $H_{orb}=0$. Otherwise the expression for H_{orb} is:

$$H_{orb} = -2\mu_B \langle r^{-3} \rangle_{3d} \langle L_z \rangle$$

where $\langle r^{-3} \rangle_{3d}$ is the reciprocal of the average cubed radius of the 3d electrons and L_z is the average z-component of the orbital angular momentum. In the event that the orbital momentum is quenched and the electronic currents circulate in the x-y plane only then:

$$H_{orb} = -2\mu_B \langle r^{-3} \rangle_{3d} (g-2) \langle S_z \rangle$$

There are two distinct dipolar fields, one from surrounding magnetic atoms, the other from the spin of the parent atom. In sulphide spinels the distance between magnetic atoms is $\sim 4-5\text{\AA}$ so that dipole fields from the surroundings are rather small. The dipole field from the parent atom is given by:

$$H_{\text{dip}} = -2\mu_B \left\langle \frac{3\mathbf{r}(\mathbf{S}\cdot\mathbf{r}) - S^2}{r^5} \right\rangle$$

Choosing the z axis as the axis of quantization:

$$H_{\text{dip}} = -2\mu_B \langle 3\cos^2\theta - 1 \rangle \langle r^{-3} \rangle_{3d} \langle S_z \rangle$$

where θ is the polar angle in an ordinary spherical co-ordinate system. Notice that this term is zero for spherical and cubic symmetry since $\langle 3\cos^2\theta - 1 \rangle = 0$ under these circumstances.

The local field consists of any externally applied field H_{app} plus the Lorentz field and the demagnetizing field. The expression for H_1 is then:

$$H_1 = H_{\text{app}} + \frac{4}{3} \cdot \underline{M} - \underline{DM}$$

In general, in an ordered compound all three hyperfine interactions are present simultaneously and except in one or two special cases, the Hamiltonian has no closed form solutions and the eigenvalues and transition probabilities must be computed. Such computing facilities are available in our laboratory and further comments will be made on this point in a later section. The problem arises because, in the most general case, the quadrupole interaction introduces off diagonal elements in the Hamiltonian

when the magnetic field direction is taken as the axis of quantization. These elements are too large to be ignored unless $e^2qQ \ll \mu_{hf}H_{hf}$. If we suppose that this condition does in fact obtain, then the eigenvalues for the case where the E.F.G. makes an angle θ with the hyperfine field and $\eta = 0$ are:

$$E(3/2) = g_{3/2} \beta H_{hf} m_I + (-1)^{|m_I + 1/2|} \frac{e^2 q Q}{4} \left\{ \frac{3 \cos^2 \theta - 1}{2} \right\}$$

$$E(1/2) = g_{1/2} \beta H_{hf} m_I$$

with neglect of the isomer shift.

There are a few points worth noting about these results.

- (i) When $\theta = 0$, there are only six allowed transitions between the ground and excited states corresponding to $\Delta m_I = 0, \pm 1$ and the relative probabilities are:

$$\left. \begin{array}{cc} -1/2 & -3/2 \\ +1/2 & +3/2 \end{array} \right\} 3 \quad \left. \begin{array}{cc} -1/2 & -1/2 \\ +1/2 & +1/2 \end{array} \right\} 2 \quad \left. \begin{array}{cc} -1/2 & +1/2 \\ +1/2 & -1/2 \end{array} \right\} 1$$

- (ii) When $\theta \neq 0$, there are eight allowed transitions corresponding to $m_I = 0, \pm 1, \pm 2$. The transition probabilities depend on the magnitude of $e^2 q Q / \frac{3}{2} \beta H_{hf}$.
- (iii) When $\theta = \cos^{-1}(1/\sqrt{3})$, the spectrum looks superficially as though there were no

quadruple interaction and the intensities of the lines must be carefully examined to see whether deviations from the expected 3:2:1 ratios are acceptable, for frequently, the two $\Delta m_I = \pm 2$ lines are of rather small intensity and may not show up as distinct absorption peaks. This critical condition is not beyond the realms of possibility. It is easy to determine that the angle between $\langle 001 \rangle$ and $\langle 111 \rangle$ is precisely $\cos^{-1}(1/\sqrt{3})$ in a cubic crystal and if the easy axis of magnetization is a cube axis and a small trigonal distortion occurs along $\langle 111 \rangle$ the situation has been realized.

3.3 The Mössbauer Spectrometer.

The spectrometers ⁽⁶⁾ in our lab. have been most thoroughly and comprehensively described previously {41}. There is nothing more to add, but for the sake of completeness a block diagram of the spectrometer is given in figure 21. The transducer, on which the source ⁵⁷Co in a Cr matrix is mounted ⁽⁷⁾ allows the energy of photons emitted from the source to be modified according to equation (II.22). The

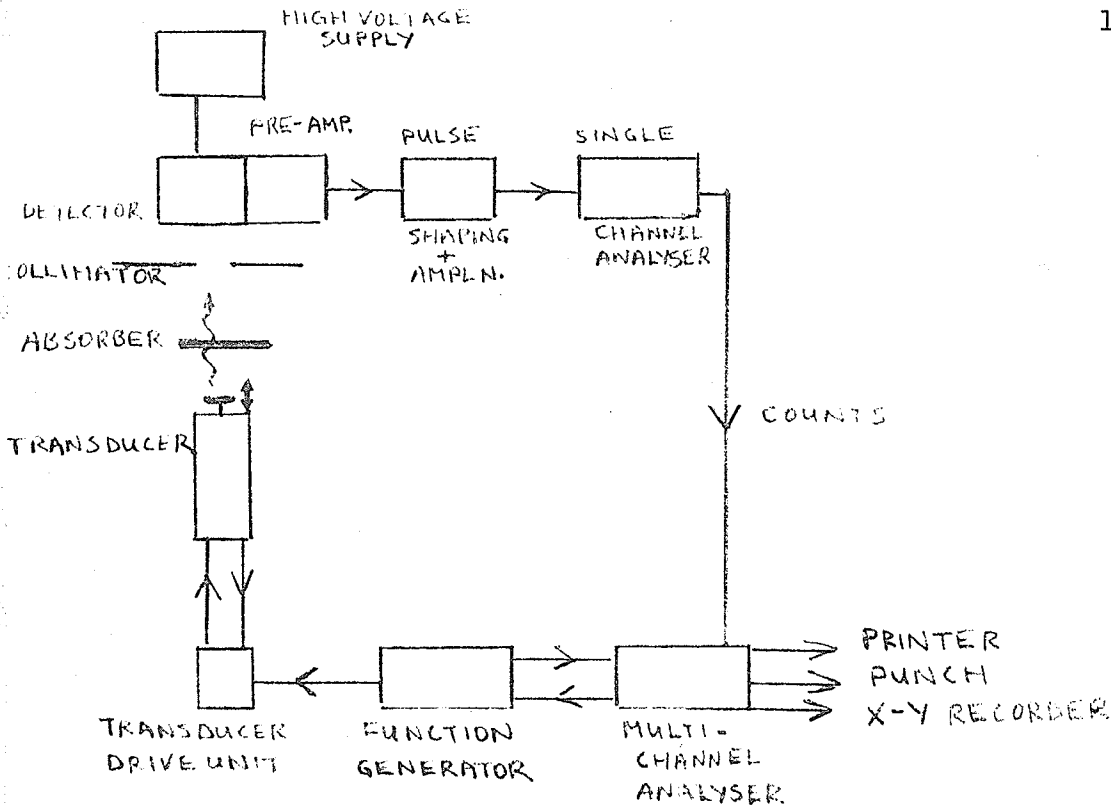


Figure 21. Block diagram of the Mössbauer spectrometer.

photons pass through the absorber and of those whose energy corresponds to the energy separation of states between which transitions are allowed, a fraction is absorbed. A detector counts the number of photons passing into it after collimation. The detector is either a crystal scintillator⁽⁸⁾ or a proportional counter⁽⁹⁾. Pulses from the counter are shaped and amplified, energy analysed and recorded. The method of recording depends on whether the transducer is used in the constant acceleration or the constant velocity mode. For the latter, the transducer stays in one

velocity channel for a pre-determined length of time and the total number of counts is recorded in a scaler and printed out⁽¹⁰⁾. If constant acceleration is used then the transducer is driven through the whole pre-selected velocity range in a pre-determined number of steps. A multichannel analyser⁽¹¹⁾ scales synchronously and the number of counts per velocity step is recorded in a memory bank. Subsequently, the memory is read out onto punched paper tape⁽¹²⁾ and printed paper⁽¹⁰⁾. The data may also be recorded graphically by means of an x-y recorder fitted with a point plotter⁽¹⁰⁾.

3.4 Ancillary Equipment.

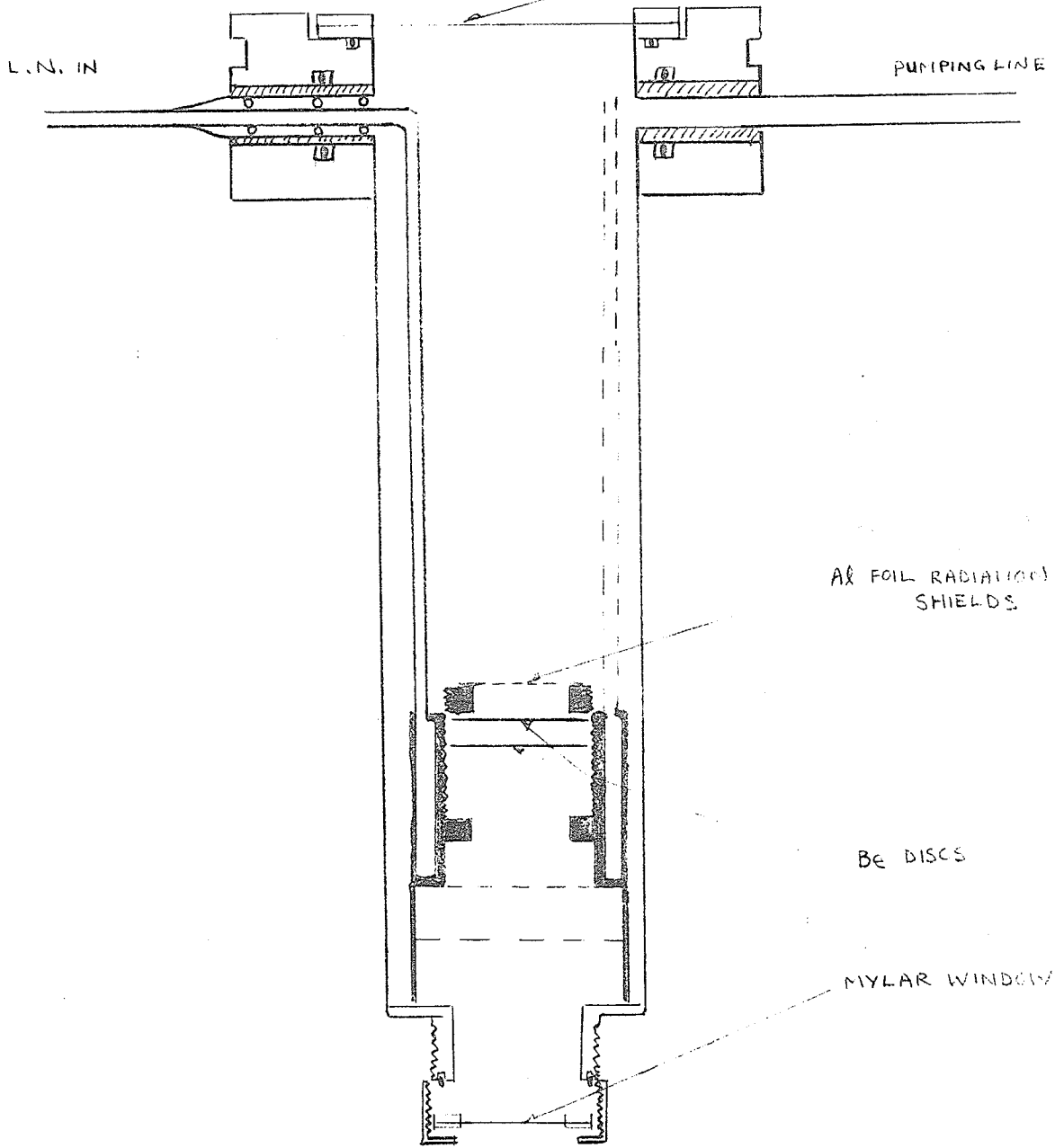
A great deal of the ancillary equipment used in these experiments has been described previously. A description of the furnace used to collect spectra in the range $300^{\circ} < T < 700^{\circ} \text{ K}$ can be found in {42,43}. Several people have described our 50kOe superconducting solenoid {41,43,44} as it is used in Mössbauer Effect studies with and without the room temperature bore in position. We can however, contribute a description of a liquid nitrogen flow through cryostat for use in the solenoid room temperature bore and a description of a cryostat which was custom built for us⁽¹³⁾, and used to collect spectra in the range $2^{\circ} \text{ K} < T < 250^{\circ} \text{ K}$.

The flow through cryostat is sketched in figure 22. The temperature achieved by the sample is $81 \pm 2^\circ \text{K}$ as measured with a copper constantan thermocouple. The instrument found some use {41,43} but it will soon be replaced by a rather more sophisticated cryostat. It is very simple in design. The outer case is of stainless steel 2 inches O.D. and 11 inches long. There is a 1 inch diameter mylar window at the lower end and a 2 inches diameter mylar window at the upper end. Copper tubing carries liquid nitrogen down to the sample area. The liquid flows through the rectangular cross-section annulus and back up a second tube where it exhausts to air. The absorber can be of the rigid matrix type or clamped between 1 inch diameter Be discs. Aluminum foil provides radiation shielding along the optical path and aluminised myla wrapped around the sample area and enclosing the copper feed tubes provides sufficient radiation shielding from the outer can. A 50 litre dewar of liquid nitrogen lasts about 20h. which is long enough to collect some 50-60,000 counts per channel. The top window tends to get rather cool because of the proximity of the feed tubes so it is provided with a small heater to prevent icing.

A sketch of the custom built cryostat is shown in figure 23a. In the centre, we have the

103.

MYLAR WINDOW



AL FOIL RADIATION SHIELDS

BE DISCS

MYLAR WINDOW

Figure 22. Line diagram of flow-through liquid nitrogen cryostat.

sample tube 2, at the bottom of the sample tube in the common vacuum space 3, is attached a 100 Ω , 9 watt heater that is wound on a massive copper former, 4. Three reservoirs are in thermal contact with the sample tube. The highest 5, is the main liquid helium tank, capacity 5 litres, the lowest 6, is the subsidiary helium pot, capacity 1 litre, which is used when sample temperatures below 4.2° K are required. Liquid helium is introduced into 6 from 5 via a needle valve 8, operated at the top of the cryostat. Between 5 and 6 is an exchange gas reservoir, 7. The liquid nitrogen reservoir 9 surrounds 5 and has a capacity of 15 litres. 77° K shielding is provided through the rest of the dewar by means of copper sheet. The reservoir 6, also has a 4.2° K radiation shield, 10. The lower part of the sample tube is of Be thus, providing a "wrap around" γ -ray window. The windows in the 77° K shield are mylar and the outer windows are of Be.

With the exception of the port on 6, all pumping parts come to a manifold that is valved to enable all volumes to be evacuated either at once or individually. The pumping line from 6 goes to a separate pumping station.

The absorber is introduced into the cryostat on the end of a long, thin walled, stainless steel tube. This assembly is shown in figure 23b. A flange seals

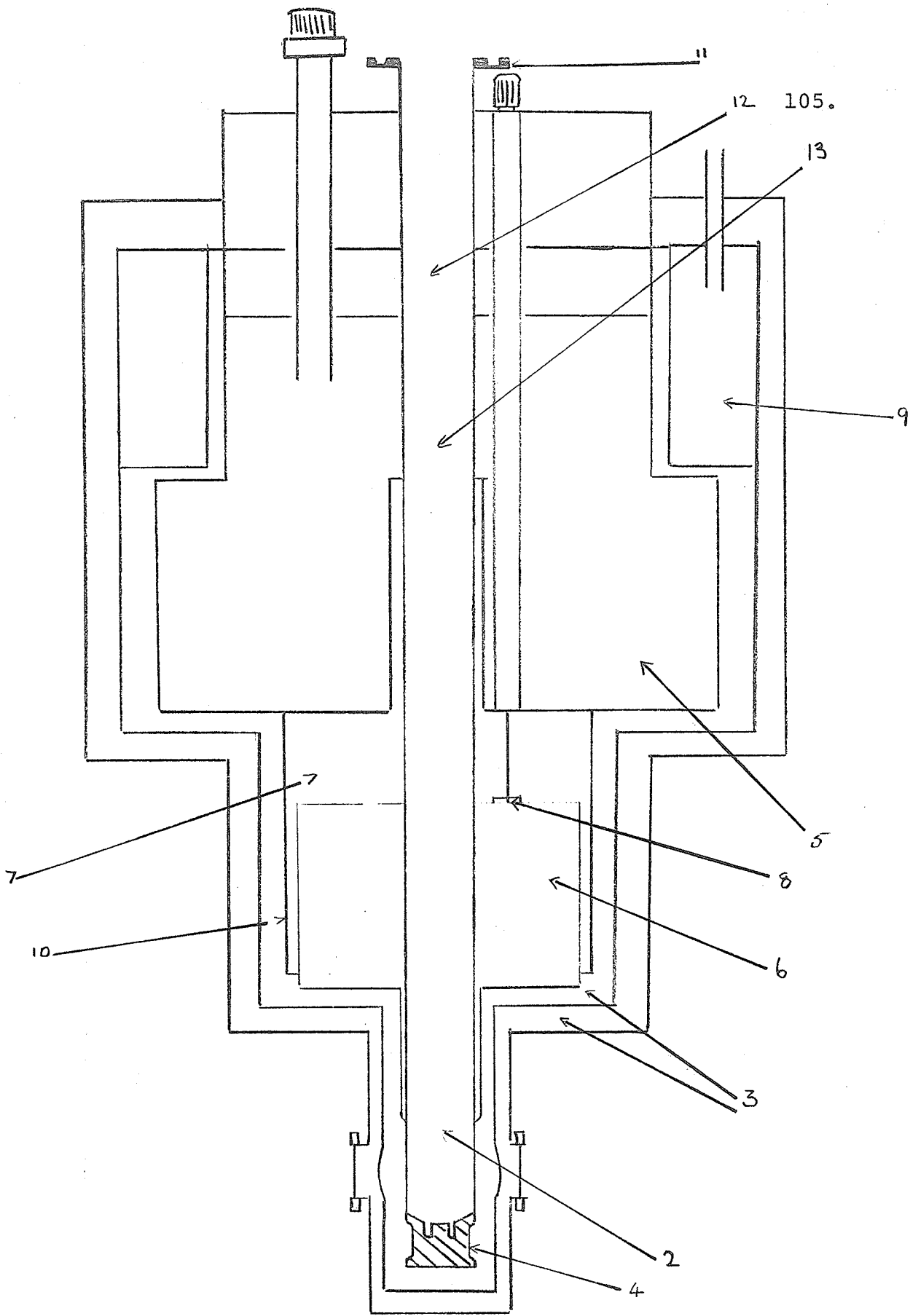


Figure 23a. Line diagram of oxford cryostat.

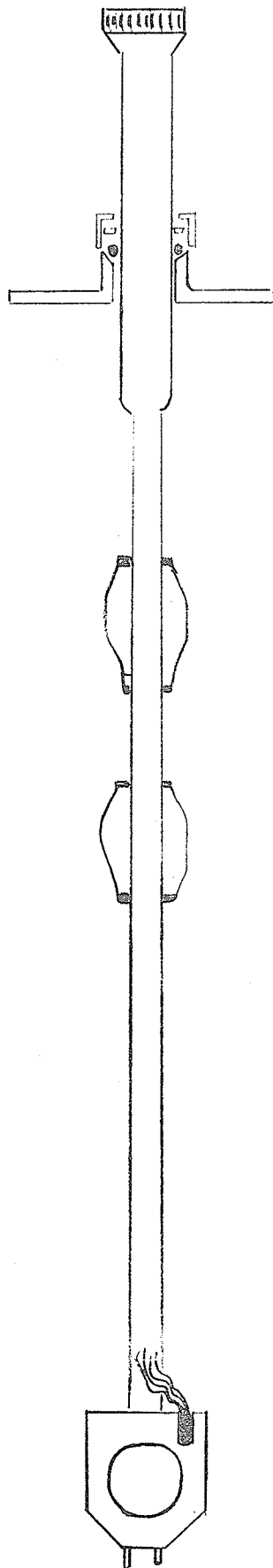


Figure 23b. Sample rod for the oxford cryostat.

the sample chamber against air via an o-ring on the top of the cryostat and another o-ring on the sample support tube. On the sample tube are two circumferential Be-Cu springs that allow thermal anchoring for the exchange gas in the sample tube. The upper spring locks onto the wall of the sample tube in the vicinity of the 77°K region 12, the lower spring locks on near to the top of the main helium pot, 13. These anchors help to induce layering of the exchange gas and provide for temperature stability. The sample support is of copper and is fairly massive. Buried in it is a germanium thermometer precision calibrated from 2.1° -99.8° K. Electrical leads from the thermometer run up through the sample tube and pass through a sealed connector at its top end. The sample temperature may also be measured using a Gold Iron/Chromel thermocouple that is fixed to the copper foot of the sample tube. In the absorber support are two stainless steel pins that provide for positive location of the absorber with respect to the optical path.

The operation of the dewar is straightforward. Before use, all reservoirs, exchange gas chambers and the needle valve capillary and seating must be thoroughly flushed with clean dry helium gas in order to prevent freeze up, icing or blocking of the various vents and access holes. The sample chamber, exchange gas chamber and lower reservoir are connected

to a supply of helium gas and the needle valve is closed (access of gas to the lower chamber can be had by means of a T junction in the pumping line). The nitrogen can is filled and about 3 litres of liquid nitrogen is poured into the main helium reservoir. Precooling of the dewar takes 5-10h. After this period, the nitrogen in the main helium reservoir is syphoned off and the reservoir is again flushed with clean dry helium gas. Liquid helium is then transferred into the reservoir, usually ~14 litres of liquid is required to complete dewar cool down to 4.2° K and fill the main reservoir.

It is simplest to describe the use of the cryostat in various temperature regions; $2.1^{\circ} \leq T < 4.2^{\circ}$ K, $T = 4.2^{\circ}$ K, $4.2^{\circ} < T < 10^{\circ}$ K, $10^{\circ} < T < 300^{\circ}$ K,

(i) $2.1^{\circ} \leq T < 4.2^{\circ}$ K.

The exchange gas reservoir and the sample chamber are evacuated. Liquid helium is admitted to the lower reservoir via the needle valve. When the boil off subsides, the needle valve is closed.

The T junction on the pumping line to the lower reservoir is now closed. The pumping line to the lower reservoir is shut and the pump is then switched on. The pumping line is opened gradually and a Bourdon gauge monitors the vapour pressure of the liquid helium in the lower pot. About $\frac{1}{2}$ h. after the pumping line has been fully opened, the sample

will achieve a steady minimum temperature $\sim 2^\circ$ K, that can be monitored with the germanium thermometer. The 1 litre capacity allows a spectrum collection time of at least 10h. Temperatures in the rest of the range can be obtained by increasing the pressure of exchange gas in the sample tube. Temperature stability is $\pm 0.2^\circ$ K for periods up to 5h. We shall be able to achieve something better than this after the pressure control for the helium pumping line is operative.

(ii) $T=4.2^\circ$ K.

If the steps prior to (i) have been adhered to the sample will be at 4.2° K. It has been found that opening the needle valve to allow liquid to fill the lower reservoir is just slightly advantageous.

(iii) $4.2^\circ < T < 10^\circ$ K.

In this range, the needle valve is closed, the exchange gas chamber and the lower reservoir are evacuated and temperatures are achieved by varying the exchange gas pressure in the sample tube.

(iv) $10^\circ < T < 300^\circ$ K.

In this range, it is possible to use a temperature controller which we shall describe briefly later. The exchange gas chamber and the lower reservoir are evacuated and the sample tube is partially evacuated to ~ 10 mmHg. Temperature stability is excellent $\pm 0.1^\circ$ K for periods up to 24h.

The temperature controller⁽¹⁴⁾ has both proportional and differential feed back loops. The output from a thermocouple junction at the sample chamber is compared with a pre-selected emf corresponding to the desired sample temperature. The difference is amplified, fed to a power stage that increases or decreases the power supplied to the cryostat heater as the difference voltage is positive or negative. A differentiating net monitors the time rate of change of the difference voltage and adjusts the power supplied to render this rate zero. An integrating net averages out large random noise fluctuations.

The cryostat and temperature controller function extremely well. Exchange gas cooling of the sample gives confidence in sample temperature homogeneity and the germanium thermometer allows precise temperature measurement even at the lowest temperatures attainable. The design of the sample chamber and the manner of sample insertion allows specimens to be changed without warming the entire cryostat. A very large temperature range can be covered. The cryostat is relatively inexpensive to run; a 5 litre fill of liquid helium will last 24 h. although it is necessary to top up the liquid nitrogen tank at 12h. intervals.

In some of our earlier work, we used a cold finger cryostat that has been described previously {43}.

3.5 Experimental Procedure.

In this section, we shall mention four aspects of Mössbauer experimental technique; absorber preparation, experimental conditions, spectrometer calibration and line shape considerations.

In all the Mössbauer work that will be described, absorbers were in the form of finely ground polycrystalline powders. One of the pre-requisites of a Mössbauer absorber is that it should have a reasonable recoilless fraction and some of the compounds investigated had a very low iron content of which ^{57}Fe represented only $\sim 2\%$ ordinarily. It was therefore, necessary to boost the ^{57}Fe content by using iron that had been enriched in ^{57}Fe (15). In order to determine by how much the ^{57}Fe content should be boosted, we adopted the following recipe. We set a minimum acceptable ^{57}Fe content of $0.03\text{mg } ^{57}\text{Fe cm}^{-2}$ in a 100mg absorber on an area of 1cm^2 . The figure of $0.03\text{mg } ^{57}\text{Fe cm}^{-2}$ was derived from experiments on $\alpha\text{-Fe}_2\text{O}_3$. Hence, if the natural iron content of the compound is $X\text{wt}\%$, then of the $X\text{mgFe}$ in the absorber $\frac{2.17.X}{100}$ mg are ^{57}Fe , if this weight:

$$\frac{2.17}{100} x \geq 0.03 \quad \text{i.e.} \quad x \geq 15\%$$

then there was no need to enrich the samples. For example, FeCr_2S_4 has 20% iron by weight. If the inequality did not hold, then a weight F of the iron was added as ^{57}Fe where:

$$F = 0.03 - \frac{2.17}{100} x \quad \text{mg}$$

The powders must be contained in some fashion for use in the spectrometer. In some of our experiments, low temperature absorbers were made by mixing the powder with G.E. varnish and allowing this mixture to set in a 0.6 inch diameter disc on a clean aluminum foil. In later experiments, we have clamped the powders between 1 inch diameter Be discs in a manner which is similar to that used for the high temperature ($T > 300^\circ \text{K}$) absorbers. For experiments where an external field was applied, absorbers were made by mixing the powder with a thermosetting plastic. This immobilizes the granules and makes a rigid, self supporting, absorber but this rigid matrix puts strain on the granules {45} and we think this strain has some unfortunate effects. We shall discuss this possibility later.

The experimental conditions have already been mentioned to some extent and here, we remark that we attempted to gather information about the

three hyperfine interactions as a function of temperature in the range $2^\circ \leq T \leq 500$ K. Some experiments were made in applied external fields up to 50kOe.

The Mössbauer spectrometer must be calibrated using some standard absorber. In the course of our experiments, we have used iron foil, α -Fe₂O₃ and sodium nitroprusside, table 6 shows the calibration data that has been employed {46}.

Table 6. Calibration Data for Mössbauer Spectrometer.

| Standard Absorber | Isomer Shift Relative to ⁵⁷ Co in Cr (mm.s ⁻¹) | Peak Separations (mm.s ⁻¹) | | | Q.S. (mm.s ⁻¹) | H _{eff} kOe |
|--|---|--|-------------|-------------|----------------------------|----------------------|
| | | $\Delta 16$ | $\Delta 25$ | $\Delta 34$ | | |
| Iron Foil | 0.152 | 10.657 | 6.167 | 1.677 | | 330 |
| α -Fe ₂ O ₃ | 0.512 | 16.70 | 9.66 | 2.63 | | 517 |
| Sodium Nitroprusside | 0.105 | | | | 1.712 | |

Calibration of the spectrometer for experiments in applied external fields is of particular importance, for, inspite of precautions taken against it {43}, the stray field from the solenoid affects the motion of the transducer. Therefore, it is necessary to calibrate the spectrometer at each field used and to maintain precisely the same geometry for the calibration

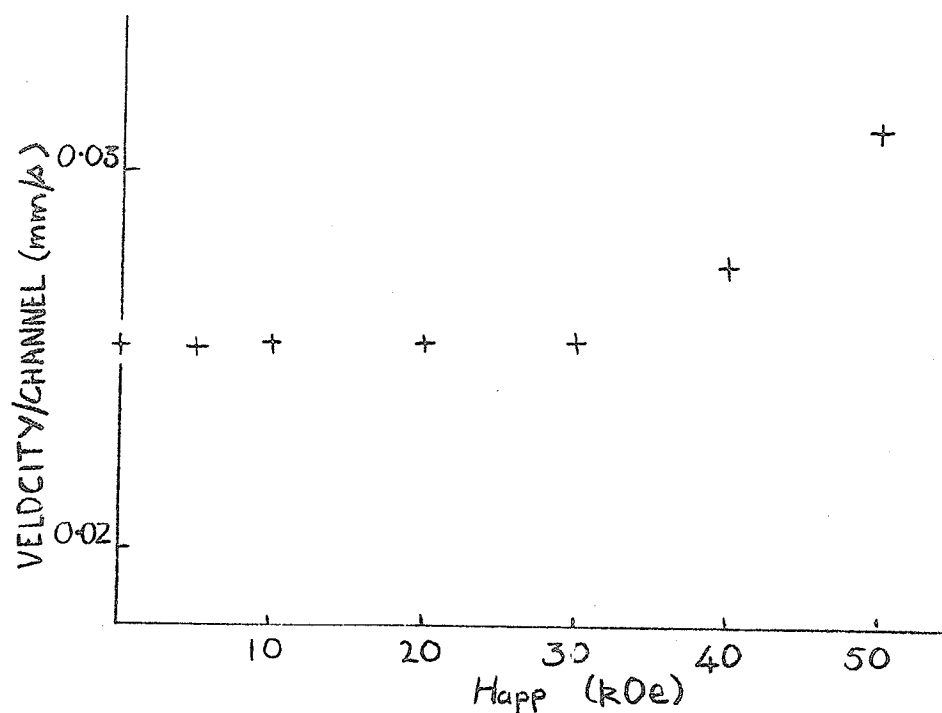


Figure 24. Effect of stray fields on velocity calibration.

as for the experiment. In figure 24, we show the calibration constants for our spectrometer as a function of external field as determined during a particular experimental run. The stray fields are $\sim 10^2$ Oe but it can be seen that their effect is remarkable, especially on the velocity calibration.

Calibrating with iron foil allows some assessment to be made of the linearity of the velocity scale. We have found that linearity in our spectrometer is $\geq 2\%$.

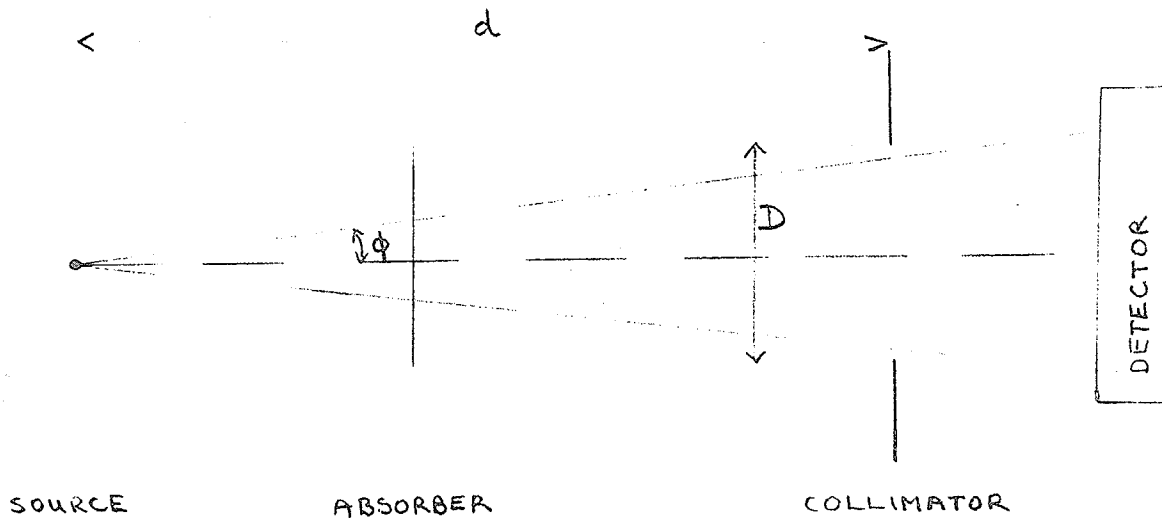


Figure 25. To illustrate collimation geometry.

$$\text{i.e. } (\Delta_{12} - \Delta_{56}) / \Delta_{12} \lesssim 0.02$$

The final point concerns the collimation of the spectrometer. The problem of collimation effects has been dealt with by several authors and a survey is given in {47}. In figure 25, a schematic arrangement of a point source, a collimator and a detector is shown. If it were possible, we would like to detect only those γ -rays emitted parallel to the source velocity but this so severely attenuates the counting rate that it is impractical. Therefore,

a finite solid angle is allowed. This solid angle is characterized by ϕ or the ratio $D/2d$ indicated in figure 25. Whether a point source or, a more realistic, extended source {47}, is considered the line broadening introduced by a non-zero ϕ is found to increase as $(D/2d)^2$ and to be greater, the greater is the displacement of the absorption line from the zero of velocity on the spectrometer. This effect is illustrated in figure 26 where we plot some experimentally determined line widths at various velocities for various values of $(D/2d)$. Also,

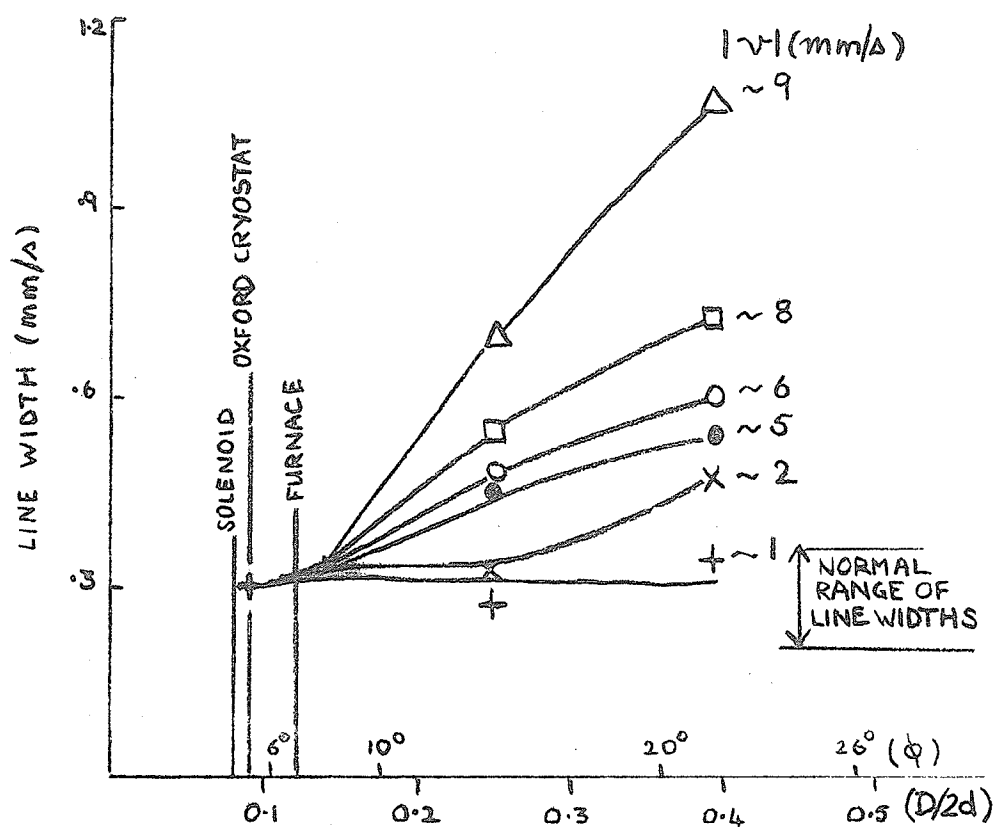


Figure 26. Line widths as a function of collimation angle for various line positions.

indicated in figure 26 are the values of $(D/2d)$ usually obtained in the various laboratory set ups. The line widths plotted in figure 26 were obtained from the spectra of figure 27 which are from an $\alpha\text{-Fe}_2\text{O}_3$ absorber. These spectra also illustrate the other effect of increasing collimation angle, i.e. the velocity shift of each peak position. This effect does not matter provided the spectrometer geometry is held constant.

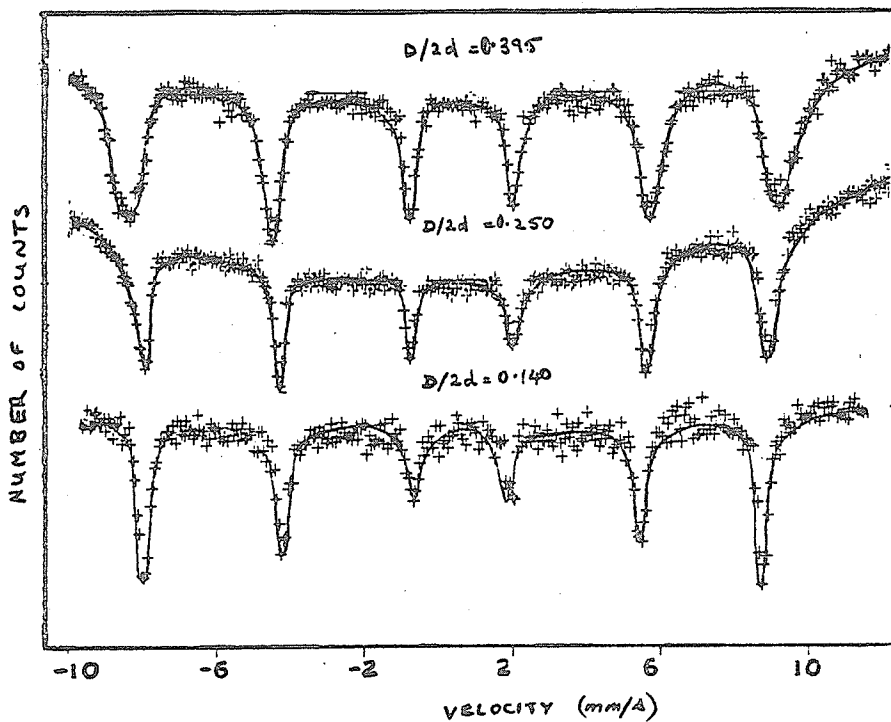


Figure 27. Illustrating the effect of collimation on $\alpha\text{-Fe}_2\text{O}_3$ line widths and positions.

3.6 Data Analysis

Mössbauer spectroscopy produces a very large amount of data that is usually analysed initially with the aid of a computer. At this university, we are fortunate to have an I.B.M. 360 system. Data from the spectrometer on punched paper tape can be readily converted to card form by means of an I.B.M. 1620 machine. Following this there are two routes that may be taken:

- (i) If the spectrum is obviously simple, then a least squares fit to the peak positions is usually sufficient for the various Mössbauer parameters to be extracted;
- (ii) If the spectrum is fairly complicated then a least squares fit of the exact nuclear Hamiltonian to the data is required. This type of fit is then checked against the rather freer fit given in (i).

The fitting program used in (i) is known as "MONKEY" and was given to us by the Applied Mathematics Division at Argonne. The fitting in (ii) is accomplished by means of a programme called "POWDER" that utilizes as a subroutine the solutions obtained for the complete nuclear Hamiltonian by the author of {48}.

These programmes are described in a little more detail in appendix D.

Literature Cited in Chapter II

1. A.H. Morrish, *The Physical Principles of Magnetism*, John Wiley, New York, 1965.
2. J.S. Smart, *Effective Field Theories of Magnetism* Saunders, Philadelphia, 1966.
3. J.H. Van Vleck, *The Theory of Electric and Magnetic Susceptibilities*, Oxford University Press, 1965.
4. J.M. Ziman, *Principles of the Theory of Solids*, Cambridge University Press, 1965.
5. C. Kittel, *Introduction to Solid State Physics*, John Wiley, New York, 1968.
6. G.K. Wertheim, *Mössbauer Effect Principles and Applications*, Academic Press, New York, 1964.
7. H. Fraunfelder, *The Mössbauer Effect*, Benjamin, New York, 1963.
8. J. Danon, *Lectures on the Mössbauer Effect*, Gordon & Breach, New York, 1968.
9. E.F. Bertaut, *Magnetism III*, Edited by G.T. Rado and H. Suhl, Academic Press, New York, 1963.
10. L. Néel, *Ann. Phys. (Paris)* 3, 137, 1948.
11. E.W. Gorter, *Philips. Res. Rep.*, 9, 321, 1954; 9, 403, 1954.
12. G. Blasse, *Philips, Res. Rep. Suppl. number 3*, 1964.
13. T.A. Kaplan, K. Dwight, D. Lyons, and N. Menyuk, *J. Appl. Phys.*, 32, 133, 1961.
14. K. Dwight and N. Menyuk, *Phys. Rev.*, 163, 435, 1967.
15. A. Yoshimori, *J. Phys. Soc. Japan*, 14, 807, 1959.
16. J. Villain, *J. Phys. Chem. Solids*, 11, 303, 1959.
17. T.A. Kaplan, *Phys. Rev.*, 116, 888, 1960.

18. I.E. Dzialoshinsky, *J. Phys. Chem. Solids*, 4, 241, 1958.
19. F.K. Lotgering, *J. de Phys.*, 32, C-1, 34, 1971.
20. H.A. Kramers, *Physica*, 1, 182, 1934.
21. P.W. Anderson, *Phys. Rev.*, 79, 350, 1950; *Phys. Rev.*, 115, 2, 1959.
22. J.B. Goodenough, *J. Phys. Chem. Solids*, 6, 287, 1958.
23. J. Kanamori, *J. Phys. Chem. Solids*, 10, 87, 1959.
24. J.A. Eaton, Ph.D. Thesis University of Manitoba, 1970
L.K. Leung, Ph.D. Thesis University of Manitoba, 1972.
25. S. Foner, *Rev. Sci. Inst.*, 30, 7, 1959.
26. P. Weiss and R. Forrer, *Ann. Phys. (Paris)*, 5, 153, 1926.
27. S. Akajcs and G.R. Dunmyre, *Phys. Stat. Sol.*, 21, 191, 1967.
28. C. Hass, *Rev. Solid State Sci.*, 1, 47, 1970,
Chemical Rubber Co., Cleaveland, Ohio.
29. T. Kasuya, *Solid State Commun.*, 8, 1635, 1970.
30. T. Kasuya, A. Yanase and T. Takeda, *Solid State Commun.*, 8, 1543, 1970; 8, 1551, 1970.
31. A. Yanase, T. Kasuya and T. Takeda, *Proc. Int. Conf. on Ferrites*, Japan, 1970.
32. J.R. Drabble and T.D. White, *J. Phys. E.*, 3, 515, 1970.
33. R.L. Mössbauer, *Z. Phys.* 151, 124, 1958, *Naturwiss.*, 45, 538, 1958, *Z. Naturforsch.*, 149, 211, 1959.
34. W.E. Lamb, *Phys. Rev.*, 55, 190, 1939.
35. L.R. Walker, G.K. Wertheim and V. Jaccarino, *Phys. Rev. Lett.*, 6, 98, 1961.
36. R.V. Pound and G.A. Rebka, *Phys. Rev. Lett.* 4, 274, 1960.

37. B.D. Josephson, Phys. Rev. Lett., 4, 341, 1960.
38. S.S. Bashkirov and G.Y. Selyutin, Phys. Stat. Sol.,
26, 253, 1968.
39. Y.A. Iosilevskii, J.E.T.P., 27, 495, 1968.
40. J.M.D. Coey, G.A. Sawatsky and A.H. Morrish, Phys.
Rev., 184, 334, 1969.
41. J.M.D. Coey, Ph.D. Thesis University of Manitoba, 1971.
42. G.A. Sawatsky Ph.D. Thesis University of Manitoba, 1969.
43. M.R. Spender and A.H. Morrish, Can. J. Phys., 50,
1125, 1972.
44. L.K. Leung, Ph.D. Thesis University of Manitoba, 1972.
45. A. Gerard, P. Imbert, H. Prange, F. Varret and M.
Wintenberger, J. Phys. Chem. Solids,
32, 2091, 1971.
46. Mössbauer Effect Data Index, 1958-1965, Edited by
A.H. Muir, K. Ando and H.M. Coogan,
John Wiley, 1966.
47. F. Aramu and V. Maxia, Nucl. Inst. Methods, 80,
35, 1969.
48. W. Kundig, Nucl. Inst. Methods, 48, 219, 1967.

Manufacturers and Suppliers.

- (1) PRINCETON APPLIED RESEARCH, P.O. Box 565, Princeton,
New Jersey, U.S.A. 8540;
Magnetometer Model FM1,
High temperature facility model.
- (2) MAGNION, 144, Middlesex Turnpike, Burlington, Mass.
U.S.A. 01804;
Field Control Unit Model FFC4.
- (3) RAWSON ELECTRICAL INSTRUMENT CO., 101 Potter Street,
Cambridge, Mass, U.S.A.;;
Gaussmeter Model 920 M.C.M.
- (4) ANDONIAN ASSOCIATES, 26, Thayer Road, Waltham 54,
Mass, U.S.A.;;
Cryostat to P.A.R. Spec.
- (5) DANA LABORATORIES, Irvine, California, U.S.A., 92664;
D.V.M. Model 5270.
- (6) ELSCINT, P.O. Box 5258, Haifa, Israel,
ELRON, 9701, N. Kenton Ave., Skokie, Illinois, U.S.A.,
60076.
- (7) NEW ENGLAND NUCLEAR, 11475, Cote de Liesse, Dorval,
Quebec.
- (8) HARSHAW CHEMIE, Strijkviertel, 95, De Meern, Holland;
Crystal Scintillator 6SHDO 2M/2G-Q
Photomultiplier Tube E.M.I. 9656.
- (9) 20TH CENTURY ELECTRONICS, Surrey, England;
Argon/Methane Proportional Counter
PX 130f/A.
- (10) HEWLETT PACKARD, 395 Page Mill Road, Palo Alto,
California, U.S.A., 94306;
Printer Model J18565A.
X-Y Recorder Model 7004AX-Y.
- (11) NUCLEAR DATA, P.O. Box 451, Palatine, Illinois, U.S.A.,
60067.
- (12) TALLY CORP., 1310 Mercer Street, Seattle, Washington,
98109;
Punch Model 1505.

- (13) OXFORD INSTRUMENT CO., Osney Mead Road, Oxford,
England.
- (14) HARWELL TEMPERATURE CONTROLLER, SUPPLIERS, OXFORD
INSTRUMENT CO.
- (15) OAK RIDGE NATIONAL LABORATORY, Oak Ridge, Tenn.,
U.S.A. 37830.

III EXPERIMENTAL WORK ON FOUR COMPOUNDS.

In this, the first of two chapters describing experimental work, we present and discuss the results of our investigations of four quite different compounds. Three of these compounds Fe_3S_4 , $\text{Fe}\{\text{Cr}_2\}\text{S}_4$ and $\text{Cd}\{\text{Cr}_2\}\text{S}_4$ were known to exist before we started our work. They had been investigated in various experiments and explanations of many of their properties were either established or at least suspected. We have reviewed, albeit briefly, the results of relevant experimental work, in an attempt to place our own investigations in perspective. Our studies of these compounds are described in sections 1, 2, and 3 respectively. The fourth compound is described in section 4. We suspected its existence but so far only rather impure samples have been prepared.

1. A STUDY OF $\text{Fe}[\text{Fe}_2]\text{S}_4$.

The work described in this section has been reported previously [1,2] and is given here in much the same form.

1.1 Introduction.

In contrast to the iron oxides, a large variety of phases are found in the compounds of iron and sulphur, many of which have recently been reviewed [3]. Two structures are known for the compound Fe_3S_4 and both have been identified from natural minerals. Smythite has an hexagonal layer structure rather like pyrrhotite [4] and it appears to be difficult to synthesize pure material [5,6]; greigite has the spinel structure [7]. It is an extremely rare mineral and a number of syntheses have been proposed, all of which yield reasonably pure greigite with small crystallite size [6,8,9,10,11,12].

By comparison with magnetite, its isomorphous oxide, greigite has not been very extensively studied. It has been shown to be thermodynamically unstable relative to pyrrhotite [14] but natural greigite shows no tendency to decompose in air at room temperature. When heated in vacuum, it is stable up to 280°C [7] where it decomposes to pyrrhotite. Under other

conditions, there is a much more limited range of stability {9}.

The compound crystallizes in the spinel structure with an ideal cubic sulphur array {7,9}. The lattice parameter is 9.876 Å but values between 9.81 and 9.90 Å have been reported for the synthetic material. Some workers {6} report a distortion in the structure although this is not mentioned by anyone else.

In addition to x-ray studies, synthetic Fe_3S_4 has been studied by electron diffraction {8,9,10,15,16} and it has recently been shown that anisotropy can be induced by an electrostatic field above 313°K {17}. Some magnetic properties have been reported {9,10,16}. No coercivity was detected, the saturation magnetization was $1.3\mu_B$ per formula unit ($\approx 24\text{emu/g}$) and an ordering temperature of 580°K was deduced from low temperature measurements.

Mössbauer spectra have also been reported {6,16,18}. These show several superposed spectra with hyperfine fields 300kOe.

Our study of Fe_3S_4 was conducted on synthetic samples that we found to be rather poorly crystallized and non-stoichiometric to varying extents. Based on

their Mössbauer spectra alone however, we judged them to be no worse and in some cases slightly better than other samples studied previously. Put another way, they are typical of samples of synthetic greigite and since the natural mineral was unavailable, it seemed that a study of synthetic material was the practical way to study the compound. We, therefore, judged it to be very important to make some attempt to distinguish between observations pertinent to the compound proper and observations resulting from deficiencies in sample characterization.

1.2 Preparation of Samples.

This compound was not prepared in the manner outlined in chapter 1.5, that method does not work in this case. We used the method reported in {9}. The precise details of the method are given in appendix E since it makes tedious reading. Suffice to say here that we made thirty samples. For the first 20 attempts, equal quantities 5ml of 0.15M Mohr's Salt $\text{Fe}(\text{NH}_4)_2(\text{SO}_4)_2 \cdot 6\text{H}_2\text{O}$ and 0.2M sodium sulphide were used and the yield was 100-200mg. In an effort to produce larger quantities, 0.6M Mohr's Salt and 1.6M sodium sulphide were mixed in a 2:1 ratio for the last 10 batches, the yield was ~1g.

The final product varied considerably and although we can offer no definite explanation of this fact there are several factors that may contribute:

- (i) The preparation method is a hydrothermal synthesis and the reaction temperature is critical;
- (ii) There must be a very rapid quench of the final product to prevent the formation of other phases;
- (iii) Fe_3S_4 tends to oxidise when in contact with water so washing and filtering the final product may have had a bad effect, especially on small crystallites.

We examined our 30 samples visually and only 20 that were black in colour and attracted by a hand magnet were retained for x-ray examination.

X-ray diffractometer traces were obtained for the samples and Debye-Sherrer photographs were taken of those that showed strong greigite reflections. Manganese filtered $\text{FeK}\alpha$ radiation was used throughout. The high angle lines were rather broad but all except the very weak spinel reflections could be identified. We also found some extra lines in each sample that did not belong to the spinel pattern. In some cases these lines were identified by their d values, we found different impurities in different samples. This

suggests that the problem is not a systematic fault of the preparation but rather a consequence of the ability of iron to form a large number of sulphides.

In table 7 we show the x-ray powder patterns for three of our samples together with the published pattern {7} for natural greigite. The spurious reflections are indicated by asterisks and we conclude that samples 7 and 24 contain traces of pyrrhotite and that sample 14 contains smythite and a trace of some unidentified phase. The amounts of pyrrhotite must be <5% since its Mössbauer pattern does not appear in our spectra, on the other hand, there must be >1% for the x-ray pattern to show up. Therefore, the purity of our samples is estimated as being between 95-99%.

Table 7. Part of the powder pattern from synthetic Fe_3S_4 samples; the intensities were estimated visually and the radiation was $\text{FeK}\alpha/\text{Mn}$

| <i>hkl</i> | 7 | | 14 | | 24 | | Greigite | |
|------------|-----------|-------|-----------|-------|-----------|-------|-----------|-------|
| | d_0 (Å) | I_R |
| 111 | 5.72 | 2 | 5.691 | 2 | 5.720 | 2 | 5.720 | 8.0 |
| 220 | 3.472 | 4 | 3.467 | 3 | 3.482 | 3 | 3.498 | 31.5 |
| 311 | 2.968 | 10 | 2.972 | 10 | 2.975 | 10 | 2.980 | 100.0 |
| 222 | 2.853 | 1 | — | N.O. | 2.839 | <1 | 2.855 | 3.9 |
| * | 2.637 | 2 | 2.909 | 1 | 2.637 | 2 | | |
| * | | | 2.537 | 2 | | | | |
| 400 | 2.471 | 6 | 2.466 | 5 | 2.466 | 5 | 2.470 | 54.8 |
| 331 | — | N.O. | — | N.O. | — | N.O. | 2.260 | 1.2 |
| * | 2.062 | 3 | | | 2.062 | 3 | | |
| 422 | 2.014 | 1 | 2.004 | 1 | 2.012 | 1 | 2.017 | 9.2 |
| 333 | 1.902 | 5 | 1.897 | 3 | 1.902 | 3 | 1.901 | 28.6 |
| 511 | | | | | | | | |
| 440 | 1.746 | 9 | 1.736 | 10 | 1.745 | 9 | 1.746 | 76.8 |
| 840 | 1.104 | 4 | 1.098 | 2 | 1.104 | 3 | 1.105 | 16.4 |
| 844 | 1.006 | 4 | 1.003 | 3 | 1.007 | 5 | 1.008 | 30.9 |

*Reflections not belonging to the spinel pattern.

From the high angle spinel reflections, we determined the lattice parameters given in table 8 and these same reflections were used to determine the apparent crystallite size D . According to {19} :

$$D = (\lambda/\beta) \cos \theta$$

where λ is the x-ray wavelength θ is the Bragg angle and β is the line broadening. We assumed that:

$$\beta = \beta_{\text{OBS}} - \beta_{\text{INST.}}$$

where β_{OBS} is the observed full width at half maximum intensity and $\beta_{\text{INST.}}$ is the instrumental broadening determined from a standard. The three samples described in tables 7 and 8 are among the best that we made. We chose to study them further because we believed that a strong correlation existed between bulk properties and apparent crystallite size.

Chemical analyses of the iron contents of samples 14 and 24 are given in table 8 but we had a very low yield of sample {7} and no chemical analysis was made, but where necessary, later, we shall assume the iron content of sample 7 to be the same as that of sample 14, since in some other respects the two samples are similar. The formula Fe_3S_4 has 56.64% of iron by weight. Some of the discrepancy between observed and expected iron content is presumably a result of non stoichiometry which we assume manifests itself in the form of B-site vacancies. Some of the difference

Table 8. Crystallographic and magnetic data for synthetic Fe_3S_4

| Sample | Size $D \pm 10$ (Å) | Lattice parameter $a_0 \pm 0.01$ (Å) | Wt. % Fe (Wet chemical analysis) | Magnetic moment 4.2°K. $H \rightarrow \infty$ $\mu_B/\text{formula unit}$ | |
|--------|---------------------------|---|--|---|-------------|
| | | | | Observed | Corrected * |
| 7 | 137 | 9.86 | — | 2.05 | 2.26 |
| 14 | 117 | 9.83 | 54.6 | 2.04 | 2.25 |
| 24 | 91 | 9.87 | 49.0 | 1.58 | 2.21 |

*See page 148.

however, may arise from water absorbed onto the particles' surface, an idea that we were able to check by means of infra-red absorption spectra. Figure 28a shows the absorption spectrum of sample 13, it is compared there to a spectrum taken from a natural crystal of pyrite $\text{Fe}(\text{S}_2)^{\bar{2}}$ (b). It may be seen that there is strong absorption at 1450 cm^{-1} in both cases. These absorption bands are characteristic of H-OH or OH^- , but the test is not altogether conclusive, although the absorption is stronger in Fe_3S_4 than in $\text{Fe}(\text{S}_2)^{\bar{2}}$.

1.3 Magnetization Measurements.

The equipment and techniques described in Chapter II sections 1.2, 3 were used to determine the complete magnetization curve for two samples 7, and 24 in the temperature range $4.2\text{-}300^\circ\text{K}$. For these samples we also measured the first part of the curve in the range from $300\text{-}700^\circ\text{K}$. Our objectives were:

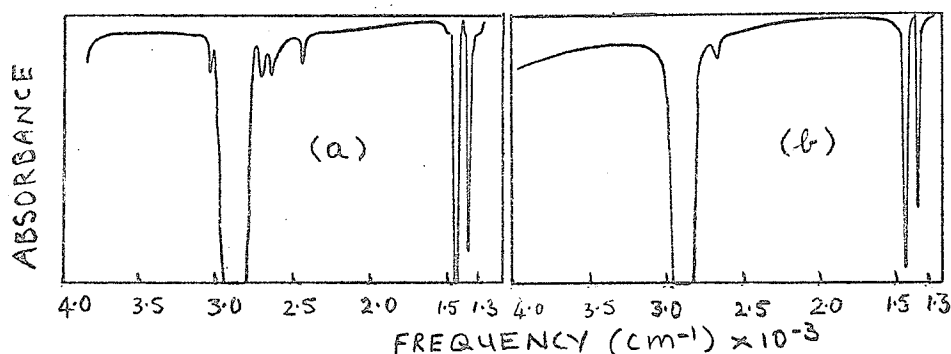


Figure 28. Infra-red absorption spectra from (a) Fe_3S_4 (b) FeS_2 . The deep absorption at $\sim 3000 \text{ cm}^{-1}$ comes from the organic binder used to disperse the powders. The absorption at $\sim 1450 \text{ cm}^{-1}$ is typical of OH^- infra-red spectra but the fact that it occurs in both sulphides is curious when one of them (b) was a well crystallized natural sample.

- (i) To determine the low temperature moment;
- (ii) To determine the magnetic ordering temperature;
- (iii) To find out whether there was any evidence for a Verwey type transition as in Fe_3O_4 {20}.
- (iv) To see whether there was any evidence of superparamagnetic behaviour.

We made thermal scans of the remanence and of the magnetization in various fixed applied fields to determine the long range ordering temperature as more conventional techniques failed on account of the tendency of the compound to decompose after long periods, at elevated temperatures.

In figure 29 we show the variation of H_C with temperature for samples 7 and 24 while figure 30 shows the temperature variation of the function M_R/M_∞ . In figure 31, M_∞ is plotted against temperature for samples 7 and 24. At low temperatures the magnetization is a slowly varying function of temperature and shows no discontinuities. At 4.2°K, M_∞ is 37.6 and 28.5 e.m.u./g for the two samples respectively. The corresponding moments per Fe_3S_4 formula unit are given in column 5 of table 8.

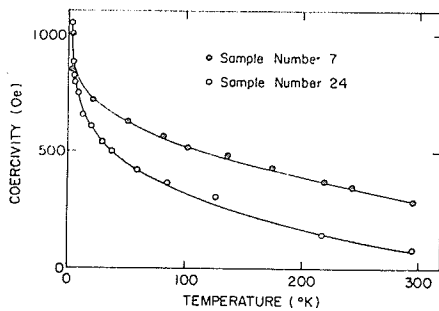


Figure 29. H_C versus T
 $D(7)=137 \text{ \AA}$, $D(24)=91 \text{ \AA}$

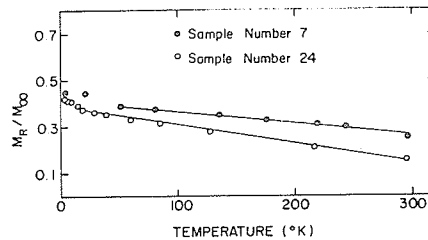


Figure 30. M_R/M_∞ versus T
 $D(7)=137 \text{ \AA}$, $D(24)=91 \text{ \AA}$

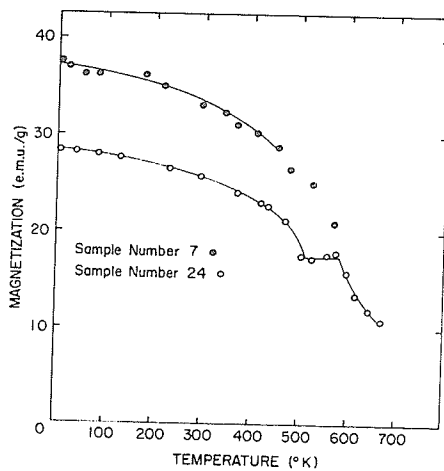


Figure 31. M_∞ versus T
 $D(7)=137 \text{ \AA}$, $D(24)=91 \text{ \AA}$

The high temperature behaviour of the magnetization shows the thermal decomposition of the compound. The magnetization levels off at about 500°K and then continues to fall above 600°K. After heating to 670°K, the greigite had decomposed to a dark brown powder and we could find no trace of the original reflections in the x-ray powder pattern. The phases present were not identified.

The thermal scans in the fixed applied fields are shown in figure 32. Following {21} we attribute the peak in the curve at high temperatures to the balance of anisotropy and magnetization energies and conclude that it occurs below the ordering temperature. We, therefore, extrapolated the steeply falling parts of the curves above the peaks to $M=0$

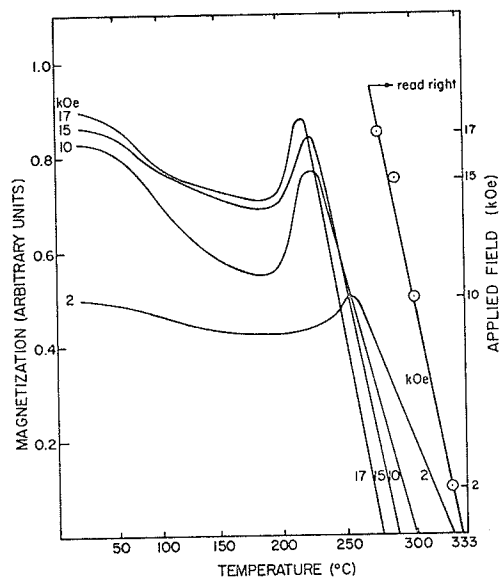


Figure 32. Thermal scans of magnetization in various applied fields and extrapolation of $T_c(H)$ to $H=0$.

and obtained the four ordering temperatures that are plotted against applied field in figure 32. A linear extrapolation of these data to $H=0$ yields an ordering temperature of 606°K . A scan of the remanence, however, yielded 570°K for the temperature at which $M_R=0$.

1.4 Electrical Measurements.

We were unable to make any decisive electrical measurements because we could not produce any high density samples. The powders we did have could not be sintered because of their low decomposition temperature. We did, however, press some powders into discs that we estimated to have about 55% theoretical x-ray density. We could not solder leads to these discs so a four point probe was used. We found resistivities in the range $1-10^2\Omega\cdot\text{cm}$. By compressing the discs between brass contacts, we found lower resistivities and a decrease of about a factor of four when the temperature was lowered from 300 to 4.2°K . We do not have much regard for these results and consider them, at best, indicative of semimetallic behaviour.

1.5 Mössbauer Effect Spectroscopy.

Spectra were recorded for 12 samples at room temperature. All consisted of a six line magnetic

pattern with a hyperfine field of about 310kOe superposed on a central doublet. Both the magnetic pattern and the central doublet had rather broad lines that suggested the presence of more than one spectrum. The intensity ratio of the doublet/magnetic pattern varied quite a bit from sample to sample. In figure 33 the patterns of three samples are displayed, and marked at the right hand side of each pattern are the results of the room temperature measurements of M_{∞} and H_C together with the intensity ratio of doublet/magnetic pattern. More detailed investigations were made on samples 7, 14 and 24, and their room temperature spectra are shown in figure 34. If the area under the outer pair of lines is assigned a value 3, then table 9 shows the ratio of intensities for outer pair: middle pair: central area. It can be seen that the intensity of the central portion increases as the effective crystallite size decreases. The quadrupole splitting and isomer shift of this central doublet are estimated to be 0.64 and 0.52 mm/s respectively.

In figure 35, the temperature dependence of the Mössbauer spectrum of sample 24 is shown. The central peaks are reduced in intensity as the temperature is lowered, in fact, by 100°K, 78% of all the absorption is in the magnetically split pattern. By

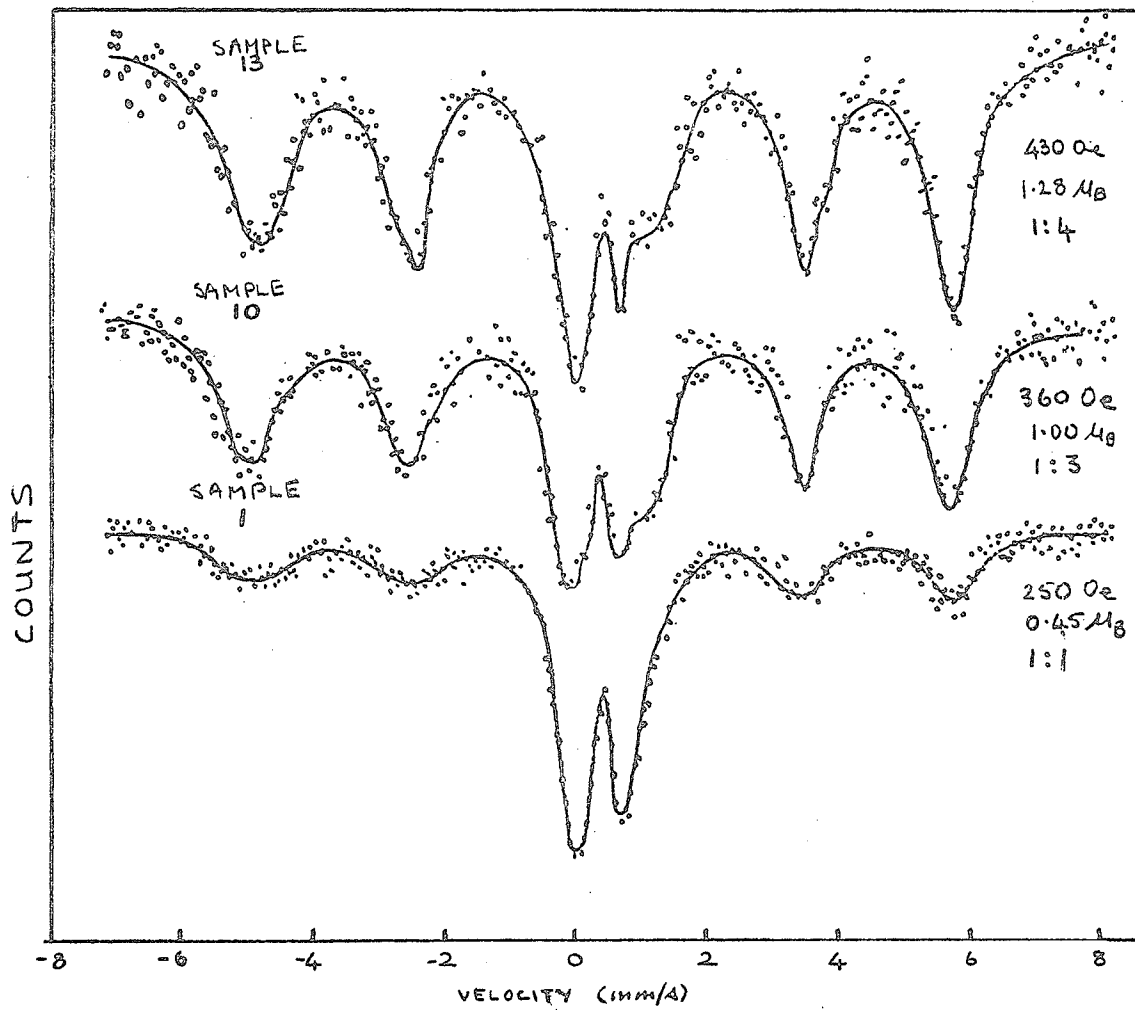


Figure 33. Mössbauer spectra at 296°K for various samples of synthetic Fe_3S_4 .

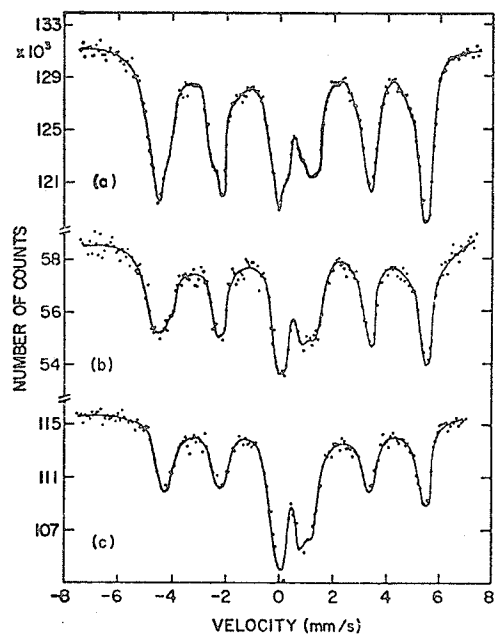


Figure 34. Mössbauer spectra 296°K

- (a) Sample 7 $D=137 \text{ \AA}$,
 (b) Sample 14 $D=117 \text{ \AA}$,
 (c) Sample 24 $D=91 \text{ \AA}$.

Table 9. Intensity ratio of outer, inner and middle pairs of lines.

| Experimental conditions | Sample number | | |
|--|-----------------|----------------|----------------|
| | 7 | 14 | 24 |
| 296 °K | 3.00:2.07:2.45* | 3.00:2.14:3.10 | 3.00:2.00:4.79 |
| 296 °K, $H = 50 \text{ kOe}$ | 3.00: — :1.40 | — | — |
| 100 °K | — | — | 3.00:2.23:2.84 |
| 296 °K after prolonged cooling | 3.00:2.21:4.02 | — | 3.00:1.76:7.08 |
| 100 °K after prolonged cooling | — | — | 3.00:1.98:6.70 |
| 270 °K, $H = 90 \text{ kOe}$ after cooling to 115 °K | — | — | 3.00: — :5.34 |

*Errors are ± 0.15 .

4.2°K, however, the spectrum again becomes complex. It appears to be composed of three magnetically split patterns with intensity ratios 2:2:1. The most widely split pattern has very broad outer lines $\sim 1.45\text{mm/s}$ and a hyperfine field of 470kOe. The other two patterns resemble each other and have fields of about 327 and 313kOe. These results are collected in table 10. On returning to room temperature, the magnetically split pattern is weaker, relative to the central portion, than in the original room temperature spectrum. This may be seen by comparing figure 35a with figure 34c or by considering the

Table 10. Hyperfine parameters for sample 24 deduced from zero field spectra.

| Pattern | 296 °K | | 100 °K | | 4.2 °K | |
|---------|-----------------------|--------|-----------------------|------|------------------------|-----------|
| | H_{hf} (kOe) | IS^* | H_{hf} (kOe) | IS | H_{hf} (kOe)† | IS^{**} |
| 1 or A | 308 | 0.51 | 316 | 0.57 | 313 | 0.64 |
| 2 or B | 291 | 0.60 | 321 | 0.80 | 327 | 0.77 |
| 3 | — | — | — | — | 472 | 0.61 |

*Isomer shifts are given relative to the source, 10 mCi of ^{57}Co in Cr; the units are mm/s.

†We estimate an error of ± 10 kOe.

**We estimate an error of ± 0.05 mm/s.

intensity ratios given in table 9. We found a similar effect in sample 7 and a comparison may be made between figure 34a and figure 36a. We took x-ray powder diffraction patterns after cooling these samples and found that two weak reflections had appeared at $d=3.94$

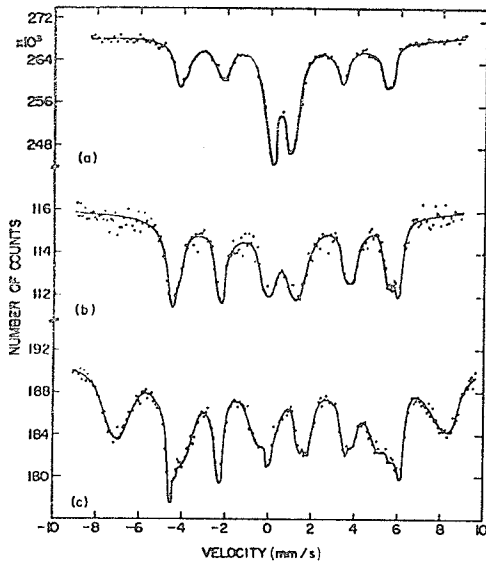


Figure 35. Mössbauer spectra of sample 24 at (a) 296°K (b) 100°K (c) 4.2°K

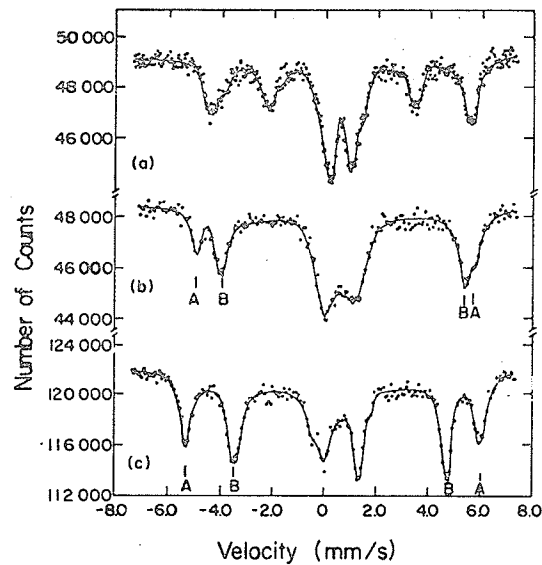


Figure 36. Mössbauer spectra of sample 7 in applied fields; (a) $H_{app}=0$ (b) $H_{app}=20kOe$ (c) $H_{app}=50kOe$.

and 2.19 \AA and we conclude that prolonged cooling induces an irreversible change in the structure that has an appreciable effect on the Mössbauer spectrum.

In order to determine the spin arrangement in Fe_3S_4 , Mössbauer Spectra were obtained for several samples in an applied field of 50kOe and the field dependence was found for sample 7. Some of the spectra are shown in figure 36 and the variation of effective field with applied field is shown in figure 37. Each of the outer lines of the magnetic pattern are split by the applied field into two lines of unequal intensity, these are marked A and B in figure 36, and the middle lines disappear when H_{app}

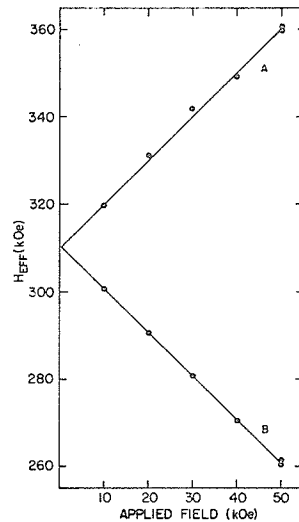


Figure 37. Variation of H_{eff} with H_{app} for the two sublattices.

exceeds 10kOe. There are three points to be made:

- (i) The splitting of the original pattern indicates the presence of two magnetic sublattices;
- (ii) The disappearance of the middle lines indicates that the magnetizations on the two sublattices are collinear;
- (iii) The data in figure 37 shows that at one sublattice, the effective field decreases while at the other, it increases indicating that the magnetizations are antiparallel.

The third point requires some explanation and in figure 38 we have tried to illustrate how the conclusion can be drawn. We recall figure 20 and note that H_s is directed opposite to the ionic 3d spin. In figure 38, \underline{M}_B is supposed to be larger than \underline{M}_A so that

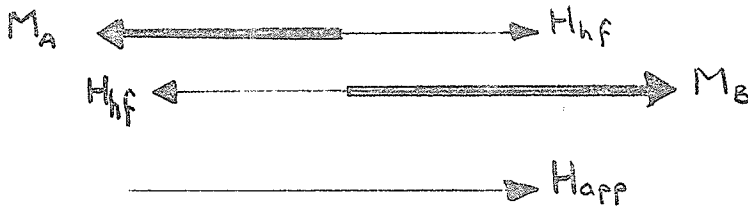


Figure 38. To illustrate the effect of H_{app} on H_{hf} .

H_{app} aligns the dipoles associated with B ions and therefore, H_{app} is opposed to H_{hf} for B ions so that for B ions $H_{eff} = H_{hf} - H_{app}$. If we suppose that \underline{M}_A is antiparallel to \underline{M}_B then at A ions we have:

$$H_{eff} = H_{hf} + H_{app}$$

As a broad principle then, we can say that for Mössbauer spectra in applied fields H_{app} adds to H_{hf} for sublattices whose magnetizations are antiparallel to the net sample magnetization, and vice versa. It is now clear why points (i) and (iii) can be made, so for completeness, we explain point (ii). To understand this, we first recall that the middle pair of lines correspond to transitions where $\Delta m_I = 0$. The angular dependence of the radiated intensity from these transitions has the form $3\sin^2\theta$, where θ is the angle between the axis of quantization and the direction of the emitted γ -ray,

there is therefore, zero intensity along the quantization axis where $\theta=0$. When H_{app} has aligned all the dipoles, it defines the axis of quantization and if $H_{app} \parallel \gamma$ -ray velocity, the $\Delta m_I=0$ transitions vanish.

The transitions corresponding to $\Delta m_I = \pm 1$ have intensities with angular dependencies $9/4(1+\sin^2\theta)$ and $3/4(1+\cos^2\theta)$ respectively which are 9/2 and 3/2 when $\theta=0$. As a corollary, if H_{app} cannot align all the dipoles e.g. if H_{app} is too small to saturate the magnetization, or if there is a canted spin arrangement, then the $\Delta m_I=0$ transitions do not completely disappear because under these circumstances, θ is not zero for all crystallites, a fact that can be used to determine canting angles $\{22\}$.

To return to the original discussion, there is one other point to make, from the spectrum in figure 36c, we can determine the relative intensities of the A and B patterns. This turns out for sample 7 to be:

$$1:1.8 \pm 0.1$$

and a similar analysis for sample 24 gave:

$$1:1.5 \pm 0.1$$

The line widths for the two patterns were 0.38 and 0.59mm/s for sample 7 and 0.62 and 0.67mm/s for sample 24. Finally, we remark that the hyperfine fields and

isomer shifts for the two patterns extrapolated to $H_{app}=0$ are given in table 11.

Table 11. Hyperfine interaction parameters in some iron sulphides.

| Compound | Formal Ionic State | Co-ordination of Iron Site | Isomer Shift Relative to Cr | Hyperfine Field or Quadrupole Splitting | Comments | References |
|----------------------|--------------------------|----------------------------|-----------------------------|---|---|------------|
| Fe_3S_4 (greigite) | Fe^{3+} | tetrahedral | 0.41 mm/s | 311 kOe | Hyperfine fields and isomer shifts extrapolated to zero applied field | 1,2 |
| | Fe^{2+} or $Fe^{2.5+}$ | octahedral | 0.70 | 310 kOe | | |
| | Fe^{11} | (octahedral) | 0.52 | 0.64 mm/s | | |
| Fe_3S_4 (smythite) | Fe^{2+} | octahedral | 0.71 | 295 kOe | | 24 |
| | Fe^{11} | octahedral | 0.48 | 0.69 mm/s | | |
| FeS (pyrrhotite) | Fe^{2+} | octahedral | 0.93 | ~260 kOe | Several hyperfine patterns depending on vacancy distribution | 5 |
| FeS_2 (pyrite) | Fe^{11} | octahedral | 0.48 | 0.61 mm/s | Low-spin ferrous iron | 5 |
| $CuFeS_2$ | Fe^{3+} | tetrahedral | 0.36 | 360 kOe | | 25,26 |
| $FeCr_2S_4$ | Fe^{2+} | tetrahedral | 0.75 | 206 kOe | Normal spinel H_{hf} at 77°K | 27 28 |
| $FeIn_2S_4$ | Fe^{2+} | octahedral | 0.96 | 3.3 mm/s | Inverse spinel | 27 29 |

1.6 Discussion of Bulk Properties.

We consider the characteristic feature of the Mössbauer spectra for Fe_3S_4 to be the magnetically split patterns and justify this apparently arbitrary assumption in the following way. The intensity ratio expected for the spinel structure for iron on all the A and B sites is 1:2; the ratios that we found were 1:1.8 and $1:1.5 \pm .1$; however, if non-stoichiometry leads to B-site vacancies in Fe_3S_4 as it does in pyrrhotite, smythite and non-stoichiometric magnetite, then the discrepancies can be accounted for. Our chemical analyses showed that the iron deficiency in

sample 24 was 13.4% and with the assumption stated earlier, the iron deficiency in sample 7 is 3.5%. If all the discrepancy is reflected in B-site vacancies, then in sample 24, 20% of the B-sites are vacant and the intensity ratio expected is 1:1.6, whereas for sample 7, we estimate 5% B-site vacancies and expect an intensity ratio of 1:1.9. If we take into consideration the errors introduced into the chemical analysis by adsorbed water, we are justified in concluding that the observed intensity ratios are in good agreement with what is expected. An additional refinement is in order if the recoilless fraction at the two sites is different, for example in Fe_3O_4 :

$$f_B/f_A = 0.94 \pm 0.02$$

at room temperature {23}.

The extrapolated zero field data indicate that the hyperfine field at both A and B-sites is the same ≈ 310 kOe and this is a curious result if Fe_3S_4 contains both ferrous and ferric iron. Certainly the isomer shift at the A-site is considerably less than that at the B-sites suggesting that Fe_3S_4 may be directly compared to magnetite where the inverse spinel cation arrangement pertains with Fe^{3+} on A-sites and $\text{Fe}^{2+} + \text{Fe}^{3+}$ on B-sites.

In chapter II section 3.2, we discussed the isomer shift and the ambiguity that arises when

chemical bonds contain substantial covalent contributions. In Fe_3S_4 we encounter such a problem. In table 11, we collect together hyperfine field and isomer shift data for various iron sulphides and we shall make use of these data in the following discussion. The isomer shift data of table 11 indicates that if an iron sulphide has an isomer shift > 0.7 mm/s relative to chromium, then it is essentially a high spin ferrous species. For octahedral sites, the range of isomer shifts for such species is 0.96 or 0.93 to 0.71 mm/s. Now in the spinel lattice, the volume of the two sites is different so that the same iron species would show a smaller isomer shift on a tetrahedral site than on an octahedral site because of the extra covalency on the smaller A-site. The covalent reduction may be expected to be the same at both ends of the isomer shift range. So, if we take the isomer shift of iron in FeCr_2S_4 as an upper limit for high spin ferrous iron on A-sites and compare it with the isomer shift of Fe^{2+} in FeIn_2S_4 , we obtain a scaling factor that allows an estimate to be made of the lower limit of isomer shifts of high spin ferrous iron in tetrahedral sites. To summarise, high spin ferrous iron in octahedral and tetrahedral sites in sulphides may show isomer shifts in the ranges:

0.71 - 0.96 mm/s and 0.56 - 0.75 mm/s respectively.

The A-site iron in Fe_3S_4 appears to be ferric in view of the considerations above, the B-site iron presents more problems. For purely ionic bonding, half would be Fe^{2+} and half would be Fe^{3+} , the observed isomer shift (0.70 mm/s) is at the bottom of the rough, estimated range, above but there are several arguments to suggest that in sulphides, octahedrally co-ordinated iron is invariably ferrous:

- (i) In wet sulphurous solutions iron is always in the ferrous state;
- (ii) In the case of pyrrhotite, the combined evidence of Mössbauer and transport studies shows that all the iron is ferrous and that there are holes in an anion-anion overlap band {1};
- (iii) The mineral smythite has the same chemical formula as greigite, Fe_3S_4 , but Mössbauer studies show that the mineral is a ferromagnet and all the iron is ferrous {24};
- (iv) There is considerable doubt concerning the existence of Fe_2S_3 which would contain only ferric iron and be analogous to Fe_2O_3 {1}.

One effect of non-stoichiometry has been discussed in terms of B-site vacancies that lead to a discrepancy between the observed and ideal A:B-site intensity ratios. We shall discuss a second plausible

effect later but we shall mention now that non-stoichiometry probably leads also to local regions of strongly covalent bonding that cause low, rather than high spin ferrous states to exist in these regions. These low spin ions reduce the expected magnetic moment since they have $S=0$. Thus in each molecule of Fe_3S_4 containing a B-site vacancy, we propose that the other B-site will be low spin. This is consistent with the view that all the B-site iron is ferrous. It follows then that the magnetic moments measured for samples 7 and 14 should be increased by $\sim 10\%$ and that of sample 24 by $\sim 40\%$ since we have already estimated 5% and 20% B-site vacancies in these samples. These corrections lead to the figures shown in table 8, column 6. We, therefore, conclude that a magnetic moment of $2.2 \pm .3 \mu_B$ /molecule is typical of Fe_3S_4 . This figure is inconsistent with any arrangement of high or low spin cations on the A and B-sites that would yield the observed field dependence of the Mössbauer spectrum. Further, the conductivity check indicates that at least some of the charge carriers must be delocalized.

In order to account for these results in terms of a band scheme, the cation valencies should be known. As we have seen, there is some uncertainty concerning this point and as a result, we shall propose

two band schemes. The first is based on the proposal that Fe_3S_4 has an average of ferric and ferrous iron on the B-sites. It has its origins in the scheme suggested for magnetite {30,31} and is shown in figure 39b. The scheme in figure 39a is that for magnetite and in keeping with ionic considerations for the oxide, it results from the effect of intra-atomic exchange on crystal field split d-orbitals at octahedral and tetrahedral sites. In the sulphide, as we have remarked in chapter I, section 3, we should take account of the extra d-electron covalent overlap {32} with the anions so in figure 39b the $t_{2g}(A)e_g\uparrow(B)e_g\uparrow(A)$ orbitals constitute a σ^* band. Exchange splitting is supposed to be smaller in the sulphide than in the oxide so that $t_{2g}\downarrow B$ overlaps σ^* . As a first approximation, the electrons in σ^* are supposed to be collective and σ^* is unpolarized. If it is to remain so, then $t_{2g}\downarrow(B)$ accepts electrons from it in pairs so that the magnetic moment is:

$$(2(3-x)-2)\mu_B \text{ per molecule}$$

where $2x$ is the number of $t_{2g}\downarrow(B)$ electrons per molecule. The measured moment shows that $x \approx 1$ so that the B-site cations have an electron configuration like $(t_{2g}^4, \sigma^*1.5)$, an intermediate spin state similar to that proposed in {33} for Ru^{3+} in

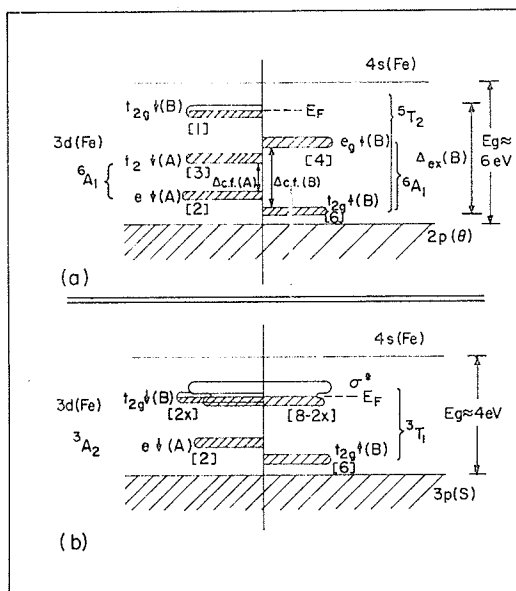


Figure 39. Proposed one-electron energy band schemes for (a) Fe_3O_4 and (b) Fe_3S_4 . In (b), the $t_{2g}^{\downarrow}(\text{B})$ band has $2x$ electrons per formula unit, leaving $8-2x$ in the unpolarized σ^* band. The Fe (B) electronic configuration is approximately $t_{2g}^4 \sigma^* 1.5$.

LaRuO_3 . A moment greater than $2\mu_B$ /molecule will result if σ^* is polarized suitably. Conduction in this model is presumably via σ^* electrons with some contribution from $t_{2g}^{\downarrow}(\text{B})$.

The second band scheme is based on the idea that Fe_3S_4 has only ferrous iron on the B-sites. This scheme is sketched in figure 40. In order that the B-sites have only ferrous iron, the sulphur lattice must reduce one ferric ion per molecule to the ferrous state so that there is one hole per molecule in the valence band. The Fe^{2+} levels are below the top of the valence band. Figure 40 shows the positions

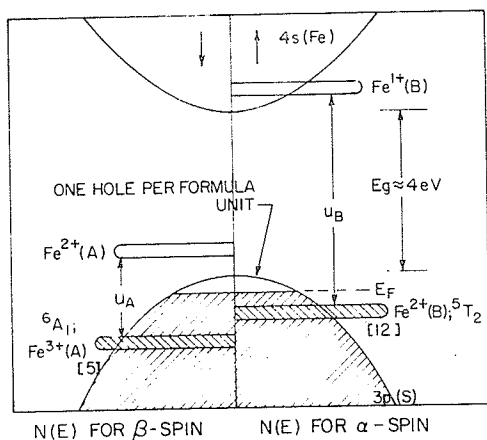


Figure 40. Alternative energy band scheme for Fe_3S_4 assuming that only ferrous ions are stable on octahedral sites in the sulphur lattice.

of the ionic terms not the one electron orbitals of figure 39 and the energy U is that needed to add an extra electron to convert an Fe^{n+} to an $\text{Fe}^{(n-1)+}$ ion. These excited states lie above the Fermi level E_F . The magnetic moment in this case is $3\mu_B/\text{molecule}$. This may be reduced by spin polarization of the valence band in the sense suggested in {34} for CuCr_2S_4 but an opposite valence band polarization was suggested for CdCr_4S_4 {32}. Conduction in this model would be via holes in the valence band.

Our study does not allow us to choose between these models although the magnetization measurements tend to favour the first.

1.7 Discussion of Sample Peculiarities.

As we said earlier, this study had two

parts, the second of which will be discussed in this section. It will, by now, be apparent that the Mössbauer spectra of Fe_3S_4 are not what would be suggested for an ideal spinel with iron on A and B-sites; all the samples show a central doublet; our samples are, however, typical of synthetic greigite. In case some basis of comparison is required, the spectrum from our sample 1, figure 33 shows about as much magnetically split absorption as the spectrum for greigite in {6}. There are four points to be made about the central absorption:

- (i) It is of greater intensity relative to the magnetic pattern as (a) the apparent crystallite size is smaller (b) the deviation from stoichiometric iron content is larger;
- (ii) It tends to disappear from the Mössbauer spectrum as the temperature is decreased;
- (iii) It diminishes only slightly at room temperature on the application of an external field;
- (iv) It has a quadrupole splitting and an isomer shift similar to that of pyrite {5} and the doublet that is observed in synthetic samples of smythite {24}.

Points (i)a and (ii) suggest that perhaps the samples are partially superparamagnetic, although (iii) indicates

that most of the central absorption arises from some other source {35}, initial efforts to determine the origins of the central absorption consisted of testing for superparamagnetism. We shall first outline briefly the basic ideas behind the tests.

Suppose we consider a magnetically ordered solid with one easy axis of magnetization. Under normal circumstances, there exists an anisotropy energy barrier KV , where K is the anisotropy energy per unit volume and V is the volume of the solid, that causes the magnetization to be in a well defined direction parallel to the easy axis. If the volume of the solid becomes so small that:

$$KV \sim kT$$

then the solid can become superparamagnetic, which means that the magnetization flips back and forth along the easy axis. The existence of such behaviour was first predicted by Néel {36,37} and although more sophisticated analyses of the phenomenon are available {38}, the relationship he proposed between the superparamagnetic relaxation time τ , and K, V and T is still of immense value. This relationship is:

$$1/\tau = Q \exp[-Kv/kT] \quad (\text{III.1})$$

where the constant $Q \approx 10^{10}/s$. Superparamagnetism is observable experimentally when $\tau \lesssim \tau_c$ where τ_c is the characteristic time of the experimental measurement.

In static magnetization measurements, the characteristic time is ~ 1 s and the disappearance of remanence and coercivity indicate superparamagnetism. The magnetization curve tends to follow the Langevin function {39}. In Mössbauer measurements, superparamagnetism is evidenced by the collapse of the hyperfine splitting and the characteristic time is $\sim 10^{-8}$ s i.e. the Larmor precession time of the nucleus in the hyperfine field. The nine orders of magnitude difference in these two τ_c means that the same sample can be superparamagnetic in magnetization measurements and yet stable in Mössbauer measurements {35,40}.

The magnetization data of figures 29 and 30 cannot be unambiguously interpreted. In figure 29, it may be seen that H_c is a decreasing function of T for both samples but it is lower at ordinary temperatures for sample 24 which had the smaller apparent crystallite size. Figure 30 shows that M_R/M_{∞} decreases steadily with increasing temperature but at a faster rate for the sample with the smaller apparent crystallite size. At no time is H_c or $M_R/M_{\infty} = 0$ as would occur if the entire sample was superparamagnetic but there exists a strong possibility that part of each sample is superparamagnetic on account of a distribution of particle sizes. It is also worth noting that in other investi-

gations {9,10,16} no coercivity was detected.

Before we look at the evidence from the Mössbauer investigation we must consider the implications of the possible distribution of particle sizes. There will be a range of volumes in any real powder sample and we can define a critical volume V_c at each temperature for which $\chi = \chi_c$. Those particles with $V > V_c$ will be stable and give a magnetically split pattern, those with $V < V_c$ will give a central superparamagnetic peak. There will in fact be a small fraction with $V \approx V_c$ that gives an intermediate relaxed spectrum. For example, if we assume a normal distribution of particle volumes between 0 and 10^6 \AA^3 , $K=10^6 \text{ erg/cm}^3$ and $T=300^\circ \text{K}$ in (III.1), 10% of the particles have:

$$10^{-9} < \chi_c < 10^{-7} \text{ s}$$

Equation (III.1) suggests two tests for superparamagnetism:

- (i) The central peaks should be more intense for samples with smaller crystallite size;
- (ii) The central peaks should gradually disappear as the temperature is lowered.

From our previous remarks, we see that there is some qualitative agreement with these predictions. To be specific, if in figure 34 we assume that the observed central pair of peaks belonging to the magnetically

split spectrum have $1/3$ the intensity of lines 1 and 6, then, the magnetic absorption represents 81, 75, and 61% of the total and decreases with decreasing particle size. Figure 35 shows that the central absorption does tend to disappear as the temperature is lowered.

A third test for superparamagnetism is suggested by the analogy of a superparamagnetic particle with a single ion of very large spin ($\sim 10^4 \mu_B$). That is, it ought to be possible to polarize the particles by the application of a large enough magnetic field {35} and therefore, remove the central peaks. On applying this test, we find that for sample 7 the central intensity decreases from 19 to 9% in a 50 kOe field while for sample 24 the decrease was from 48 to 35% in a 90 kOe field at room temperature. We, therefore, conclude that only about 10% of the particles are superparamagnetic in Mössbauer measurements at room temperature. As a check, we can assume a normal distribution of particle volumes and make use of (III.1) and the known ratio of the characteristic times viz. $10^{-8}/10^0$ to calculate the ratio of critical volume in magnetization measurements to that in Mössbauer measurements ie. 5/1 which leads, with the assumption above, to the prediction that 40% of

particles will be superparamagnetic in magnetization measurements at room temperature. As a result, M_R/M_∞ should decrease by 40% on raising the temperature from 4.2°K (where we assume no superparamagnetism) to room temperature. For sample 7 the decrease is ~45% while for sample 24, the figure is ~60%. When we consider the approximations made, the agreement is not at all bad.

We are still left, however, with the problem of explaining almost all of the central absorption. We hinted at our explanation earlier. We propose that it is associated with the B-site vacancies in the following way. The effect of the defect structure regions is to deplete the anion p-orbitals of electrons and as suggested in chapter I, section 2, this should lead to the formation of the complex anion $S_2^{=}$ at least in localized regions. Any d-electron overlap with such a large anion is bound to be much greater and lead to a considerable increase in the covalent nature of the bond. As a result, the octahedral site e_g orbitals forming the σ^* band are even more destabilized and in the local region, the iron takes a low spin, $^1A_{1g}$ state. Furthermore, $S_2^{=}$ has axial rather than point symmetry and a small quadrupole interaction arises because of the disymmetry of the surrounding anions. In keeping with the estimates

made for the magnetic moment corrections, we should find about 10% absorption from this effect for sample 7 and about 40% for sample 24. In fact, the room temperature spectra in applied fields give 9% for sample 7 and 35% for sample 24. These numbers appear to be in decent agreement so we conclude that this explanation is reasonable.

The last of our findings to be discussed is the appearance of the extra magnetic pattern at low temperatures. What we observe is that, at 4.2°K there is no central absorption, but instead, an extra magnetically split pattern that accounts for the same absorption intensity as the original central doublet. We propose that the observations can be accounted for by way of the following:

- (i) A vacancy ordering must occur;
- (ii) The ${}^1\text{A}_{1g}$ state is somehow changed to a state where $S \neq 0$;
- (iii) The ordered structure must be antiferromagnetic since no sharp changes are observed in M_0 at low temperatures.

The first and third points seem quite reasonable. The iron-sulphur system is replete with vacancy ordered structures $\{1\}$ and even in the spinel structure, cation ordering can occur but we doubt whether this vacancy ordering is in any way comparable with the Verwey

transition in magnetite. It probably bears more resemblance to the A-site ordering observed in $\text{In}_{0.5}\text{Cu}_{0.5}\text{Cr}_2\text{S}_4$ {41}. In fact, the extra reflection at $d=2.19\text{\AA}$ observed after cooling the specimen, corresponds fairly precisely to a reflection from (4,2,0) planes which is a known A-site superstructure reflection for the spinel lattice.

It is difficult to arrive at a reasonable explanation of the second point. It may be a simple matter of asserting that the two states, $(t_{2g}^4 e_g^2)^5 T_{2g}$ and $(t_{2g}^6 e_g^0)^1 A_{1g}$, are very close together and very small changes in covalency allows their positions, on an energy scale, to be reversed. On the other hand, it may be necessary to consider the ways in which π bonding destabilizes the $^1 A_{1g}$ state to the point where it is easy for the anion lattice to oxidize the ferrous iron to the ferric state and create a $^6 A_{1g}(\text{Fe}^{3+})$ state. Such a state would have to be extremely well localized, presumably in the band gap. The spectrum shift of the extra spectrum is given in table 10 as 0.61 ± 0.05 mm/s at 4.2°K which would not be unreasonable for Fe^{3+} at this temperature {42}. On the other hand, this isomer shift is too low for high spin Fe^{2+} on B-sites since our earlier crude, estimated lower limit was 0.71 mm/s and this was for room temperature. There is of course the possibility

that the spectrum arises from high spin ferrous iron on A-sites.

1.8 Conclusions.

The compound Fe_3S_4 is a ferrimagnet and has a Néel temperature of 606°K . The low temperature magnetic moment is $2.2 \mu_{\text{B}}$ /molecule and this figure, combined with the conductivity check and the field dependence of the Mössbauer spectrum, indicates that the d-electrons must be regarded as partly localized and partly delocalized. It is hard to be certain as to the cation arrangement because of the large degree of covalency in the cation-anion bonds, but, as far as our measurements go, an inverse arrangement like that in magnetite seems to be more in keeping with the data.

The preparation method used, produces samples of reasonable purity but of varying quality in as much as the specimens tended to be poorly crystallized and non-stoichiometric to varying extents. The small crystallite sizes leads to some superparamagnetism that contributes to a central absorption at room temperature. Most of the central absorption, however, arises from low spin ferrous iron formed because of the depletion of the anion p-orbitals. There is some evidence of a vacancy ordering at low

temperatures and there may be some interesting ramifications concerning the behaviour of octahedral site ferrous iron in sulphides.

2. A STUDY OF FeCr_2S_4 .

2.1 Introduction.

The compound FeCr_2S_4 is known to exist naturally as the mineral daubrelite {43}, so far as we are aware, only its x-ray structure has been examined. This is presumably because it is a very rare mineral occurring in some meteorite fragments mixed with other sulphides. Synthetic samples are, however, easy to make, and as such, the compound has been quite extensively studied.

The compound crystallizes into the spinel structure with a lattice parameter of 9.996 \AA {44,45,46} and a special position parameter $u=0.385$ {47}. The strong octahedral site preference of Cr^{3+} causes the compound to be a normal spinel with only iron on the A and chromium on the B-sites. This cation distribution has been confirmed by neutron diffraction measurements {47} and it was also shown that the spin arrangement was of the Néel ferrimagnetic type and that the structure remained cubic down to 4.2° K . The structure has also been studied by means of x-rays {48} and found to remain cubic to 77° K .

The magnetic properties have been reported by various authors and in table 12, we summarise the results of ordering temperatures and low temperature moments with appropriate references to the literature.

Table 12. Magnetization data for FeCr_2S_4 from literature.

| Ordering Temp. ($^{\circ}\text{K}$) | Magnetic moment (μ_{B} /molecule) | Experimental Conditions | References |
|---------------------------------------|---|--|------------|
| 195 | 1.5 | $T \rightarrow 0^{\circ}\text{K}$ | 49 |
| 180 | 1.52 | 1.5°K $H \rightarrow \infty$ | 50 |
| 195 | 1.55 | 4.5°K $H=9$ kOe | 51 |
| 177 | 1.79 | $T \rightarrow 0^{\circ}\text{K}$ $H=0$ | 52 |
| 180 | 1.59 | | 47 |
| | 1.86 | $T \rightarrow 0^{\circ}\text{K}$ $H \parallel \langle 100 \rangle = 18$ kOe | 53 |
| | 1.44 | $T \rightarrow 0^{\circ}\text{K}$ $H \parallel \langle 111 \rangle = 18$ kOe | |

Most of the experiments were performed on polycrystalline powders and yield magnetic moments rather lower than the spin only value of $2 \mu_{\text{B}}$ /molecule. One experiment, {53} was made on single crystals and it was found that a moment of $1.86 \mu_{\text{B}}$ is obtained parallel to the $\langle 100 \rangle$ direction but only $1.44 \mu_{\text{B}}$ /molecule is achieved parallel to the $\langle 111 \rangle$ direction.

The Mössbauer spectra of FeCr_2S_4 have been

reported by a few workers {27,28,53,54,55,56,57}. At room temperature, the spectrum is a singlet with a shift of 0.75 mm/s. This spectrum remains a singlet until $\sim 170^\circ$ K when a magnetically split hyperfine pattern appears and, rather interestingly, a quadrupole shift. The hyperfine field increases steadily as the temperature decreases, until 70° K when the field starts to decrease. In this respect the temperature dependence of the hyperfine field resembles that of the magnetization of polycrystalline samples.

The appearance of a quadrupole shift in the Mössbauer spectrum of FeCr_2S_4 has prompted three explanations. The first {56} was given in terms of a magnetically induced electric field gradient (E.F.G.) and the calculation of the expectations of this model is given in appendix C. The second explanation was given in terms of magnetostriction effects, {28,57} although no detailed calculations have as yet appeared. The third {54,55} was given in terms of a Jahn-Teller (J-T) stabilization of the $^5\text{E}(\text{Fe}^{2+})$ ground state.

The electrical transport properties of FeCr_2S_4 have also been studied {44,45,58,59,60}. The compound shows p-type conductivity and is a semiconductor. Magneto-resistance measurement indicate that the resistivity falls on the application of a magnetic field with a maximum effect close to the

magnetic ordering temperature. There is an anomaly in the thermopower just below T_{FN} that has been attributed to magnon-drag {58}. In the plot of $\log \rho - T^{-1}$ three distinct activated conduction regions appear and there is a region just below T_{FN} where conduction is non-activated.

2.2 Theoretical Considerations.

From Chapter I, section 4, it is clear that a Fe^{2+} ion in a tetrahedral site has a ground state 5E that is doubly degenerate. Jahn and Teller {61} have shown that degenerate ground states may be stabilized by a spontaneous distortion of the site to some lower symmetry that removes the degeneracy. The physical reason being that the distortion can be regarded as a small perturbation of the crystal field and treated in first order perturbation theory. In this theory energy is conserved so that the distorted state has a lower energy than the high symmetry state. Moreover, the elastic energy of the lattice increases as the square of the distortion so that there is a well defined minimum energy for the complex {62} at any given temperature.

The magnitude of the J-T stabilization depends on the strength of the coupling between the electronic states and the lattice vibrational modes

that govern the positions of the anions in the complex. At high enough temperatures thermal energy becomes comparable with the stabilization energy and allows a complex to re-orientate the distortion, in a stochastic fashion, along any one of three equivalent crystal axes. This is referred to as dynamic J-T stabilization and was first recognized by the authors of {63}. The situation described earlier is the limiting case of the dynamic stabilization and is commonly referred to as the static limit. The approach to the static limit from the dynamic regime is of interest and is the kernel of the important work by Ham {64}. What emerges from this work is that, provided the electronic and the vibrational co-ordinates are simultaneously transformed, then, the Hamiltonian describing the complex has the full symmetry of the undistorted configuration and the degeneracy of the complete electronic-vibrational ("vibronic") problem is not lifted. What the coupling does is to associate the electronic and vibrational parts of the wavefunction in different ways for the various vibronic eigenstates.

To deal with the problem, the concept of "reduction factors" is introduced. These measure the overlap between the wavefunctions describing the equivalent distorted configurations. Then, in a

formal fashion, the static limit is reached when the overlap integrals vanish. In case this sounds like a tautology, we should remark that the overlap integrals diminish as the J-T coupling increases.

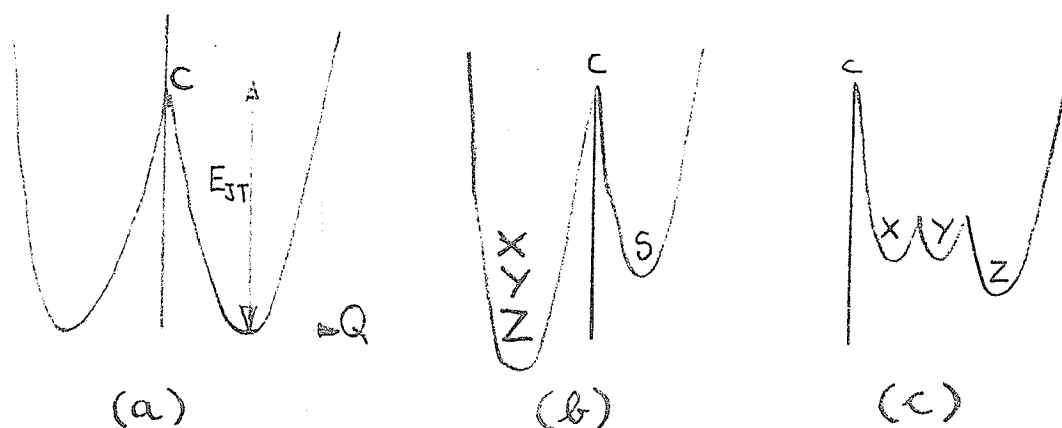


Figure 41. To illustrate the potential well for the vibronic problem (a) weak coupling (b) intermediate to strong coupling (c) static limit.

The problem is quite difficult to visualize although some insight can be obtained by thinking in terms of a potential well that gradually changes shape as the coupling increases. In figure 41a, the high temperature, weak to zero coupling limit, is illustrated. The potential well has rotational symmetry about C the undistorted configuration. The J-T stabilization is indicated E_{JT} , and the complex vibrates freely but always avoiding C. As the coupling

increases, figure 41b, the three distortions become well defined and separated by saddle points S. The rotation is hindered and may be thermally activated or occur by coherent tunnelling. Finally in figure 41c, some perturbation has set the distortion Z at much lower energy than either of the other configurations and there is no overlap between the eigenfunctions describing X, Y, Z.

In fact, it is not possible to see why the situation in c should occur at all without introducing some influence external to the complex. Therefore, static limits occur only because of anisotropy in elastic strains in the crystal or by the application of some external, magnetic field or stress.

To be more specific, we now consider the case of the ${}^5E(\text{Fe}^{2+})$ ground state for ferrous iron in a tetrahedral site. This ground state is doubly degenerate, the orbitals describing it are ϕ_1 , and ϕ_2 of chapter I, section 4 and for each of these orbitals $m_1=0$ so there is no spin orbit coupling. Group theoretical considerations dictate that the electronic states will only couple to vibrational modes that are also doubly degenerate. Two modes do exist for the tetrahedral site that subtend the doubly degenerate representation E; these are referred

to as Q_2 and Q_3 and in figure 42, we have attempted to illustrate the motions of the anions associated with them.

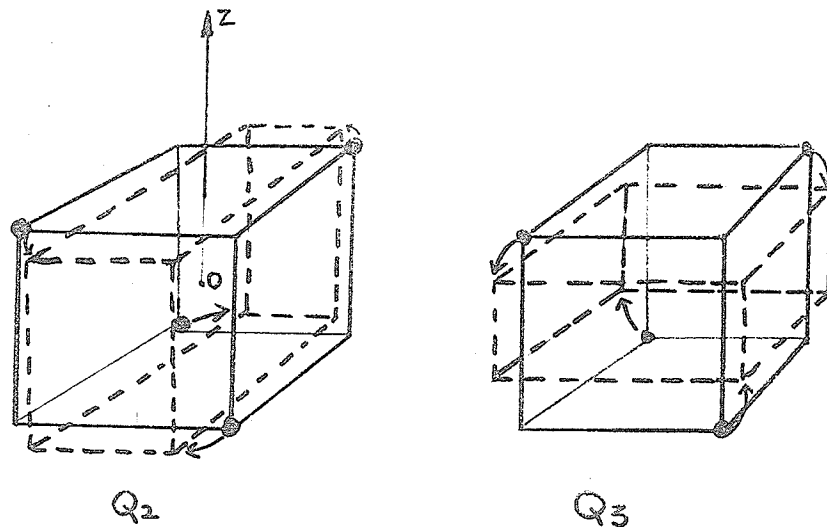


Figure 42. To illustrate the nature of the two degenerate modes associated with a tetrahedral site.

Q_2 represents a twisting of the complex about Oz say, while Q_3 represents a flexing. The cation-anion distances remain fixed but the anion-cation-anion bond angles change. If in a solid, the net elastic anisotropy that dominates the J-T stabilization of the complex favours Q_3 , then the static distortion is to tetragonal with c/a either greater or less than one. If the elastic anisotropy favours Q_2 , then the distortion is to orthorhombic {65}.

There is, of course, a vast literature on the subject of the J-T effect most of which is

reviewed in a recent book {66}.

The few notes presented here represent only the most rudimentary ideas given in the hope that later discussion will be at least a little clearer.

As it is, we have rather begged the question of why we favour a J-T stabilization rather than one of the other explanations for the non-zero E.F.G. in FeCr_2S_4 . Basically, when considering the possible causes of a crystallographic distortion or some other manifestation of deviation from cubic symmetry, it is necessary to consider the relative magnitudes of two terms in the Hamiltonian describing the d-electrons. These are the non-cubic part of the crystal or ligand field V_{c} and the term that results from spin orbit coupling V_{LS} . The J-T effect puts a non-degenerate orbital lowest in energy and thereby quenches L_z , on the other hand, if the stabilization that results from a spin orbit coupling is greater than that from the J-T stabilization, the V_{LS} term quenches the J-T effect. Thus, J-T effects may be anticipated if the cubic ligand field itself quenches the orbital angular momentum. This situation exists for ${}^5\text{E}(\text{Fe}^{2+})$ in a tetrahedral site.

It is necessary however, to be circumspect

for the experimental evidence does not altogether support this view. For example, in ZnS:Fe^{2+} , the optical spectra appear to be consistent with the view that a straightforward crystal field approach is all that is required to explain the observed effects {67}. Spin orbit coupling, that in second order, couples ${}^5\text{E}$ and ${}^5\text{T}_2$, splits the ${}^5\text{E}$ ground state into five spin-orbit levels and accounts for all the observed optical transitions. On the other hand, in CdTe:Fe^{2+} , there is good evidence {68} that the J-T dynamic coupling introduces extra optical transitions. Neither is the situation completely clear when the spinel structure is considered. In FeCr_2O_4 , the transition at 135°K {69} appears to be induced by a J-T stabilization of the ${}^5\text{E}(\text{Fe}^{2+})$ state, however, in FeAl_2O_4 no crystallographic transitions occur down to 80°K {65}. We shall return to these points later and discuss a possible underlying correlation.

2.3 Preparation of Samples.

Our samples were prepared in the manner described in Chapter I, section 5. Debye-Sherrer x-ray powder diffraction patterns were obtained and showed that the compound was a spinel. In table 13, we show the reflections obtained and the indices

Table 13. X-ray* powder diffraction data for FeCr_2S_4 .

| h k l (Spinel) | d_{cal} | d_{obs} | I_{R}^{**} |
|-------------------|------------------|------------------|---------------------|
| 111 | 5.771 | 5.779 | 1 |
| 220 | 3.535 | 3.535 | 2 |
| 311 | 3.014 | 2.998 | 6 |
| 222 | 2.886 | 2.888 | 1 |
| 400 | 2.499 | 2.489 | 4 |
| 331 | - | - | N.O.*** |
| 422 | 2.040 | 2.001 | 2 |
| 333,511 | 1.924 | 1.914 | 4 |
| 440 | 1.767 | 1.764 | 10 |
| 531 | 1.690 | 1.689 | 1 |
| 442 | - | - | N.O. |
| 620 | 1.580 | 1.580 | 1 |
| 533 | 1.524 | 1.523 | 1 |
| 622 | 1.507 | 1.507 | 1 |
| 444 | 1.443 | 1.441 | 3 |
| 711,551 | 1.400 | 1.401 | 1 |
| 642 | 1.336 | 1.334 | 2 |
| 731,553 | 1.301 | 1.300 | 3 |
| 800 | 1.249 | 1.249 | 3 |
| 733 | - | - | N.O. |
| 644 | - | - | N.O. |
| 822,660 | 1.178 | 1.179 | 1 |
| 751,555 | 1.154 | 1.156 | 2 |
| 662 | - | - | N.O. |
| 840 | 1.117 | 1.118 | 3 |
| 753,911 | - | - | N.O. |
| 842 | - | - | N.O. |
| 664 | - | - | N.O. |
| 931 | 1.0481 | 1.049 | 5 |
| 844 | 1.0202 | 1.0207 | 8 |
| 862 | 0.9800 | 0.9806 | 3 |

* Radiation was $\text{FeK}\alpha/\text{Mn}$, $T=298^\circ\text{K}$.** I_{R} estimated visually from powder photograph.

***N.O.=Not observed.

assigned. We used Mn filtered FeK α radiation at room temperature. The lattice parameter, obtained from the high angle reflections, was 9.996 Å.

2.4 Magnetization Measurements.

We used the equipment and techniques described in Chapter II, section 1 to measure M_S , H_C , and χ_M . In figure 43, the temperature dependence of H_C is displayed. The quantity H_C falls rapidly as T is increased from 4.2° K and appears to level off by about 77° K. We show M_S and χ_M^{-1} as functions of T in figure 44. The main results of these experiments are summarised in table 14. We find $M_S=1.35 \mu_B/\text{molecule}$ at $T=4.2^\circ\text{K}$ while $M_S(4.2)=1.55 \mu_B/\text{molecule}$. The Curie constant, estimated from the linear portion of the χ_M^{-1} - T curve is 7.0 while $\theta=-330\pm 10^\circ\text{K}$. From the steeply falling part of the M_S - T curve, we estimate a long range ordering temperature of $170\pm 4^\circ\text{K}$.

These results are in fair agreement with other published work for the compound; they should be viewed in relation to the expected cation distribution and the expected spin arrangement. We expect the B-sites to be occupied by Cr³⁺ ions and the A-sites by Fe²⁺ ions with their spins aligned in a simple Néel ferrimagnetic fashion. The expected spin only

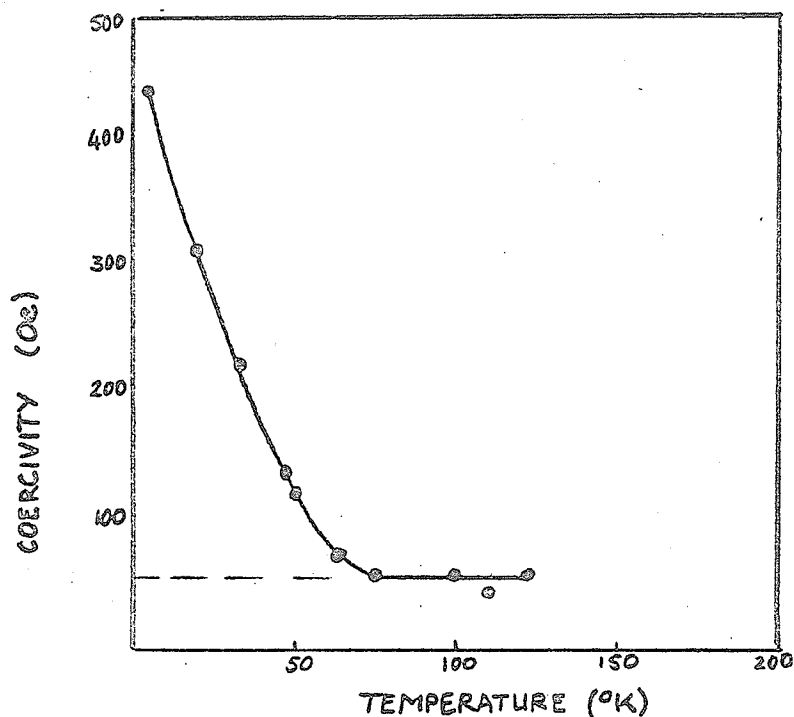


Figure 43. Temperature dependence of H_c .

Table 14. Magnetic crystallographic and electrical resistivity data for FeCr_2S_4

| | |
|-------------------------------------|--------------------------------|
| Lattice Parameter | 9.996 \AA |
| M_S (4.2°K) | $1.35 \mu_B/\text{molecule}$ |
| M_∞ (4.2°K) | $1.55 \mu_B/\text{molecule}$ |
| Weiss Parameter | $-330 \pm 10^\circ \text{K}$ |
| Ordering Temperature | $170 \pm 4^\circ \text{K}$ |
| C_M | 7.0 |
| ρ (296°K) | $10.03 \Omega \cdot \text{cm}$ |
| ρ (77°K) | $119.0 \Omega \cdot \text{cm}$ |

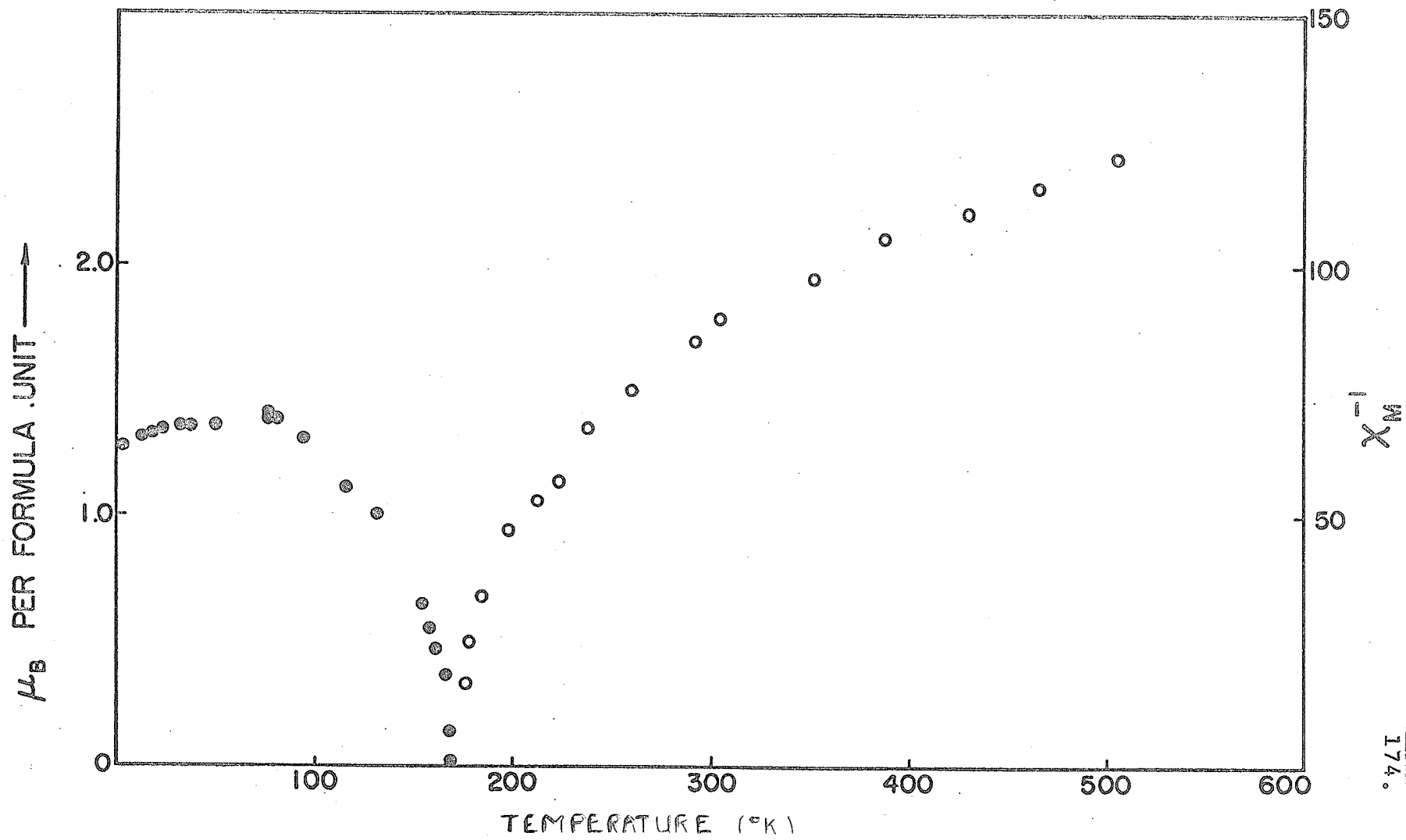


Figure 44. Temperature dependence of magnetic moment and inverse molar susceptibility for FeCr₂S₄.

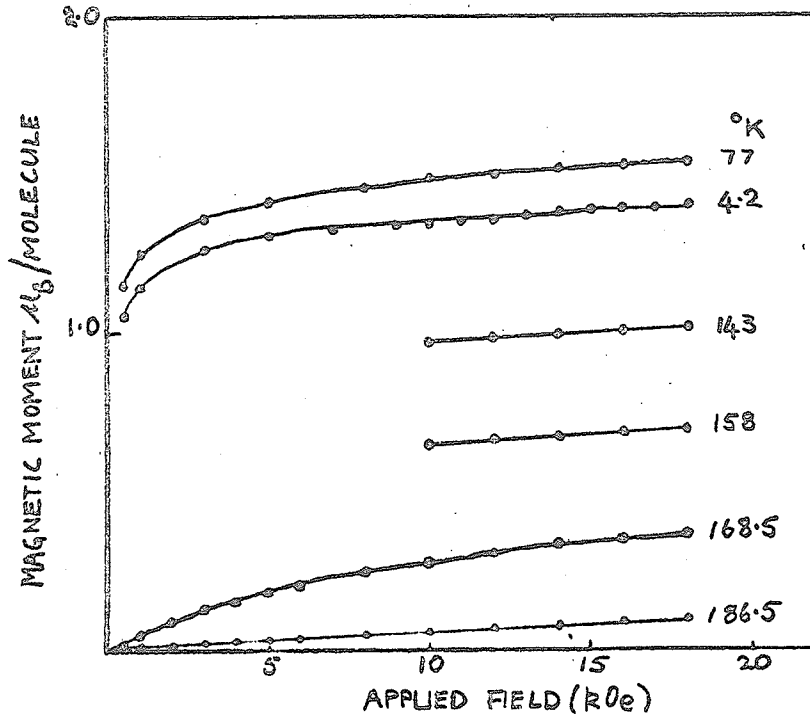


Figure 45. Magnetic moment at various temperatures as a function of applied field.

molar Curie constant is in that case, 6.75, and the low temperature magnetic moment for the spin only situation is $2\mu_B$ /molecule.

In figure 45, we show some of the magnetization data in the form of magnetic moment versus applied field. It may be seen that the slope on the curve obtained at 4.2°K is rather large, in fact, in the range from 10 to 18 kOe, it is ~ 10 times the value predicted by M.F.T.

2.5 Electrical Measurements.

We made measurements of the resistivity and magneto-resistance as a function of temperature in the range 30 - 296°K using the methods of sample preparation and techniques discussed in Chapter II,

section 2. In figure 45, we show the temperature variation of the resistivity. It may be seen that $\log \rho$ is a fairly linear function of T^{-1} in the range $300 - 170^\circ \text{K}$ at which point ρ decreases until $T \approx 140^\circ \text{K}$. There is then a second, non-linear, increase until $T \approx 60^\circ \text{K}$. At this temperature $\log \rho$ versus T^{-1} again becomes a linearly increasing function. The solid lines are drawn in accordance with equation (II.20) and yield the high and low temperature slopes 0.0496 eV and 0.0146 eV from which we may conclude that the energy gap between the highest occupied state and the conduction band is 0.1 eV $T > 170^\circ \text{K}$ and 0.03 eV $T \leq 60^\circ \text{K}$. Although no great significance can

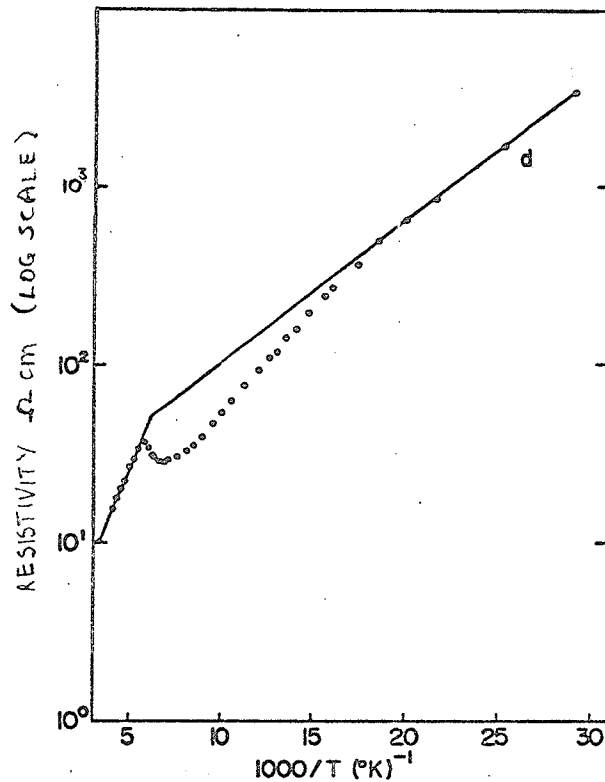


Figure 46. Temperature dependence of the resistivity.

be attached to the value of ρ ($T=296^\circ\text{K}$), $\sim 10\Omega\cdot\text{cm}$ because of the nature of the samples, we remark that our value is in reasonable agreement with other published values and that the behaviour of $\log\rho - T^{-1}$ is similar to that observed by other workers. It is important to note that the behaviour is essentially semi-conducting over most of the temperature range. The curious anomaly at $T\sim 170^\circ\text{K}$ requires some explanation and coupled with the comparatively low value of ρ it seems to indicate that at around 170°K the electrons become at least partially delocalized. The subsequent recovery, however, indicates that this is only a temporary event and that behaviour consistent with localized electrons may be expected at high and low temperature limits.

The magneto-resistance measurements show that the resistivity decreases on applying a field when $T\sim T_{\text{FN}}$. In the temperature ranges just above and just below T_{FN} , there is an increase in resistance as a result of the applied field. In figure 47, the variation of resistance with applied field is shown for a few temperatures and in figure 48, we show the function $\Delta R/R$ in a field of 10 kOe as a function of temperature.

2.6 Mössbauer Effect Studies.

We collected Mössbauer spectra in the

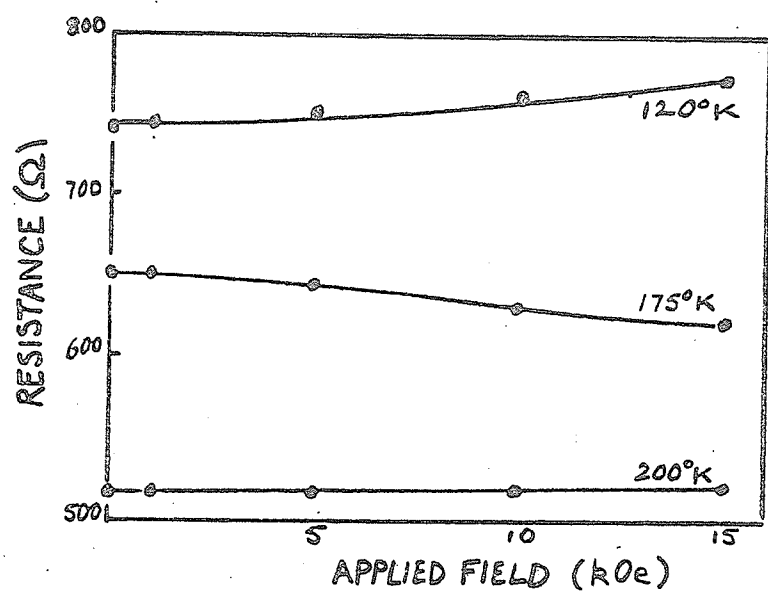


Figure 47. Variation of resistance with applied field at various temperatures.

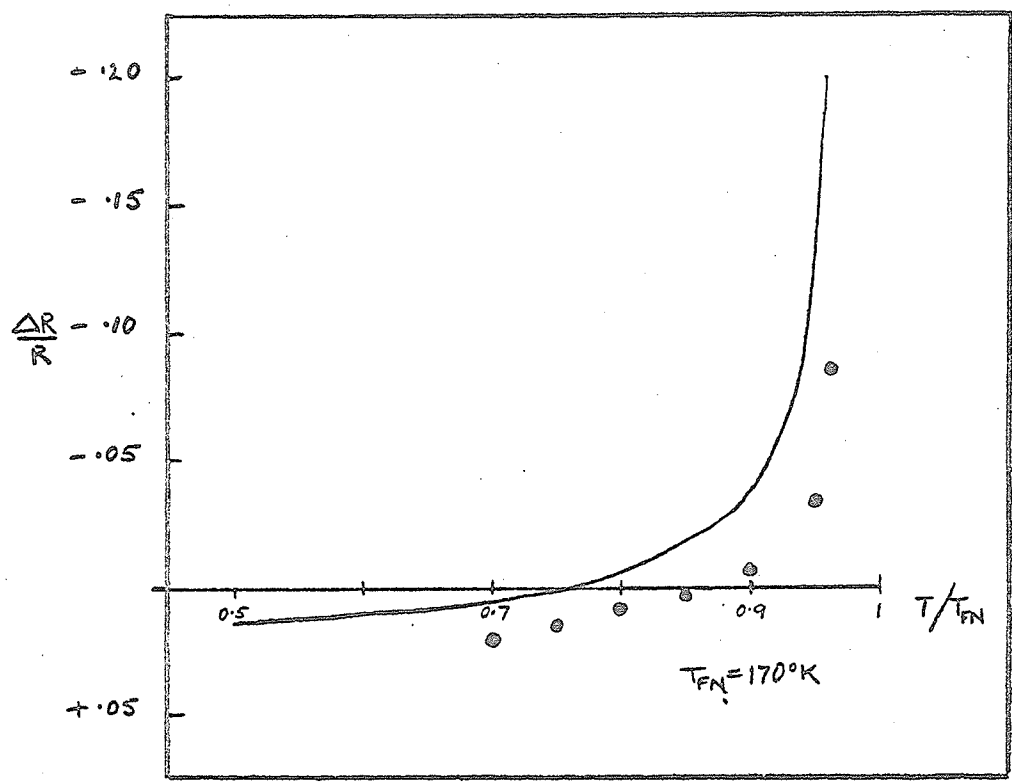


Figure 48. Magneto-resistance in 10 kOe field as a function of temperature. The solid line was calculated from the theory in reference {76}.

temperature range 2 - 500° K, using the equipment described in Chapter II, section 3. In figures 49, 50, 51, we show some of the spectra typical of temperatures below $\sim 170^\circ$ K, (at higher temperatures the spectra are simple singlets). In accordance with the findings of other workers, we find a magnetically split spectrum with a non-zero quadrupole interaction. We also notice a curious line width effect. Consider for example figure 49b, this appears to be a simple six line absorption spectrum, it was actually collected through the bore of our superconducting solenoid so there are no collimation effects and yet, although line 2 and line 5 are almost equidistant from the zero of velocity, line 5 is almost twice the width of line 2. Even more strikingly different are the widths of lines 1 and 6. In spite of the fact that line 1 is somewhat nearer to the zero of velocity than line 6, it is more than twice the width. This is a feature that we also noticed in the published spectra in {28}. There, no attempt was made to explain the feature and indeed the spectra were fitted with line widths constrained equal. Only near to the ordering temperature do we find that the line widths in the spectra are equal.

Another observation is illustrated by comparing figure 51a and figure 50a. Both spectra

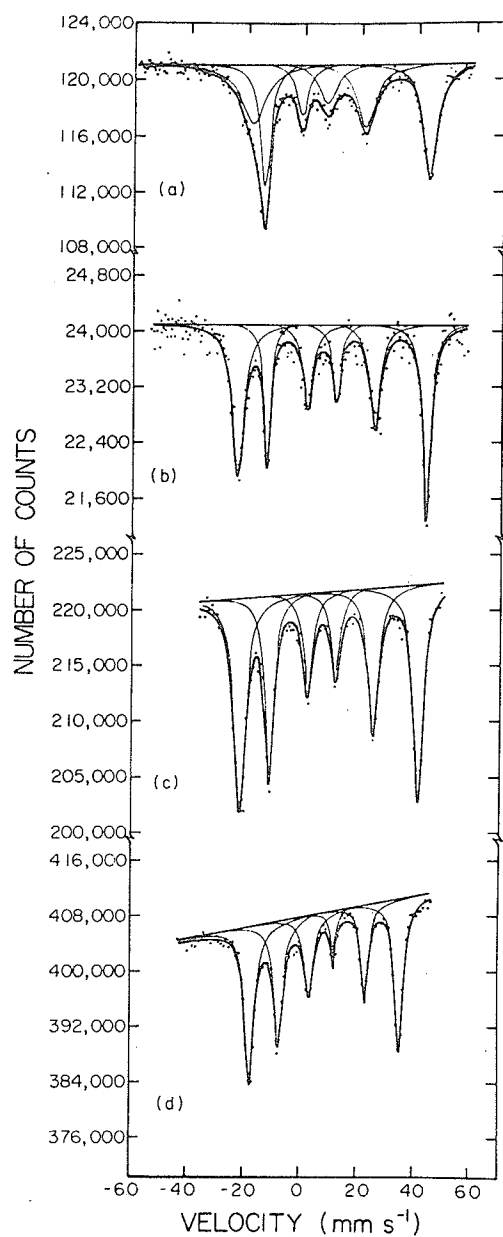


Figure 49. Typical spectra at various temperatures:
(a) 7°K (b) 81°K (c) 104°K (d) 137°K.

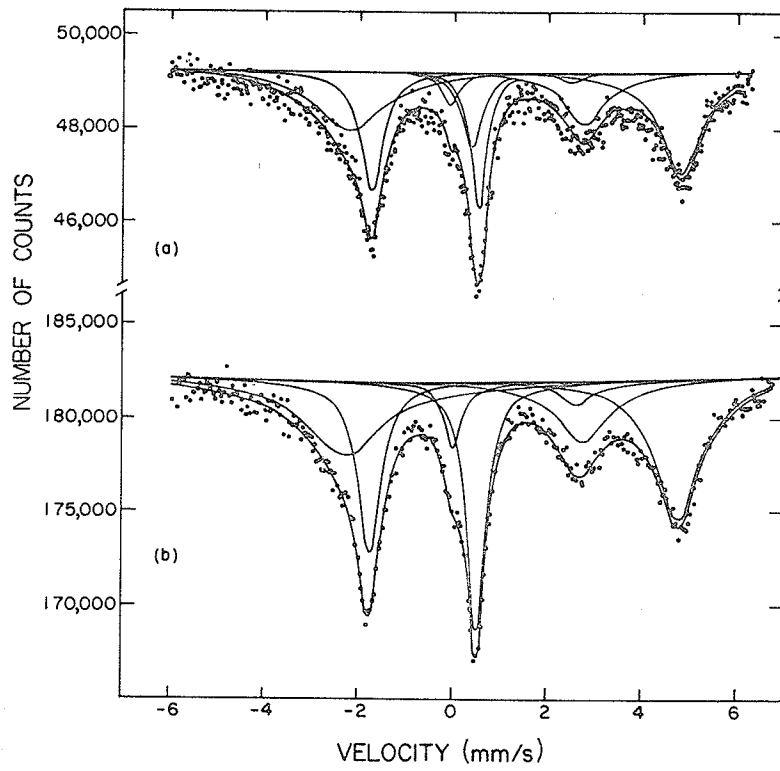


Figure 50. Mössbauer spectra of FeCr_2S_4 collected:
(a) 2°K (b) 4.2°K using rigid absorbers.

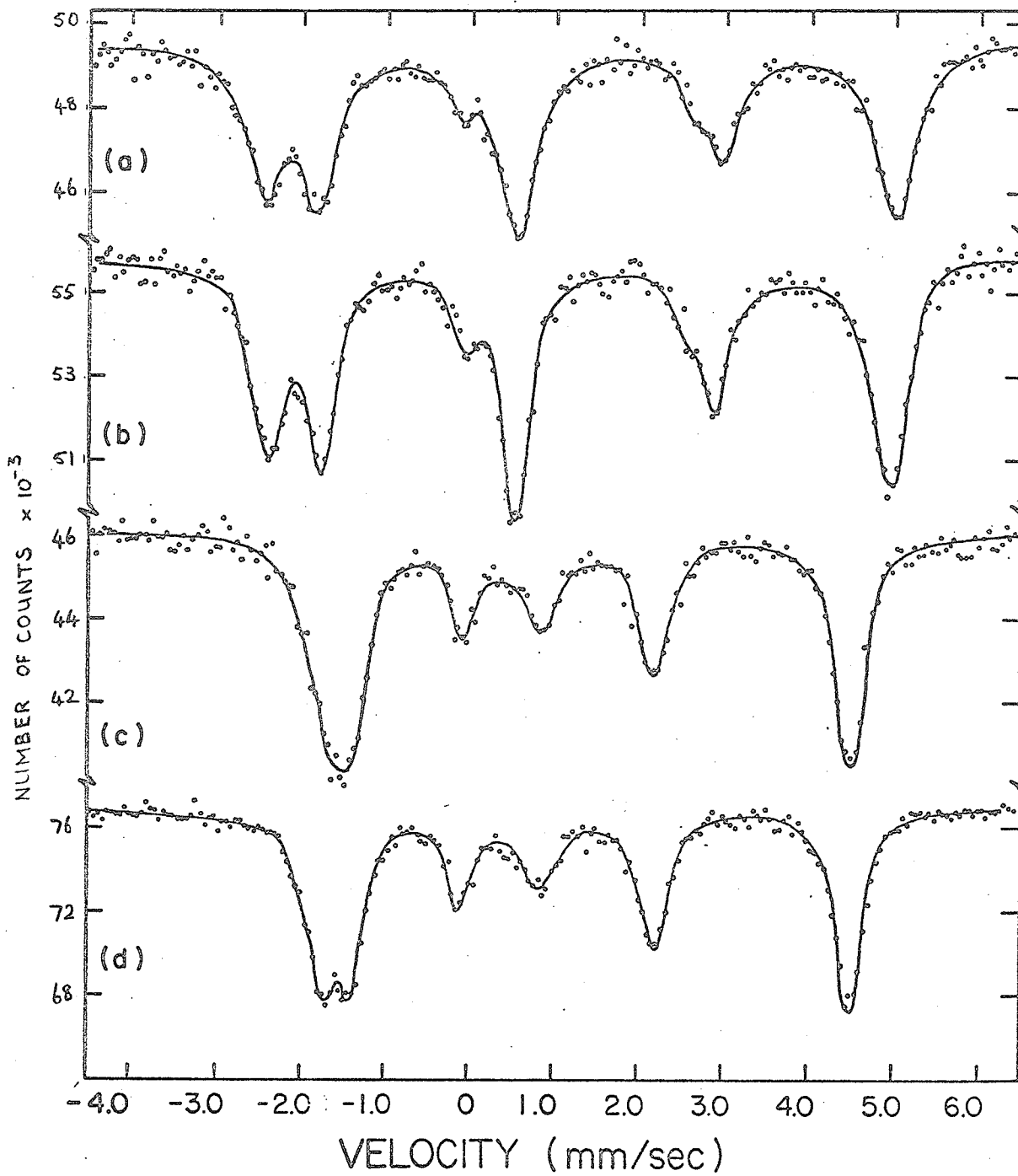


Figure 51. Mössbauer spectra from powdered absorbers at (a) 2°K (b) 6.7°K (c) 13.8°K (d) 19°K.

were collected through the custom built cryostat at 2° K. There are clearly some qualitative differences between the two spectra and experimentally, the difference is that for figure 50a, the absorber was in the form of a rigid disc of thermo-setting plastic whereas, for figure 51a, the absorber was a loose powder clamped between Be discs. The conclusion is that the plastic matrix exerts a strain on the crystallites and causes the loss in resolution, especially in lines 1 and 2. There are also some quantitative differences between the spectra of figure 50 and those found when the sample was a loose powder. This may arise either because of the loss in resolution or because of some more fundamental effect of the strain on the behaviour of the Fe^{2+} ground state {70}.

The data that may be extracted from the spectra are shown in various ways. In figure 53, we show the temperature variation of the hyperfine field $T > 20^\circ \text{K}$ and compare our results with those of other workers. In figure 52, the temperature dependence of the quadrupole shift $T > 20^\circ \text{K}$ is shown. The definition of \mathcal{E} is:

$$\mathcal{E} = 2 \left[\frac{1}{2} (E_1 + E_6) - \frac{1}{4} (E_1 + E_2 + E_5 + E_6) \right]$$

where the E_i , $i=1,6$, are the positions of observed absorption lines. The quantity \mathcal{E} is related to the quadrupole interaction $\frac{1}{2} e^2 q Q$ but the exact nature of

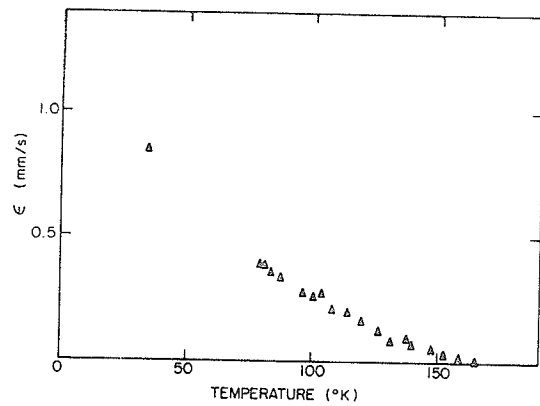


Figure 52. The temperature dependence of $\xi = 2 \left[\frac{1}{2}(E_1 + E_6) - \frac{1}{4}(E_1 + E_2 + E_5 + E_6) \right]$.

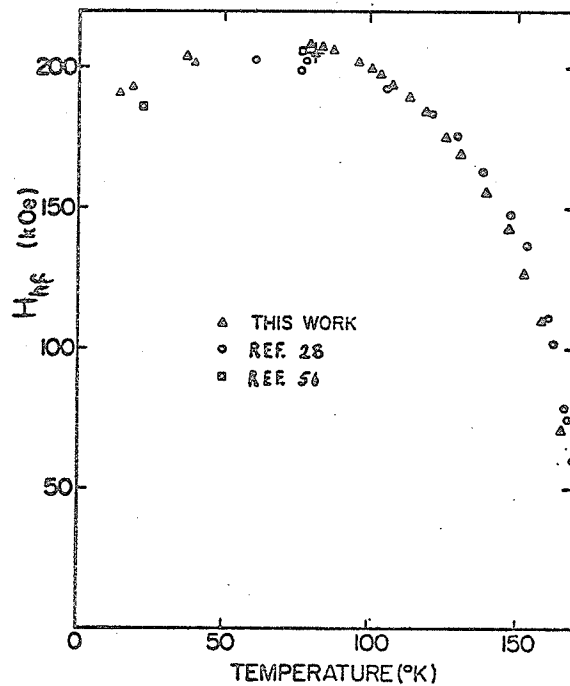


Figure 53. The temperature dependence of the hyperfine field, \triangle This work powdered absorbers, + rigid absorber.

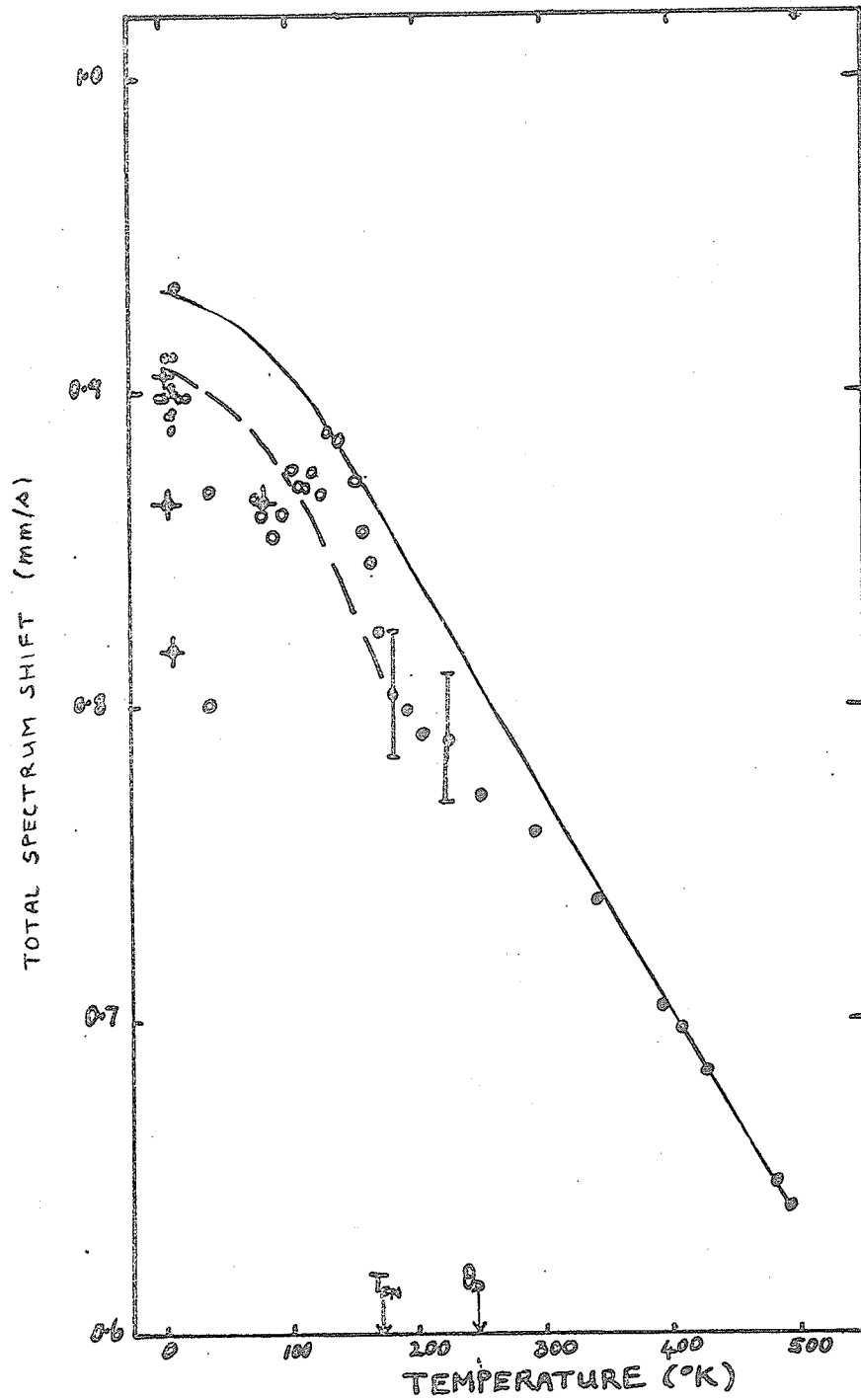


Figure 54. The total spectrum shift in FeCr₂S₄ as a function of temperature: paramagnetic spectra ●, ordered spectra ○, +rigid absorbers.

relationship depends on how the spectra are fitted and the values found for θ , η and ϕ . The quantity ϵ is to be regarded as raw data. In figure 54, the temperature dependence of the total spectrum shift is indicated. Open circles with crosses indicate data obtained from rigid absorbers, open circles otherwise indicate data obtained from magnetically split spectra while closed circles show data obtained from paramagnetic spectra.

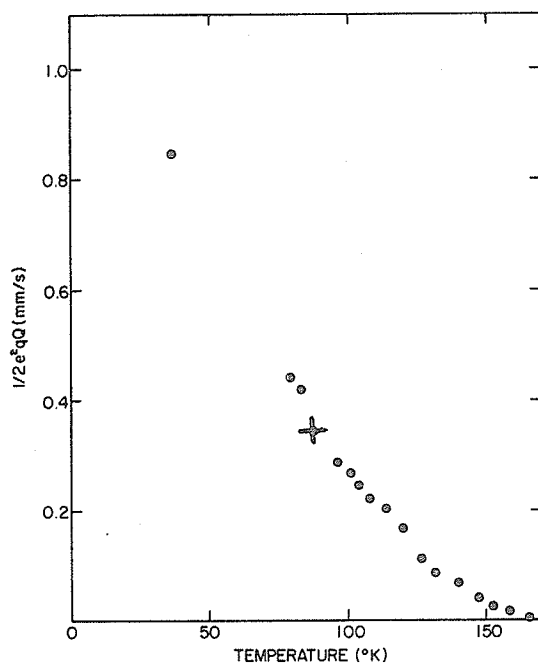


Figure 55. The temperature dependence of the quantity $\frac{1}{2}e^2qQ$, $T \geq 20^\circ \text{K}$: \odot powder absorbers, $+$ rigid absorbers.

Figure 55, shows the temperature dependence of the quantity $\frac{1}{2}e^2qQ(T > 20^\circ \text{K})$ found after fitting the spectra according to the discussion in Chapter II, section 3.6 and appendix D. We found for the spectra above 20°K that θ was $11 \pm 1^\circ$, that η was zero and ϕ was zero.

The detailed variation of all the hyperfine parameters at the lowest temperatures $2 < T < 20^\circ \text{K}$ is shown in figure 56. Crosses show data obtained from rigid absorbers, otherwise these data were obtained with powders clamped between Be discs. For the powder absorbers, the hyperfine field, 55a, has a cusp like minimum at $\approx 9^\circ \text{K}$ when the spectra are collected with T decreasing. When the spectra are collected with T increasing, the minimum seems to be displaced to slightly higher temperatures $\approx 10^\circ \text{K}$. The quantity $\frac{1}{2}e^2qQ$, figure 56b, has a most striking temperature dependence on account of the sign change at $\approx 10^\circ \text{K}$. The various parameters are listed in table 15. So far as we can tell, η remains zero until $T=9^\circ \text{K}$ and then begins to increase to a flat maximum of 0.24 ± 0.03 by about 5°K . It is clear that something different dominates the behaviour of the absorbers in the rigid matrix compared with those used as loose powders.

We must be careful in dealing with the data that was collected with applied external fields. For these experiments, it is absolutely necessary to

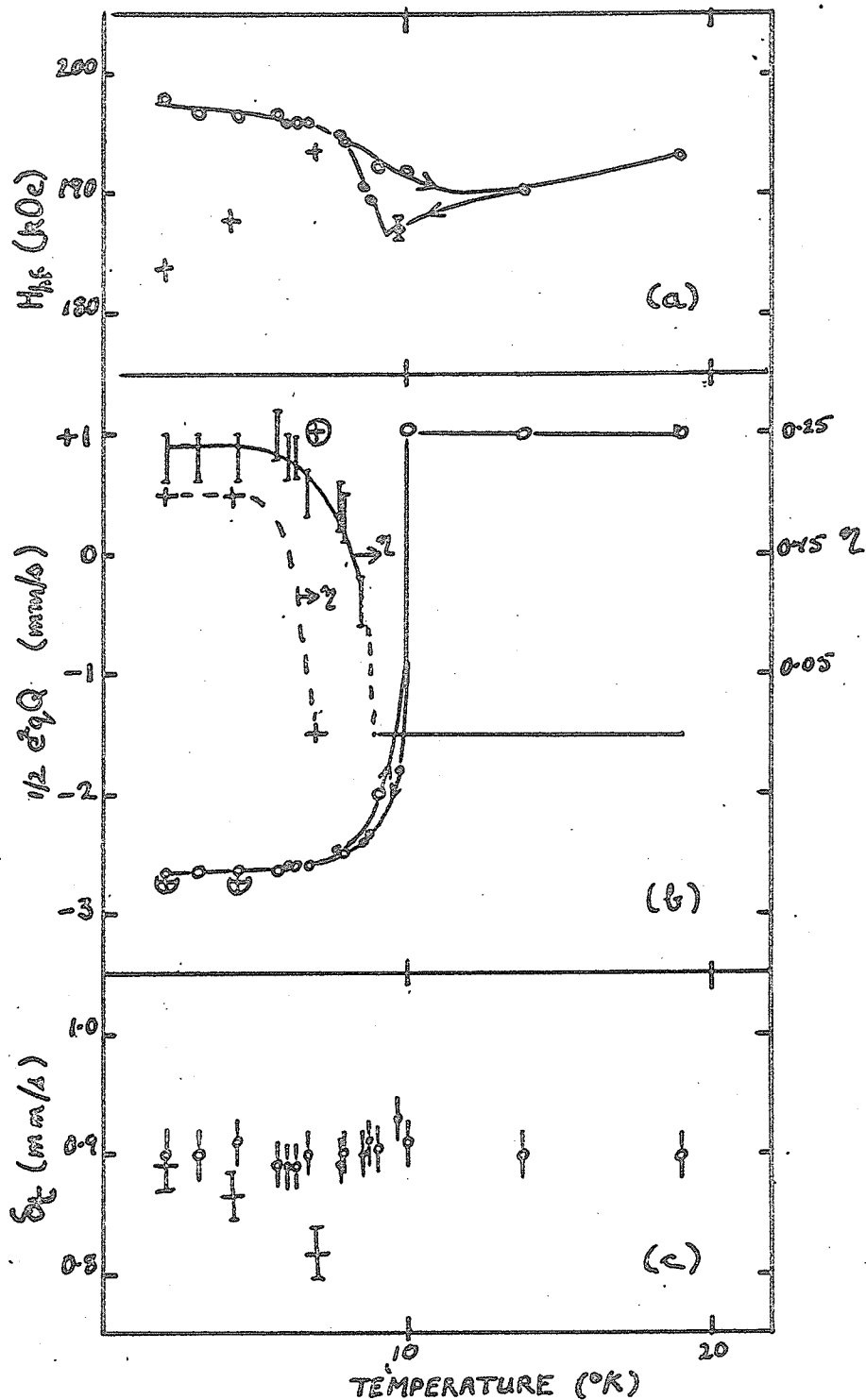


Figure 56. The temperature dependence of (a) the hyperfine field (b) the quantity $\frac{1}{2}e^2qQ$ (c) the total spectrum shift o temperature increasing, \ominus temperature decreasing, + rigid absorbers.

Table 15. Hyperfine Parameters for FeCr_2S_4 Mössbauer Spectra, Powder Absorbers.

| T (°K) | H_{hf} (kOe) | $\frac{1}{2}e^2qQ$ (mm/s) | δ_t (mm/s) | θ (deg) | ϕ (deg) | η |
|-----------|--------------------------|--|----------------------|-------------------|-----------------|--------|
| 2.0 | 197.8 | -2.67 | 0.898 | 90 | 0 | 0.23 |
| 3.1 | 196.6 | -2.66 | 0.898 | 90 | 0 | 0.23 |
| 4.4 | 196.6 | -2.65 | 0.911 | 90 | 0 | 0.23 |
| 5.7 | 196.6 | -2.66 | 0.892 | 90 | 0 | 0.25 |
| 6.0 | 195.9 | -2.61 | 0.892 | 90 | 0 | 0.23 |
| 6.3 | 195.9 | -2.61 | 0.888 | 90 | 0 | 0.23 |
| 6.7 | 195.9 | -2160 | 0.901 | 90 | 0 | 0.20 |
| 7.8 | 194.4 | -2.49 | 0.893 | 90 | 0 | 0.19 |
| 7.9 | 194.4 | -2.40 | 0.900 | 90 | 0 | 0.18 |
| 8.5 | 190.6 | -2.23 | 0.902 | 90 | 0 | 0.11 |
| 8.7 | 193 | FITTING WAS UNRELIABLE IN THIS REGION, | | | | |
| 9.0 | 192 | PERHAPS BECAUSE TEMPERATURE FLUCTUATIONS | | | | |
| 9.3 | 196 | BECOME VERY IMPORTANT HERE. | | | | |
| 9.7 | 186.9 | -1.81 | 0.933 | 90 | 0 | 0 |
| 10.0 | 191.9 | +1.04 | 0.911 | 5 | 0 | 0 |
| 13.8 | 190.3 | +1.00 | 0.898 | 4 | 0 | 0 |
| 19.0 | 193.1 | +1.02 | 0.898 | 6 | 0 | 0 |
| 39.5 | 200.6 | 0.87 | 0.868 | 12 | 0 | 0 |
| 77 | 206.6 | 0.50 | 0.871 | 11 | 0 | 0 |

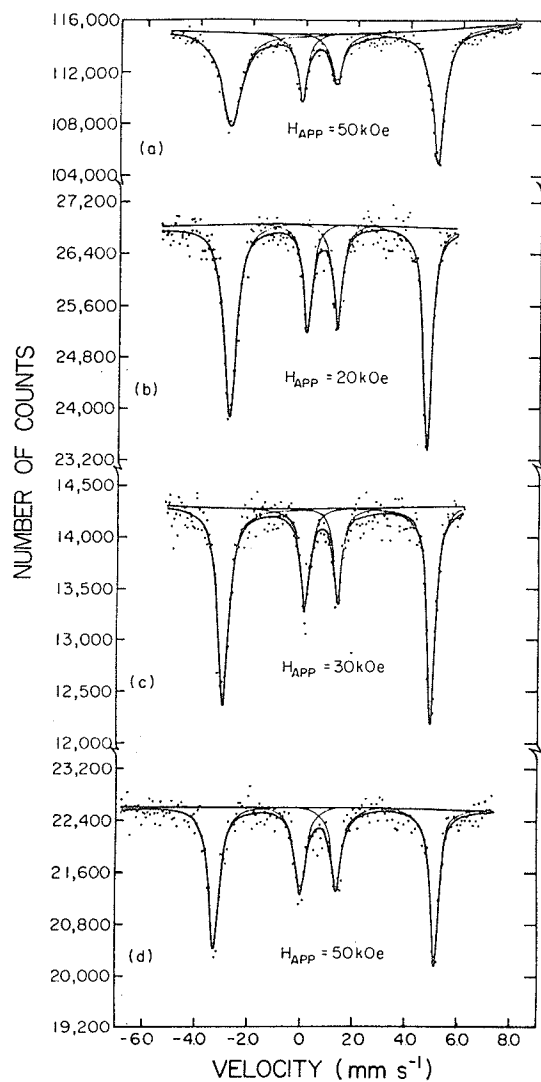


Figure 57. Spectra obtained in applied fields: (a) 7°K, (b), (c), (d) 81°K. The field was applied parallel to the γ -ray velocity.

mix the powder with something that will give a rigid matrix. If this is not done, then the particles simply align their easy axes with the field. One of the objects of the applied field experiments was to determine whether the E.F.G. occurred because of a static crystal distortion. This can only be done if the particles are immobilized for then any quadrupole shift is absent from the spectrum because of the random arrangement of the crystallites. The spectra that we obtained are shown in figure 57 and the data extracted are shown in figures 58 and 59. First we

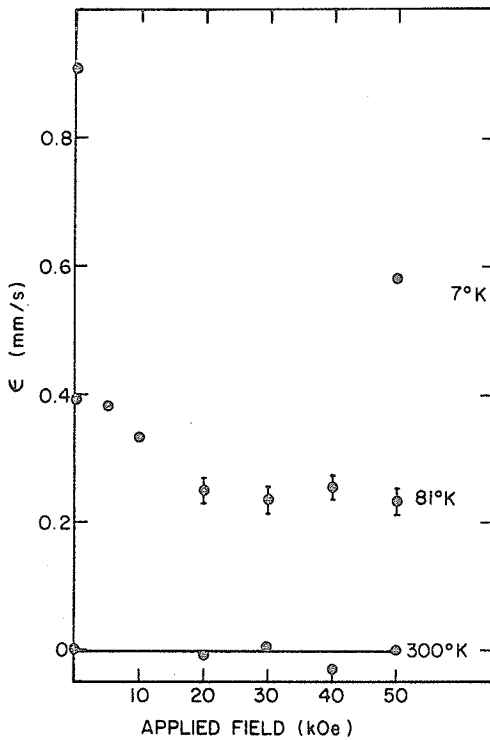


Figure 58. The variation of ϵ with applied field at various temperatures:

$$\epsilon = 2 \left[\frac{1}{2}(E_1 + E_6) - \frac{1}{4}(E_1 + E_3 + E_4 + E_6) \right]$$

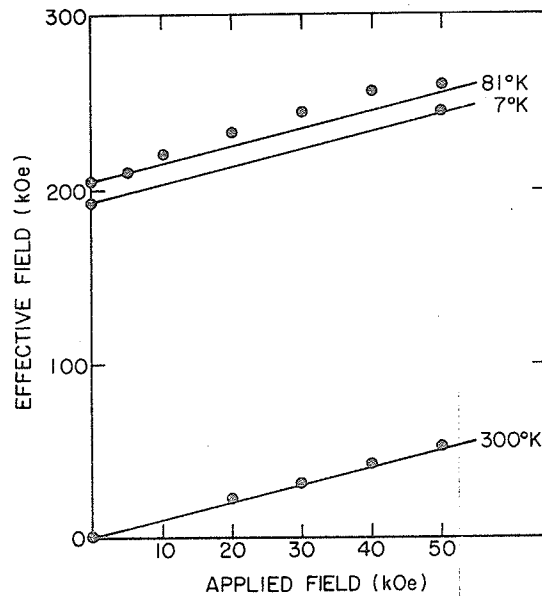


Figure 59. The variation of effective field with applied field at various temperatures.

note that the data obtained in zero field at 81°K with the rigid absorber are in decent agreement with data obtained at similar temperatures with ordinary absorbers. As we have already noted, the data at 7°K is not in reasonable agreement. It appears that we can only make use of the 81°K data. It is clear from the spectra of figure 57b,c,d, that the quantity ξ where:

$$\xi = 2 \left[\frac{1}{2}(E_1 + E_6) - \frac{1}{4}(E_1 + E_3 + E_4 + E_6) \right]$$

is not zero in an applied external field. The field dependence of ξ , figure 58 indicates that the quantity decreases from its zero field value and becomes essentially constant when $H_{\text{app}} > 20 \text{ kOe}$. It is also clear that the magnetization is saturated for $H > 20 \text{ kOe}$ because then the $\Delta m_I = 0$ lines are absent. The effective field shown in figure 59 increases with H_{app} almost linearly at 81°K and exactly linearly at 300°K and 7°K . This result for 81°K and 7°K does not contradict the postulated Néel ferrimagnetic spin arrangement and the absence of the $\Delta m_I = 0$ lines shows that there is no canting of the A-site spins.

2.7 Discussion.

So much is known about this compound that in our discussion it is important to pay attention to details rather than offer something that merely covers

the broad features. With this in mind, we shall discuss and set down those items that must be explained by or incorporated into any energy band diagram for FeCr_2S_4 .

At high temperatures, both the magnetic and the electrical properties support the idea of localized electron behaviour. The conduction is of the activated type but the energy gap is fairly small, we find 0.1 eV. In {58}, the Hall mobility is reported as $10 \text{ cm}^2/\text{V}\cdot\text{sec}$ which is consistent with narrow band carriers {32} so the low resistivity (compared with other ferrimagnetic semiconductors {45}) means that there is a large number of carriers. The Curie constant is somewhat higher than the spin only value but this may be because the g-factor for Fe^{2+} is not exactly two. Allowing a spin orbit coupling of ${}^5\text{E}$ with ${}^5\text{T}_2$, a second order perturbation gives:

$$g = g_0 - 4\lambda/\Delta = 2.133$$

where $g_0 = 2$, λ is the spin orbit coupling constant $\sim -100 \text{ cm}^{-1}$ for the free ion and Δ is the cubic crystal field splitting $\sim 3000 \text{ cm}^{-1}$. In {52}, a figure of 2.10 is calculated, however, the value of C_M with the number above is 7.16 which is fairly close to the value measured. We should remark that the g-factor at the Cr^{3+} ion has been carefully measured by ferromagnetic resonance in CdCr_2S_4 and found to be 1.993 {71}.

The value of the Weiss parameter, -330°K indicates that the dominant exchange interaction in this compound is antiferromagnetic which suggests that the interaction involved is the $\approx 125^\circ$ super-exchange between $\text{Fe}^{2+}(\text{A})$ and $\text{Cr}^{3+}(\text{B})$. In {52}, a molecular field theory fit to the paramagnetic susceptibility and the magnetization gave $J_{\text{AB}}/k = -10^\circ\text{K}$ and $-1^\circ < J_{\text{BB}}/k < +1^\circ\text{K}$. We checked this using the high temperature series given in {72} and although our results probably suffer from truncation errors (there were only six terms in the series) they do not differ too greatly from the M.F.T. result. We found:

$$J_{\text{AB}}/k = -12^\circ\text{K} \quad \text{and} \quad J_{\text{BB}}/k = +2^\circ\text{K}$$

These results are certainly in keeping with the criteria for the stability of the Néel spin arrangement given in {73}. The basic arguments, in terms of the super-exchange rules, that justify the magnitude and signs of the interactions have been given in {32}.

At the B-sites, electron transfer creates two excited Cr^{2+} states; a high spin state, $^5\text{E}_g$ and a low spin state $^3\text{T}_{1g}$. Ferromagnetic coupling between Cr^{3+} ions results from the coupling of the $^4\text{A}_{1g}(\text{Cr}^{3+})$ ground states via $^5\text{E}_g(\text{Cr}^{2+})$ whereas, antiferromagnetic coupling results if $^4\text{A}_{1g}(\text{Cr}^{3+})$ states interact via $^3\text{T}_{1g}(\text{Cr}^{2+})$. According to our calculation, the former dominates in FeCr_2S_4 ie. J_{BB} is positive. Antiferromagnetic A-B

coupling is effected by a coupling of the ${}^5E(\text{Fe}^{2+})$ state with the ${}^3T_{1g}(\text{Cr}^{2+})$ excited state via the sixth d-electron on the Fe^{2+} ion whose spin is parallel to the B-site magnetization.

As the temperature is lowered to $\sim 170^\circ\text{K}$, we have two effects to account for: the first is the decreasing resistivity, the second is the deviation of the Mössbauer isomer shift from the Debye model calculation. We believe these two effects are related. We deal with the isomer shift results first. The solid line in figure 54 is the expected shape of δ_D calculated from (II.24) numerically, using the value of θ_D that best suited the slope of the spectrum shift data in the range $400\text{--}500^\circ\text{K}$, the value of θ_D is 250°K . The solid line is clearly a reasonable fit at high temperatures but not below 300°K . It is not reasonable to expect a change in θ_D in the paramagnetic region. For the region below T_{FN} , there are problems, three possibilities were discussed in Chapter II, section 3.2, the predictions of reference {39} there are indicated by the dotted line. The possibility of changes in θ_D or δ_i at T_{FN} make us doubt whether a realistic interpretation of the data $T < T_{FN}$ may be utilized at least initially. In addition to this, there are obvious criticisms that may be made concerning the accuracy with which δ_T may be determined for ordered Mössbauer

spectra unless very special steps are taken. In the paramagnetic region, we are on safer ground, and even allowing an error of ± 0.02 mm/s for these data, there is a very clear departure from the Debye prediction towards smaller δ_i values.

We first described this decrease in δ_i in terms of delocalization of the β -spin Fe^{2+} electron. This is reasonable, in view of the positive temperature coefficient of the resistivity, however, we should also have noted that, in passing from the localized to the collective regime, an increase in cation-anion covalency is required, in keeping with the discussion in Chapter I, section 4. Thus, the decreasing δ_i ($300 > T > 170^\circ \text{K}$) may reflect the covalency increase that presages the change over to the collective regime.

Decreasing the temperature to $\sim 140^\circ \text{K}$ apparently causes the d-electrons to become localized because the conduction once more becomes activated. The simplest explanation of this would be via the mechanism of exchange narrowing of the d-electron bands. While we have no data of our own to support this idea, we recall that there is an anomaly in the thermopower reported in {58a}. Analysis of the data led to the conclusion that the effective mass of the charge carriers had first to increase and then to decrease as T was increased through T_{FN} . The

authors rejected exchange narrowing in favour of magnon-drag because of the difficulty in explaining the decrease in m^* . If however, covalency increases continuously with decreasing temperature, because of the contraction of the lattice, then this difficulty disappears. We note that the shape of the $\log \epsilon - T^{-1}$ curve is non-linear between 140 and 60° K, a fact that suggests at least two factors determine the energy gap. One of them is likely to be increasing covalency that tends to diminish the band gap, another, the effect of increasing magnetic order within each crystallite that tends to further narrow the bands. We note that the slope is greatest just after the minimum in ϵ and starts to decrease at about 80° K, our conclusion is that band narrowing is complete by 80° K and that the flattening results from covalency increases. There must also be a third factor involving the J-T effect that we propose causes the E.F.G. at the Fe^{2+} site. Furthermore, we expect that the J-T stabilization will eventually determine the energy gap at the lowest temperatures $T < 50^\circ \text{K}$, via the splitting of the e_g orbitals in a manner essentially consistent with a tetragonal distortion. At this point then, we refer to figure 60, where our proposed band diagram is sketched.

The band gap is estimated as $\sim 2\text{eV}$ from work

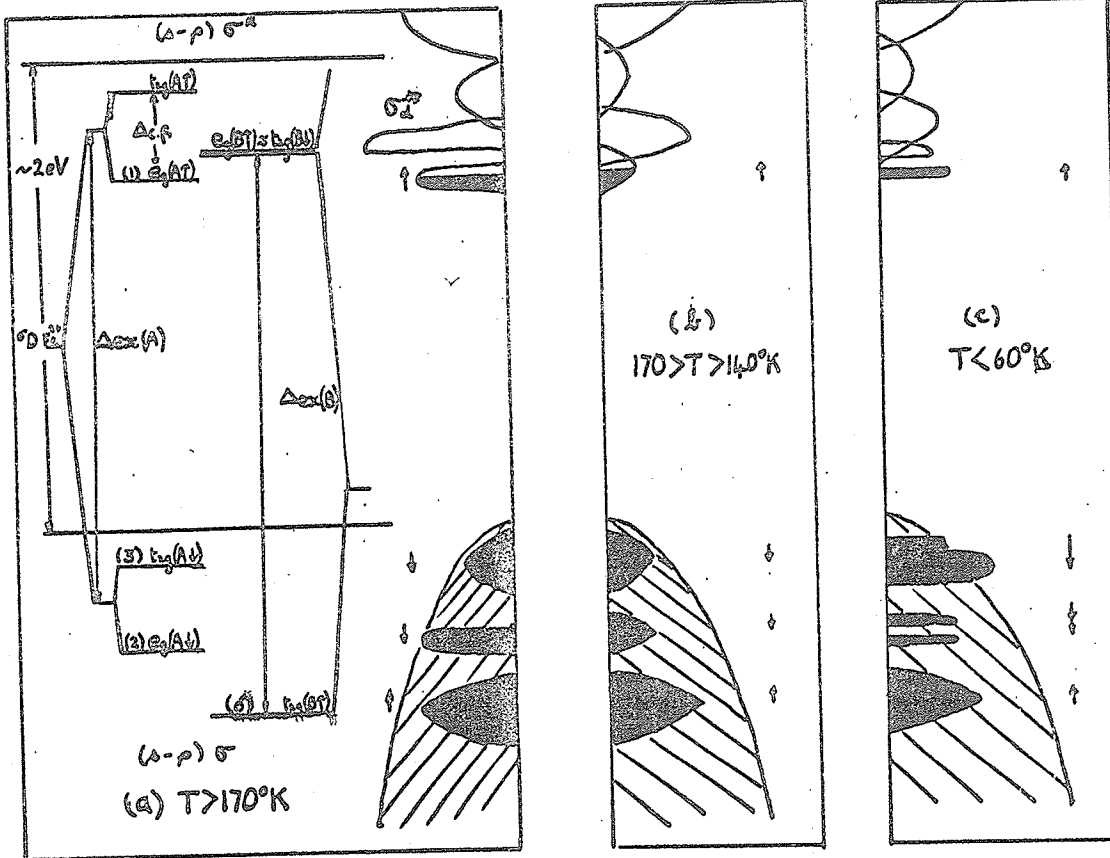


Figure 60. Suggested band scheme for FeCr_2S_4 :
 (a) Showing 1 electron orbitals and the positions of the various d-bands $T > 170^\circ\text{K}$;
 (b) Illustrating the destabilizing effect of covalency on ${}^5\text{E}(\text{Fe}^{2+})$ state $T \sim 160^\circ\text{K}$;
 (c) Illustrating the effect, at $T < T_{\text{FN}}$, of exchange narrowing and the J-T stabilization of the ${}^5\text{E}(\text{Fe}^{2+})$ state $T < 60^\circ\text{K}$.

on CdIn_2S_4 {74, 32}. Optical measurements on CdCr_2S_4 place the $e_g \uparrow B$ orbitals about 1.8 eV above the top of the valence band {75, 32} and since Cr^{3+} has $\Delta_{\text{ex}} \approx \Delta_{\text{c.f.}}$ this is also the approximate position of the $t_{2g} \downarrow B$ orbitals. This positions the ${}^5\text{E}_g(\text{Cr}^{2+})$ and ${}^3\text{T}_{1g}(\text{Cr}^{2+})$ created by electron transfer among the B-sites. Our

electrical resistivity measurements yield 0.1 eV for the separation of the ${}^5E(\text{Fe}^{2+})$ state below the excited Cr^{2+} states so that the positions of one electron orbitals at the A-sites can be estimated assuming $\Delta_{\text{c.f.}}=0.37$ eV and $\Delta_{\text{ex}}=2.2$ eV {31}.

Conduction in figure 60a is via holes in a narrow Fe^{2+} band because of the excitation of the spin up e_g electrons into what becomes a σ^* d-band in the crystal. As T decreases and covalency increases, the gap between $e_g(A\uparrow)$ and σ^* vanishes, at least for some crystal directions, and leads to a non-activated semimetallic type of conduction. Finally, figure 60c, the effects of exchange narrowing and J-T stabilization reassert the energy gap but it is now diminished to ~ 0.03 eV, a number deduced from our conductivity tests.

Magneto-resistance measurements in the region of T_{FN} should indicate that the exchange interaction J_{AK} between the A-site d-electron spin and the holes responsible for conduction should be considerably greater than the corresponding interaction J_{BK} at the B-sites. The solid line in figure 48 was calculated in {59} using the theory given in {76} with $J_{\text{AK}}/J_{\text{BK}}=10$. The agreement is not too bad and had we used $T_{\text{FN}}=174^\circ\text{K}$ instead of 170°K , it would have been excellent.

We now justify the idea that the E.F.G. is produced by a J-T stabilization of the ${}^5E(\text{Fe}^{2+})$ ground state. First we note that the isomorphous oxide FeCr_2O_4 exhibits a distortion at 135°K {69} that has been attributed to a J-T distortion {65}. We note that our Mössbauer spectra collected below 9°K are qualitatively similar to those obtained for FeCr_2O_4 {77} when $T < 50^\circ\text{K}$ and that the low temperature x-ray studies on FeCr_2O_4 {78} are eminently consistent with a tetragonal distortion to $c/a < 1$. Moreover, the electric field gradient in FeCr_2O_4 is negative, consistent with a stabilization of the orbital Q_1 . Since magnetization measurements on single crystals of FeCr_2S_4 show $\langle 100 \rangle$ to be the easy axis, and our E.F.G. is negative with $\theta = 90^\circ$ ($T < 9^\circ\text{K}$), we conclude that $c/a < 1$. The small non-zero η indicates that the distortion is not due entirely to mode Q_3 but that some of the Q_2 mode is mixed in and a small orthorhombic component is also present. The possibility that the ground state would be complicated in this way was first discussed in {79}. It happens because of the complexity of elastic strains in the crystal. The principal strain arises because of the non-ideal u parameter that prevents an ideal octahedron of anions around the B-sites. The distortion to $c/a < 1$ allows a more cubic arrangement of these anions {65}. The

conclusion is that the low temperature transition in FeCr_2S_4 is the result of a J-T distortion.

It follows then, that for $T > 9^\circ\text{K}$ the E.F.G. is essentially consistent with $c/a > 1$. The fact that $\theta \neq 0$ precludes the magnetically induced E.F.G. because H_{hf} is parallel to $\langle 100 \rangle$ and V_{zz} should then be parallel to H_{hf} . The fact that $\theta = 11^\circ$ does not preclude a J-T effect since this is mostly an orbital effect and is spin independent. Although we have not excluded magneto-striction effects we offer this thought. There is no evidence of anything but a simple Néel spin arrangement in FeCr_2S_4 so it is extremely difficult to understand why the E.F.G. should reverse sign.

We conclude that above 9°K the E.F.G. is caused by a dynamic J-T distortion, in the manner suggested in {82}. Several arguments support this view:

- (i) The fact that the line widths depend on temperature, suggests the presence of a relaxation effect {80-84};
- (ii) The fact that the average line width is proportional to the quadrupole shift down to $\sim 77^\circ\text{K}$ as shown in figure 61, suggests that the relaxation is slow compared with the Lamor precession frequency {81} and

manifests itself as lifetime broadening of the nuclear states.

- (iii) The fact that the experiment in applied fields at 81°K does not yield a zero quadrupole shift indicates that whatever causes the E.F.G. is not a static crystal distortion, neither is it particularly sensitive to the spin direction.

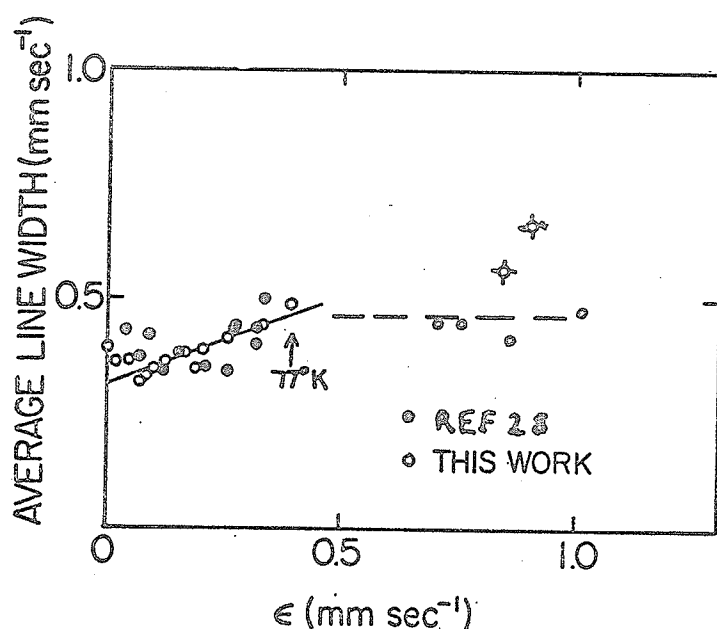


Figure 61. Dependence of average line width on the quadrupole shift in the spectra, \circ this work powder absorbers, \diamond this work rigid absorbers.

Our explanation is, that for fields > 20 kOe, the spin and orbital angular momentum can be decoupled.

This allows the magnetization to saturate ie. $\Delta m_I = 0$ lines are absent but the dynamic J-T stabilization is not precluded provided the anisotropy introduced by the applied field does not exceed the splitting of the vibronic states of the complex {62}. There is however, a different anisotropy in each crystallite, with a maximum related to the maximum magnetic anisotropy $3 \times 10^6 \text{ erg/cm}^3$ at 4.2°K {53}. The E.F.G. that originally made an angle $\sim 10^\circ$ with H_{hf} now makes a different angle with H_{eff} in each crystallite because the (elastic + magnetic) anisotropy is different to the zero field (elastic only) anisotropy. There is however, a maximum angle determined by the additional magnetic anisotropy. Thus there is a "built in" saturation effect, the magnitude of which we can estimate in the following simplified fashion. The greatest magnetic anisotropy energy difference is between the $\langle 100 \rangle$ and $\langle 111 \rangle$ directions; therefore, by assuming that the E.F.G. makes all angles θ with H_{app} between 0 and $\theta = \cos^{-1}(1/\sqrt{3})$ the expectation value of $(3\cos^2\theta - 1)$ for this range of θ values can be found viz., $2/3$ and we may expect the observed \mathcal{E} to be reduced by about this factor. In zero field $\mathcal{E} = 0.38 \text{ mm/s}$, in 50 kOe $\mathcal{E} = 0.22 \text{ mm/s}$ so the reduction is 0.58 compared with an estimate of 0.67.

There are still a couple of details that

need consideration. Not least of these is the question of why the results from rigid absorbers at low temperatures differ from those from powders. The effect of strain on the Mössbauer spectra of Fe^{2+} in tetrahedral sites has apparently been known for some time {85} but unfortunately, it was rather new to us. The effect is apparently rather severe presumably because the J-T coupling at these sites is extremely sensitive to strain {65}. It may be that random strain is one reason why different samples examined at different laboratories seem to yield slightly different Mössbauer properties.

The last point that we shall concern ourselves with is the interpretation of the total spectrum shift data below T_{FN} . Starting at the lowest temperatures, the first question is, if there is a J-T distortion at $\sim 9^\circ\text{K}$ why is there no obvious sign in the data of a first order phase change. In FeCr_2O_4 the tetragonal distortion leads to $c/a = 0.975$, we have shown {55} that the distortion in the sulphide is probably an order of magnitude less than this so $\Delta c \sim 0.0025 \text{ \AA}$. We can make use of the relationship {86} that:

$$\partial \ln |\psi_{4s}(0)|^2 / \partial \ln V = -1$$

where V is the volume and $|\psi_{4s}(0)|^2$ is the 4s electron density at the nucleus and write:

$$\partial |\psi_{4s}(0)|^2 / |\psi_{4s}(0)|^2 = - \ln V = 0.0025$$

Then using the isomer shift calibration {87,88}, we can find the shift expected ie. $\Delta \delta_i(4s) = 0.004$ mm/s.

This is rather too small to show up in our experiments.

We note however, that there is a very slight "blip"

in the data so it would be interesting to compare

data for FeCr_2O_4 , it seems that isomer shift data for this compound are not available as yet.

The larger anomaly at $T \sim 170^\circ \text{K}$ is, therefore, due either to a much larger volume change that does not show up in x-ray measurements or to covalency effects such as we have already discussed.

2.8 Conclusions.

The compound FeCr_2S_4 has properties that appear to be mainly dominated by the sixth (β -spin) electron associated with the Fe^{2+} ion. At both high and low temperatures, the compound should be described in terms of a localized electron picture. The combined magnetic and electric properties support this view and for low enough temperatures there is good evidence that the Fe^{2+} ground state ^5E , is stabilized by a J-T distortion. At intermediate temperatures the compound tends to exhibit properties that are closer to those expected of collective electrons and we conclude that this is brought about by the effect of covalent overlap

of the β -spin electron with surrounding anions.

3. A COMMENT ON CdCr_2S_4 .

3.1 Introduction.

We include our comments on this compound partly because the discovery that it existed as a ferromagnet sparked the interest in chalcogenide spinels in our lab. and partly because it is still an academically interesting compound. Although a great deal is known about it, the question of the spin arrangement is, so far as we know, still in doubt.

According to [89], the compound was first investigated as part of a Ph.D. program [90] but the work received no attention. Only the paramagnetic susceptibility was measured from which it was found that θ was positive ($\sim 130^\circ\text{K}$) and, on the basis of M.F.T., it was predicted that ferromagnetic ordering would occur somewhere below this temperature. In the early nineteen sixties, the compound was re-discovered. The first published work [91] revealed that $\theta = +152\text{ K}$, $C_M = 3.7$, $T_C = 84.5^\circ\text{K}$ and the low temperature magnetic moment was $5.15\mu_B$ per molecule. Almost simultaneously the properties of the compound were reported in [92], there $\theta = +156^\circ\text{K}$, $C_M = 3.66$, $T_C = 86^\circ$ and $\mu(4.2^\circ\text{K}) = 5.55\mu_B/\text{molecule}$, so there was reasonable

agreement.

Electrical transport and crystallographic properties have also been reported. The compound crystallizes in the spinel structure with a lattice parameter of 10.244 Å and a u -parameter of 0.390 {89}. In conductivity measurements {89,93}, the compound shows semi-conducting behaviour with ρ (296°K) = $2 \times 10^3 \Omega \cdot \text{cm}$ and ρ (77°K) = $2.86 \times 10^9 \Omega \cdot \text{cm}$. The Seebeck coefficient has been reported {93} as $-60 \mu\text{V}/^\circ\text{K}$ indicating n -type conductivity; the Hall mobility was apparently too low to measure but it was $< 0.5 \text{ cm}^2/\text{Vsec}$. The resistivity showed no discontinuities near the ordering temperature. These results are consistent with a localized electron picture, the conductivity arising from a hopping type mechanism. By doping with acceptor and donor type impurities, it is found that holes have a very large mobility, presumably from valence band conduction, and that electrons have a very low mobility {94}.

A variety of optical and magneto-optical experiments have been performed {75,95,96,97,98}. Originally it was thought {75}, that the absorption edge occurred at $\sim 1.6 \text{ eV}$ ($12.9 \times 10^3 / \text{cm}$). With this assignment, the absorption edge was found to have a "blue" shift {95,97}, whereas, most magnetic semiconductors show a red shift {96,99}, as the temperature

is lowered; the assigned absorption edge also began to show considerable structure with decreasing temperature. Three explanations were given {32,100,101} and the absorption spectrum was re-investigated {75}. It then turned out that the strong absorption found at $\sim 7800 \text{ \AA}$ was not the semi-conductor band gap absorption at all, but the long wavelength tail of the ${}^4A_{2g}(\text{Cr}^{3+}) \rightarrow {}^4T_{2g}(\text{Cr}^{3+})$ crystal field transition. As the photon energy was increased, the absorption peaked at 6700 \AA , fell and then rose to a second peak at 5500 \AA . This was assigned to the ${}^4A_{2g}(\text{Cr}^{3+}) \rightarrow {}^4T_{1g}(\text{Cr}^{3+})$ crystal field transition. This second peak is resolved only at low temperatures as it overlaps the true band edge absorption at $\sim 5000 \text{ \AA}$ ($= 2.5\text{eV}$) in agreement with results on CdIn_2S_4 {74}. A third, rather low intensity absorption was also found at 7600 \AA and tentatively assigned to ${}^4A_{2g}(\text{Cr}^{3+}) \rightarrow {}^2E_g(\text{Cr}^{3+})$; however, the oscillator strength is four orders of magnitude too large for this assignment and the transition might result from some other source.

Another type of experiment was reported in {98} where the Raman scattering of the solid was studied. It was found that there were certain Raman lines whose intensity depended quite strongly on temperature. There was a sharp decrease in intensity as T was increased through T_c . A qualitative explanation,

based on a theory given in {102}, was offered. It is suggested that through the spin orbit interaction of an excited state, the spin system is coupled to the lattice phonon modes. Essentially, the "breathing" mode of the anions around a tetrahedral (Cd^{2+}) site, modulates the bond lengths of the 90° Cr^{3+} -S- Cr^{3+} n.n. superexchange paths, and, since the magnetic exchange interaction depends on the anion positions, the Raman intensity can be temperature dependent in a manner qualitatively similar to the spin correlation.

3.2 Magnetization Measurements.

We used the equipment and techniques described in Chapter II, section 1 to measure the full magnetization curve for CdCr_2S_4 samples that were synthesized in the manner described in Chapter I, section 5. Our x-ray powder diffraction pattern is given in table 16. From the high angle lines, we found $a_0 = 10.242 \text{ \AA}$ in good agreement with previous values.

At no temperature could we find any remanent magnetization or coercivity. The material does not appear to be superparamagnetic, however, because an attempt to fit all the magnetization data on a universal curve {39} of M versus (H/T) failed. The conclusion is that the material has a very low anisotropy consistent with a completely quenched orbital angular

Table 16. X-ray* powder diffraction pattern for CdCr₂S₄.

| hkl (Spinel) | d _{obs} (Å) | d _{calc} (Å) | I _R ** |
|-----------------|-------------------------|--------------------------|-------------------|
| 220 | 3.610 | 3.621 | 5 |
| 311 | 3.099 | 3.088 | 7 |
| 400 | 2.560 | 2.560 | 1 |
| 331 | 2.350 | 2.349 | 1 |
| 422 | 2.095 | 2.091 | 5 |
| 333,511 | 1.974 | 1.971 | 6 |
| 400 | 1.813 | 1.810 | 10 |
| 620 | 1.620 | 1.619 | 1 |
| 533 | 1.571 | 1.562 | 2 |
| 642 | 1.370 | 1.368 | 2 |
| 731,553 | 1.331 | 1.333 | 2 |
| 800 | 1.281 | 1.280 | ½ |
| 733 | 1.251 | 1.251 | ½ |
| 822,660 | 1.208 | 1.207 | 1 |
| 751,555 | 1.184 | 1.183 | 3 |
| 931 | 1.074 | 1.0737 | 3 |
| 844 | 1.046 | 1.0453 | 6 |
| 933,755 | 1.029 | 1.0293 | ½ |
| 1020,862 | 1.005 | 1.0041 | 4 |
| 951,773 | 0.9905 | 0.9905 | 9 |

* Mn filtered FeK α radiation at room temperature.

** Estimated from powder photograph.

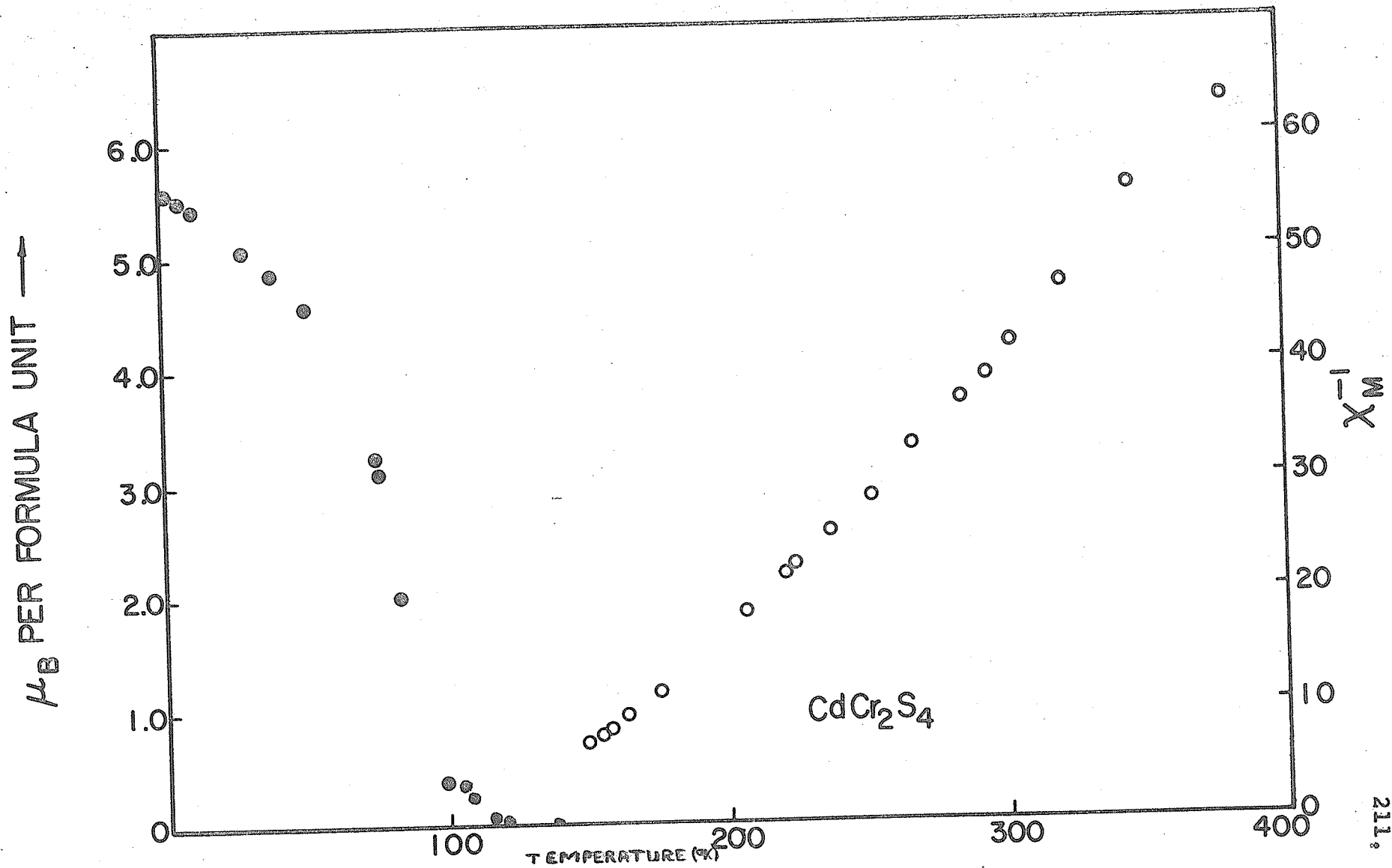


Figure 62. Temperature dependence of M_s (closed circles) and χ_M^{-1} (open circles) for CdCr_2S_4 .

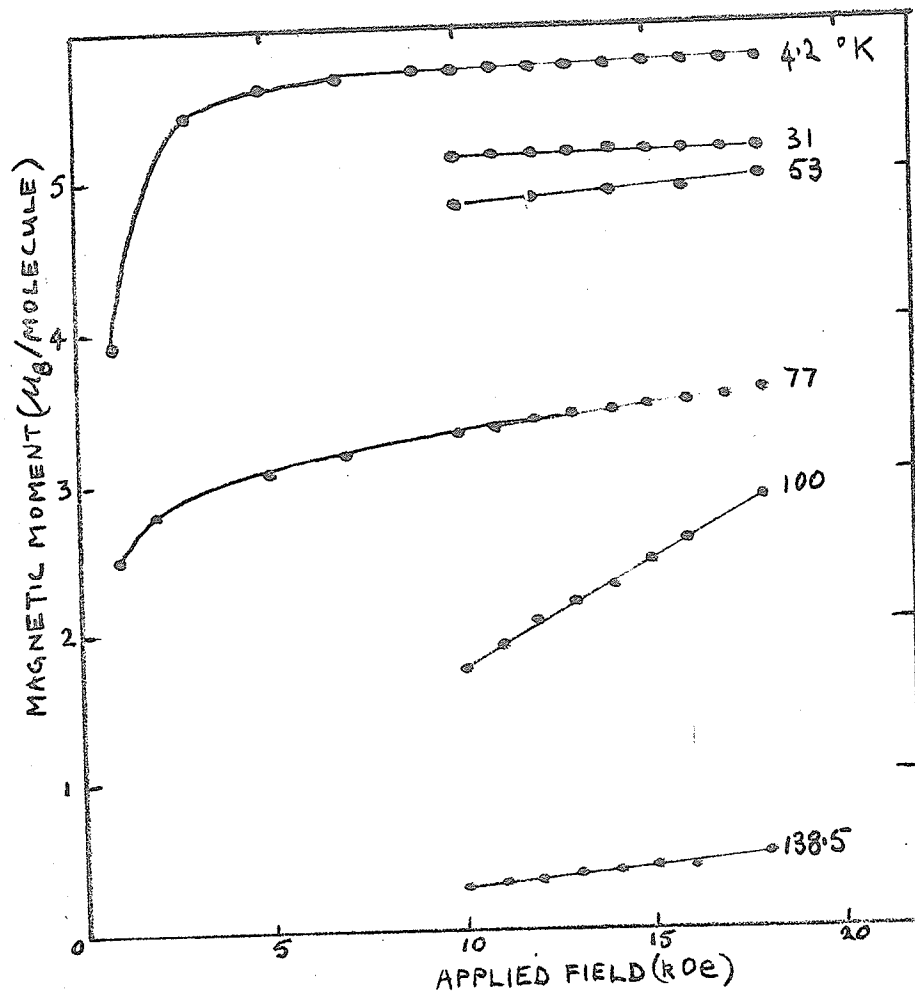


Figure 63. Magnetization as a function of applied field at various temperatures for CdCr_2S_4 .

Table 17. Magnetic and Crystallographic Data from CdCr_2S_4 .

| | |
|--------------------------------------|--------|
| Lattice parameter \AA | 10.242 |
| M_S (4.2°K) μ_B /molecule | 5.65 |
| M_∞ (4.2°K) μ_B /molecule | 5.82 |
| T_C (°K) | 86±4 |
| θ (°K) | +151±3 |
| C_M | 3.7 |

momentum at the B-sites that are occupied by Cr^{3+} ions.

We show M_s and χ_M^{-1} as functions of temperature in figure 62. While in figure 63, we show the variation of M_s with applied field for a few temperatures. In table 17, we show the results of the investigation.

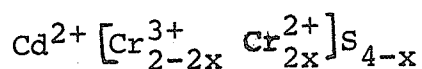
It is worth pointing out that from the value of θ and equation (11-16) a value of $J_{BB}/k=10^\circ\text{K}$ is found which is in fair agreement with the value obtained in {89} using a high temperature expansion, $J_{BB}/k=11.8^\circ\text{K}$. We also remark that the compound shows a considerable degree of short range order above the long range ordering temperature.

3.3 Discussion.

We first consider the value found for C_M ie. 3.7; this is to be compared with expected spin only value of 3.75. If we take account of the ferromagnetic resonance results in {71}, where $g(\text{Cr}^{3+})$ was found to be 1.993 then $C_M=3.73$. We might therefore, conclude that our sample has the desired composition. The question that must be asked then is, why is the low temperature moment not $5.98\mu_B/\text{molecule}$ (6.0 for spin only values)? The highest reported value {103} is $5.86\mu_B/\text{molecule}$ at 1.5°K obtained after extrapolation to $1/H=0$, in agreement with our value of $M_\infty=5.82\mu_B/\text{molecule}$ at 4.2°K after extrapolation to

$1/H=0$. At the other end of the scale, the moments reported range from 5.15 to $5.65 \mu_B$ /molecule.

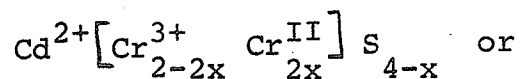
According to {103} the deviation occurs because of the presence of Cr^{2+} antiferromagnetically coupled to Cr^{3+} on B-sites and the Cr^{2+} is there because of an anion deficiency. If this is the case, then our sample composition should be written:



and the magnetic moment would be:

$$(6-14x) \mu_B / \text{molecule}$$

from which $x=0.013$ and C_M would then be 3.78(4) assuming $g=2$ for ${}^5E_g(\text{Cr}^{2+})$. Two similar possibilities are that, Cr^{2+} is present in a low spin state or that cation rather than anion vacancies exist. Given these possibilities, our value of C_M indicates $x=0.01$ in the formulae:



where the symbol \square^+ indicates a hole in the anion p-orbital and we can assume these holes to be localized by way of vacancy trapping {104}. The expected low temperature magnetic moment is then $5.94 \mu_B$ /molecule. From our work on Fe_3S_4 , we would favour an explanation in terms of cation vacancies; however, this does not lead to the correct values of the low temperature

moment which seems to be $5.84 \pm 0.02 \mu_B$ /molecule. On the other hand, postulating high spin Cr^{2+} to obtain the correct low temperature moment leads to a C_M value that is outside the spread of measured values 3.66-3.7. Our conclusion is that in CdCr_2S_4 some explanation other than vacancies or high and low spin Cr^{2+} must be found to explain the low temperature moment. In view of the large number of competing exchange interactions that exist in such compounds {89,105,106}, it seems reasonable to postulate a non-collinear spin arrangement. Estimates of the canting angle from the low temperature moments yields values between 31 and 13° .

Substituting small amounts of Co^{2+} or Ni^{2+} into the compound to replace Cr^{3+} replacing a suitable amount of Cd^{2+} by In^{3+} and then finding that the low temperature moment is roughly consistent with an antiferromagnetic alignment of Cr^{3+} with the guest ions {103} does not prove the existence of Cr^{2+} in the compound. The slope on the magnetization curves of these doped compounds, even at 1.5°K , indicates the presence of strong anisotropy. Extrapolation to $1/H=0$ should overestimate the magnetic moment. The fact that all the observed moments fall below the values calculated for A.F. alignment shows that the model is incorrect in detail. Our explanation would

be that the substitution weakens the n.n. exchange and therefore, makes possible larger canting angles among the B-site spins. In fact, the difference between observed and expected moments for these doped compositions is greater than the deviation from expected moment of the pure composition.

A neutron diffraction study of the compound is required. This would be expensive because the cadmium used would need to be 99.999% free of ^{113}Cd in order to reduce the capture cross section to reasonable values. Material like this typically costs \sim \$10/mg so the cost of 1g of compound would be \$4,000. Alternatively, an investigation might be made in the following manner. Put a small amount of some transition metal on the A-site that will produce a strong anisotropy and will provide a strong A-B interaction. Under these circumstances, we can be almost certain that a collinear B-site arrangement will pertain. Unless there is overwhelming evidence of a co-operative distortion of the spinel lattice, in which case a Yaffet-Kittel arrangement may be expected {107}.

The energy band diagram for the compound can be deduced from the optical measurements {75} and we sketch it in figure 64. The broad conduction band is formed from the (s-p) σ^* antibonding orbitals and

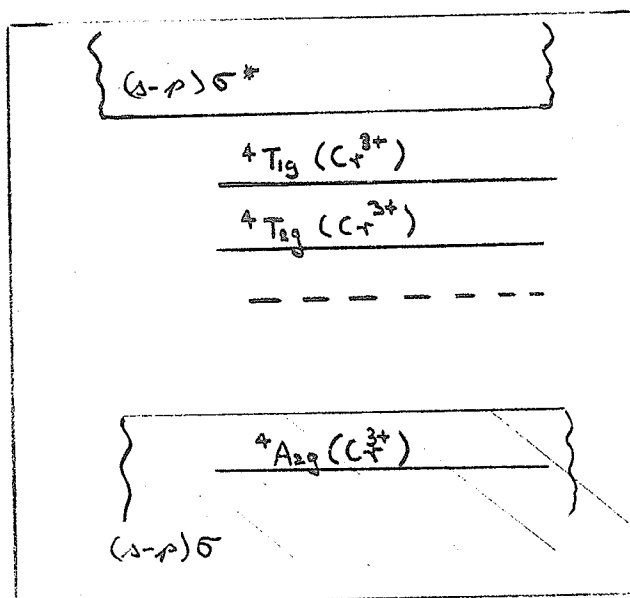


Figure 64. Suggested energy band scheme for CdCr_2S_4 in terms of multi-electron crystal field states; the stable Cd^{2+} state is not shown but is likely to be well below the valence band.

is empty, the valence band is full. The band gap is 2.48 eV. The positions of the ionic terms are indicated and the dotted line shows the position of the weak lowest energy absorption. It is not assigned but some of the possibilities are:

- (i) $4A_{2g}(\text{Cr}^{3+}) \rightarrow 2E_g(\text{Cr}^{3+})$;
- (ii) Magnon assisted α -spin valence electron
 $\rightarrow 5E_g(\text{Cr}^{2+})$;
- (iii) Phonon assisted electron transfer among
 B-sites $\rightarrow 5E_g(\text{Cr}^{2+})$;
- (iv) Magnetic Polaron peak?

3.4 Conclusions.

Most properties of this compound seem to be well understood. There is some evidence that the spin arrangement is non-collinear.

4. EXPERIMENTS ON FeRh_2S_4 .

4.1 Introduction.

In an attempt to study tetrahedral site Fe^{2+} ions without the complication of magnetic B-site ions we decided to make $\text{Fe}[\text{Rh}_2]\text{S}_4$. Although a literature search revealed no previously published work on the compound there was good reason to believe it existed. The spinel compounds $\text{Co}[\text{Rh}_2]\text{S}_4$ and $\text{Cu}[\text{Rh}_2]\text{S}_4$ have been synthesized {108,109,110,58} and there is also a report on $(\text{Fe}_{0.5}\text{Cu}_{0.5})[\text{Rh}_2]\text{S}_4$ {111}. On octahedral sites the e_g orbitals of $\text{Rh}^{3+}(4d^6)$ are so heavily destabilized by covalent overlap that Rh^{3+} always takes the low spin configuration ${}^1A_{1g}(t_{2g}, 6 \uparrow^*, 0)$. It, therefore, has $S=0$ and is essentially diamagnetic.

It is perhaps surprising to find that $\text{Co}[\text{Rh}_2]\text{S}_4$ orders antiferromagnetically at a much higher temperature than the corresponding ferrimagnet {112,52} $\text{Co}[\text{Cr}_2]\text{S}_4$, 400°K compared with 220°K . The compound $\text{Cu}[\text{Rh}_2]\text{S}_4$ is metallic and shows only a Pauli temperature independent paramagnetism yet $\text{Cu}[\text{Cr}_2]\text{S}_4$ is a metallic ferromagnet {105, 32, 58} with $T_c \sim 400^\circ\text{K}$. On the other

hand, substitution of half the copper in $\text{Cu}[\text{Rh}_2]\text{S}_4$ by iron leads to antiferromagnetism with $T_N=140^\circ\text{K}$ {111}. The same substitution in the chromium thiospinel reduces the ordering temperature to $\sim 300^\circ\text{K}$.

The conduction in $(\text{Fe}_{0.5}\text{Cu}_{0.5})[\text{Rh}_2]\text{S}_4$ is reported {111} as semiconducting with a Seebeck coefficient of $+159\mu\text{V}/\text{deg}$, the $\log \rho - T^{-1}$ plot is weakly curved with $\rho(296^\circ\text{K})=1.1\Omega\text{cm}$ and $\rho(88^\circ\text{K})=15.1\Omega\text{cm}$. The susceptibility is field independent down to 4.2°K however, the temperature dependence of the inverse susceptibility is unlike that of $\text{Co}[\text{Rh}_2]\text{S}_4$. It is observed that χ_M^{-1} increases from 4.2°K reaches a flat plateau around 50°K falls to a weak minimum around 140°K and, thereafter, follows a Curie law. From the high temperature data, a $C_M=2.32$ is deduced and a $\theta=-420^\circ\text{K}$ is found. The value of C_M is supposed to be a result of Fe^{3+} rather than Fe^{2+} on the A-sites consistent with Cu^{1+} as the other A-site ion. No Mössbauer study was made but this would provide a check on these cation valencies especially in view of the semiconducting behaviour of the compound. The neutron diffraction study, however, found $S=1.95$ for one A-site and zero for the other. It is suggested that this lower than expected result arises because of about 20% inversion of the A-sites from a true 1:1 ordering but the possibility of Fe^{2+} is not considered.

There still exists some controversy over the ways in which the energy band schemes of the copper containing Rh and Cr thiospinels account for their observed properties {32,99}. Although the properties of $(\text{Cu}_{0.5}\text{Fe}_{0.5})[\text{Rh}_2]\text{S}_4$ may not be directly applicable to our experiments any scheme suggested for $\text{Fe}[\text{Rh}_2]\text{S}_4$ must, with suitable modification, be capable of explaining the properties of the similar compound.

4.2 Preparation of Samples.

We found one reason why no reports have appeared on this compound when we tried to prepare it by the methods in Chapter I, section 5. It is indeed difficult to synthesize as a single phase spinel. We tried a variety of heat treatments and had partial success. This is in keeping with results on $\text{Co}[\text{Rh}_2]\text{S}_4$ [113]. There also, some spurious reflections are found in the x-ray powder pattern. These difficulties may be caused by the nobility of rhodium which makes it slow to react or there may be some more fundamental reason associated with the bonding of the sulphur lattice in rhodium thiospinels.

In our first attempt at synthesis, we ground stoichiometric quantities of the elements together and fired them for 2 days in an evacuated

quartz ampul at 1100°C. Slow cooling produced at least two phases. From a room temperature Mössbauer spectrum, it was found that one phase was ordered, the other was not. The product was not attracted to a hand magnet.

We reground the product and refired for a further two days at 1100°C and this time quenched the ampul into ice water. A powder photograph showed all the spinel reflections and several fairly intense spurious lines. A room temperature Mössbauer spectrum showed what appeared to be an asymmetric doublet which in all likelihood was two doublets superposed with different isomer shifts. Further Mössbauer spectra collected at increasing temperatures showed that this doublet gradually disappeared and on returning to room temperature, the spectrum was quite different. A second x-ray powder picture showed that some of the hitherto intense spurious reflections had disappeared and all the others had been reduced in intensity. A Mössbauer spectrum of this "annealed" sample at 77°K showed that the compound had ordered by this temperature but a small amount immersed in liquid nitrogen was not attracted to a hand magnet. A Mössbauer spectrum of the as quenched material showed no evidence of magnetic order at 77°K.

A series of quenching tests showed that the

Table 18. X-ray** powder diffraction pattern for FeRh_2S_4 .

| hkl (Spinel) | d_{obs} (Å) | d_{cal} (Å) | I_{R}^{***} |
|-----------------|-------------------------|-------------------------|----------------------|
| 111 | 5.496 | 5.722 | 3 |
| 220 | 3.431 | 3.504 | 1 |
| * | 3.248 | - | $\frac{1}{2}$ |
| * | 3.101 | - | $\frac{1}{2}$ |
| 311 | 3.029 | 2.988 | 8 |
| 222 | 2.812 | 2.860 | 1 |
| * | 2.626 | - | $\frac{1}{2}$ |
| 400 | 2.444 | 2.478 | 6 |
| * | 2.391 | - | $\frac{1}{2}$ |
| 311 | 2.271 | 2.273 | 1 |
| * | 2.202 | - | 1 |
| 422 | 2.008 | 2.023 | 2 |
| 333,511 | 1.900 | 1.907 | 5 |
| 400 | 1.744 | 1.752 | 10 |
| 442 | 1.622 | 1.652 | 4 |
| 620 | 1.610 | 1.567 | 1 |
| 533 | 1.509 | 1.511 | 1 |
| 622 | 1.487 | 1.494 | 1 |
| 444 | 1.438 | 1.430 | 3 |
| 711,551 | 1.382 | 1.388 | 2 |
| 642 | 1.321 | 1.324 | 1 |
| 731,553 | 1.292 | 1.290 | 4 |
| 800 | 1.238 | 1.239 | 2 |
| 644 | 1.206 | 1.211 | $\frac{1}{2}$ |
| 751,555 | 1.143 | 1.144 | 3 |
| 840 | 1.108 | 1.108 | 7 |
| 753,911 | 1.087 | 1.088 | 3 |
| 931 | 1.039 | 1.039 | 4 |
| 844 | 1.010 | 1.011 | 5 |
| 933,755 | 0.997 | 0.996 | 3 |

* Reflection not belonging to the spinel pattern.
 ** Mn/FeK α radiation was used at room temperature.
 *** Estimated from the photograph.

(spinel + spurious lines) type of pattern could be obtained at all temperatures down to 950°C with an upper limit (determined by the softening of the quartz) of 1400°C .

Our final approach was based on the previous findings together with a prior knowledge that rhodium is a very noble metal. We ground stoichiometric quantities of the elements together, pelleted the mix, fired in a sealed quartz ampul for two weeks at 1100°C , and quenched into ice water. The ampul was then placed in a furnace at 500°C for two more weeks, then slowly cooled to room temperature. A Debye-Sherrer x-ray powder diffraction pattern containing all the spinel reflections plus 5 weak or very weak extra lines was obtained from the final product. In table 18, the pattern obtained is shown together with the indices assigned. The spurious reflections are marked with asterisks. The conclusion is that the product has a small amount $\sim 5\%$ of some second phase but it is essentially a spinel.

From the high angle reflections, we determined the lattice parameter as $9.91 \pm 0.01 \text{ \AA}$. The error is large because the high angle lines were rather diffuse, as might be expected if these were quenched in random strains.

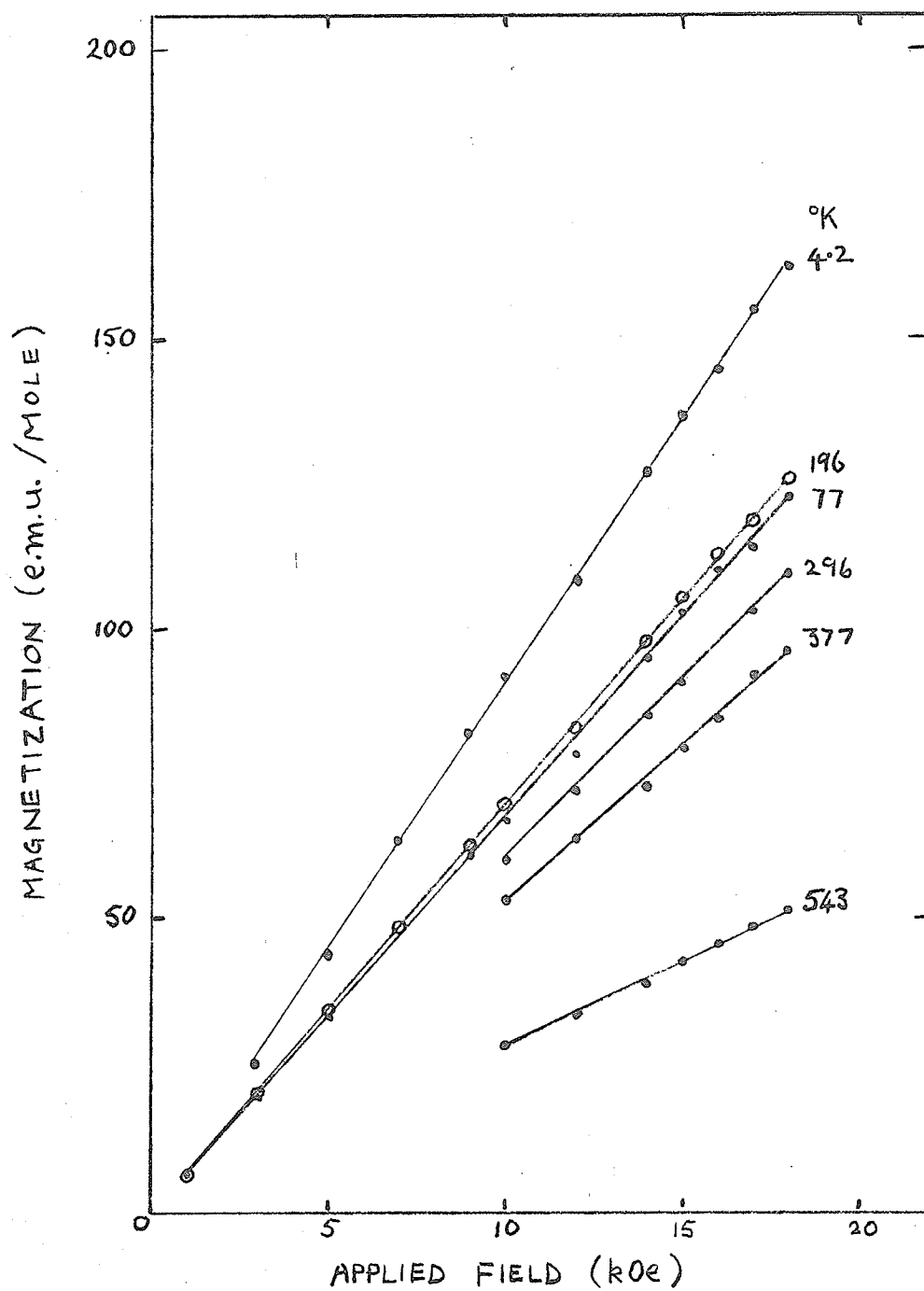


Figure 65. Magnetization of FeRh_2S_4 as a function of applied field for various temperatures.

4.3 Magnetization Measurements.

We used the equipment and methods described in Chapter II, section 1.3 to measure the first part of the magnetization curve. We found no evidence of a permanent magnetic moment at any temperature. Figure 65 shows some of the magnetization data as a function of field for various temperatures. It may be seen that the magnetization is independent of field at 4.2°K , 77°K , and 196°K . The slope of the curves gives χ_M and in figure 66, we show χ_M^{-1} versus T.

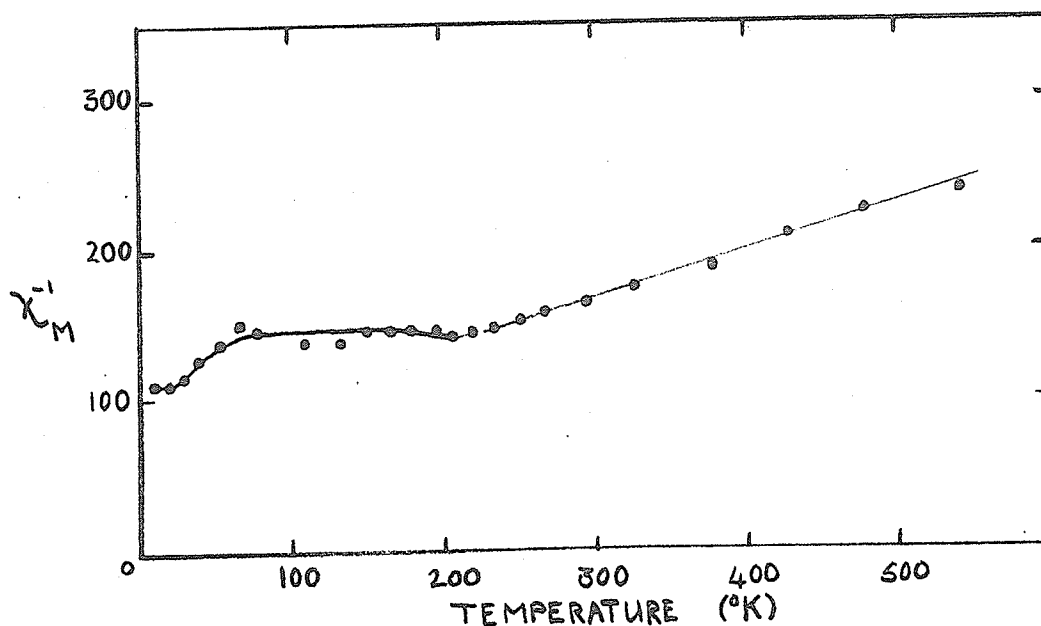


Figure 66. Inverse molar susceptibility of FeRh_2S_4 as a function of temperature.

Above 220°K , χ_M^{-1} follows a Curie law and we find $\theta = -240^\circ\text{K}$ and $C_M = 3.2$. The change in slope at $\sim 210^\circ\text{K}$ is interpreted as the Néel point. Table 19 summarises the various results. If spin only considerations are

in order, we would expect $C_M=3.0$ and a $\mu_{\text{eff}}=4.9 \mu_B/\text{molecule}$.

Table 19. Magnetic and Crystallographic Data for FeRh_2S_4 .

| | |
|------------------------------------|----------------|
| Lattice Parameter (\AA) | $9.91 \pm .01$ |
| C_M | 3.2 |
| θ ($^\circ\text{K}$) | -240 ± 5 |
| T_N ($^\circ\text{K}$) | 210 ± 10 |
| μ_{eff} | 5.06 |

At much lower temperatures, the susceptibility shows a complicated behaviour. It is similar, in every respect, to the behaviour reported for $(\text{Fe}_{0.5}\text{Cu}_{0.5})[\text{Rh}_2]\text{S}_4$, over the temperature range 100-300°K, we measure 1.75 times the susceptibility reported in {111}.

4.4 Electrical Measurements.

This compound appears to sinter quite readily and after the final heat treatment, the measured density was 97% of the theoretical density calculated using the lattice parameter above. It is readily wetted by In.15%Sn solder so conductivity and magneto-resistance measurements were made in the manner described in Chapter II, section 2.2. The results are shown in figure 67. A positive magneto-resistance is found over

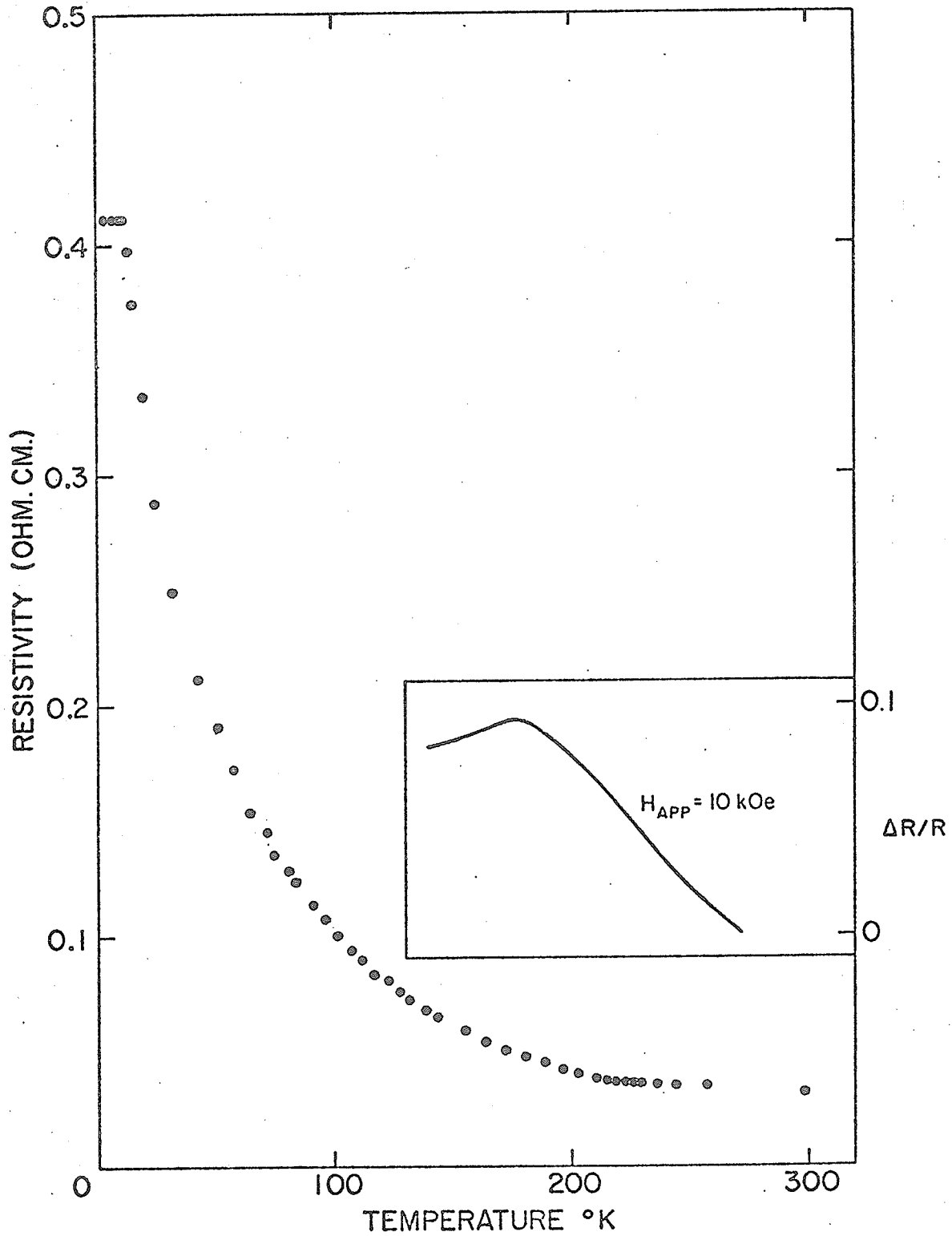


Figure 67. The temperature dependence of the resistivity and magneto-resistance (insert) of FeRh_2S_4 .

the temperature range investigated and the resistivity increases steadily with decreasing temperature until about 15°K when there appears to be a leveling off. At high enough temperatures $T > 250^\circ\text{K}$, a plot of $\log \rho - T^{-1}$ is linear with a slope corresponding to an activation energy $0.14 \times 10^{-3} \text{eV}$. At higher temperatures, the plot is gently curving. The resistivity takes values of 3.2×10^{-2} , 1.34×10^{-1} and $4.1 \times 10^{-1} \Omega \cdot \text{cm}$ at 296, 77 and 4.2°K respectively.

4.5 Mössbauer Effect Studies.

In addition to the spectra examined in connection with the preparation of the compound, we collected a series of spectra in the temperature range 4.2 - 700°K. Some of the spectra are shown in figures 68 and 69. First we consider the room temperature spectrum figure 68b. In order to fit this spectrum adequately, we required 4 lines. The major part of the absorption was fitted as a singlet. It turned out to be broad $\sim 0.5 \text{ mm/s}$ and has a total shift of 0.71 mm/s. In fact, it is probably a narrow doublet. On the shoulder of this line, there is every indication of a second doublet which we fitted with constraints on the full widths and intensities. This resolved doublet constituted 10% of the total absorption. The line widths were 0.3 mm/s and their centre of gravity

was shifted 0.75 mm/s. Their splitting was 1.4 mm/s. The fourth line turned out to be a broad singlet of low intensity constituting 10% of the total absorption with a total shift of 0.21 mm/s, this, we associate with impurities in the compound.

As the temperature is raised, most of the structure is lost from the spectrum (68a), such spectra were fitted as broad singlets only for the purpose of determining the spectrum shift. As the temperature is lowered the appearance of the spectra remains substantially the same as at 296°K, although by 230°K, there is evidence of an ordered phase giving weak absorption in the base line of the absorption curve, figure 68c.

On cooling further, the spectra become magnetically ordered. The temperature at which this occurred was found to be $215 \pm 5^\circ\text{K}$ which agrees fairly well with the T_N adduced from the magnetization measurements. Superficially, these ordered spectra appear to be fairly simple, figure 69. Six well defined absorption peaks are found and there is a second very weak ordered spectrum with a larger splitting. On fitting the spectra however, it is found that the intensity in the central region is much stronger than it should be. Furthermore, our best fits to the spectra show that just below T_N

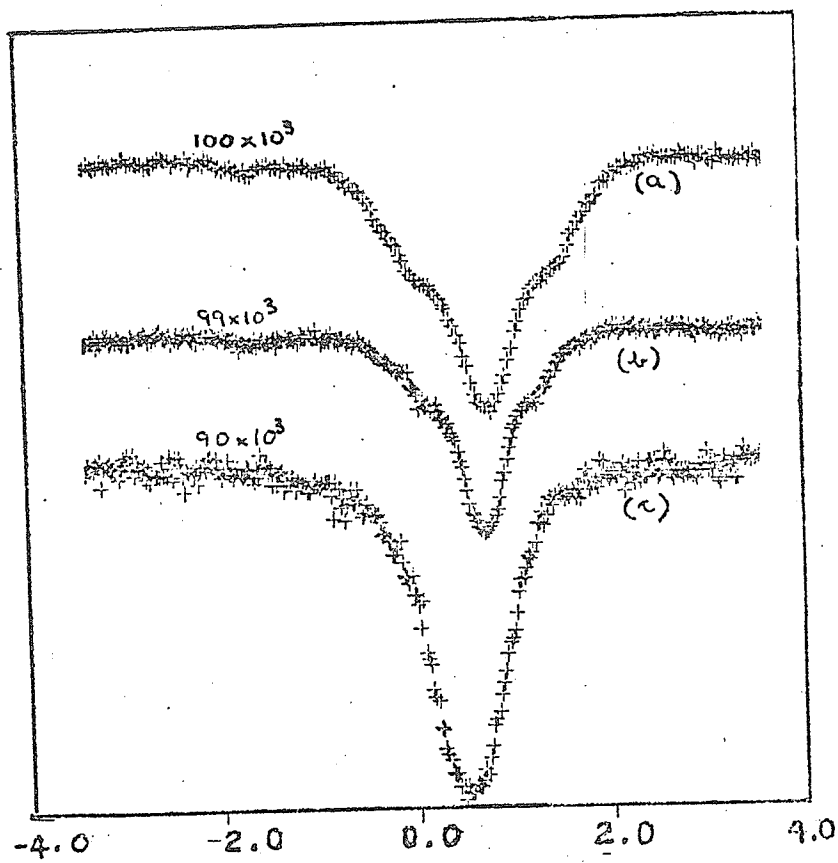


Figure 68. Mössbauer spectra of FeRh_2S_4 at:
(a) 234°K
(b) 296°K
(c) 413°K

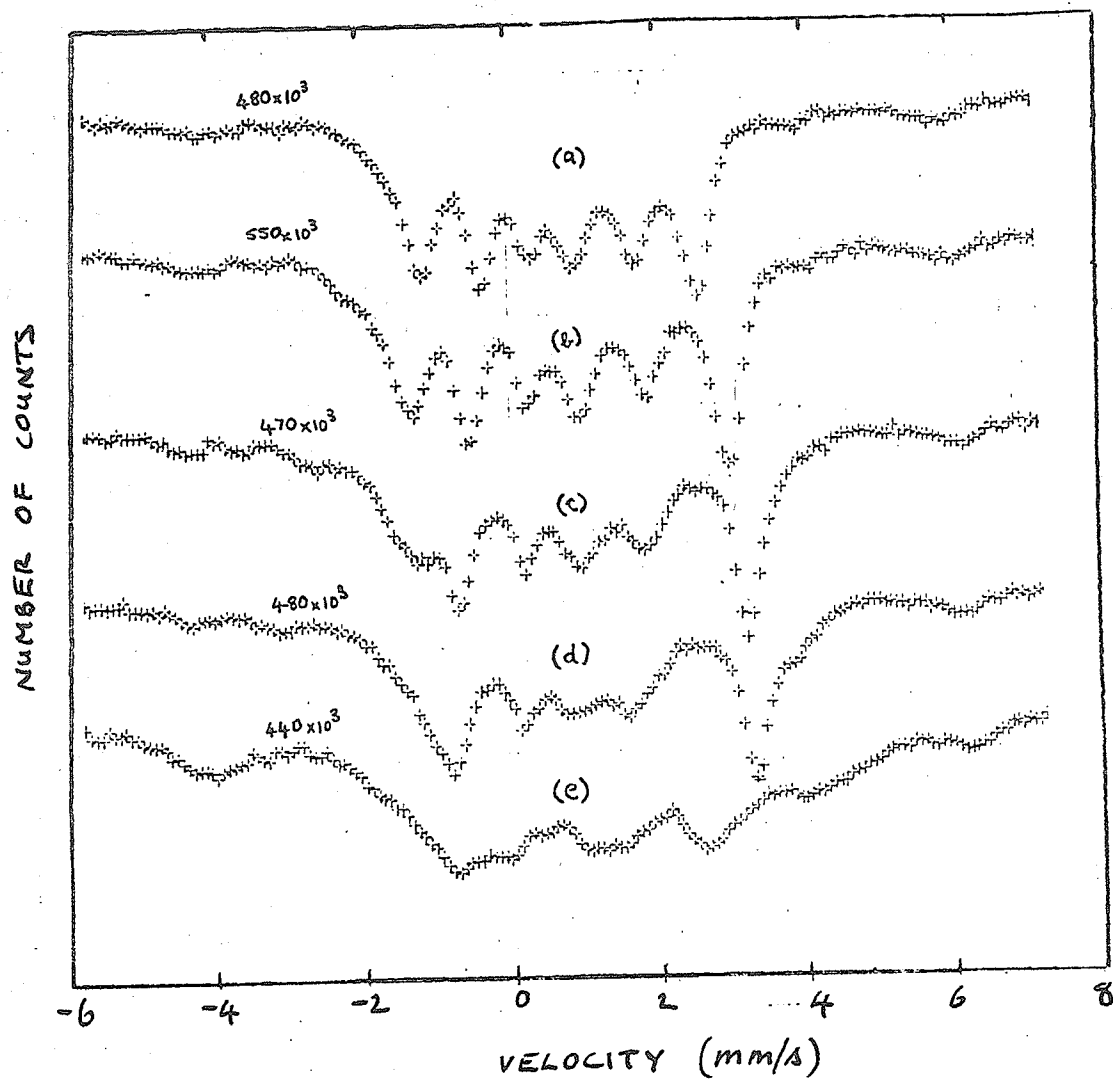


Figure 69. Mössbauer spectra from FeRh_2S_4 below T_N
 (a) 182°K
 (b) 126°K
 (c) 123°K
 (d) 77°K
 (e) 4.2°K

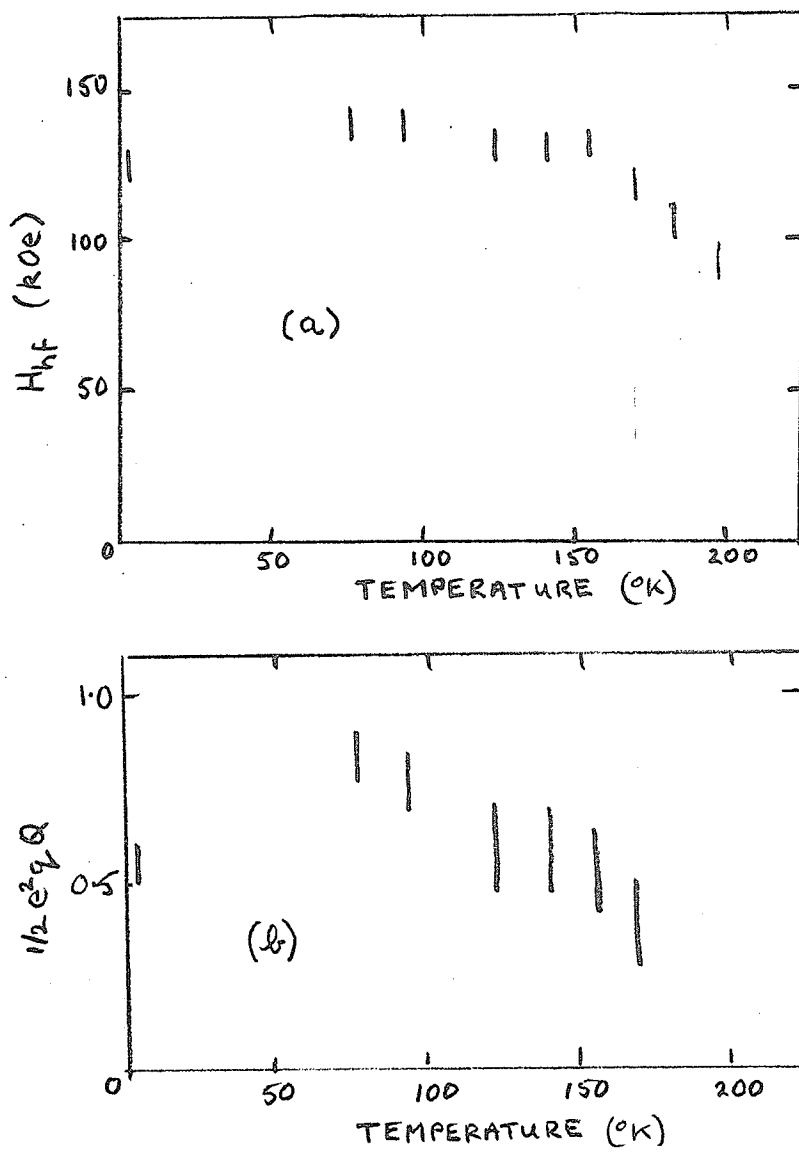


Figure 70. Temperature dependence of (a) H_{hf} and (b) $\frac{1}{2} e^2 q Q$ for FeRh₂S₄.

$\theta=59^\circ$, figure 69a, that by 126°K, figure 69b, $\theta=50^\circ$ and the spectrum shown in figure 69c has $\theta=20^\circ$. At 4.2°K, $\theta=10^\circ$ and at 77°K $\theta=15^\circ$. The values of θ are only approximate because the "Powder" program converges only very slowly under conditions where $\theta=40-60^\circ$ (see appendix D) and we did not always obtain a set of final values. Only for a selection of the spectra did we allow the computer to iterate to conclusion and even then, it was necessary to constrain ξ and η equal to zero. As a result, the quantity $\frac{1}{2}e^2qQ$ is determined only very roughly and the values found are shown in figure 70b. The errors placed on these data result from allowing a $\pm 5^\circ$ error on θ and taking no account of errors introduced by the constraints on ξ and η . Figure 70a shows the values found for H_{hf} and in figure 71 we show the variation with temperature of the total spectrum shift.

4.6 Discussion.

It is necessary to be cautious in drawing conclusions about this compound from the results of this particular investigation. The reasons are fairly clear. In the first place, we could not produce a single phase sample and in the second, the magnetization data suggest interpretations that are

not apparently supported by the Mössbauer Effect studies.

The magnetization data indicates that the compound is a simple antiferromagnet with ordering of the first kind $|\theta/T_N|=1.1$ consistent with the expected arrangement of magnetic cations on A-sites only. The Curie Constant is close to that expected and could be brought closer by either allowing g to be slightly greater than two or by making a correction $\{111\}$ for the temperature independent susceptibility of Rh^{3+} . For a mole of $\text{A}\{\text{Rh}_2^{3+}\}\text{S}_4$, the Van Vleck contribution is estimated as $\sim 3.8 \times 10^{-4}$ e.m.u./mole and the diamagnetic contribution as $\sim -2 \times 10^{-4}$ e.m.u./mole, a net contribution of $+1.8 \times 10^{-4}$ e.m.u./mole. Such a correction gives $C_M=3.01$ and $\theta = -215^\circ\text{K}$. From our value of θ , and assuming just one magnetic exchange interaction, we estimate $J/k=-15^\circ\text{K}$. The data is somewhat complicated at low temperatures but there may be important Van Vleck contributions here or more likely, impurity effects. A localized electron picture seems reasonable and is confirmed by the resistivity data which shows essentially a semiconducting type of behaviour. The low temperature flat region is likely a result of impurity conduction.

When we come to consider the Mössbauer Effect data, however, the picture is distinctly less

encouraging. We might have expected a doublet or a broad singlet plus an impurity peak but the observation of the other doublet is confusing. If we take account of the fact that we had to quench the compound, then we may expect a small amount of B-site iron. If this is where the resolved doublet originates, then in view of the fact that its spectrum shift indicates high spin ferrous iron $\{2\}$, we should expect the compound to be a ferrimagnet, similar to the compounds $\text{Co}[\text{Rh}_{1-x}\text{Cr}_x]\text{S}_4$ $\{113\}$. The estimated low temperature moment would be $\geq 0.4 \mu_B$ /molecule assuming a triangular spin arrangement and taking note that the doublet absorption represents 10% of the total. Two things prevent us from assigning this absorption to low spin iron on B-sites as was the case for Fe_3S_4 . We have mentioned the spectrum shift. For low spin iron, we expect $0.50 \pm .02$ mm/s from table 11. The other feature is that the quadrupole splitting is temperature dependent, something that is never observed for low spin iron. We, therefore, sought other explanations for the origins of this extra doublet.

First, we considered the possibility that the doublet resulted from another impurity phase in addition to that associated with the impurity peak having chemical shift ~ 0.2 mm/s. This places the total impurity content at 20% and makes nonsense of

the magnetization data and probably the conductivity and x-ray data. It is highly unlikely that the observed C_M would be as close to that expected, if the compound had this much impurity. In addition, a comparison may be made between our susceptibilities and those in {111} for $(Cu_{0.5} Fe_{0.5})[Rh_2]S_4$. Table 20 indicates the nature of the comparison.

Table 20. Comparison of the paramagnetic susceptibilities of (A) $(Cu_{0.5} Fe_{0.5})[Rh_2]S_4$ and (B) $Fe[Rh_2]S_4$.

| | A* | B |
|---------------------------------|-----------------------|-----------------------|
| χ_M 300°K (e.m.u./mole.Oe) | 3.24×10^{-3} | 5.95×10^{-3} |
| χ_M 500°K (e.m.u./mole.Oe) | 2.54×10^{-3} | 4.35×10^{-3} |
| effective spin | 1.95** | 2.1*** |

* Calculated from the quoted C_M and θ {111}.

** Neutron diffraction result {111}.

*** Estimated from $C_M=3.3$ and $g=2$.

Although the authors of {111} claim Fe^{3+} rather than Fe^{2+} as the magnetic ion, models do exist that suggest ferrous rather than ferric iron. Their measured effective spin is certainly closer to that expected for ferrous ($S=2$) than for ferric ($S=2.5$) iron. The fact that $\chi(B) \sim 1.75 \chi(A)$, then suggests that our compound is reasonably pure.

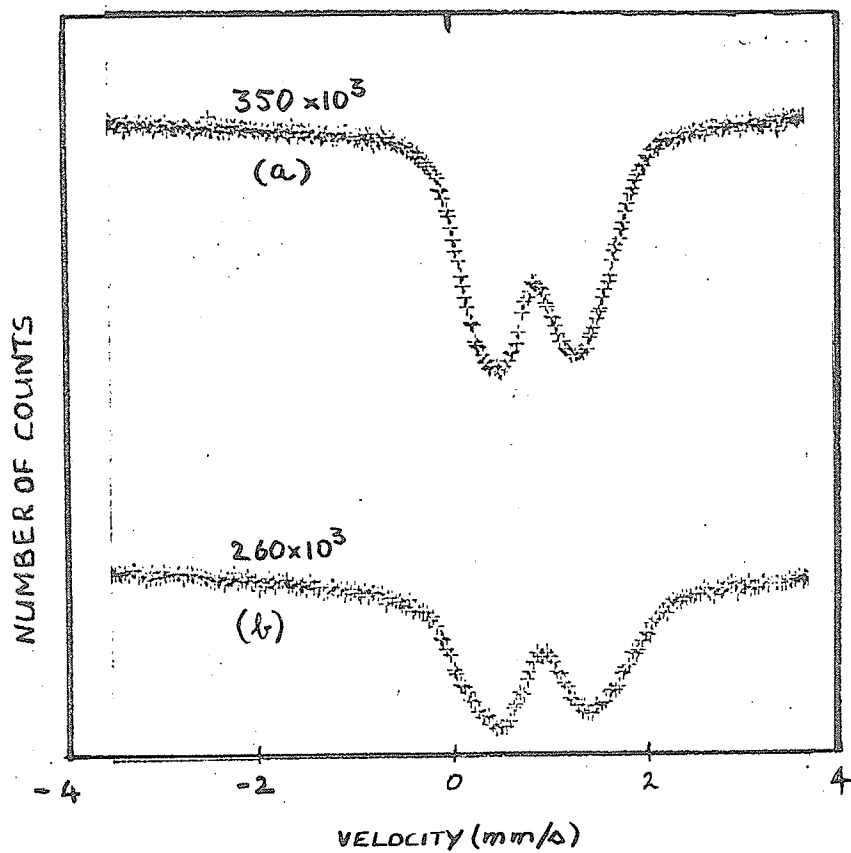


Figure 72. Mössbauer spectra of FeRh_2S_4 after quenching from 1100°K temperatures are:

(a) 77°K

(b) 296°K

The total shift of each spectrum is ~ 0.9 mm/s.

Our second explanation was suggested by the work on FeCr_2O_4 {77,78} where slight shoulders are detected on a broad singlet just above the crystallographic transition temperature. An explanation of this feature was offered in {83} in terms of coherent tunnelling between equivalent J-T distortions. This explanation would be suitable since now all the iron could be assigned to A-sites, a localized picture for the d-electrons would hold and consistency with the magnetization data could be argued. One of the predictions of the theory in {83} is that the four line spectrum that results from the tunnelling effect is symmetrical and we did not find this result. In addition, computer fits to the spectra showed that, below the temperature at which the bulk of the material ordered, there was extra intensity in the central region that must be explained.

Our third and most plausible explanation is based on the observation that the as quenched material does not order magnetically above 77°K. Two spectra from as quenched material are shown in figure 72. We make use of this to explain the extra central intensity below 200°K and argue that an additional doublet may be expected at room temperature.

The extra doublet arises because the

annealing temperature is too low to completely remove all quenched in strain (We may not use much higher temperatures because we know that another phase is formed.). That such random strain can have this effect on A-site Fe^{2+} ions is established in {85}, from a study of $\text{ZnS}_4\text{Fe}^{2+}$ in both the zinc blend and wurtzite structures. There, isomer shifts range from 0.81 mm/s to 0.89 and the quadrupole splitting of doublets superposed on singlets range from 0.56 mm/s to 1.15 mm/s. They find the greatest splittings when pairs of dopants are n.n. separated by an anion as in the wurtzite structure, but the exact origin of the strain is unknown.

With this explanation, we can conclude that the Mössbauer data are in keeping with our other results. We can offer no explanation for the fact that the angle between V_{zz} and H_{hf} changes as the temperature is lowered. It is reasonable to assume that the easy axis of magnetization will be either $\langle 111 \rangle$ or $\langle 100 \rangle$ as is generally found for spinels. The nature of the strain field is a complete unknown. If a situation similar to that in FeCr_2S_4 pertains, then the principal strain axis is roughly $\langle 100 \rangle$ and as such, the easy axis of magnetization would be $\langle 111 \rangle$ just below T_N and rotate towards $\langle 100 \rangle$ as the temperature is lowered below $\sim 100^\circ\text{K}$. It seems more

likely, however, that a more complex situation exists in which the strain field changes with temperature and causes V_{zz} to alter direction.

The type of band scheme we would suggest is sketched in figure 73.

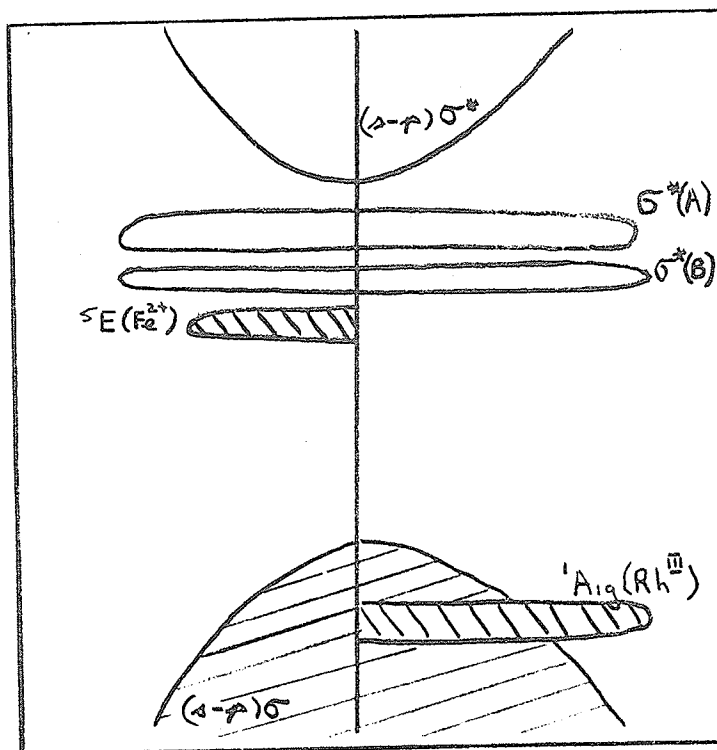


Figure 73. Suggested band scheme for $\text{Fe}\{\text{Rh}_2\}\text{S}_4$.

The positions of the ionic terms are shown. The Rhodium ions are in the low spin ($^1A_{1g}$) state while the iron is in the 5E state. The empty e_g orbitals associated with the B-sites form a σ^* band only 1×10^{-3} eV above the $^5E(\text{Fe}^{2+})$ state. Conduction may be via holes in a Fe^{2+} band or via electrons in the

σ^* band. Since there is a stringent requirement that Rh^{III} remain diamagnetic, any electron excited into σ^* must be accompanied by another with spin antiparallel to the first. This demands that the A-site Fe^{2+} ions be antiferromagnetically coupled because it is the β -spin electron on these ions that is most easily transferred between A and B-sites.

To go over to the $(\text{Fe}_{0.5}\text{Cu}_{0.5})\text{Rh}_2\text{S}_4$, we would take the view that the copper was essentially $2+$ but the t_{2g} orbitals form a σ^* A(Cu) band carrying no magnetic moment. This requires quite a lot of covalent overlap for the copper d-orbitals, nevertheless, since the compound is ordered, ie. one A sublattice is occupied by iron ions, the other by copper, the $^5\text{E}(\text{Fe}^{2+})$ states can still be quite well localized. The same conduction mechanism might hold provided the σ^* A(Cu) band is sufficiently narrow.

4.7 Conclusions.

The properties of this compound would bear further investigation especially if better samples could be prepared. From this investigation, however, we conclude that $\text{Fe}\{\text{Rh}_2\}\text{S}_4$ does exist in the spinel form but there are some difficulties associated with its preparation. The iron occupies the A-sites and from its Mössbauer isomer shift at 296°K , we conclude

that it is in the ferrous state. The compound orders antiferromagnetically at 220°K. The value of $|\theta/T_N| \approx 1$ is consistent with the expectation that the ordering is of the first kind. Above the Néel temperature, the Curie constant is in fair agreement with the spin only value. We note that the ordering temperature is the second highest reported for A-A ordering in the spinel lattice, the highest being 400°K for $\text{Co}\{\text{Rh}_2\}\text{S}_4$, and that the ordering temperature is higher than that of the corresponding ferrimagnet $\text{Fe}\{\text{Cr}_2\}\text{S}_4$.

The magnetic and electrical properties support the idea of a localized electron picture where the β -spin Fe^{2+} electron is most easily transferred to other sites.

It is difficult to analyse the Mössbauer spectra properly; therefore, our values of H_{hf} and $\frac{1}{2}e^2qQ$ below T_N are only approximate. There is evidence that random strain causes local distortions at about 10% of the A-sites so that these sites yield a different Mössbauer spectrum to the rest at all temperatures, eventually ordering independently at or close to 77°K.

We note that the main spectrum at 77°K is remarkably similar to that which we obtained for $\text{Fe}\{\text{Cr}_2\}\text{S}_4$ using a rigid absorber at 4.2°K. This tends to confirm our earlier suspicions that these rigid absorbers were strained by the plastic matrix.

Literature Cited in Chapter III

1. J.M.D. Coey, M.R. Spender and A.H. Morrish, *Solid State Commun.*, 8, 1605, 1970.
2. M.R. Spender, J.M.D. Coey and A.H. Morrish, *Can. J. Phys.*, 50, 2313, 1972.
3. J.C. Ward, *Rev. Pure Appl. Chem.*, 20, 175, 1970.
4. R.C. Erd, H.T. Evans, and D.H. Richter, *Am. Min.*, 42, 309, 1957.
5. D.T. Richard, *Nature*, 218, 356, 1967.
6. J.A. Morice, L.V.C. Rees and D.T. Richard, *J. Inorg. Nucl. Chem.*, 31, 3797, 1969.
7. B.J. Skinner, R.C. Erd and F.S. Grimaldi, *Am. Min.*, 49, 543, 1964.
8. S. Yamaguchi, and T. Katsurai, *Kolloid Z.*, 170, 147, 1960.
9. M. Uda, *Am. Min.*, 50, 1487, 1965.
10. M. Uda, *Z. Anorg. Allgem. Chem.*, 350, 105, 1967.
11. A.M. Freake and D. Tate, *J. Biochem. Microbiol., Technol. Eng.*, 3, 29, 1961.
12. E. Flaig, H.P. Boem and B. Nuber, *Naturwissenschaften*, 54, 515, 1967.
13. R.A. Berner, *J. Geol.*, 72, 293, 1964.
14. R.A. Berner, *Am. J. Sci.*, 265, 773, 1967.
15. D.P. Bobrovnik, *Mineral. Sb.*, 21, 282, 1967.
16. M. Uda, *Sci. Pap. Inst. Phys. Chem. Res.*, 62, 14, 1968.
17. S. Yamaguchi, H. Wada, and H. Nozaki, *J. Phys. C.*, 4, L172, 1971.
18. D.J. Vaughan and M.S. Ridout, *J. Inorg. Nucl. Chem.*, 33, 741, 1971.

19. L.V. Azaroff, Elements of X-ray Crystallography, McGraw Hill, New York, 1968.
20. E.J.W. Verwey and E.L. Heilman, J. Chem. Phys., 15, 174, 1947, 15, 181, 1947.
21. J. Smit and P.J. Wijn, Ferrites, Phillips Tech. Library, Eindhoven, 1957.
22. See for example L.K. Leung, Ph.D. Thesis University Manitoba, 1972.
23. G.A. Sawatzky, F. Van der Woude and A.H. Morrish, Phys. Rev., 183, 383, 1969.
24. E.F. Makardv, A.S. Marfinin, A.R. Mkrtchyan, G.N. Nadzharyan, V.A. Povitskii, and R.A. Stukan, Fiz. Tvr. Tela., 11, 495, 1969. (Eng. Transl. Sov. Phys. Solid State., 11, 391, 1969).
25. N.N. Greenwood and H.J. Whitfield, J. Chem. Soc., A, 1697, 1968.
26. G. Donnay, L.M. Corliss, J.D.H. Donnay, N. Elliot, and J.M. Hastings, Phys. Rev., 112, 1917, 1968.
27. C.M. Yagnik and H.B. Mathur, Solid State Commun., 5, 841, 1967.
28. G.R. Hoy and K.P. Singh, Phys. Rev., 112, 514, 1968.
29. M. Eibschutz, E. Herman and S. Shtrikman, Solid State Commun., 5, 529, 1967.
30. J.B. Goodenough, Progress in Solid State Chemistry, Edited by H. Reiss, Pergamon Press, London, 5, 145, 1971.
31. D.L. Camphausen, J.M.D. Coey and B.K. Chakraverty, Phys. Rev. Lett., 29, 657, 1972.
32. J.B. Goodenough, J. Phys. Chem. Solids, 30, 261, 1969.
33. J.B. Goodenough, Mat. Res. Bull., 6, 967, 1971.
34. R.P. Van Stapele and F.K. Lotgering, J. Appl. Phys., 36, 1088, 1965.
35. J.M.D. Coey and D. Khalafalla, Phys. Status. Solidi., 11a, 229, 1972.

36. L. Néel, *Compt. Rendu (Paris)*, 228, 604, 1949.
37. L. Néel, *Ann. Geophys.*, 5, 99, 1949.
38. A. Aharoni, *Phys. Rev.*, 177, 793, 1969.
39. I.S. Jacobs and C.P. Bean, *Magnetism III*, Edited by G.T. Rado and H. Suhl, Academic Press, New York.
40. W.J. Schwele, S. Shtrikman and D. Treves, *J. Appl. Phys.*, 36, 1010, 1965.
41. F.K. Lotgering, R.P. Van Stapele, G.H.A.M. Van der Steen and J.S. Van Wieringen, *J. Phys. Chem. Solids*, 30, 799, 1969.
42. J.M.D. Coey, Ph.D. Thesis, University of Manitoba, 1971.
43. C. Palache, H. Berman and C. Frondel, *The System of Mineralogy*, John Wiley, New York, 1946.
44. F.K. Lotgering, *Phillips Res. Rep.*, 11, 218, 1956.
45. R.J. Bouchard, P.A. Russo and A. Wold, *Inorg. Chem.*, 4, 685, 1965.
46. M.R. Spender and A.H. Morrish, *Can. J. Phys.*, 49, 2659, 1971.
47. C. Shirane, D.E. Cox and S.J. Pickart, *J. Appl. Phys.*, 35, 954, 1964.
48. P. Gibart and A. Begouen-Demeaux, *C.R. Acad. Sci.*, 268c, 816, 1969.
49. P.F. Bongers, C. Haas, A.M.J.G. Van Run and G. Zanmarchi, *J. Appl. Phys.*, 40, 958, 1970.
50. M. Robbins, R. Wolfe, A.J. Kurtzig, R.C. Sherwood, and M.A. Miksovsky, *J. Appl. Phys.*, 41, 1086, 1970.
51. F.K. Lotgering, R.P. Van Stapele, G.A.M. Van der Steen, and J.S. Van Wieringen, *J. Phys. Chem. Solids*, 30, 799, 1969.
52. P. Gibbart, J.L. Dormann, and Y. Pellerin, *Phys. Stat. Solidi*, 36, 187, 1969.

53. R.P. Van Stapele, J.S. Van Wieringen and P.F. Bongers, *J. de Phys.*, 32, C-53, 1971.
54. M.R. Spender and A.H. Morrish, *Can. J. Phys.*, 50, 1125, 1972.
55. M.R. Spender and A.H. Morrish, *Solid. State. Commun.*, 11, 1417, 1972.
56. M. Ebschutz, S. Shtrikman, and V. Tenebaum, *Phys. Lett.*, 24-A, 563, 1967.
57. A.M. Van Diepen, *Int. Conf. on the Mössbauer Effect.*, Israel, August, 1972.
58. G. Haake and L.C. Beagle (a) *Phys. Rev. Lett.*, 17, 427, 1966;
(b) *J. Phys. Chem. Solids*, 28, 1699, 1967;
(c) *J. Appl. Phys.*, 39, 656, 1968.
59. L. Goldstein and P. Gibbart, *A.I.P. Conference Proceedings, Magnetism and Magnetic Materials*, Edited by C.D. Graham and J.J. Rhyne, 1971, pages 883-886.
60. F.K. Lotgering, *Solid, State. Commun.*, 2, 55, 1964.
61. H.A. Jahn and E. Teller, *Proc. Roy. Soc.*, A-161, 220, 1937.
62. F.S. Ham, *J. de Phys.*, 32, C 1-952, 1971.
63. A. Abragam and M. Pryce, *Proc. Phys. Soc.*, (London), A-63, 409, 1950.
64. F.S. Ham, *Phys. Rev.*, 106, 1195, 1964; *Phys. Rev.*, 166, 307, 1968.
65. J.B. Goodenough, *J. Phys. Chem. Solids*, 25, 151, 1964.
66. R. Engleman, *The Jahn-Teller Effect in Crystals and Molecules*, John Wiley, New York, 1972.
67. G.A. Slack, S. Roberts and F.S. Ham, *Phys. Rev.*, 155, 170, 1967.
68. J.T. Vallin, *Phys. Rev. B.*, 2, 2390, 1970.
69. E.R. Whipple and A. Wold, *J. Inorg. Nucl. Chem.*, 24, 23, 1962.

70. A. Gerrard, P. Imbert, H. Prange, F. Varret and M. Wittenberger, J. Phys. Chem. Solids, 32, 2091, 1971.
71. S.B. Berger and H.L. Pinch, J. Appl. Phys., 38, 942, 1967.
72. P.J. Wojtowicz, Int. Conf. Mag., Nottingham, 1964, pages 11-14.
73. T.A. Kaplan, K. Dwight, D. Lyons and N. Menyuk, J. Appl. Phys., 32, 13S, 1961.
- 74a. M. Koelmans and H.G. Grimmeiss, Physica, 25, 1287, 1959.
b. H.L. Pinch and S.B. Berger, J. Phys. Chem. Solids, 24, 2091, 1968.
75. S. Wittekoek and P.F. Bongers, Solid State Commun., 7, 1719, 1969.
P.K. Larson and Wittekoek, Phys. Rev. Lett., 29, 1597, 1972.
76. C. Haas, Phys. Rev., 168, 531, 1968.
77. P. Imbert and E. Martel, C.R. Acad. Sci. (Paris), 261, 5404, 1965.
78. G.L. Bacchela, P. Imbert, P. Meriel, E. Martel and M. Pinot, Bull. Soc. Sci. (Bretagne), 121, 39, 1964.
79. J.H. Van Vleck, J. Chem. Phys., 7, 72, 1939.
80. F. Van der Woude and A.J. Dekker, Phys State. Solid, 9, 775, 1965.
81. M.J. Clauser, Phys. Rev. B., 3, 3748, 1971.
82. J.A. Tjon and M. Blume, Phys. Rev., 165, 456, 1968.
83. F. Hartman-Boutron, J. de Phys., 29, 47, 1968.
84. M. Blume and J.A. Tjon, Phys. Rev., 165, 446, 1968.
85. A. Gerard, P. Imbert, H. Prange, F. Varret, and M. Witenberger, J. Phys. Chem. Solids, 32, 2091, 1971.
86. R.V. Pound, G.B. Benedeck and R. Drever, Phys. Rev. Lett., 7, 405, 1961.
87. W.R. Walker, G.K. Wertheim and V. Jaccarino, Phys. Rev. Lett., 6, 98, 1961.

88. J. Danon, Lectures on the Mössbauer Effect, Gordon and Breach, New York, 1968.
89. P.K. Baltzer, P.J. Wojtowicz, M. Robbins and E. Lopatin, Phys. Rev., 151, 367, 1966.
90. K. Stegemann, Ph.D. Thesis, Technische Hochschule, Berlin, 1941.
91. P.K. Baltzer, H.W. Lehmann and M. Robbins, Phys. Rev. Lett., 15, 493, 1965.
92. N. Menyuk, K. Dwight, R.J. Arnott and A. Wold, J. Appl. Phys. 37, 1386, 1966.
93. H.W. Lehmann and M. Robbins, J. Appl. Phys. 37, 1387, 1966.
94. H.W. Lehmann, Phys. Rev., 163, 488, 1967.
95. G. Harbeke and H. Pinch, Phys. Rev. Lett., 17, 1090, 1966.
96. G. Busch, P. Junod, and P. Wachter, Phys. Lett., 12, 11, 1964.
97. G. Busch, B. Magyar and P. Wachter, Phys. Lett., 23, 438, 1968.
98. E.F. Stegmeir and G. Harbeke, Phys. Kondens. Materie., 12, 1, 1971.
99. C. Haas, Rev. Solid State Sci., 1, 47, 1970.
100. E. Callen, Phys. Rev. Lett., 20, 1045, 1968.
101. W. Baltensperger and J.S. Helman, Helv. Phys. Acta., 41, 668, 1968.
102. W. Baltensperger, J. App. Phys., 41, 1052, 1970.
103. M. Robbins, M.A. Miksovsky and R.C. Sherwood, J. Appl. Phys., 40, 2466, 1969.
104. J.M.D. Coey, A.H. Morrish and G.A. Sawatzky, J. de Phys., 32, C1-271, 1971.
105. F.K. Lotgering, Proc. Int. Conf. Magnetism, Nottingham, 1964, 533.
106. K. Dwight and N. Menyuk, Phys. Rev., 163, 435, 1967.

107. T.A. Kaplan, Phys. Rev., 116, 888, 1959.
108. G. Blasse, Phys. Lett., 19, 110, 1965.
109. F.K. Lotgering, Solid. State. Commun., 3, 347,
1965.
110. G. Blasse and D.J. Shipper, J. Inorg. Nucl. Chem.,
26, 1467, 1964.
111. F.K. Lotgering and R. Plumier, Solid. State. Commun.,
8, 477, 1970.
112. F.K. Lotgering, Philips, Res. Rep., 11, 190, 1956.
113. F.K. Lotgering, J. Phys. Chem. Solids, 29, 699, 1968.

IV EXPERIMENTAL WORK ON A MIXED SYSTEM.

This chapter describes the investigation we have made of the properties of the mixed crystals $(\text{Cd}_{1-x}\text{Fe}_x)\text{Cr}_2\text{S}_4$. Mixed systems have been studied in our laboratory in the past for they promise, but rarely give, a chance to study the dependence of exchange interactions on cation separation. The reasons why such studies tend to have only partial success are numerous.. For example, changes in covalency may be at least as important as changes in lattice parameter even given that the mixed crystals form very precisely the same crystal structure. Dissimilar cations in the same lattice may produce rather subtle changes that are not obvious from x-ray measurements. For example, differences in crystal anisotropy that lead to superparamagnetism at low

enough dilutions of the magnetic ions or tiny random crystal strains that are difficult to allow for and even distinct changes in spin arrangements. It is probably better to accept that all these possibilities are probabilities and to treat each member of a mixed system as a separate entity. After studying the properties of interest, it may be possible to discern and correlate similarities observed as the system is unravelled. In the opposite approach, the assumption that there will be a systematic variation of properties needs to be justified.

1. THE FAMILY OF COMPOUNDS $\text{Cd}_{1-x}\text{Fe}_x\text{Cr}_2\text{S}_4$.

1.1 Introduction.

This family of compound was investigated rather briefly {1}. The magnetic moments, Curie Constants, Curie-Weiss parameters and ordering temperatures of 3 members were reported. The data was not given in detail; the numbers in table 21 below, were taken from graphical presentations.

Table 21. Magnetization data from reference {1}.

| x | T_C (°K) | θ (°K) | C_M | M_S (μ_B /molecule at 0°K) |
|-----|------------|---------------|-------|-----------------------------------|
| 0.1 | 112 | +150 | 3.7 | 5.4 |
| 0.3 | 130 | +100 | 4.0 | 4.6 |
| 0.7 | 160 | -100 | 5.3 | 2.9 |

The trend of the results is as follows. As the iron content is increased from zero, the ordering temperatures increase and both magnetic moment and Curie Constant decrease. It was also reported there that a complete series of cubic spinels was formed although no lattice parameters were given.

When the compounds are doped with acceptors for example silver, fairly large magneto-resistance effects are observed {1}. The resistance decreases on applying a magnetic field, the ratio $\Delta R/R$ being about ten times that observed in "pure" FeCr_2S_4 .

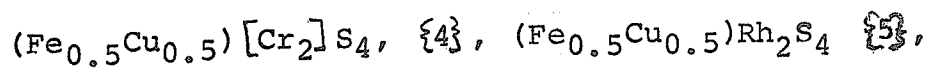
There has also been a Mössbauer Effect study made on one member with $x=0.02$ {2}. A magnetic hyperfine pattern is observed below 96°K and at a low enough temperature $\sim 78^\circ\text{K}$ a quadrupole splitting appears. This latter result has been explained using the magnetically induced field gradient discussed earlier and in appendix C.

Our own magnetization study {3} included a greater number of members and forms the first part of this chapter.

1.2 Preparation.

All the compounds for this study were prepared in the manner described in Chapter 1, section 5. Debye-Sherrer x-ray powder diffraction patterns were

obtained for all of the compounds using manganese filtered $\text{FeK}\alpha$ radiation at room temperature. All the reflections obtained could be indexed on the basis of a spinel structure with no extra lines. The high angle reflections were very well defined with good resolution between the $\text{FeK}\alpha_1$, and $\text{K}\alpha_2$ wavelengths. We, therefore, feel confident that the purity of the samples is better than 99%, that the samples are homogeneous and tolerably strain free. The patterns obtained are given in tables 23 and 24, together with the indices assigned. To save space and tedious references of the form, the member with $x=.5$ or the compound $\text{Cd}_{0.9}\text{Fe}_{0.1}\text{Cr}_2\text{S}_4$ etc., a simple code has been introduced as shown in table 22. Consideration of tables 23 and 24 shows that the compounds certainly have the spinel structure and, in view of the heat treatment given to them, there is every reason to believe that the cation distribution will be the expected one, ie. only chromium on the B-sites and iron or cadmium on the A-sites. In addition, it is possible that CD50 has a 1:1 ordering of Fe^{2+} and Cd^{2+} ions on the A-sites. This would be in keeping with results from similar spinels, eg.



and $(\text{In}_{0.5}\text{Cu}_{0.5})[\text{Cr}_2]\text{S}_4, \{4\}$. Although we inspected

Table 22. Magnetic and crystallographic data for members of the family $(\text{Cd}_{1-x}\text{Fe}_x)\text{Cr}_2\text{S}_4$.

| x (Nominal) | Code | Lattice Parameter (Å) | M_B^S (μ_B /molecule) | M_∞ | C_M^* | θ (°K) | Ordering Temperature (°K) |
|------------------|------|-----------------------------|---------------------------------|------------|---------|------------------|---------------------------------|
| 0.05 | CD95 | 10.232 | 5.62 | 5.91 | 3.87 | 130 | 96 |
| 0.10 | CD90 | 10.222 | 5.20 | 5.83 | 3.98 | 127 | 108 |
| 0.20 | CD80 | 10.195 | 4.70 | 5.40 | 4.00 | 117 | 123 |
| 0.40 | CD60 | 10.141 | 3.51 | 4.16 | 4.08 | 60 | 132 |
| 0.50 | CD50 | 10.120 | 3.35 | 3.75 | 4.76 | -70 | 140 |
| 0.80 | CD20 | 10.050 | 2.16 | 2.66 | 5.79 | -134 | 160 |
| 0.90 | CD10 | 10.023 | 1.72 | 2.06 | 6.06 | -223 | 165 |

*The values of C_M and θ in the case of CD50 have been changed from those given in {4} as a result of extra, high temperature, data.

the x-ray diffraction pattern for the reflection corresponding to the (4,2,0) superstructure reflection expected for such ordering, we were unable to find it. The x-ray scattering powers of iron and cadmium should be far enough apart to allow the reflection to show up but possibly the ordering is incomplete. In table 22 we collect together the lattice parameters determined from the photographs and show them graphically in figure 74. It may be seen that a linear dependence on composition exists. The solid line joins the parameters for the two end members of the series CdCr_2S_4 and FeCr_2S_4 . There is obviously something that may be said about the

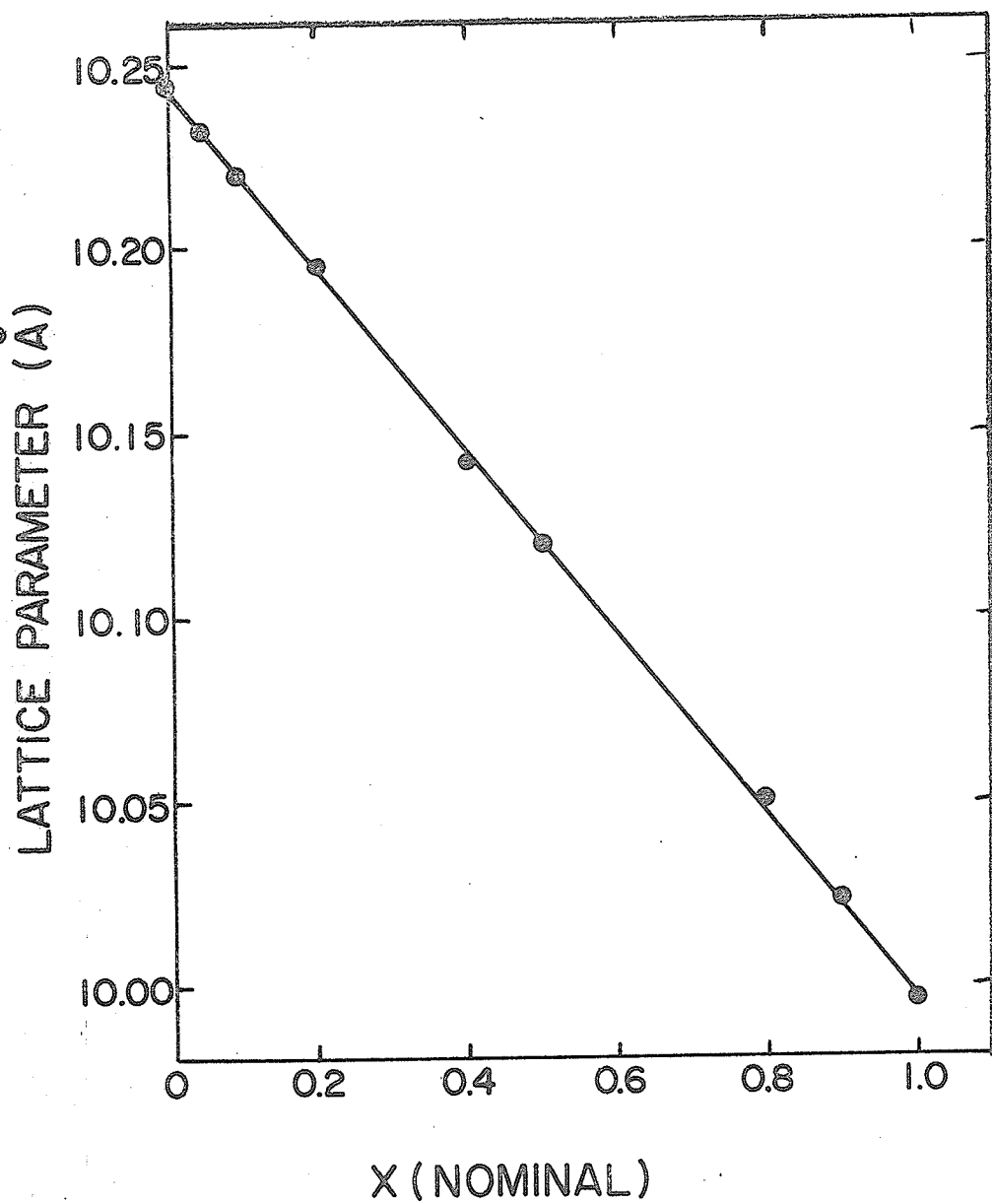


Figure 74. Compositional dependence of the lattice parameters of members of the family $\text{Cd}_{1-x}\text{Fe}_x\text{Cr}_2\text{S}_4$.

Table 23. X-ray powder diffraction patterns for four members of the family $Cd_{1-x}Fe_xCr_2S_4$.

| hkl (Spinel) | CD95 | | CD90 | | CD80 | | CD60 | |
|-----------------|-------------|-------------|-------------|-------------|-------------|-------------|-------------|-------------|
| | dobs (Å) | dcal (Å) | dobs (Å) | dcal (Å) | dobs (Å) | dcal (Å) | dobs (Å) | dcal (Å) |
| 111 | | | | | | | | |
| 220 | 3.61 | 3.618 | 3.60 | 3.614 | 3.57 | 3.605 | 3.57 | 3.586 |
| 311 | 3.09 | 3.085 | 3.09 | 3.081 | 3.05 | 3.074 | 3.04 | 3.057 |
| 222 | | | | | | | | |
| 400 | 2.55 | 2.558 | 2.55 | 2.555 | 2.53 | 2.548 | 2.53 | 2.535 |
| 331 | 2.35 | 2.347 | 2.34 | 2.344 | 2.33 | 2.339 | 2.31 | 2.326 |
| 422 | 2.09 | 2.089 | 2.09 | 2.086 | 2.07 | 2.081 | 2.07 | 2.070 |
| 333,511 | 1.97 | 1.969 | 1.97 | 1.967 | 1.95 | 1.962 | 1.95 | 1.952 |
| 400 | 1.81 | 1.809 | 1.809 | 1.807 | 1.793 | 1.802 | 1.791 | 1.792 |
| 442 | | | | | | | | |
| 531 | | | | | | | | |
| 620 | 1.62 | 1.618 | 1.62 | 1.616 | 1.61 | 1.612 | 1.606 | 1.603 |
| 533,731 | 1.56 | 1.560 | 1.56 | 1.558 | | | | |
| 622 | | | | | | | | |
| 444 | | | | | 1.47 | 1.471 | 1.463 | 1.464 |
| 711,511 | | | | | | | | |
| 642 | 1.37 | 1.367 | 1.367 | 1.366 | 1.360 | 1.362 | 1.356 | 1.355 |
| 731,553 | 1.335 | 1.332 | 1.330 | 1.330 | 1.326 | 1.327 | 1.321 | 1.320 |
| 800 | 1.281 | 1.279 | 1.280 | 1.278 | 1.273 | 1.274 | 1.269 | 1.269 |
| 733 | 1.252 | 1.250 | 1.250 | 1.249 | 1.244 | 1.245 | 1.239 | 1.238 |
| 644 | | | | | | | | |
| 822,660 | 1.208 | 1.206 | 1.206 | 1.204 | 1.200 | 1.201 | 1.197 | 1.195 |
| 751,555 | 1.182 | 1.181 | 1.181 | 1.180 | 1.176 | 1.177 | 1.173 | 1.171 |
| 662 | | | | | | | | |
| 840 | | | | | 1.1397 | 1.1398 | 1.136 | 1.134 |
| 753,911 | | | | | 1.1185 | 1.1191 | 1.115 | 1.113 |
| 842 | | | | | | | | |
| 664 | | | | | 1.0871 | 1.0868 | | |
| 931 | 1.071 | 1.072 | 1.069 | 1.071 | 1.0682 | 1.0687 | 1.0617 | 1.0604 |
| 844 | 1.045 | 1.033 | 1.0415 | 1.0395 | 1.0405 | 1.0405 | 1.0341 | 1.0343 |
| 1020,862 | 1.004 | 1.003 | 1.0015 | 1.0019 | 0.9998 | 0.9995 | 0.9944 | 0.9942 |
| 773,951 | 0.9899 | 0.9896 | 0.9871 | 0.9884 | 0.9857 | 0.9859 | 0.9807 | 0.9807 |

Table 24. X-ray diffraction patterns for three members of the family $\text{Cd}_{1-x}\text{Fe}_x\text{Cr}_2\text{S}_4$.

| hkl (Spinel) | CD50 | | CD20 | | CD10 | |
|-----------------|-------------------------|-------------------------|-------------------------|-------------------------|-------------------------|-------------------------|
| | d _{obs} (Å) | d _{cal} (Å) | d _{obs} (Å) | d _{cal} (Å) | d _{obs} (Å) | d _{cal} (Å) |
| 111 | | | | | 5.80 | 5.786 |
| 220 | 3.57 | 3.578 | 3.53 | 3.554 | 3.54 | 3.544 |
| 311 | 3.05 | 3.051 | 3.01 | 3.030 | 3.02 | 3.021 |
| 222 | | | | | | |
| 400 | 2.53 | 2.530 | 2.50 | 2.513 | 2.50 | 2.506 |
| 331 | 2.31 | 2.320 | | | 2.34 | 2.299 |
| 422 | 2.06 | 2.065 | 2.05 | 2.051 | 2.04 | 2.045 |
| 333,511 | 1.949 | 1.948 | 1.93 | 1.934 | 1.93 | 1.929 |
| 440 | 1.780 | 1.789 | 1.775 | 1.776 | 1.77 | 1.772 |
| 442 | | | | | | |
| 531 | | | | | | |
| 620 | 1.595 | 1.600 | 1.587 | 1.589 | | |
| 533,731 | 1.540 | 1.543 | 1.534 | 1.533 | | |
| 622 | | | | | | |
| 444 | 1.457 | 1.461 | 1.447 | 1.451 | 1.446 | 1.447 |
| 711,551 | | | | | | |
| 642 | 1.350 | 1.352 | 1.344 | 1.343 | 1.339 | 1.339 |
| 731,553 | 1.316 | 1.316 | 1.308 | 1.308 | 1.305 | 1.305 |
| 800 | 1.265 | 1.265 | 1.257 | 1.256 | 1.254 | 1.253 |
| 733 | 1.236 | 1.236 | | | | |
| 644 | | | | | | |
| 822,660 | 1.193 | 1.193 | 1.185 | 1.184 | 1.180 | 1.181 |
| 751,555 | 1.167 | 1.168 | 1.160 | 1.160 | 1.158 | 1.157 |
| 662 | | | | | | |
| 840 | 1.130 | 1.131 | 1.124 | 1.124 | 1.120 | 1.121 |
| 753,911 | | | | | | |
| 842 | | | | | | |
| 664 | | | | | | |
| 931 | 1.061 | 1.061 | 10.53 | 1.053 | 1.051 | 1.051 |
| 844 | 1.033 | 1.033 | 1.0254 | 1.0257 | 1.023 | 1.023 |
| 1020,862 | 0.993 | 0.992 | 0.9853 | 0.9853 | 0.9826 | 0.9826 |
| 773,951 | 0.978 | 0.978 | 0.9715 | 0.9719 | 0.9693 | 0.9693 |

packing of the atoms under the circumstances. Clearly, even in FeCr_2S_4 , the sulphur lattice is far from being close packed so that gradual substitution of the iron by cadmium causes a smooth continuous expansion. Based purely on volume considerations, we may expect a steady decrease in d-electron covalency in the A-sites. By the same token, B-site covalency should also decrease so that any $\sigma^*(B)$ band ought to be narrower at the cadmium rich end of the series than in FeCr_2S_4 .

1.3 Magnetization Measurements.

We used the equipment and techniques described earlier to measure M_s , M_o and H_c at 4.2°K . We also determined the temperature dependence of M_s . The susceptibility above the ordering temperatures was also measured as a function of temperature. The main results are collected in table 22. The various data are shown graphically in the next dozen or so figures.

In figures 75 and 76, the magnetic moments of the compounds are shown as functions of temperature. So far as we can tell, the amount of short range order in the mixed crystals is very much less than in the "pure" CdCr_2S_4 . Members with $x > 0.5$ show anomalous magnetization curves similar to that observed in FeCr_2S_4 .

Figure 77 shows the temperature dependence of the inverse susceptibilities for the members studied.

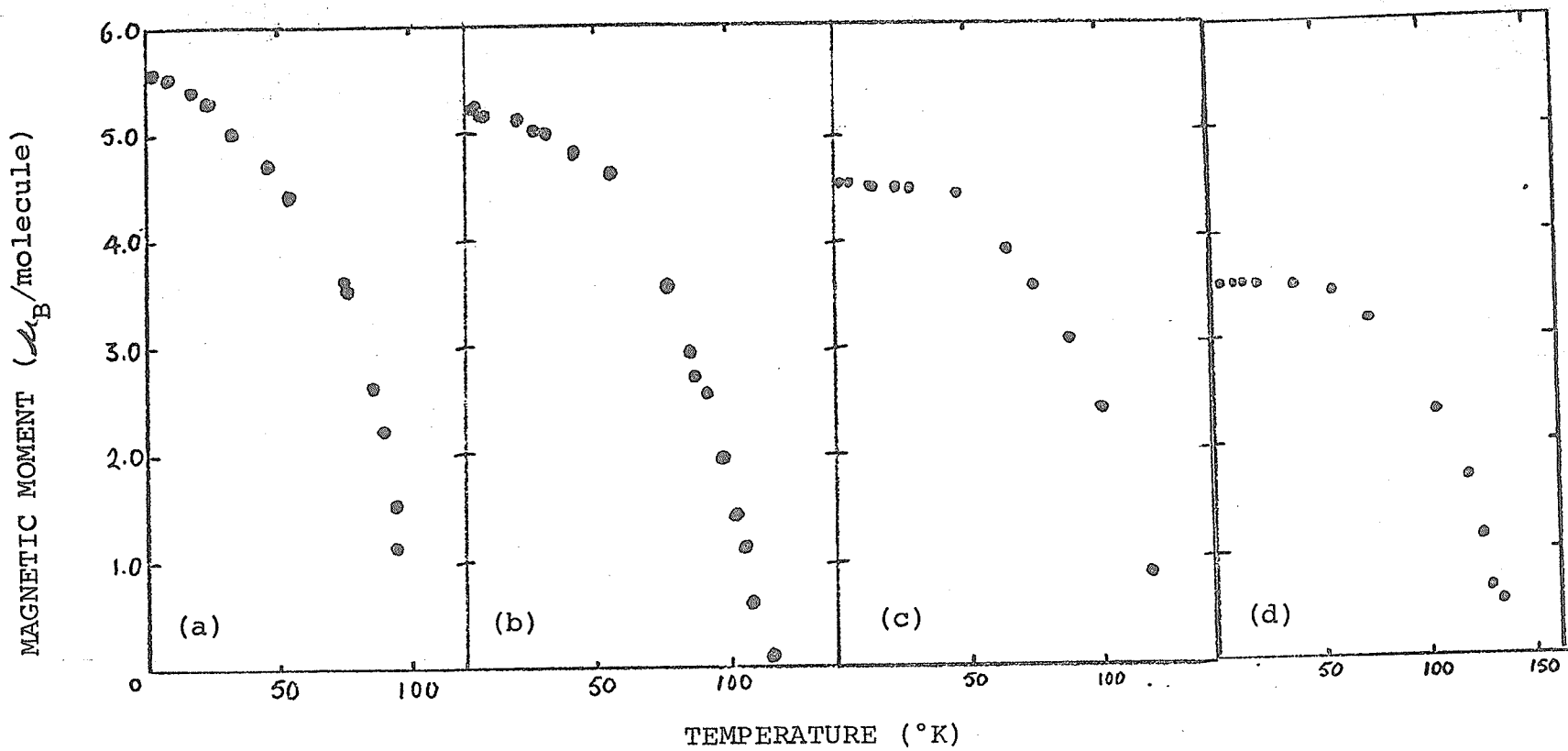


Figure 75. Magnetic moments of (a) CD95 (b) CD90 (c) CD80 (d) CD60 as a function of temperature.

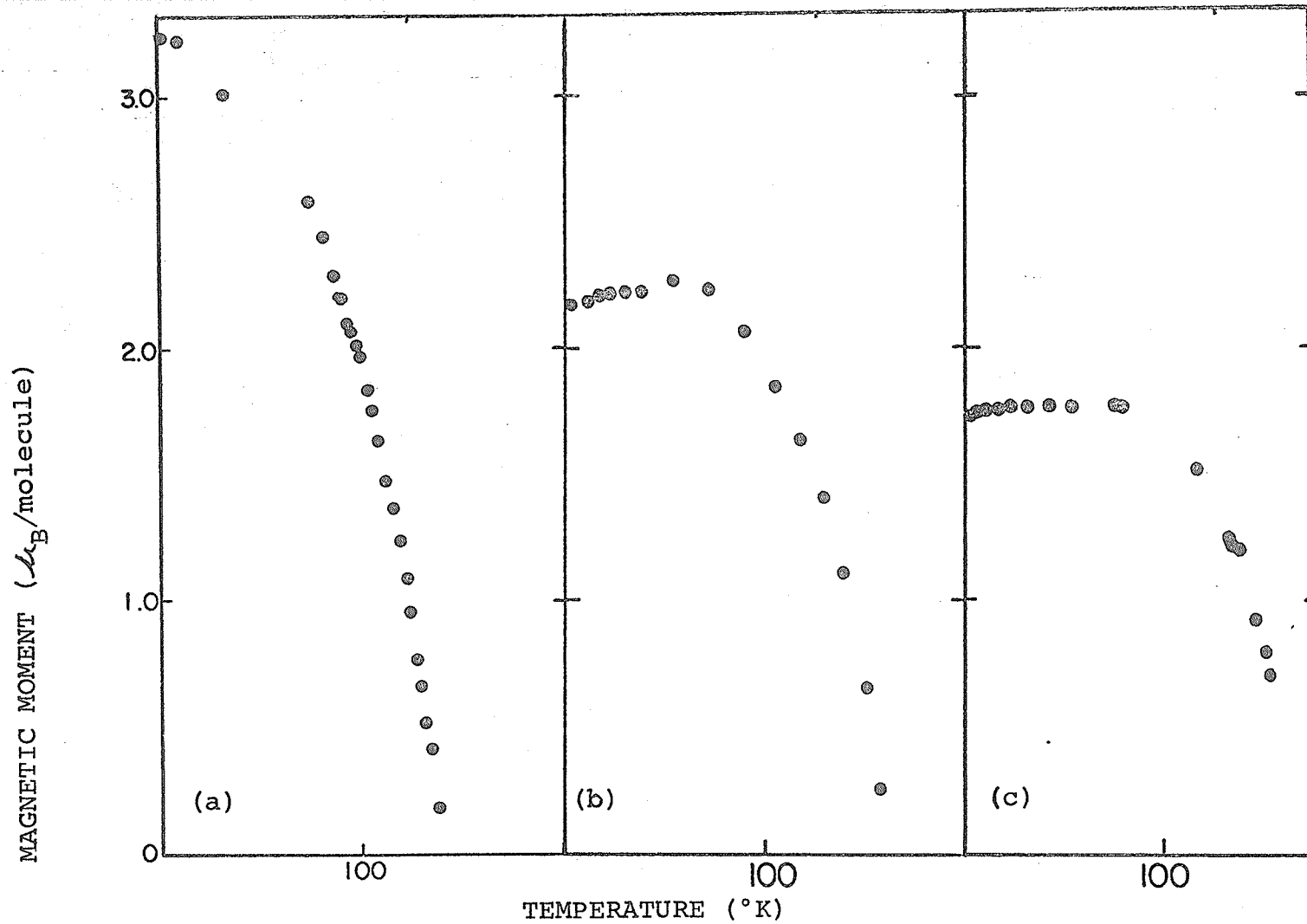


Figure 76. Magnetic moments of (a) CD50 (b) CD20 (c) CD10 as a function of temperature.

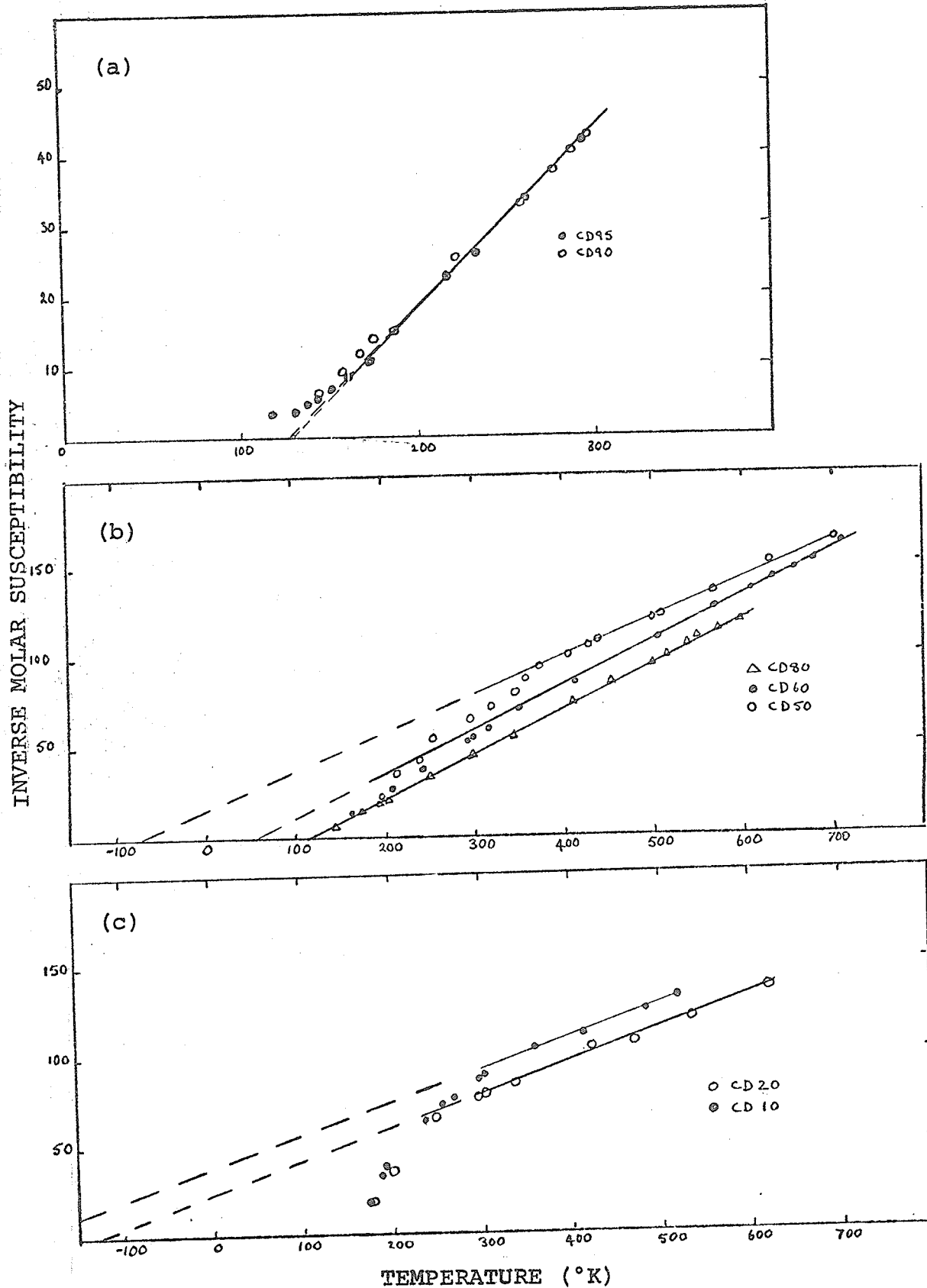


Figure 77. Inverse molar susceptibility of (a) CD95 and CD90 (b) CD80, CD60, CD50 and (c) CD20 and CD10 as a function of temperature.

It may be seen that beginning at the Cd rich end, the χ_M^{-1} -T plots are concave downwards, become linear at $x \sim 0.2$ and are then concave upwards for $x \geq 0.5$.

Figure 78a shows the compositional dependence of the ordering temperatures. These were estimated from the steeply falling parts of the magnetization curves and errors of $\pm 4^\circ\text{K}$ are given. We note that the ordering temperature increases rapidly with x at first and then more slowly. The dependence of θ on x is rather different. The data are shown in figure 78b. It may be seen that θ falls slowly with increasing x until $x \sim 0.4$ and then there is a very sudden change and θ changes sign. The errors on θ rather depend on the shape of the susceptibility curve, for curves that are concave upwards, the error is $\pm 20^\circ\text{K}$.

Figure 78c shows the compositional variation of M_S and M_∞ . The solid line I shows the spin only result expected for ferrimagnetic alignment of Fe^{2+} (A-site) and Cr^{3+} (B-site) ions, while line II indicates the result expected if our result for FeCr_2S_4 gives correctly the Fe^{2+} moment in such compounds. Neither line properly fits to all the data but it should be noted that M_∞ is larger than the spin only result for CD95, CD90 and CD80. Finally, figure 78d shows

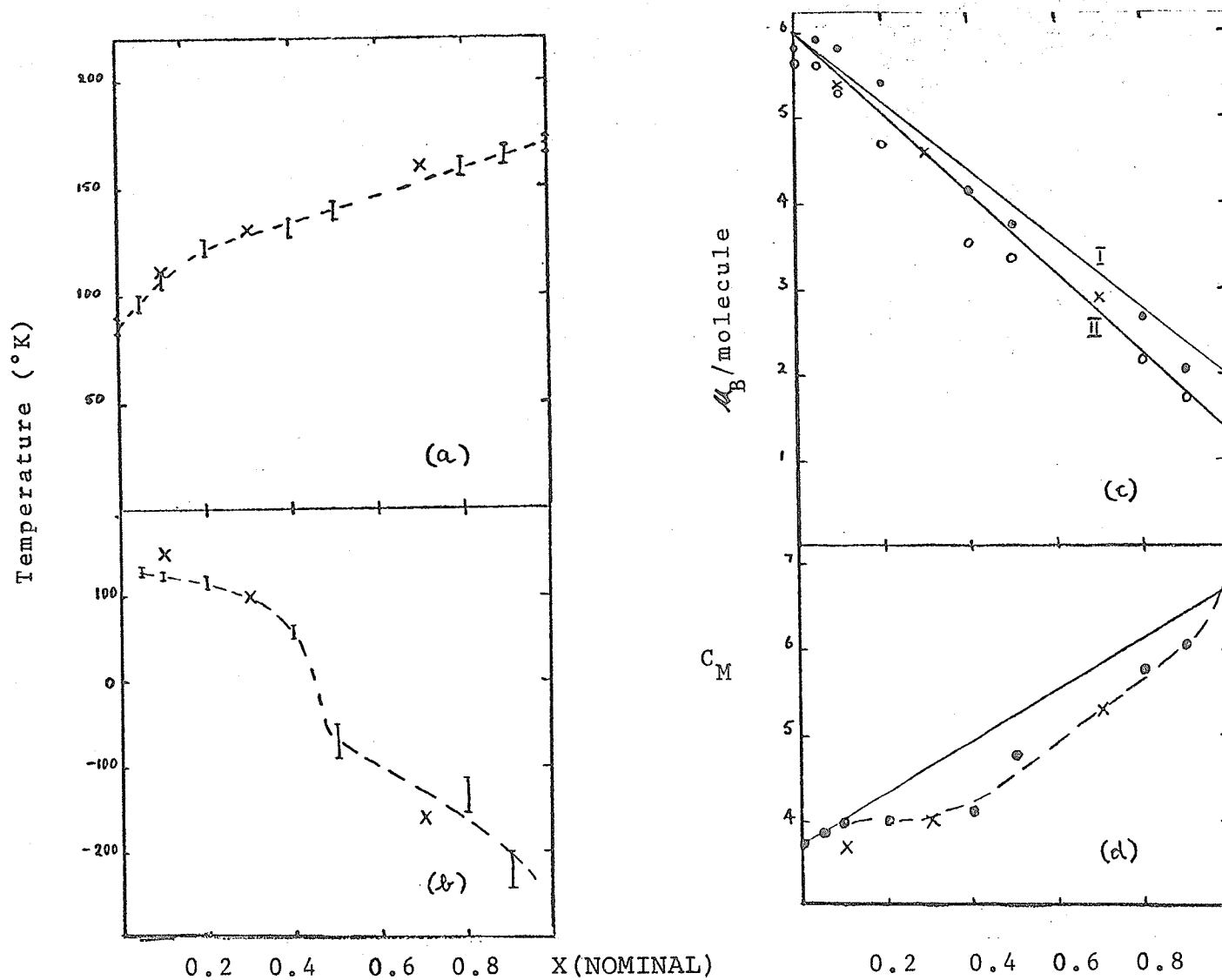


Figure 78. Compositional dependence of (a) Ordering temperatures (b) Curie-Weiss parameters (c) Magnetic moments and (d) Curie constants for members of the family $\text{Cd}_{1-x}\text{Fe}_x\text{Cr}_2\text{S}_4$.

the variation with x of the molar Curie Constants. The solid line indicates the spin only result from which there is a clear departure.

Although some general trends are evident in the data the most striking feature is that the magnetic properties do not vary in a systematic fashion. In fact, three distinct regions exist; a region $0 < x < 0.2$ where $M_s \sim$ spin only value, $M_w \sim$ spin only value and $C_M \sim$ spin only value; a region $0.7 < x < 1$ where the data are reasonably extrapolated from data on FeCr_2S_4 ; and a central region $0.2 < x < 0.7$ where there are obviously some very peculiar effects. In figure 78, the data indicated by crosses are from reference {1}.

1.4 Electrical Measurements.

We made conductivity and magneto-resistance measurements on CD90, CD80, CD60, CD50, CD20 and CD10. It may be seen from the data in figure 79a,b,c,d,e,f that all the compounds show semi-conducting characteristics i.e. the resistivity increases with decreasing temperature. Figure 80 shows results of magneto-resistance measurements in a field of 10 kOe, it may be seen that all compounds exhibit negative magneto-resistance with maxima close to the ordering temperatures, CD90 shows the largest magneto-resistance effect. Table 25,

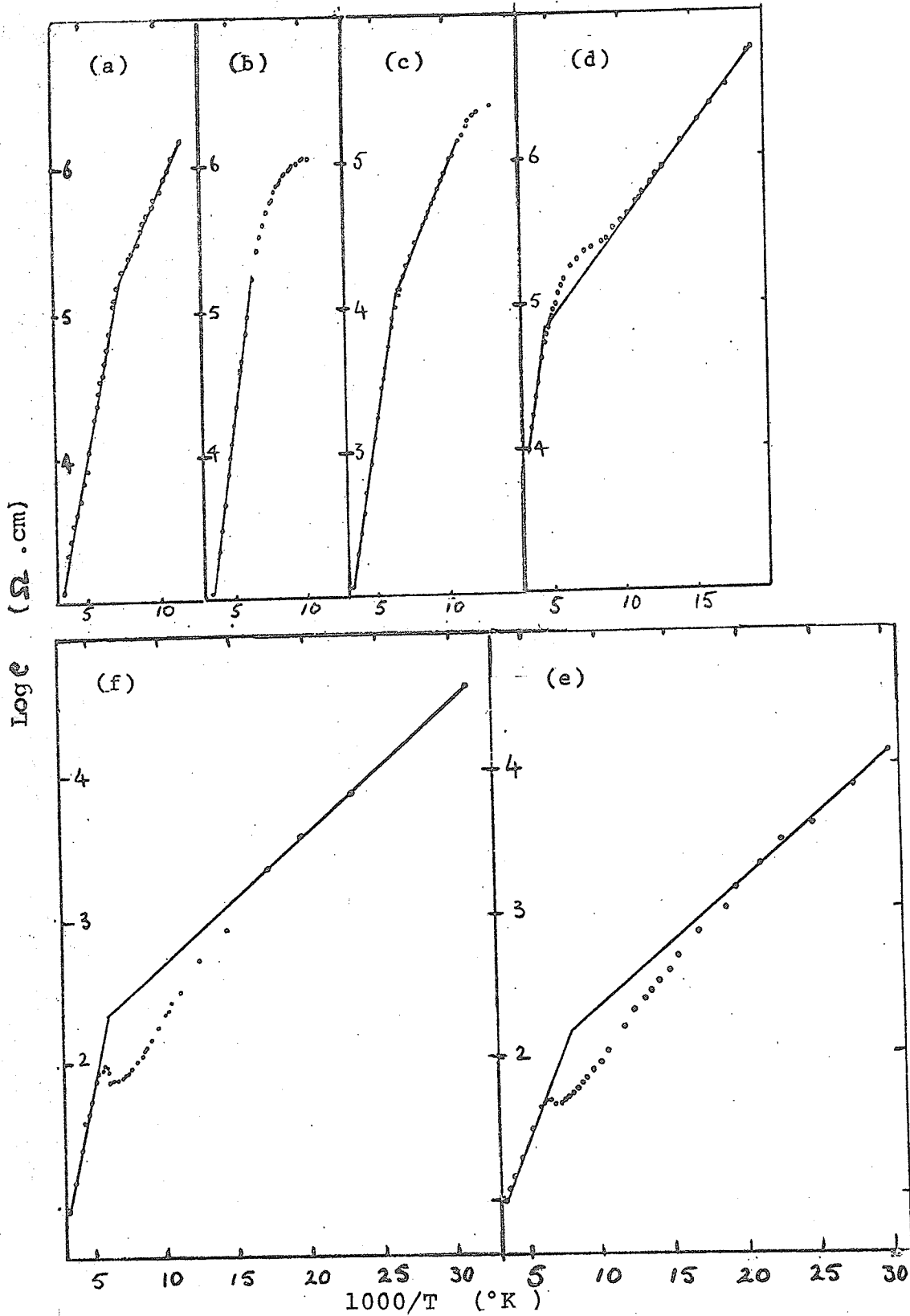


Figure 79. Temperature dependence of the resistivity of (a) CD90 (b) CD80 (c) CD60 (d) CD50 (f) CD20 (e) CD10.

collects the room temperature resistivities and the high and low temperature energy gaps that may be deduced from the data.

Table 25. Resistivity data from some members of the family $\text{Cd}_{1-x}\text{Cr}_2\text{S}_4$.

| x | (296°K) (Ω .cm) | Energy Gap $T > T_c$ (eV) | ($T < T_c$) (eV) | Density % Theoretical |
|-----|----------------------------|------------------------------|--------------------|--------------------------|
| 0.1 | 1.34×10^3 | 0.200 | 0.086 | 94.9 |
| 0.2 | 1.12×10^3 | 0.306 | - | 96.3 |
| 0.4 | 1.16×10^2 | 0.250 | 0.096 | 96.1 |
| 0.5 | 9.67×10^3 | 0.266 | 0.050 | 95.3 |
| 0.8 | 9.76 | 0.100 | 0.034 | 95.4 |
| 0.9 | 9.36 | 0.190 | 0.04 | 95.7 |

Apart from CD50, the resistivities fall as x is increased; this would be expected since CdCr_2S_4 is an almost insulating ($\rho(296^\circ\text{K}) \sim 10^4$) and FeCr_2S_4 is a semi-conductor with $\rho(296^\circ\text{K}) \sim 10 \Omega$.cm. At the mid-way composition, however, the resistivity is nearly an order of magnitude higher than that of CD90. The densities of these samples are comparable, so we conclude that this result is evidence of cation ordering on the A-sites as is found in $(\text{Cu}_{0.5}\text{Fe}_{0.5})[\text{Cr}_2]\text{S}_4$.

All the compounds show some change in the slope of the $\log \rho - T$ curve. The changes are not, in general, simple in character.

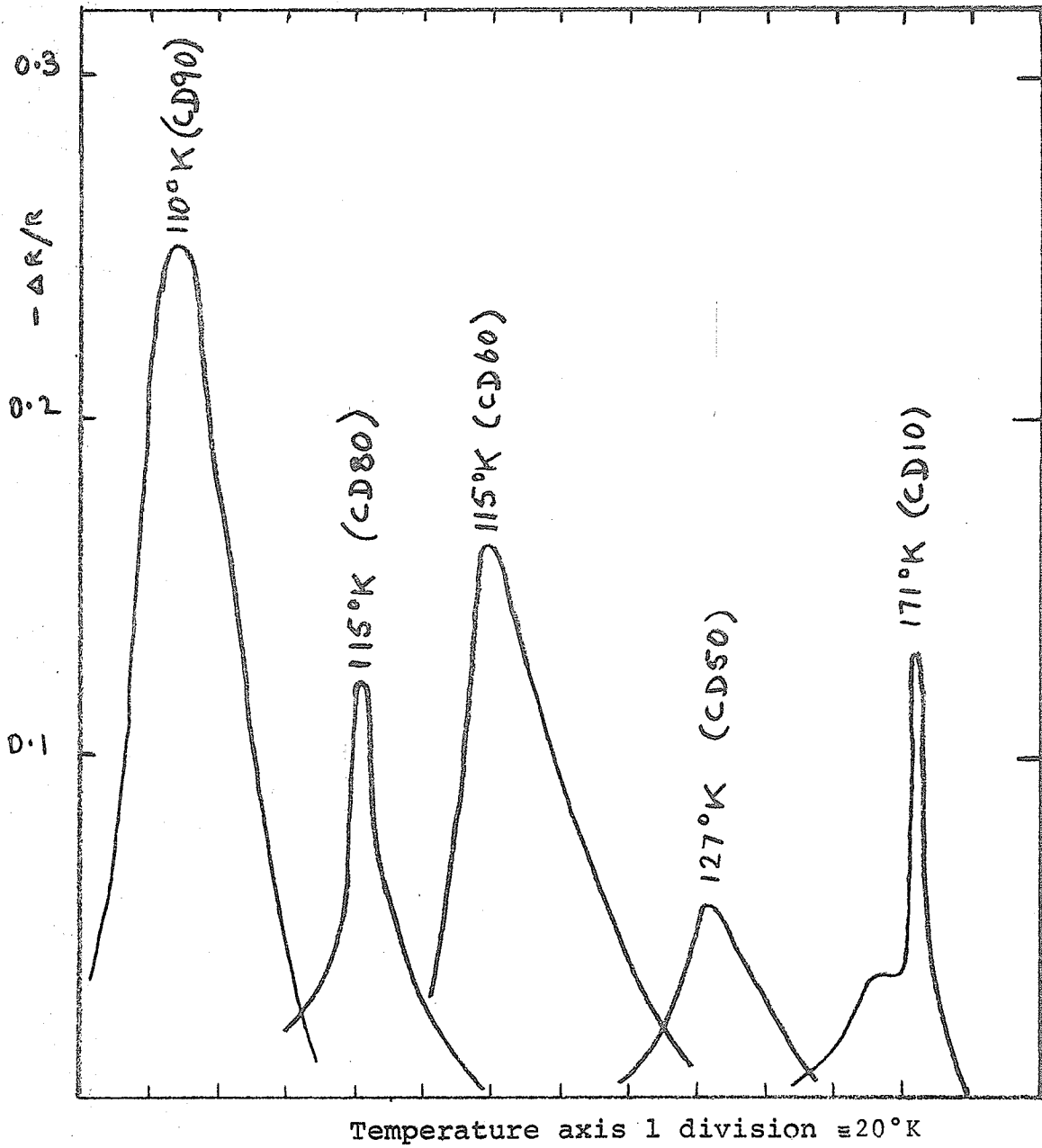


Figure 80. Magneto-resistance of several members of the family $\text{Cd}_{1-x}\text{Fe}_x\text{Cr}_2\text{S}_4$ in a 10 kOe field.

For CD10 and CD20, the behaviour is similar to that observed in FeCr_2S_4 . In CD50 $\log \rho$ rises above the predictions of equation (II.20) which are represented by the solid lines in figure 79. In CD90, we obtain a simple magnetic semiconductor result, the break in the slope occurs at 133°K , 25°K above the magnetic ordering temperature. Departure from the high temperature linear behaviour occurs above the ordering temperatures for all the compounds with closest agreement in the iron rich members.

Once again three distinct regions in the compositional range may be distinguished. The resistivity decreases as x is increased from zero until $x \sim 0.4$. On the other hand, ρ also decreases as x is decreased from ~ 1.0 and there, therefore, exists a central region where ρ increases again as x is increased from ~ 0.7 . The member with $x=0.5$ is clearly a special case. The behaviour of the whole system mirrors that observed in $\text{Cu}_{1-x}\text{Fe}_x\text{Cr}_2\text{S}_4$ but we shall return to this later.

1.5 Mössbauer Effect Investigation.

This part of our study turned out to be most difficult. The main reason for this was that the Mössbauer spectra appeared to us to be very complex. We shall deal with three regions of the

composition range, present the spectra and, where possible, the data extracted.

- (i) This region is the cadmium rich end of the series exemplified by CD95 and CD90;
- (ii) This region is the iron rich end exemplified by CD20 and CD10;
- (iii) The central region exemplified by CD50.

1.5.1 The cadmium rich region.

Sets of spectra covering the entire temperature range investigated are shown for CD95 and CD90 in figure 81. In both compounds there is evidence of a quadrupole interaction above the ordering temperatures. The doublets are not well resolved in CD95 but the lines are far too broad to be singlets. Just below the ordering temperatures, however, the spectra appear to be six line patterns with no quadrupole interaction.

It is very difficult to envisage a situation where an E.F.G. exists at one temperature then disappears only to reappear again when T approaches 77°K . Our conclusion is that the E.F.G. exists at all temperatures and it is only the quadrupole shift of the spectra that vanishes for $T \sim T_M$. (We shall use T_M to mean magnetic ordering temperature since we do

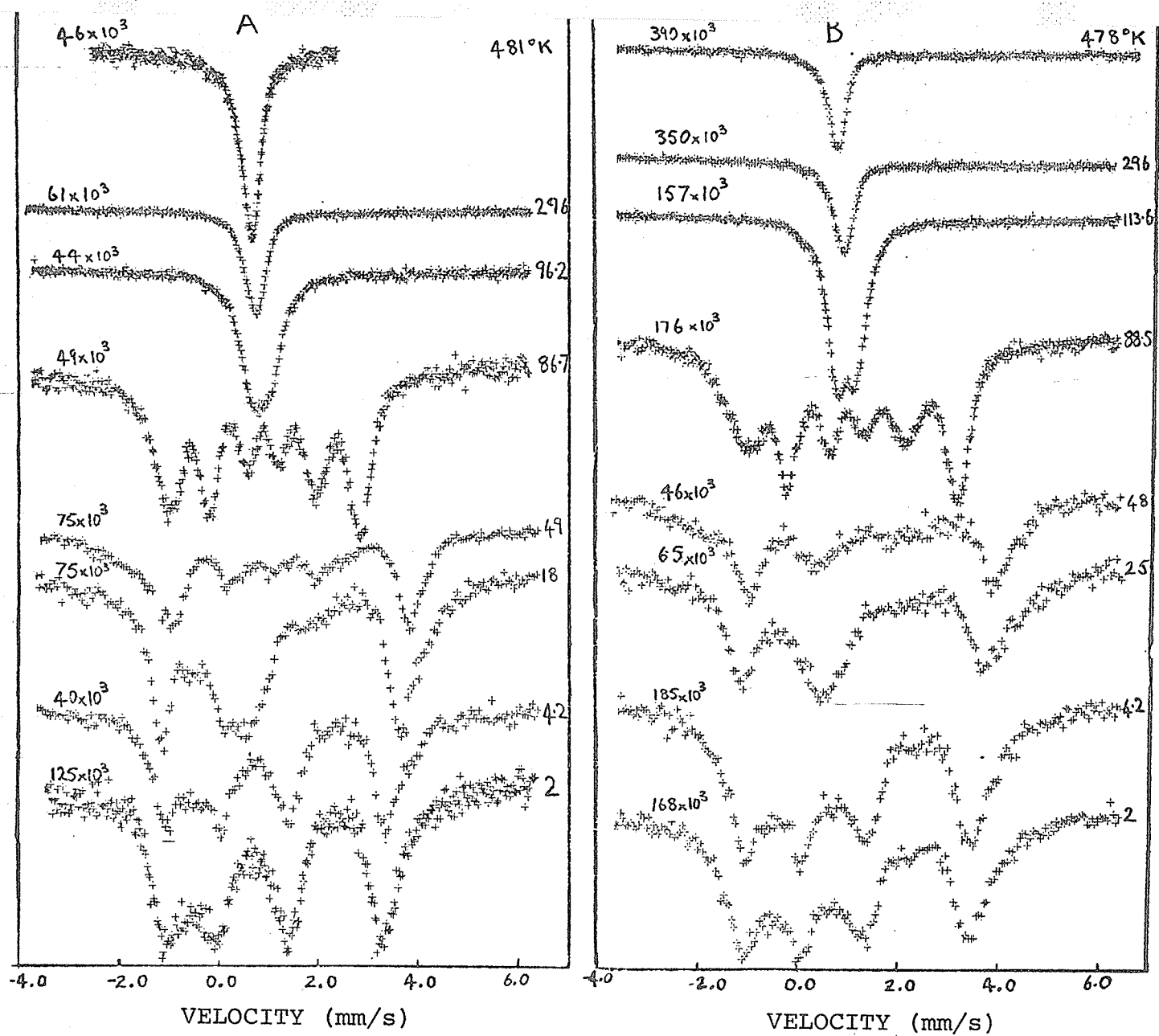


Figure 81. Mössbauer spectra of (A) CD95 and (B) CD90 at various temperatures.

not wish to categorise the compounds at this stage.)

In the case of CD95, we fitted the spectra $T > T_M$ with a single line and in figure 82, the temperature dependence of $1/3$ the line width is shown. Also shown in that figure is the observed quadrupole splitting for CD90 $T_M < T < 150^\circ\text{K}$ but for $T > 150^\circ\text{K}$, $1/3$ the observed line width is plotted. The spectra below T_M gave immense difficulty, not because they cannot be fitted but because they cannot be fitted in a manner that might be considered physically meaningful.

We already know that interactions between A-sites can be quite strong, stronger in fact than the net interaction between B-site ions. Most of the magnetic A-sites in these "dilute" compounds have 4 cadmium n.n. A-site ions, but an appreciable proportion have 1 or more magnetic A-site n.n., assuming a random A-site distribution of Cd and Fe. The actual numbers are given in table 26. This variety of environments may give slight differences in $\frac{1}{2}e^2qQ$ and H_{hf} and, therefore, to differences in the ratio:

$$\frac{1}{2}e^2qQ/g_{\frac{1}{2}}\beta H_{hf}$$

The shape of the spectrum is extremely sensitive to this ratio. The superposed spectra are not well resolved so although the correct way to fit the spectra might be to fit the several spectra in their correct probabilities, the results are somewhat less than

convincing. We adopted a pragmatic approach in which the observed peaks were taken as averages and we found the set of parameters H_{hf} , $\frac{1}{2}e^2qQ$, θ , ϕ , η , and δ_t that best gave the observed peak positions. As an additional criterion, we demanded that $\frac{1}{2}e^2qQ$ be continuous through the magnetic transition. This yields the rest of the data $T < T_M$ in figure 82. At the lowest temperatures achieved these difficulties vanish, as may be seen in the spectra of figure 81. At 4.2 and 1.6°K, the spectra are reasonable and can be fitted quite easily with $\frac{1}{2}e^2qQ=3.0$ mm/s $\theta=0^\circ$ $\phi=0^\circ$ $\eta=0$. In the case of the unresolved doublets, we took 1/3 the line width because this was roughly the ratio between line width and observed splitting in the CD90 paramagnetic spectra below 150°K.

Table 26. Probability P(N) of N nearest neighbour magnetic A-site ions for various x, assuming random distributions.

| N \ x | P(N) for various x | | | | |
|-------|--------------------|-------|-------|-------|-------|
| | 0.05 | 0.1 | 0.5 | 0.8 | 0.9 |
| 0 | 0.815 | 0.656 | 0.063 | 0.002 | 0.000 |
| 1 | 0.172 | 0.292 | 0.250 | 0.025 | 0.003 |
| 2 | 0.013 | 0.049 | 0.375 | 0.153 | 0.049 |
| 3 | 0.000 | 0.003 | 0.250 | 0.41 | 0.292 |
| 4 | 0.000 | 0.000 | 0.063 | 0.41 | 0.656 |

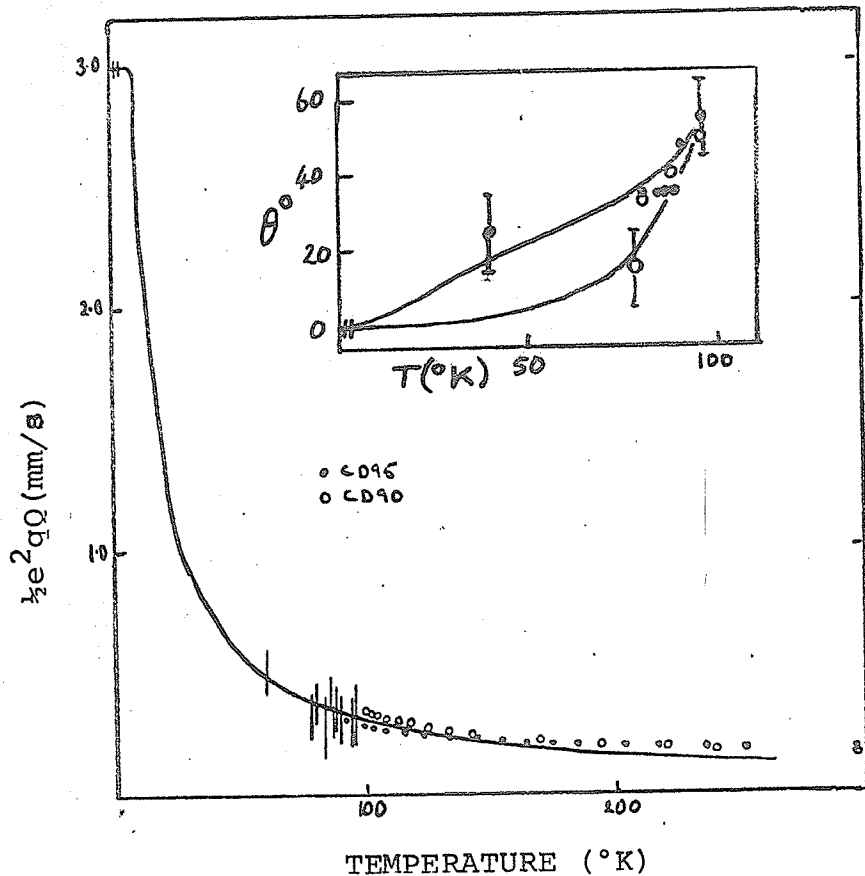


Figure 82. Temperature dependence of $\frac{1}{2}e^2qQ$ in CD95 and CD90. The insert shows the temperature dependence of θ .

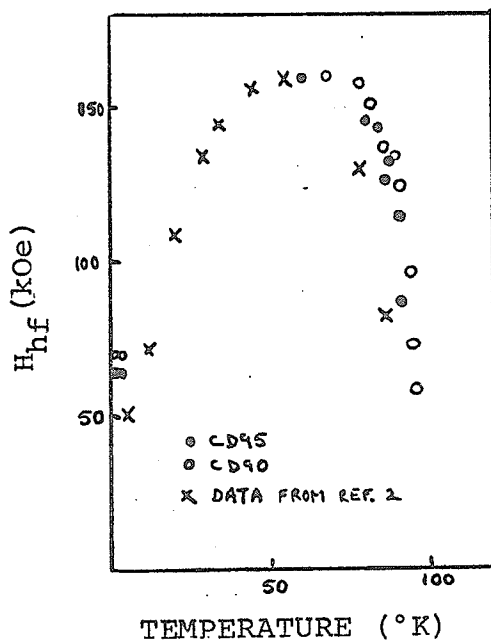


Figure 83. Temperature dependence of H_{hf} in CD95 and CD90; crosses are data from ref. 2.

Given that the value of $\frac{1}{2}e^2qQ \approx 1/3$ the observed line width then the values of $\frac{1}{2}e^2qQ$ for both compounds can be approximately fitted onto a curve:

$$E_Q(T) = E_Q(0) \tanh(\Delta/2kT)$$

where Δ is the ground state splitting and $\Delta/k=20^\circ\text{K}$ $\Delta E_Q(0)=3.0$ mm/s. This is the solid line in figure 82. The data in figure 83 are the results for the hyperfine fields, at least all the values we could actually obtain. It may be seen that the behaviour in both compounds is similar. The crosses in figure 83 are data taken from {2} for the member with $x=0.02$. The magnetic hyperfine field was observed below $91 \pm 3^\circ\text{K}$ in CD95 and below $101 \pm 3^\circ\text{K}$ for CD90. These figures are in fair agreement with the estimates from the magnetization data. We leave the subject of the total spectrum shifts until later.

1.5.2 The iron rich end.

Spectra covering the temperature range investigated are shown in figure 84 for CD20 and CD10. Once more the spectra are complex and in the paramagnetic regions quite definite structure appears in the absorption of CD20 below $\sim 250^\circ\text{K}$. In the case of CD10, the absorption remains a broad singlet down to T_M . Since we could see the structure in the case of

NUMBER OF COUNTS

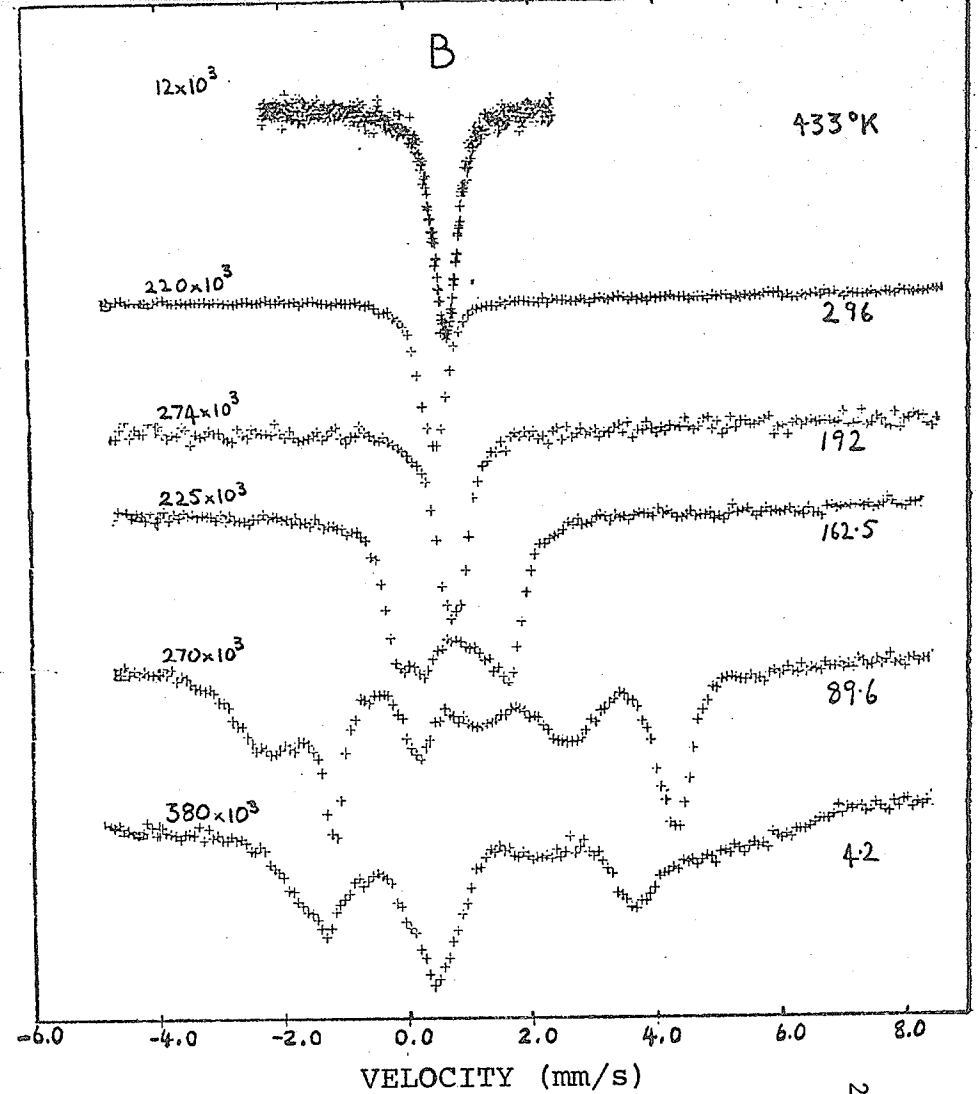
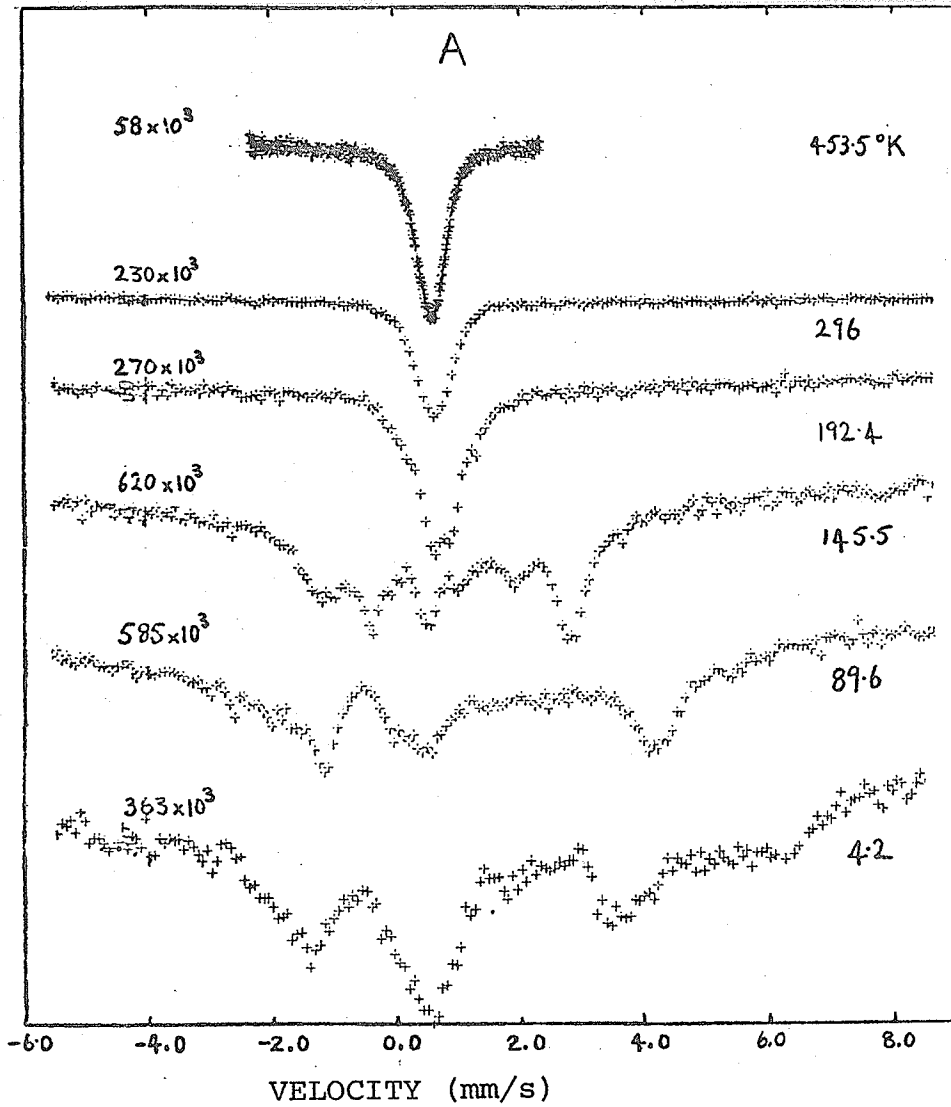


Figure 84. Mössbauer spectra of (A) CD20 and (B) CD10 at various temperatures.

CD20, we considered that the many environment approach to the fitting should be employed. The main doubt about results obtained in this fashion arises from the fact that an enormous number of parameters are introduced and it is difficult to decide whether the better fits really reflect a significant model or whether they arise because of the extra parameters.

We made our first investigation using CD10 paramagnetic spectra. These we considered could be fitted with two singlets constrained to have equal full widths but heights constrained in the ratio indicated in table 26 for 4 and 3 magnetic n.n.. The result was that the absorption ascribed to the 3-1 environment occurred at a slightly higher energy than that from the 4-0 environment. In addition, the centre of gravity of the entire absorption occurred close to the peak of the 4-0 absorption. We then used these results as criteria for testing similar fits to the paramagnetic spectra of CD20. Here, there were three environments with significant probabilities 4-0, 3-1 and 2-2. Now there are several ways the spectra might be fitted:

- (i) Three singlets all full widths equal;
- (ii) Three singlets with a variety of full widths and total absorption constrained in the correct ratios;

- (iii) Two singlets and one doublet, one singlet and two doublets, all with or without a variety of full widths;
- (iv) Three doublets;
- (v) A systematically varying choice of fit depending on the temperature.

Choice (v) was found to give the best fits to the spectra.

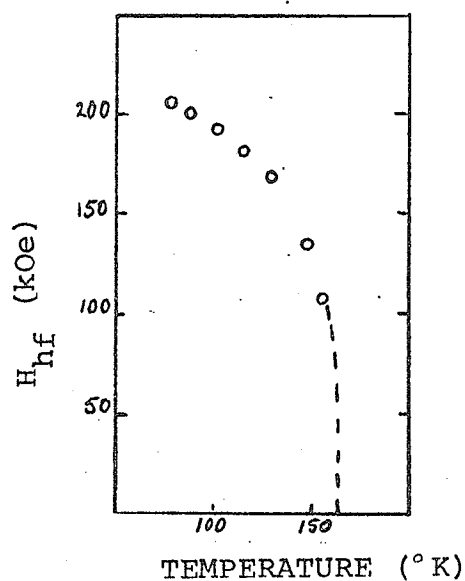


Figure 85. The temperature dependence of H_{hf} in CD10.

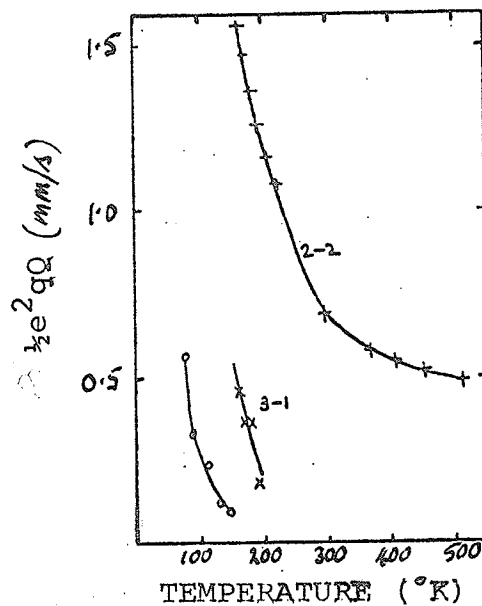


Figure 86. Quadrupole interactions in CD10 and CD20. In CD10, open circles, there is an E.F.G. below T_M with $\theta=10^\circ$, $Q=0$, $\eta=0$. For CD20, we show the apparent quadrupole splitting for 2-2(+), and 3-1(x), type environments $T > T_M$.

The results were that absorption from the 4-0 environment was always a singlet with the smallest spectrum shift, absorption from the 2-2 environment was always a doublet whose spectrum shift was roughly equal to the centre of gravity of the entire absorption pattern and finally absorption from the 3-1 environment changed in character from a narrow singlet at high temperatures to a broad singlet at $T \sim 200^\circ\text{K}$ to a doublet at $T < 200^\circ\text{K}$. One conclusion that may be drawn from this is that, at these concentrations of magnetic A-site ions, the behaviour of the Fe^{2+} ion is extremely sensitive to lattice imperfections even when the source of the perturbation is quite far away. This means that the primary cause is long range in nature. We note that the paramagnetic spectra bear a strong resemblance to those obtained in {6}. It is then a short step to the conclusion that the type of perturbation we are observing is associated with the strain field in the crystal and therefore, the problem in understanding the spectra resolves itself to finding out how the cadmium ions affect this strain field.

Below T_M for these compounds we had some success in fitting the spectra at least down to 77°K . Below this temperature, the spectra become far too complex. Figure 85 shows the temperature dependence of H_{hf} and figure 86, the temperature dependence of

$\frac{1}{2}e^2qQ$. We note that CD10 shows no quadrupole splitting above T_M rather like $FeCr_2S_4$, but CD20 has a splitting, at least that is what the fits to the spectra above T_M indicate. It is also interesting to note the CD10 spectrum at $162^\circ K$. This temperature is perhaps $1^\circ K$ below T_M and the spectrum shows quite conclusively that $\frac{1}{2}e^2qQ$ is positive {7}. (The transitions associated with the $+\frac{1}{2}$ excited sub-state always broaden out before those associated with the $\pm 3/2$ level.) This is an important result because it bears directly on $FeCr_2S_4$. The ordering temperatures determined via the Mössbauer Effect are 158 ± 4 and $163 \pm 1^\circ K$ for CD20 and CD10 respectively in fair agreement with the values obtained from the magnetization measurements.

1.5.3 The central region.

This region was studied via CD50. Some spectra are shown in figure 87. We could fit none of the spectra collected in the ordered region ($T < 131 \pm 2^\circ K$). This temperature is lower than that estimated from the magnetization work. The way in which the spectra manifest magnetic order is extremely odd. At $139^\circ K$, the absorption is a broad doublet, by $129.5^\circ K$, the absorption is almost triangular, decreasing the temperature to $125.9^\circ K$ produces a flat almost

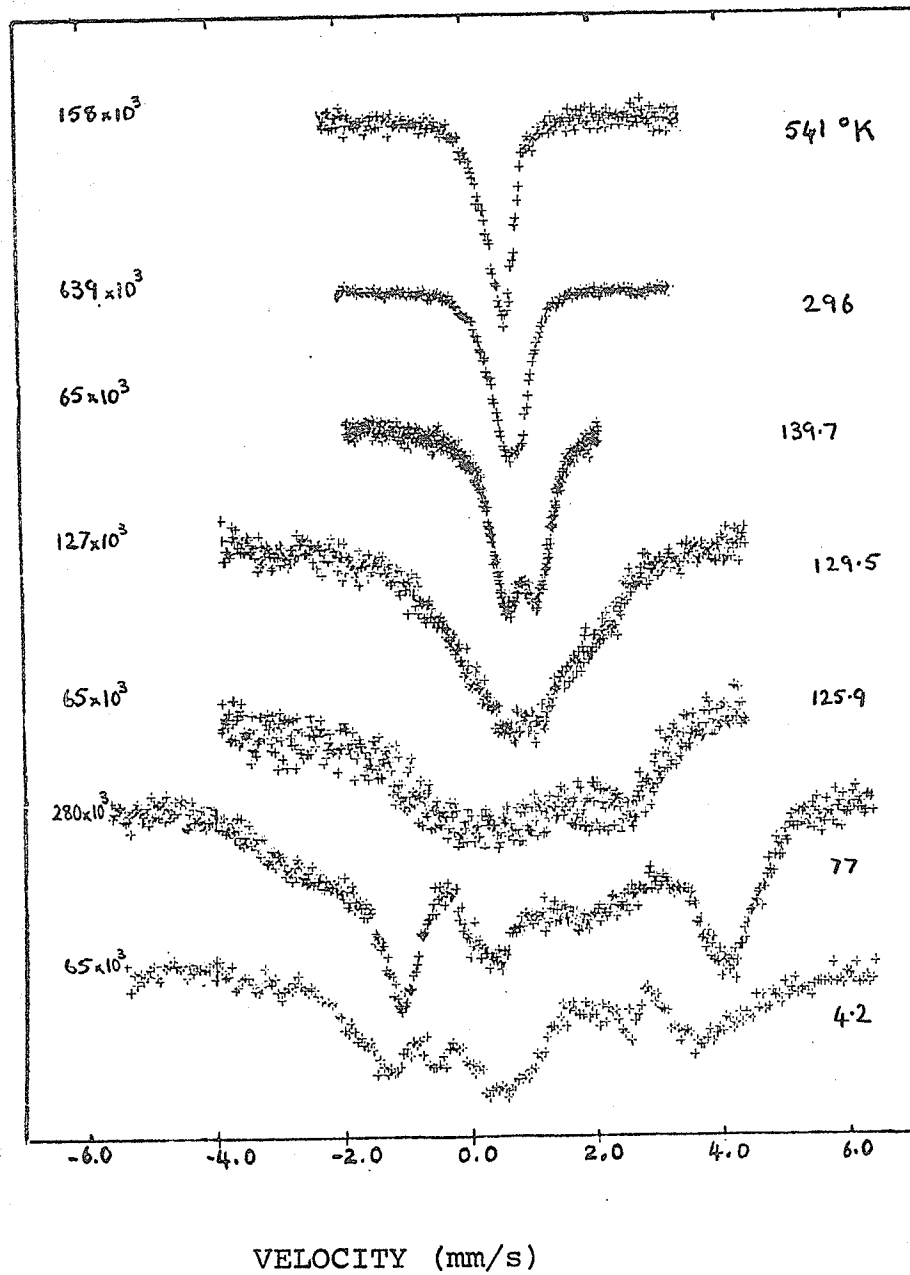


Figure 87. Mössbauer spectra of CD50 at various temperatures.

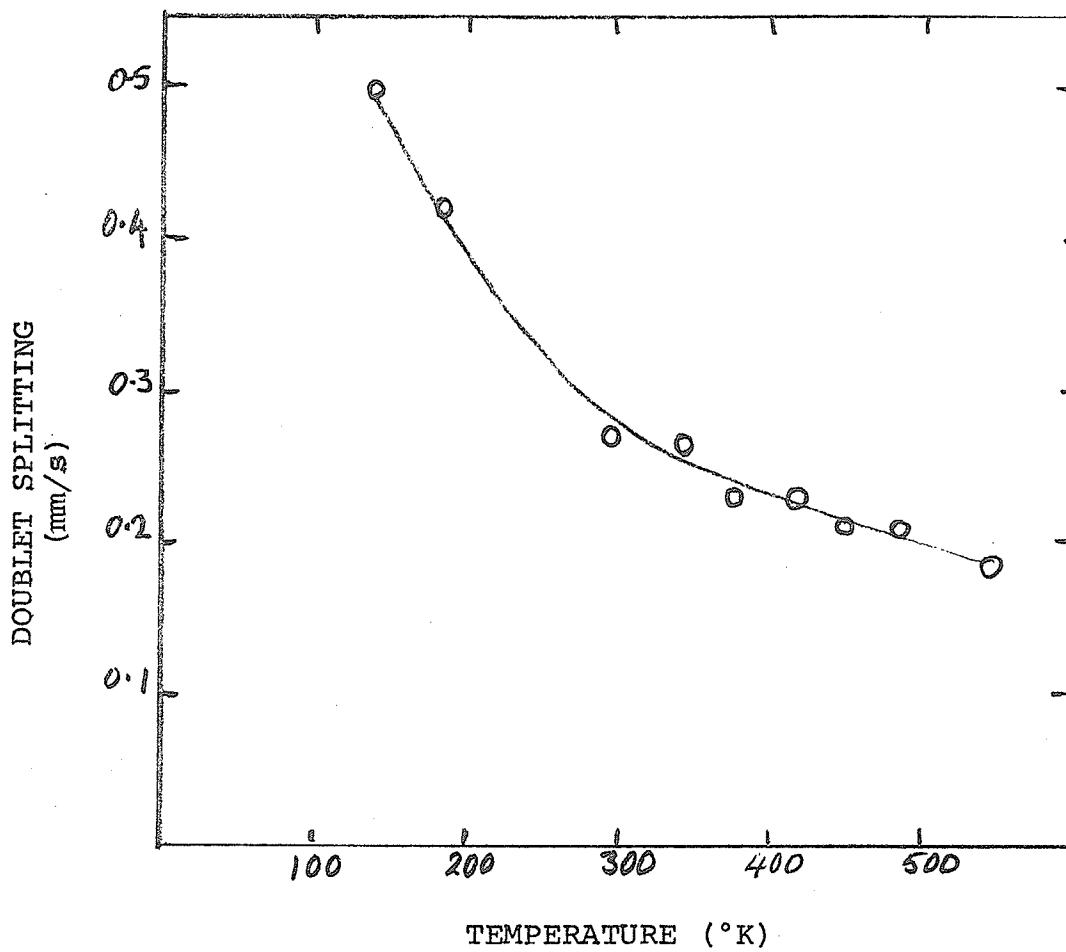


Figure 88. The temperature dependence of the splitting of paramagnetic doublets in CD50.

featureless absorption and by 77°K some structure appears. It is clear that some class of relaxation mechanism is operative. Above T_M we were able to fit the spectra with a doublet, figure 88 shows the temperature dependence of the doublet splitting.

1.5.4 Total spectrum shift.

The Debye temperatures were found by making use of (II.25). The total absorption was determined by numerical integration of the area of the absorption spectrum. The temperature region of interest was $T_M < T < 600^\circ\text{K}$. The integration is sensitive to the geometry of the spectrometer, the velocity range and number of channels utilized. To cover the range above, two experimental set ups are required so a normalizing factor, based on the ratio between the two results at room temperature, was applied to the high temperature data. This gives the data shown in figure 89. The Debye temperatures that may be inferred from the plots are collected in table 27. Equation (II.25) is supposedly valid for $T > \theta_D/2$ so that the departure from expectation in the case of CD95 $T < 200^\circ\text{K}$ cannot be regarded as significant. It seems reasonable that these compounds have Debye temperatures $\sim 300^\circ\text{K}$ compared with $\theta_D \sim 450^\circ\text{K}$ in oxides.

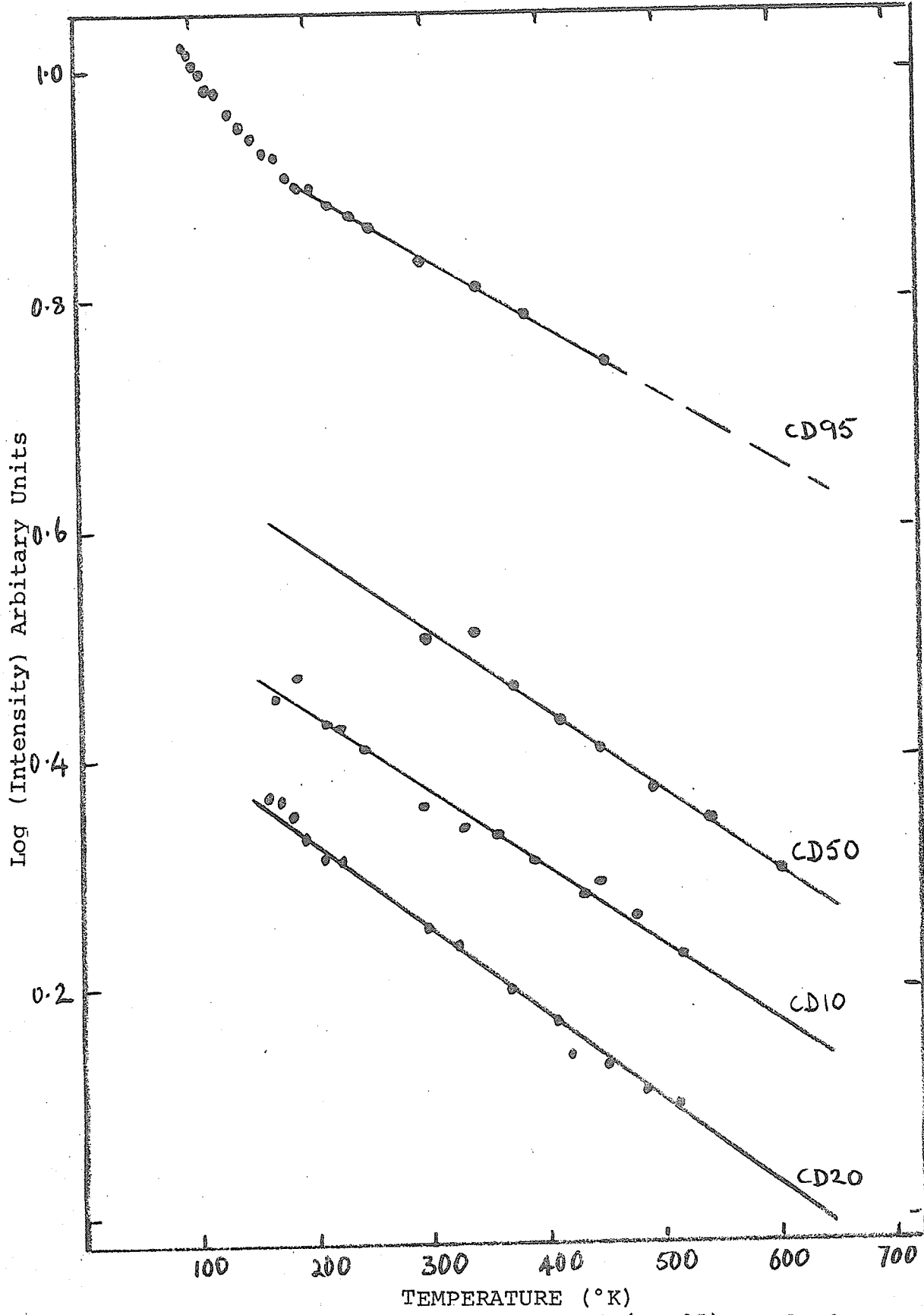


Figure 89. To illustrate the use of (II.25) to find the Debye temperatures.

The total spectrum shifts cannot be determined with much accuracy because of the complexity of the spectra. In table 27, we show the values of the room temperature shifts which were obtained from the peak positions. All spectra at 296°K were fitted with single lines for the purpose of this measurement. For CD90 we performed this kind of analysis over the whole temperature range and the results are given in figure 90.

Table 27. Total Spectrum Shift Data for some Members of the Family $\text{Cd}_{1-x}\text{Fe}_x\text{Cr}_2\text{S}_4$.

| x | θ_D (°K) | δ_t (296°K) (mm/s) |
|------|-----------------|---------------------------|
| 0.05 | 315 | 0.80 |
| 0.1 | 200 | 0.79 |
| 0.5 | 288 | 0.78 |
| 0.8 | 270 | 0.75 |
| 0.9 | 296 | 0.71 |

The data in the paramagnetic region are more reliable than those from the ordered region and show a deviation from the Debye model fit. On the other hand, figure 91 shows the result of fitting CD95 spectra with two singlets assuming the intensities to be in accord with the probabilities of 0 and 1 magnetic n.n. as given in table 27. The temperature dependence

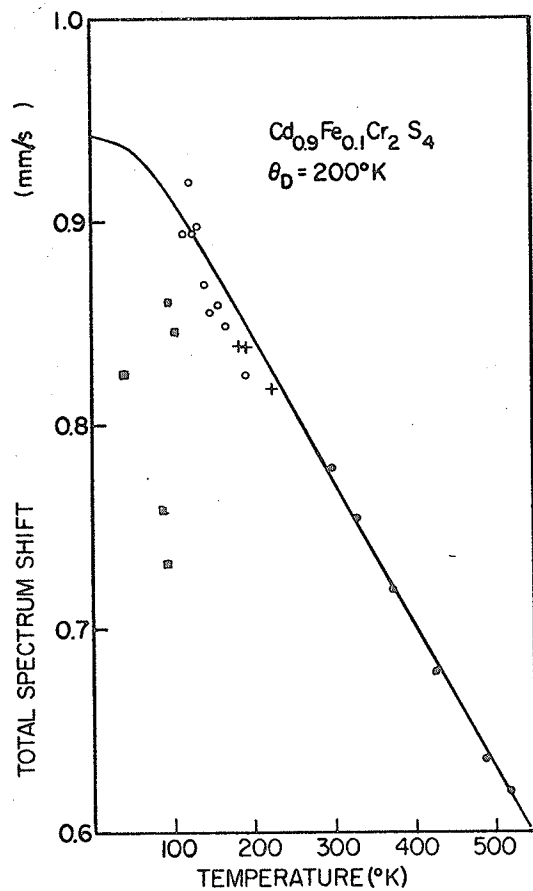


Figure 90. Temperature dependence of total spectrum shift in CD90, δ_r was found by averaging peak positions. Symbols mean; \square ordered spectra, \circ paramagnetic doublets, \bullet paramagnetic singlets, $+$ intermediate.

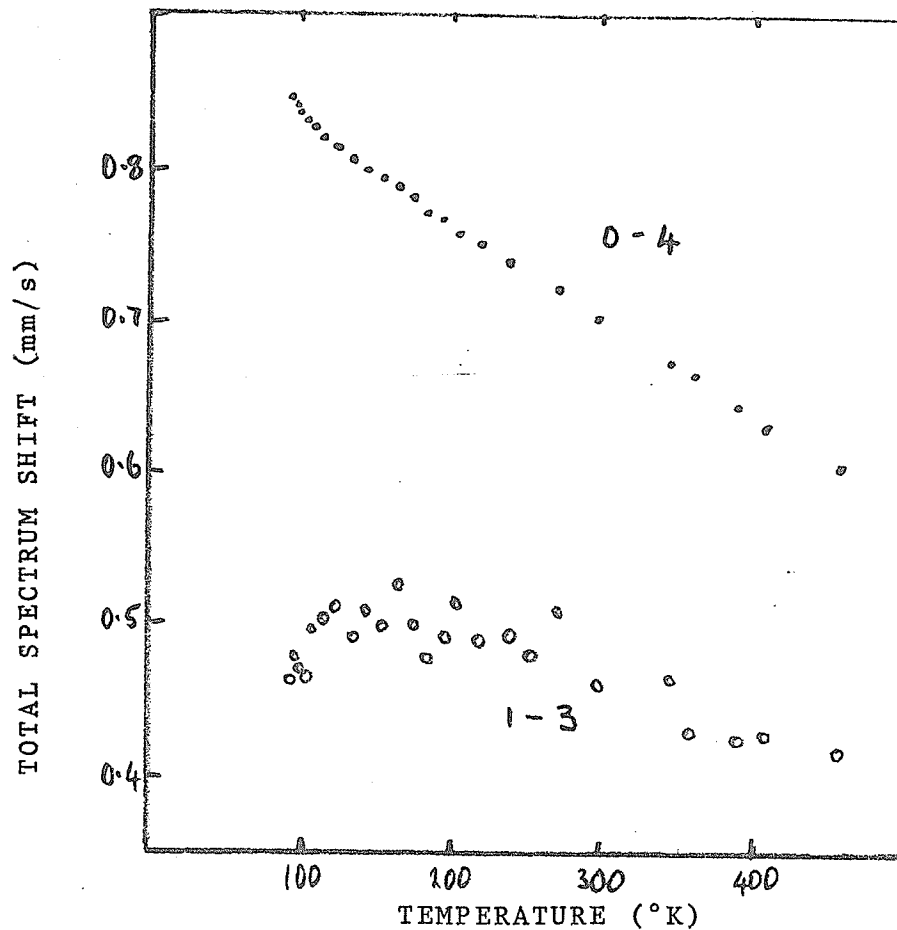


Figure 91. Temperature dependence of total spectrum shift in CD95 assuming spectra associated with different environments.

of δ_t for the 0-4 environment is in accord with the Debye model at least for $T \gg T_M$, while that for the 1-3 environment is obviously not. We also note that the total shift of the 1-3 line is not too large to be attributed to Fe^{3+} impurities. Clearly, the temperature dependence of δ_t in these compounds is problematical.

4.6 Discussion.

There are several points that may be immediately made about these compounds:

- (i) They are all essentially semiconducting;
- (ii) The iron is always in the high spin ferrous state judging from the room temperature spectrum shifts;
- (iii) They are all spinels and the room temperature Mössbauer spectra are all consistent with the view that there is iron only on the A-sites.

In view of these points, it is reasonable to expect behaviour consistent with localized d-electrons. Furthermore, it is reasonable to assume that all the compounds are ferrimagnets with antiferromagnetic alignment of the A-site ions and B-site ions because of the $\sim 125^\circ$ A-B superexchange interaction. Given this situation there seems to be no reason why the band

scheme suggested for FeCr_2S_4 should not be valid for all these compounds. Slight modifications are in order because the lattice spacing increases as the cadmium content rises. This should lead to smaller d-electron covalent overlap, at the A-sites especially but also at B-sites, giving rise to the gradually increasing values of the energy gap between occupied and unoccupied bands and gradually increasing values of the A-site spectrum shift. We, therefore, expect that the principal charge carriers will be holes in a fairly narrow Fe^{2+} band, but the role of less mobile electrons in a narrow σ^* B-band will also be important especially at the cadmium rich end of the series.

We now consider some of the details of the experimental results, starting first with the magnetization data. Initially, we test the notion suggested in Chapter III, section 3.3. What we would like to know is whether substituting some transition metal ion for the neutral Cd produces an anisotropy that allows a collinear alignment of the Cr^{3+} spins and a value of the magnetic moment closer to $6\mu_B$ /molecule for the B-sublattice. The basis of our idea is very simple and hinges on the premise that extrapolation of the magnetization data to $1/H=0$ should always overestimate the magnetic moment if the

magnetization is not saturated in ordinary fields. That this is the case for CD90 and CD95 is apparent from table 22. We, therefore, take the M_S and M_∞ data for these two compounds and extrapolate them to zero iron content. This is done in figure 92. Extrapolating M_∞ yields $5.99 \mu_B/\text{molecule}$ while the figure from M_S is $6.04 \mu_B/\text{molecule}$ neither extrapolation comes close to the figures for CdCr_2S_4 . This result, therefore, suggests that:

- (i) The spin arrangement in CdCr_2S_4 is non-collinear;
- (ii) The presence of Fe^{2+} on the A-sites provides an anisotropy of some description that produces a collinear B-site arrangement at least for small amounts of iron.

Since this anisotropy exists, it is easy to understand why the M_S results for these compounds always fall below the expected spin only result. Provided the anisotropy is strong enough, it will never be possible to saturate the magnetization in ordinary fields.

Therefore, in order to properly explain the observations, we must seek a mechanism that allows a strong, single ion anisotropy for A-site Fe^{2+} ions. This is perfectly in keeping with observations on FeCr_2S_4 where single crystal experiments reveal {8} that the

$\langle 111 \rangle$ is very hard and the $\langle 100 \rangle$ is easy.

At the iron rich end of the series, we find that our data can be reasonably extrapolated from our results on FeCr_2S_4 . Replacing Fe^{2+} by Cd^{2+} , therefore, causes a simple dilution of the A-site magnetic moments without seriously affecting the spin arrangement. The single crystal work gave a value of $1.86 \mu_B$ /molecule for FeCr_2S_4 $H \parallel \langle 100 \rangle$ so the effective moment for Fe^{2+} is $4.14 \mu_B$. Assuming that orbital and spin angular momentum are parallel at 4.2°K then a g of 2.07 is deduced for the ion.

In the centre of the series, to be precise, for $0.2 < x < 0.8$, we have problems:

- (i) The Curie constants fall well below expected values;
- (ii) both M_S and M_{30} fall below the spin only values.

It may readily be ascertained that these two points are impossible to explain by the same mechanism. If we propose that the moment associated with Fe^{2+} increases as x is decreased in order to obtain the "correct" low temperature moment, then the C_M should be greater than those expected and vice versa.

Our explanation of the low C_M {3} was given in terms of the temperature dependencies of

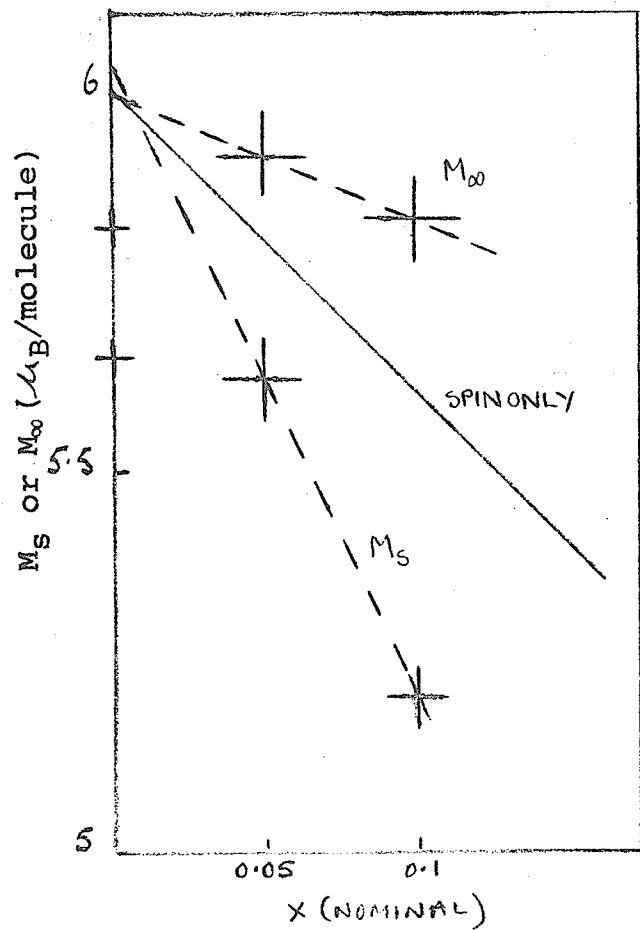


Figure 92. Extrapolation of M_s and M_∞ to zero iron content for CD95 and CD90.

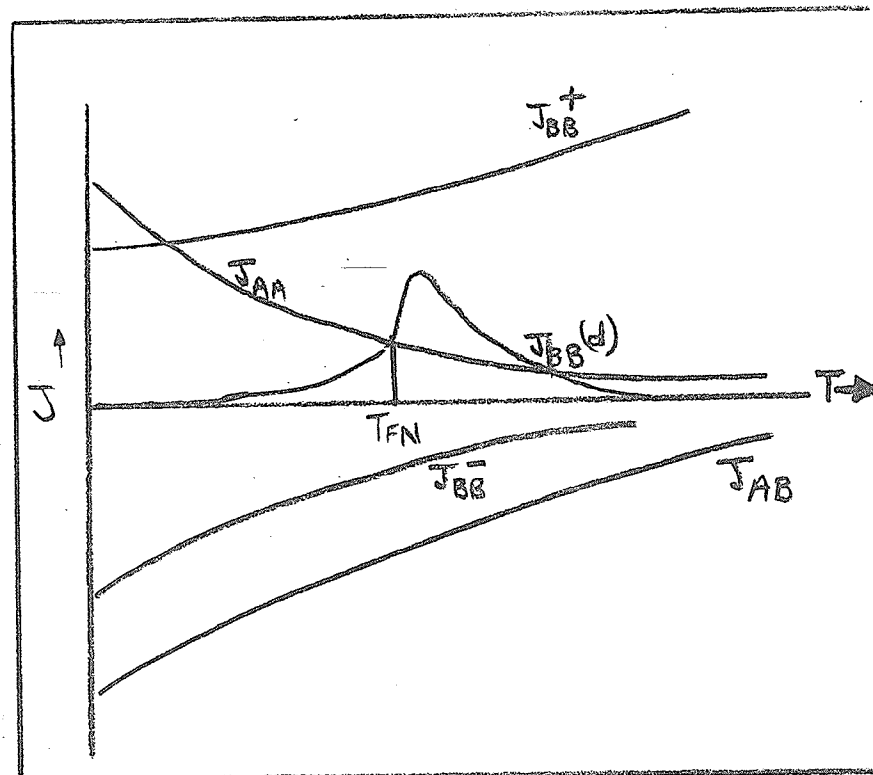


Figure 93. Qualitative representation of the temperature dependencies of some magnetic exchange interactions in $\text{Cd}_{1-x}\text{Fe}_x\text{Cr}_2\text{S}_4$.

the various exchange interactions. The lower than spin only magnetic moment results were then explained via an effective moment for the Fe^{2+} ions greater than $4.14 \mu_B/\text{ion}$. The physical basis for the low C_M is derived from the compositional dependence of the Curie-Weiss parameter θ . We consider figure 78b. The parameter θ supposedly gives the sign of the dominant magnetic exchange interaction. Now each A-site has 12 nearest neighbour B-site ions. A magnetic A-site interacts antiferromagnetically with the B-site neighbours; furthermore, substituting iron for cadmium decreases the separation of the B-site ions and this enhances the antiferromagnetic component (J_{BB-}) and decreases the ferromagnetic component (J_{BB+}) of the net B-B interaction. Therefore, we would expect θ to decrease quite quickly as the iron content is increased from zero. The fact that θ is positive until $x \sim 0.4$ suggests, therefore, that there is yet another important positive interaction that bolsters the otherwise diminishing J_{BB+} exchange. One possible origin would be J_{AA} which is positive so long as J_{AB} is effected by transfer of β -spin Fe^{2+} electrons to $^3T_{1g}(\text{Cr}^{2+})$. Another possibility is the indirect effect of charge carriers in the σ^*B -band that polarize the B-site spins in the vicinity of T_{FN} .

The temperature dependencies of the various interactions can be inferred by assuming that the lattice expands on heating and noting how the interactions change in a variety of simple compounds. In passing from ZnCr_2S_4 - CdCr_2S_4 - CdCr_2Se_4 all the quantities, lattice parameter, Curie temperature and, θ parameter increase {9}. This means that as the B-B separation increases, J_{BB^+} increases and J_{BB^-} decreases. The exchange J_{AB} must decrease with increasing lattice size because it depends for its strength on an overlap integral between cation and anion, and similarly for J_{AA} . These considerations are summarized in figure 93. The effect of σ^*_{B} electrons is indicated by $J_{\text{BB}}(\text{d})$. They are only effective in enhancing the magnetic exchange when the susceptibility of the B-site spin system is large ie. near to and just above T_{FN} . They have the character of magnetic polarons, for stability the band should be very narrow {10} and the interaction between the carriers and the B-site spin large. At both high and low temperatures they are ineffective because of spin-spin and electron-phonon scattering at high temperatures and at low temperatures the susceptibility is too small for stability. The magneto-resistance should be dominated by the properties of such carriers even if they are not the principal

current carriers in the system, and it should be large and negative. With these considerations we arrive at the temperature dependence of $J_{BB}^{(d)}$ in figure 93. It is not important to be definite about naming this interaction, only to note that it will have similar effects to magnetic polarons, that above T_{FN} , $J_{BB}^{(d)}$ has a negative temperature coefficient, and that it contributes positively to J_{BB} . As such, we can qualitatively explain how θ stays positive so far into the composition range and by considering the Weiss molecular field parameter to be temperature dependent, we can explain the low values of C_M . Suppose that:

$$N_w = N_{w0} + \alpha_w T + \dots$$

$$\text{then } \chi = C / (T - CN_w) = C_{\text{exp}} / (T - C_{\text{exp}} N_{w0})$$

where $C_{\text{exp}} = C_M / (1 - \alpha_w C_M)$ is the experimentally found Curie constant, C_M is the expected value and α_w contains all the temperature dependence of all the exchange interactions then:

$$\alpha_w = \alpha(J_{BB}^+) + \alpha(J_{BB}^-) + \alpha(J_{AB}) + \alpha(J_{AA}) + \alpha(J_{BB}^{(d)})$$

From figure 93 some of the α are positive and some are negative and low values of C_{exp} result if:

$$|\alpha^-| = |\alpha^+|$$

and vice versa.

Another explanation is suggested by the work in {6}. Here a very dilute system of Fe^{2+} ions

in tetrahedral (sulphur) sites was studied. The interesting result in question was this; at 4.2°K the system showed no induced hyperfine field in a Mössbauer spectrum even in an applied field of 30 kOe. Now this is very strange and must either mean that the spins align with the applied field for times less than the nuclear Larmor precession time ($\sim 6 \times 10^{-8}$ s in a field of 30 kOe) or that there is no spin associated with the ions. A very large trigonal distortion might produce low spin ferrous ions on a tetrahedral site, but it seems more likely that a relaxation effect is present. Whatever the cause, there is some evidence that tetrahedral site Fe^{2+} ions can behave as though they were non-magnetic, and given this possibility, we may explain the lower than spin only Curie constants in our compounds.

The last feature of the magnetization results that we wish to discuss is the abrupt variation of the Curie-Weiss constant around $x=0.4$ to 0.5 . We previously explained this {3} in terms of the way in which $J_{\text{BB}}(d)$ affected the strength of the effective B-B interaction. The magneto-resistance measurements shed some light on the matter. Magneto-resistance is determined by the extent to which the d-electrons are affected by conduction processes. In FeCr_2S_4 we suggested that conduction was via holes in a narrow

Fe^{2+} band and found $J_{AK}/J_{BK} \sim 10$. Comparison of the data for CD10 with same theory suggests $J_{AK}/J_{BK} \sim 1$. At the Cd rich end of the series, we have argued that the magneto-resistance results from a sort of magnetic polaron effect having an essential role in the B-B exchange. It follows then that any enhancement of J_{BB} resulting from electrons transferred to σ^*B or ${}^3T_{1g}(\text{Cr}^{2+})$ states must fall as x is increased and consequently so should any magneto-resistance effect. The compounds with $x < 0.5$ in figure 80, however, all show moderate magneto-resistance but at $x=0.5$ we find only a very small effect. Consequently we assume that θ is held strongly positive until $x \sim 0.5$ mainly by $J_{BB}(d)$ but that this contribution vanishes near $x=0.5$ so that J_{AB} dominates the magnetic ordering.

Although our model does not contradict any of our experimental data, it does not really help us in understanding the Mössbauer spectra. First, consider the work that has been published on such systems. In {2} the authors examined a compound very like some of ours. They state (without showing any spectra) that the paramagnetic absorption was a single line and that no quadrupole interaction appeared until $T \sim 78^\circ\text{K}$. However, they fitted the ordered spectra assuming $H_{hf} // V_{zz}$. In our view, this begs the question,

and it must be remarked that their spectrum at 78°K is qualitatively similar to ours for CD95 at 86.7°K (see figure 81) for which we found $\theta \sim 50^\circ$ in keeping with the view that an E.F.G. existed at all temperatures, the quadrupole shift of the ordered spectrum having vanished because of the value of θ (see remarks in Chapter II, section 3.2).

A system that shows rather similar effects to those we observe is $\text{Cu}_{1-x}\text{Fe}_x\text{Cr}_2\text{S}_4$. This system has been reported in several papers {4,11}, but Mössbauer spectra of interest are reported in {12}. Figure 94 collects some of the data for the two systems and we divide the compounds into metals and semiconductors at about $x=0.5$ in the copper system.

Mössbauer spectra from the region to the left of this dividing line are all rather similar in the ordered regime. It has been claimed {4} that the copper in the system is $3d^{10}$ and in {12} the authors suggest that the rather odd looking spectra result because of the coexistence of Fe^{2+} and Fe^{3+} on the A-sites and claim that their spectra show at least 9 lines. No computer fit is given and the most conclusive remark that can really be made about the spectra is that they are complex.

The main reason for the suggestion that copper is $3d^{10}$ in the system is that no magnetic

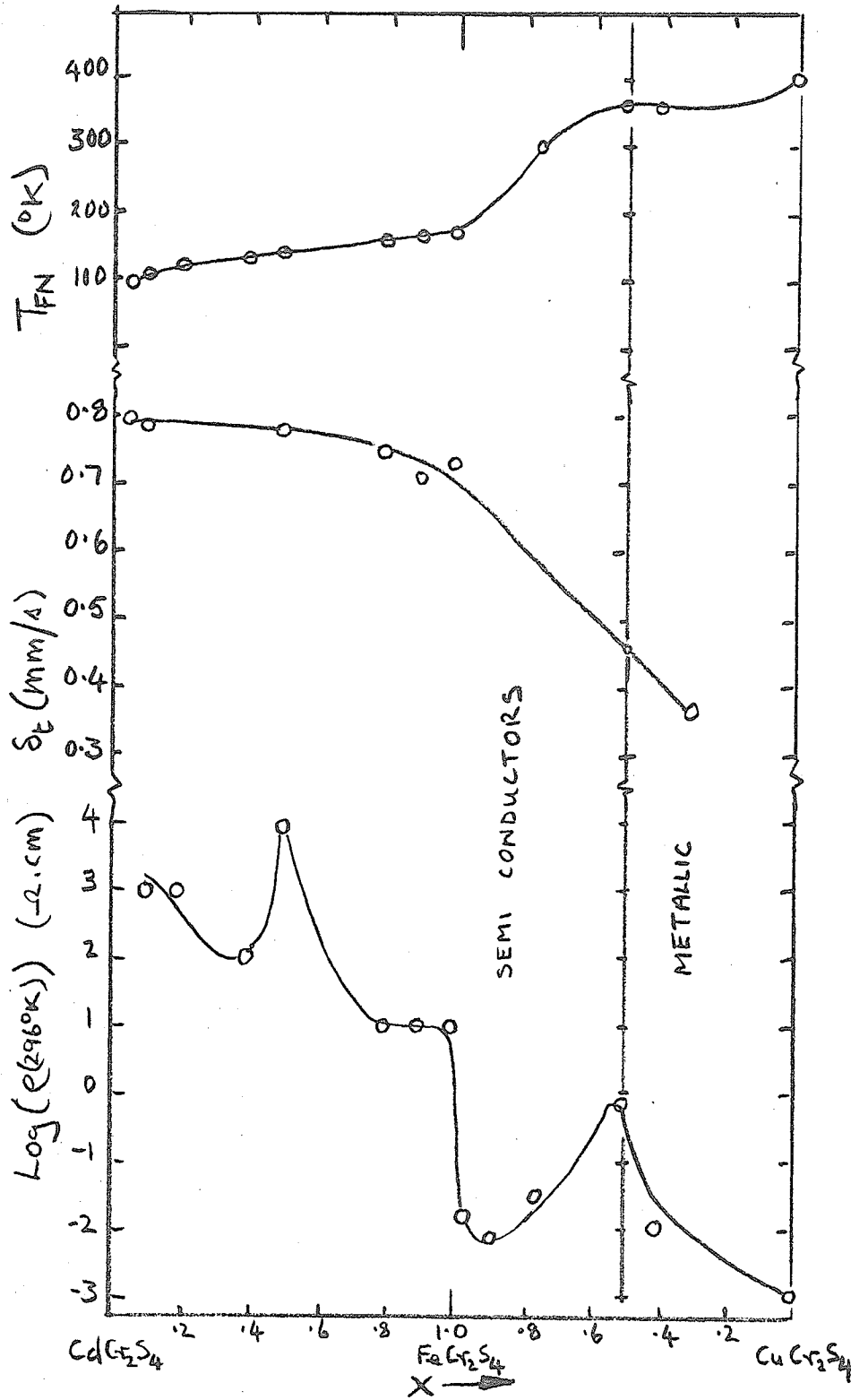


Figure 94. Correlation of properties of the two isomorphous systems $\text{Cd}_{1-x}\text{Fe}_x\text{Cr}_2\text{S}_4$ & $\text{Fe}_{1-x}\text{Cu}_x\text{Cr}_2\text{S}_4$.

moment is associated with it but then, a similar result obtains for the Fe^{2+} in {6} as we have already noted. In order to make some sense of all this we would suggest that the copper is $\text{Cu}^{2+}(3d^9)$ and, like $\text{Fe}^{2+}(3d^6)$ on a tetrahedral site is a J-T ion. In spite of the fact that Cu^{2+} should have a large spin orbit coupling that ought to quench the J-T effect, there is good evidence {13} that the coupling of the 5 t_{2g} electrons to the E modes of the tetrahedron is so strong that a J-T distortion is favoured {14} over a spin orbit stabilization. It was pointed out by Ham {15} that when the spin orbit coupling was strong enough, even the spin angular momentum of an ion could be quenched, at least partially by a dynamic J-T effect.

We are far from proving anything but evidently many of these suggestions could be investigated theoretically. The important parameters would be the J-T coupling, the spin orbit coupling, the characteristic frequency of vibration, and the effective mass of the tetrahedron. Also some account should be taken of the type of experiment performed, because in dealing with a relaxation effect, the observation time should be compatible with the relaxation time.

For the moment we remark that with this

type of explanation, the similarities between the Mössbauer spectra in $\text{Cu}_{1-x}\text{Fe}_x\text{Cr}_2\text{S}_4$ ($x=0.5$) and $\text{Cd}_{1-x}\text{Fe}_x\text{Cr}_2\text{S}_4$ can be correlated. That a dynamic J-T relaxation can produce the type of paramagnetic spectra we observe has been demonstrated {16,17,18} but the behaviour in the ordered region has not been thoroughly investigated. Proximity effects such as are observed in {6} probably result from the way in which the neighbouring atoms change the elastic anisotropy to which the A-site J-T ion is so sensitive {19}. This presumably explains why the spectra in FeCr_2S_4 are similar but considerably simpler than those in the mixed systems.

4.7 Conclusions.

We have found that all the compounds in the family $\text{Cd}_{1-x}\text{Fe}_x\text{Cr}_2\text{S}_4$ $0 < x < 1$ are spinels and are semiconducting. There appears to be some evidence that the member with $x=0.5$ is ordered although there is no confirmation from the x-ray pattern. Apart from this compound the resistivities fall with increasing x . All aspects of our investigation favour a localized electron type of model and a band diagram similar to that prepared earlier for FeCr_2S_4 is likely to be valid. As such, the indications are that the β -spin electron on the Fe^{2+} ion

has a large role in determining the properties of these compounds.

The Mössbauer effect studies present us with more problems than they solve. The iron in all compounds is ferrous. All spectra obtained show that some type of relaxation effect is present and that this is plausibly due to a dynamic J-T stabilization of the $\text{Fe}^{2+} \text{ } ^5\text{E}$ ground state, as in FeCr_2S_4 .

Some extra evidence has been offered for a non-collinear spin arrangement in CdCr_2S_4 .

Literature Cited in Chapter IV

1. P.F. Bongers, C. Haas, A.M.J.G. Van Run and G. Zanmaschi, *J. Appl. Phys.*, 40, 958, 1969.
2. A.M. Van Diepen and R.P. Van Stapele, *Phys. Rev. B*, 5, 2462, 1972.
3. M.R. Spender and A.H. Morrish, *Can. J. Phys.*, 49, 2659, 1971.
4. F.K. Lotgering, R.P. Van Stapele, G.H.A.M. Van Der Steen, and J.S. Van Wieringen, *J. Phys. Chem. Solids*, 30, 799, 1969.
5. F.K. Lotgering and R. Plumier, *Solid State Commun.*, 8, 477, 1970.
6. A. Gerard, P. Imbert, H. Prange, F. Varrett and M. Wintenberger, *J. Phys. Chem. Solids*, 32, 2091, 1971.
7. R.L. Collins and J.C. Travis, *Mössbauer Effect Methodology Volume 3*, Plenum Press, New York, 1967.
8. R.P. Van Stapele, J.S. Van Wieringen and P.F. Bongers, *J. de Phys.*, 32, C-53, 1971.
9. P.K. Baltzer, P.J. Wojtowicz, M Robbins and E. Lopatin, *Phys. Rev.*, 151, 367, 1966.
10. T. Kasuya, A. Yanase and T. Takeda, *Solid State Commun.*, 8, 1541, 1970; 8, 1553, 1970; *Proc. Int. Conf. Ferrites*, Japan 1970 pages 604-606.
11. G. Haake and L.C. Beagle, *J. Phys. Chem. Solids*, 28, 1699, 1966; *J. Appl. Phys.*, 39, 656, 1968.
12. G. Haake and A.J. Nozik, *Solid State Commun.*, 6, 363, 1968.
13. J.D. Dunitz and L.E. Orgel, *J. Phys. Chem. Solids*, 3, 20, 1957.
14. R.J. Arnot, A. Wold and D.B. Rogers, *J. Phys. Chem. Solids*, 25, 161, 1964.

15. F.S. Ham, Phys. Rev., 138, A1727, 1965.
16. M. Blume and J.A. Tjon, Phys. Rev., 165, 466, 1968.
17. J.A. Tjon and M. Blume, Phys. Rev., 165, 456, 1968.
18. F. Hartmann-Boutron, J. de Phys., 29, 47, 1968.
19. J.B. Goodenough, J. Phys. Chem. Solids, 25, 151,
1964.

V CONCLUDING REMARKS.

1. SUMMARY.

If there is a unifying factor in the work we have described, it is that the properties of all the compounds studied can be understood to greater or lesser extents, in terms of the empirical ideas offered by Goodenough {1}. It may be argued that other ideas would do just as well, but it is worth making the following point. His discussion of the relationships between a multitude of solid state parameters and the energy b available for electron transfer from overlap integrals implies an almost unique role for the β -spin electron on a ferrous ion. This arises because a single electron outside of a filled subshell of 5 d-electrons enjoys little or no exchange stabilization and is most susceptible of all d-electrons to covalency effects. Therefore, b for this electron is abnormally large and Goodenough summarises this as:

$$b_{\beta} > b_{\alpha} \quad \text{especially in Fe}^{2+} \text{ ions.}$$

This represents a testable hypothesis and in all our experiments, but one, we have pointed out how the

β -spin electron influences the behaviour observed.

Briefly, there are the following points:

- (i) In FeRh_2S_4 a plausible mechanism for very strong negative A-A exchange involves transfer of β -spin electrons into empty σ^*B orbitals while maintaining a zero net moment in σ^*B ;
- (ii) In FeCr_2S_4 we require some model that is extremely sensitive to temperature and magnetic order, to explain; a change from activated to non-activated conduction, departures from the Debye model in the temperature dependence of δ_t ($T > T_{FN}$) and a negative magnetoresistance that requires exchange between charge carriers and A-site cations to be greater than exchange between carriers and B-site cations. By taking the view that the β -spin electron was of primary importance, these various effects could be correlated, without contradicting the experimental facts, eg. strong negative A-B exchange and localized electron behaviour at high and low temperatures.
- (iii) At the cadmium rich end of the mixed system

$\text{Cd}_{1-x}\text{Fe}_x\text{Cr}_2\text{S}_4$, the compositional dependence of the Curie-Weiss parameter indicates the presence of an additional contribution to the positive component of the B-B exchange interaction. This was plausibly attributed to an indirect type of effect in which the B-site spins were polarized by charge carriers with large effective mass. It was found possible to associate this indirect contribution with transferred β -spin A-site electrons.

- (iv) While the previous points tend to be rather qualitative, an opportunity arises for a more quantitative type of test. All the compounds $\text{Cd}_{1-x}\text{Fe}_x\text{Cr}_2\text{S}_4$ with $x > 0.5$ and $\text{Fe}_{1-x}\text{Cu}_x\text{Cr}_2\text{S}_4$ with $x < 0.5$ are ferrimagnetic semiconductors with negative values of θ and the principal magnetic interaction is J_{AB} and if we are correct, this is dominated by transfer of β -spin A-site electrons into ${}^3T_{1g}(\text{Cr}^{2+})$ states. The transfer is made possible by the energy $b \sim (\lambda_{\pi}^A)^2$ where λ_{π}^A is a covalent mixing parameter. The Mössbauer spectrum shift gives information, on a

relative scale, about λ_A^A . In fact, the difference between the value of δ_t (296°K) for ionic Fe^{2+} and covalent Fe^{2+} must be at least a crude indicator. If we represent this difference by $\Delta\delta_t$ then:

$$b \sim (\Delta\delta_t)^2$$

According to either Goodenough {1} or Anderson {2}, the ordering temperature is:

$$T \propto b^2/U$$

In the group of compounds of interest, the B-site cations are always the same, the anion co-ordination of the A-site is the same so it seems reasonable to suppose that U will be substantially constant.

Therefore:

$$T_{FN} \propto b^2 \propto (\Delta\delta_t)^4$$

We took δ_t (296°K) = 1.65 mm/s for ionic Fe^{2+} and the smoothest curve through the δ_t (296°K) values shown in figure 94 to find values of $(\Delta\delta_t)$ and used the published values of the ordering temperatures of the various compounds to plot $\log T_{FN}$ versus $\log (\Delta\delta_t)$. The result is shown in figure 95. The solid line there has a slope of 3.8 so there is at least some basis for our proposals, and even if the result is not completely convincing, it is fairly interesting. In table 28 we show the numbers used in the plot.

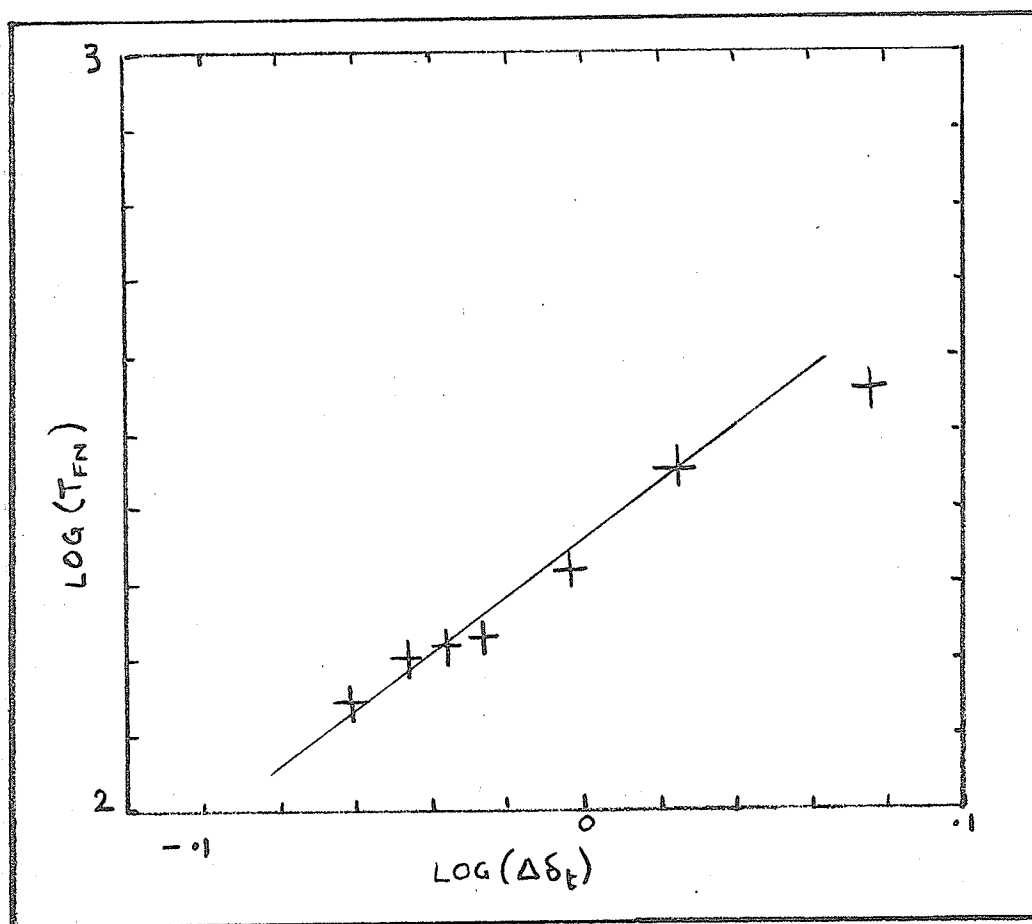


Figure 95. Illustrating a correlation between T_{FN} and the total spectrum shift.

Table 28. Data used to Plot Figure 95.

| COMPOUND | δ_t | $\Delta\delta_t$ | T_{FN} (K) |
|----------------------------------|------------|------------------|---------------|
| CD50 | 0.78 | 0.87 | 140 |
| CD20 | 0.75 | 0.90 | 160 |
| CD10 | 0.73 | 0.92 | 165 |
| FeCr ₂ S ₄ | 0.71 | 0.94 | 170 |
| CU10 | 0.66 | 0.99 | 210 |
| CU25 | 0.59 | 1.06 | 285 |
| CU50 | 0.47 | 1.18 | 360 |

We tested the idea on a different system, viz.

(Fe_{1-x}Rh_x)₂O₃ using data for $0 \leq x \leq .66$. This data was taken from {3}. The iron in the compounds is ferric rather than ferrous and the structure is corundum. A slope between 4.4 and 6 was a reasonable fit .

In the detailed results of the investigation, there are perhaps three highlights. The observation of paramagnetic doublets in the Mossbauer spectra of CD90 and the definite broadening of the paramagnetic absorption in CD95 show that, at this iron concentration, a magnetically induced electric field gradient is inadmissible. Decreasing the iron further seems to provide a favourable situation for

this mechanism but there seems little doubt that some class of relaxation mechanism is responsible for the spectra at higher concentrations, possibly a dynamic J-T stabilization of the ${}^5E(Fe^{2+})$ ground state.

The observation of what seems to be a low temperature transition in $FeCr_2S_4$ and a plausible consistency with a J-T stabilization is interesting and indicates a localized electron character in the compound. It suggests a moderate to strong J-T coupling of t_{2g} electrons to the anion modes that has a very small effect at high temperatures. An obvious extension is to suggest that this may be true for a larger number of sulphides than we think and that the outward manifestations of J-T coupling in sulphides are somewhat different to those in more ionic materials.

In $FeFe_2S_4$ we have a sulphide that is intermediate between the localized and the collective regime and studies of well crystallized samples would be of real interest. So far, we have determined the spin arrangement and the probable valence state of the A-site cations. Our studies also give, in a rather indirect fashion, the probable order of iron valence states in the sulphur lattice, viz:



2. SUGGESTIONS FOR FURTHER WORK.

The experimental study of magnetism as manifested in sulphides can be rather a messy business. It is hoped that the following experiments have some chance of success.

- (i) Magnetically induced electric field gradients can only be properly studied with single crystals and it would be well worth making some crystals of $\text{Cd}_{0.98}\text{Fe}_{0.02}\text{Cr}_2\text{S}_4$ and investigating the E.F.G. as a function of applied magnetic field. The results should be unambiguous according to the theory in {4}. There are reasonable details of growth techniques in {5}. Considerable care should be taken to anneal the crystals after growth. It is likely that some form of mosaic will be used but epoxy or other glues must be avoided as a means of immobilizing the crystal slices.
- (ii) A theoretical investigation of the type of Mössbauer spectra to be expected for an ordered material with a time dependent E.F.G. would be useful. The method of superoperators suggested in {6} might be suitable for someone with a feeling for the mathematics. A comparison with experi-

mental spectra should provide important information especially if J-T effects are present.

- (iii) A further investigation of FeRh_2S_4 would be worthwhile; there must be a way to prepare it strain free. It would be interesting to find out whether the low temperature susceptibility is affected by a Van Vleck type of temperature independent paramagnetism or whether there are some J-T effects.
- (iv) It would be worth considering whether Cu^{2+} in a tetrahedral sulphide site might satisfy the Ham/Van Vleck condition {7,8} of spin quenching. The ion nominally has a moment of $1\mu_B$ so a reduction factor of ~ 0.5 might be enough to make the moment undetectable via neutrons. If such a result is obtained, then it would help to clear up the difficulties concerning the Mossbauer spectra of $\text{Cu}_{1-x}\text{Fe}_x\text{Cr}_2\text{S}_4$ $x > 0.5$.
- (v) Finally, it seems reasonable to suggest that a proper theoretical basis for figure 95 be sought. If this is forthcoming, then simple systems dominated by 2 antiparallel electrons eg. CoCr_2S_4 could be studied by means of Mossbauer Effect spectroscopy using ^{57}Co in the samples.

Literature Cited in Chapter V

1. J.B. Goodenough, *J. Phys. Chem. Solids*, 30, 261, 1969.
2. P.W. Anderson, *Phys. Rev.*, 115, 2, 1959.
3. J.M.D. Coey, Ph.D. Thesis, University of Manitoba, 1971.
4. G.R. Hoy and K.P. Singh, Conference on Magnetism, Chania, Crete, 1969.
5. P. Gilbert and A. Begouen-Demeaux, *C.R. Acad. Sci.*, 268C, 816, 1969.
6. M.J. Clauser, *Phys. Rev. B*, 3, 3748, 1971.
7. F.S. Ham, *Phys. Rev.*, 138, A1727, 1965.
8. J.H. Van Vleck, *Physica*, 26, 544, 1960.

Appendix A The Oguchi ferromagnet in the case $S=3/2$.

A1 The model.

At the heart of the Oguchi method is the following statement. Consider a small region of the crystal and treat the exchange interaction within this region exactly then treat the interaction between the small region, and the rest of the crystal, in the effective field approximation. If we suppose that a particular atom has Z nearest neighbours, then the small region chosen is a central atom exchange coupled to one of its nearest neighbours. The Hamiltonian for the pair is:

$$\tilde{H}_p = -2JS_{\underline{i}} \cdot S_{\underline{j}} - g\mu_B (S_{iz} + S_{jz}) (\underline{H}_{\text{eff}} + \underline{H}_{\text{app}})$$

The two operators $\underline{S}_{\underline{i}} \cdot \underline{S}_{\underline{j}}$ and $(S_{iz} + S_{jz})$ commute so we seek their simultaneous eigenstates. We set:

$$S^1 = S_{\underline{i}} + S_{\underline{j}}$$

where S^1 is the total spin of the pair so that the eigenvalues of S^1 are:

$$S^1 = 0, 1, 2 \dots 2S$$

$(S_{iz} + S_{jz})$ is then just the total z component of the angular momentum of the pair, and the eigenvalues are:

$$M^1 = S^1, S^1 - 1, S^1 - 2, \dots, -S^1.$$

The eigenvalues of $-2JS_{\underline{i}} \cdot S_{\underline{j}}$ are found by considering:

$$(S^1)^2 = \underline{S}_{\underline{i}}^2 + \underline{S}_{\underline{j}}^2 + 2\underline{S}_{\underline{i}} \cdot \underline{S}_{\underline{j}} \quad \text{or} \quad -2\underline{S}_{\underline{i}} \cdot \underline{S}_{\underline{j}} = \underline{S}_{\underline{i}}^2 + \underline{S}_{\underline{j}}^2 - (S^1)^2$$

Table A1 I Eigenvalues for the case $S=3/2$.

| s^1 | M^1 | E_p | Z_p | Contribution to s_z^1 |
|-------|-------|------------|------------------------------------|----------------------------------|
| 0 | 0 | 0 | 1 | 0 |
| 1 | -1 | $11J/2+h$ | | |
| | 0 | $11J/2$ | | $2\sinh h \exp [2j]$ |
| | +1 | $11J/2-h$ | $(1+2\cosh h)$ | $\exp[2j]$ |
| 2 | -2 | $3J/2+2h$ | | |
| | -1 | $3J/2+h$ | $(1+2\cosh h+2\cosh 2h)$ | $\exp[6j]$ |
| | 0 | $3J/2$ | | |
| | +1 | $3J/2-h$ | | $2(\sinh h+2\sinh 2h) \exp [6j]$ |
| | +2 | $3J/2-2h$ | | |
| 3 | -3 | $-9J/2+2h$ | | |
| | -2 | $-9J/2+2h$ | | |
| | -1 | $-9J/2+h$ | $(1+2\cosh h+2\cosh 2h+2\cosh 3h)$ | $\exp [12j]$ |
| | 0 | $-9J/2$ | | |
| | +1 | $-9J/2-h$ | $2(\sinh h+2\sinh 2h +3\sinh 3h)$ | $\exp [12j]$ |
| | +2 | $-9J/2-2h$ | | |
| | +3 | $-9J/2-3h$ | | |

So the eigenvalues of H_p are:

$$E_p = J[2S(S+1) - S^1(S^1+1) - g\mu_B(\underline{H}_{\text{eff}} + \underline{H}_{\text{app}})M^1]$$

The partition function for the pair is then:

$$Z_p(j, h) = \sum_{M^1=-S^1}^{S^1} \sum_{S^1=0}^{2S} \exp[jS^1(S^1+1) + M^1h]$$

where $j=J/kT$ and $h = \mu_B g(\underline{H}_{\text{eff}} + \underline{H}_{\text{app}})/kT$ and where the term $J2S(S+1)$ has been omitted since it is the same for all states as it depends only on S , the expectation value of the z-component of spin of the pair is:

$$S_z^1 = \langle S_{iz} + S_{jz} \rangle = \frac{\text{Tr}(S_{iz} + S_{jz}) e^{-\tilde{H}_p/kT}}{Z_p(jh)}$$

$$S_z^1 = \frac{\sum_{M^1} \sum_{S^1} M^1 \exp[j S^1(S^1+1) + M^1h]}{Z_p(jh)} \quad \text{A1-1}$$

For the specific case of $S=3/2$, we write out the values of S^1, M^1 , and E_p and show them in table A1.I along with their contributions to $Z_p(jh)$ and S_z^1 .

A2 Specific application.

In order to obtain some specific expressions we first require a relationship for the effective field. This calculation was indicated in Chapter 2, 1.1. The expression will be rather similar but we must recall that, of the Z , nearest neighbours, one has been treated already so that only $(Z-1)$ need be considered, and:

$$\underline{H}_{\text{eff}} = 2(Z-1) \underline{J} \underline{M} / N g^2 \mu_B^2 \quad \text{A2-2}$$

where \underline{M} is the magnetization of the whole sample.

Now we must have that the magnetization of any randomly chosen pair be the same as the magnetization of the whole sample and this leads to the consistency condition that:

$$\underline{M} = \frac{1}{2} (Ng \mu_B \langle S_z^1 \rangle) \quad \text{and so} \quad \text{A2-2}$$

$$\underline{M}_0 = \frac{1}{2} (Ng \mu_B 2S)$$

is the magnetization at 0°K . The reduced magnetization is therefore:

$$\sigma = \frac{\underline{M}}{\underline{M}_0} = \frac{S_z^1}{2S} = \frac{S_z^1}{3} \quad \text{for } S=3/2 \quad \text{A2-3}$$

$$\text{thus} \quad S_z^1 = 3\sigma \quad \text{A2-4}$$

So from A2-1 and A2-4, we have:

$$\underline{H}_{\text{eff}} = 3(Z-1)J\sigma/g\mu_B \quad \text{A2-5}$$

Hence from A1-1, A2-4 and A2-5, we obtain, after substituting the values for $Z_p(j,h)$ and S_z^1 from table A1.I; an expression for σ that can be used to generate the shape of the magnetization versus temperature curve, it predicts too low a value of $\left. \frac{\partial \sigma}{\partial T} \right|_{T \rightarrow 0}$ compared with the exact result from the Heisenberg model:

$$\text{i.e. } \sigma \sim 1 + AT^{3/2} + \dots$$

We shall therefore, deal with two special solutions, viz. the result of allowing $T \rightarrow T_c$ $\sigma \rightarrow 0$ under the condition that $H_{app} = 0$; and, the result of allowing $j \rightarrow 0$ under the conditions J constant $H_{app} = 0$ but $g\mu_B H_{app}/kT \ll 1$.

The first case allows $\sinh(x) \rightarrow x$ and $\cosh(x) \rightarrow 1$, $j \rightarrow j_c$

hence,

$$\sigma(T \lesssim T_c) = \frac{2}{3} \frac{e^{2j_c} [3(z-1)\sigma j_c] + e^{6j_c} ([15(z-1)\sigma j_c]) + e^{12j_c} (42(z-1)\sigma j_c)}{1 + 3e^{2j_c} + 5e^{6j_c} + 7e^{12j_c}}$$

If we consider the case $Z=6$, then we have:

$$1 = (10j_c - 3)e^{2j_c} + 5(10j_c - 1)e^{6j_c} + 7(20j_c - 1)e^{12j_c}$$

For which we find a numerical solution namely:

$$j_c = 0.0688 = \frac{J}{kT_c}$$

so that $\frac{kT_c}{J} = 14.5$

The second case implies $j \rightarrow 0$ so that $\sinh(x) \rightarrow x$ $\cosh(x) \rightarrow x$ as $T \rightarrow \infty$ and we shall find the asymptotic limit of the susceptibility χ provided $h_a \ll 1$. Thus dividing through by H_{app} , we have for the case $Z=6$:

$$\frac{\sigma}{H_{app}} = \frac{2}{3} \left\{ \frac{e^{2j} (15j \sigma / H_{app} + g\mu_B / kT) + e^{6j} (75j \sigma / H_{app} + 5g\mu_B / kT) + e^{12j} (210j \sigma / H_{app} + 149\mu_B / kT)}{1 + 3e^{2j} + 5e^{6j} + 7e^{12j}} \right\}$$

Rearranging and solving for σ/H_{app} gives:

$$\frac{\sigma}{H_a} = \frac{e^{2j} \mu_B g/kT + e^{6j} 5 \mu_B g/kT + e^{12j} 14 \mu_B g/kT}{\left\{ \frac{3}{2} (1 + 3e^{2j} + 5e^{6j} + 7e^{12j}) - 3.5je^{2j} - 15.5je^{6j} - 42.5je^{12j} \right\}}$$

In this limit $j \rightarrow 0$ so $e^{aj} \rightarrow 1 + aj$, we also recall that

$\sigma = M/M_0$ so that:

$$\chi = \frac{M}{H_{app}} = \frac{\sigma}{H_{app}} \cdot M_0 = \frac{\sigma}{H_{app}} \cdot Ng \mu_B^{3/2} \quad (S=3/2)$$

$$\begin{aligned} \text{so that } \chi_{(T \rightarrow T_c)} &= \frac{(3/2) Ng^2 \mu_B^2}{kT} \left\{ \frac{20}{24} + \frac{200j}{-120j} \right\} \\ &= \frac{(3/2) Ng^2 \mu_B^2}{kT} \frac{20}{(24-120j)(1+10j)^{-1}} \end{aligned}$$

since j is supposedly small:

$$(1+10j)^{-1} \approx 1-10j$$

$$\text{and } \chi = \frac{(3/2)(5/2) Ng^2 \mu_B^2}{3kT} \frac{1}{(1-5j)(1-10j)}$$

$$\chi = \frac{C}{T-15J/k} \equiv \frac{C}{T-\theta}$$

where C is the Curie Constant for $S=3/2$ and $\theta = 15J/k$ $J < 0$

$$\text{Hence } \frac{J}{k\theta} = 0.0666$$

$$\text{Hence } \left| \frac{\theta}{T_c} \right| = \frac{0.0688}{0.0666} = 1.03$$

Oguchi

which may be compared with the straight M.F.T. result that

$$\left| \frac{\theta}{T_c} \right| = 1$$

A3. Short range order.

We expect to find some correlation of the spins even above the transition temperature where the long range order vanishes. If \mathcal{C} is a measure of the short range order, we may take:

$$\mathcal{C} = \frac{4}{9} \langle S_i \cdot S_j \rangle \quad \text{for } S=3/2$$

Now since

$$-2S_i \cdot S_j = S_i^2 + S_j^2 - (S^1)^2$$

The values of \mathcal{C} corresponding to the various values of S^1 (0,1,2,3) are:

$$\begin{array}{cccc} S^1 = 0 & 1 & 2 & 3 \\ = -15/9 & -11/9 & -3/9 & +1 \\ S_i \cdot S_j = -15/4 & -11/4 & -3/4 & +9/4 \end{array}$$

In general $-5/3 \leq \mathcal{C} \leq +1$, but for $J > 0$ $0 \leq \mathcal{C} \leq 1$ we have:

$$= \frac{4}{9} \cdot \frac{\text{Tr}(S_i \cdot S_j e^{-\tilde{H}_p/kT})}{\text{Tr}(e^{-\tilde{H}_p/kT})}$$

as $T \rightarrow 0$ $h, j \rightarrow \infty$ we have:

$$\mathcal{C}_{T \rightarrow 0} = \frac{4}{9} \cdot \frac{9/4(1+2\cosh h + 2\cosh 2h + 2\cosh 3h)}{(1+2\cosh h + 2\cosh 2h + 2\cosh 3h)} = 1$$

for $T > T_c$, $h \rightarrow 0$ we have:

$$= \frac{4}{9} \left\{ \frac{-15/4 - (11/4) 3e^{2j} - (3/4) 5e^{6j} + (9/4) 7e^{12j}}{1 + 3e^{2j} + 5e^{6j} + 7e^{12j}} \right\} \neq 0$$

and as T reaches very high values where the exponential terms may be expanded.

$$\chi \propto J/kT$$

so that the amount of short range order depends on the strength of the exchange coupling as well as the inverse temperature.

Appendix B Derivation of basic transport results from the Boltzmann Equation.

B1 Formal theory.

Suppose that at some time t , the number of carriers in a volume of phase space $x \rightarrow x+dx$, $y \rightarrow y+dy$, $z \rightarrow z+dz$, $u \rightarrow u+du$, $v \rightarrow v+dv$, $w \rightarrow w+dw$ is given by a function:

$$f=f(x,y,z,u,v,w,t,dxdydzdudvdw)$$

Then it is straightforward algebra to show that at time $t+dt$, f is unchanged unless extra carriers are introduced by virtue of some scattering process, hence:

$$f(x+dx \dots, u+du \dots, t+dt) - f(x \dots, u \dots, t) = \left(\frac{\partial f}{\partial t} \right)_{\text{COLL}} dt$$

We then make use of Taylor's theorem to find:

$$\frac{\partial f}{\partial t} + \frac{\partial f}{\partial x} U + \dots + \frac{\partial f}{\partial u} \frac{du}{dt} + \dots = \left(\frac{\partial f}{\partial t} \right)_{\text{COLL}} \quad \text{B1-1}$$

In the steady state $\frac{\partial f}{\partial t} = 0$

We now make sure assumptions about $\left(\frac{\partial f}{\partial t} \right)_{\text{COLL}}$ viz. suppose that the carrier distribution is disturbed, then the stimulus is removed and that f regains its equilibrium value f_0 in an exponential fashion i.e.

$$f = f_0 (1 - A e^{-t/\tau})$$

where A is a constant and τ is a relaxation time.

$$\text{Whence: } \left(\frac{\partial f}{\partial t} \right)_{\text{COLL}} = f_0 \frac{A e^{-t/\tau}}{\tau} = - \frac{[f - f_0]}{\tau} \quad \text{B1-2}$$

B2 Electrical conductivity.

In order to calculate the electrical conductivity, we need only to consider the Boltzmann equation in one dimension and to suppose that an electric field $\underline{E} = (E_x, 0, 0)$ has been applied long enough for equilibrium to obtain i.e. $\partial f / \partial t = 0$ and there is no variation of f through the medium, hence from B1:

$$\left(\frac{\partial f}{\partial t} \right)_{\text{COLL}} = \frac{\partial f}{\partial u} \frac{du}{dt} \quad \text{B2-1}$$

$$\frac{du}{dt} = \frac{e E_x}{m^*} \quad \text{B2-2}$$

where e is the electronic charge and m^* is the effective mass. Combining B1-2, B2-1, and B2-2, we have:

$$-\frac{[f - f_0]}{\tau} = \frac{e E_x}{m^*} \frac{\partial f}{\partial u} \quad \text{B2-3}$$

We set $f = f_0 + \phi$ where ϕ is supposed to be small compared to f_0 and $\frac{\partial \phi}{\partial u}$ is small compared to $\frac{\partial f_0}{\partial u}$ and we obtain:

$$f = f_0 - \frac{e E_x \tau}{m^*} \frac{\partial f_0}{\partial u} \quad \text{B2-4}$$

The current density J_x is given by:

$$J_x = e \int_{-\infty}^{+\infty} u \left[f_0 - \frac{e E_x \tau}{m^*} \frac{\partial f_0}{\partial u} \right] du dv dw$$

Since we are dealing with fermions

$$f_0 du dv dw = 2 \left(\frac{m^*}{h} \right)^3 F(\epsilon) du dv dw$$

where $F(\epsilon) = (\exp[(\epsilon - \epsilon_F)/kT] + 1)^{-1}$

$$\epsilon = \frac{1}{2} m^* (u^2 + v^2 + w^2)$$

$$\frac{\partial \epsilon}{\partial u} = m^* u$$

$$\text{So } \frac{\partial f_0}{\partial u} = \frac{\partial f_0}{\partial \epsilon} \cdot \frac{\partial \epsilon}{\partial u} = m^* u \cdot 2 \left(\frac{m^*}{h}\right)^3 \frac{\partial F(\epsilon)}{\partial \epsilon}$$

$$2 \left(\frac{m^*}{h}\right)^3 du dv dw \Rightarrow \frac{8\pi}{h^3} \sqrt{2m^*} \sqrt{\epsilon} d\epsilon$$

Considering the expression for J_x , in particular

the product $\int_{-\infty}^{+\infty} u f_0 du = 0$ because f_0 is a function of energy and is, therefore, an even function of u so $u f_0$ is odd. Also, $\langle u^2 \rangle = (2\epsilon/3m^*)$, so

$$J_x = \frac{-e^2 E_x}{m^*} \int_{-\infty}^{+\infty} \tau m^* \frac{2\epsilon}{3m^*} \frac{8\pi}{h^3} \sqrt{2m^*} \sqrt{\epsilon} \frac{\partial F(\epsilon)}{\partial \epsilon} d\epsilon$$

$J_x = \sigma E_x$ where σ is the electrical conductivity given by $\sigma = \frac{-16 e^2 \pi}{3m^* h^3} \int_{-\infty}^{+\infty} \tau \epsilon^{3/2} \frac{\partial F(\epsilon)}{\partial \epsilon} d\epsilon$ B2-5

B3 Specific application.

This expression can be evaluated for whatever type of material we are interested. In particular, for a semi-conductor where carriers are excited from a valence band to a conduction band, we can make the approximation that the carrier concentration is low enough that:

$$F = (\exp[(\epsilon - \epsilon_F)/kT] + 1)^{-1} \Rightarrow \exp\left[\frac{-(\epsilon - \epsilon_F)}{kT}\right] \text{ since } F \ll 1$$

We must also, perforce, make some assumption about

τ , and its dependence on the energy of the carriers.

Now τ is related to the average time between collisions and, if we define a mean free path λ then for lattice phonon scattering $\tau = \lambda c^{-1}$ where $\frac{1}{2}mc^2 = \epsilon$. The integral in B2-5 can be evaluated to obtain:

$$\sigma = \frac{4}{3} \frac{n e^2 \lambda}{(2\pi m^* kT)^{\frac{1}{2}}}$$

where n is the number of carriers per unit volume.

As is usual for semi-conductors, the real temperature dependence comes from the temperature dependence of n .

For this particular intrinsic semi-conductor:

$$n = N_c \exp[-(\epsilon - \epsilon_F)/kT]$$

the zero of energy being the top of the valence band.

Therefore, ϵ is the energy gap between the conduction and valence band and conductivity measurements allow us to make an estimate of this gap. Usually the result is expressed:

$$\sigma = \sigma_0 \exp[-E/kT]$$

it being understood that the Fermi energy lies mid-way between the highest occupied band or level and the conduction band.

In a magnetic semi-conductor, there is often a change in E at the ordering temperature. This occurs because of the exchange interaction between the s-p band electrons and the spin associated with the d-electron states. Thus, electrons in the s-p valence band having their spins parallel to the spin of the d-electrons are stabilized with respect to those with

spin antiparallel. To first order the centre of gravity of the states in the conduction band plus valence band remains unchanged so that for the conduction band the antiparallel spin states are stabilized and the parallel spin states destabilized. Hence, E for electrons antiparallel to the spin of d -electrons is decreased. This topic has been treated quite thoroughly by Haas in a review article [99] Chapter III.

Appendix C Notes on the electric field gradient Tensor.

C1 Definition.

Consider a point charge e at the origin of a cartesian co-ordinate system. The potential at a point (r, θ, ϕ) is: $V(r, \theta, \phi) = -\frac{e}{r}$

$$\underline{E} = -(\underline{\nabla} \cdot v) = -\left(\frac{\partial}{\partial x} + \frac{\partial}{\partial y} + \frac{\partial}{\partial z}\right) v$$

and the electric field gradient is defined as:

$$(\underline{\nabla} \cdot \underline{E}), \text{ a } 3 \times 3 \text{ tensor.}$$

As a specific example consider finding the element V_{zz} ;

$$E_z = -\frac{\partial}{\partial z} (-e/r) = \frac{\partial}{\partial z} (e/(x^2 + y^2 + z^2)^{1/2})$$

$$E_z = -ez/(x^2 + y^2 + z^2)^{-3/2}$$

$$\text{So } V_{zz} = -[e(x^2 + y^2 + z^2)^{-3/2} + ez(-3/2)(2z)(x^2 + y^2 + z^2)^{-5/2}]$$

$$V_{zz} = e(3\cos^2\theta - 1) \langle r^{-3} \rangle \equiv eq$$

where $\langle r^{-3} \rangle$ means the value of the inverse cube of the radius. The other elements can be found in a similar fashion; we shall list only the other two diagonal elements, ie:

$$V_{xx} = e \langle r^{-3} \rangle (3\sin^2\theta \cos^2\phi - 1)$$

$$V_{yy} = e \langle r^{-3} \rangle (3\sin^2\theta \sin^2\phi - 1)$$

C2 Applications.

C2-1 An electric field gradient arising from lattice asymmetries.

This is at once the easiest and the most difficult problem. It is conceptually straightforward because it is easy to see how an asymmetric charge distribution around a given nucleus could produce a non-zero electric field gradient. It is extremely difficult to calculate in practice because of an incomplete knowledge of the atomic positions or because of an incomplete knowledge of the charges on the surrounding atoms or because a point charge model is not in order. However, assuming all these factors to be accounted for, the E.F.G. is calculated by assigning a charge $(ne)_i$ to each atom and summing over the number of surrounding atoms thus:

$$V_{zz} = \sum_i \frac{(ne)_i (3\cos^2 \theta_i - 1)}{r_i^3}$$

and the asymmetry parameter $\eta = (V_{xx} - V_{yy})/V_{zz}$ is given by:

$$= \frac{1}{V_{zz}} \sum_i (ne)_i \cdot \frac{(3\sin^2 \theta_i \cos^2 \phi_i)}{r_i^3}$$

There are some important multiplicative factors that have been discussed by Sternheimer; these tend to increase the E.F.G. as calculated above and arise because of the influence of the nucleus' own electrons which tend to amplify the E.F.G. For this reason, they are called antishielding factors.

An E.F.G. such as this is important for S state ions eg Fe^{3+} or Fe^{2+} in a low spin state. Generally the contribution is fairly small and almost independent of temperature.

C2-2 An electric field gradient arising from the nucleus' own electrons.

This contribution is particularly important in the case of ferrous ions. It arises because the 3d orbitals are aspherical. For Fe^{3+} , the 3d shell is half full so the problem never arises but the sixth electron on the Fe^{2+} ion must eventually occupy one of the orbitals and so give rise to an E.F.G.

Initially, we set out to find the electric field gradient created by a single electron in each of the 3d orbital functions. A suitable basis set is that given in Chapter I, section 4. As defined there, the d-orbitals are symmetric and any E.F.G. is entirely a result of V_{zz} and the asymmetry parameter is zero. We must calculate:

$$\langle V_{zz} \rangle = -e \langle r^{-3} \rangle_{3d} \cdot \langle 3\cos^2\theta - 1 \rangle$$

where e is the charge on a proton and the introduction of the negative sign takes care of the fact that we are dealing with an electron. In the literature there is frequently confusion over this point and here, we wish to write out as plainly as possible what is going

on. To see how the calculation goes, consider ϕ_3 of Chapter 1, section 4:

$$\phi_3 \sim xy/r^2 = \sin\phi \cos\theta \sin^2\theta$$

$$\text{so } \langle V_{zz} \rangle_{\phi_3} = - \frac{\int_0^\infty \int_0^{2\pi} \int_0^\pi \langle r^{-3} \rangle_{3d} e(3\cos^2\theta - 1) \sin^2\phi \cos^2\phi \sin^4\theta r^2 \sin\theta d\theta d\phi dr}{\int_0^\infty \int_0^{2\pi} \int_0^\pi \sin^2\phi \cos^2\phi \sin^4\theta r^2 \sin\theta d\theta d\phi dr}$$

ie. we find $\langle \phi_3 | V_{zz} | \phi_3 \rangle / \langle \phi_3 | \phi_3 \rangle$ which reduces to the integration above because ϕ_3 is real. It is very important to note that $\langle r^{-3} \rangle_{3d}$ is a number that must be determined independently, usually using Hartree-Fock self consistent field calculations such as have been done by Watson and Freeman.

The result is $-4/7 (e \langle r^{-3} \rangle_{3d})$. There are similar results for all the other orbitals and these are summarised in table C1 below:

Table C1. V_{zz} for the 3d electron orbitals of Chapter I.

| Orbital Function | V_{zz} | Transform Group |
|------------------|--|-----------------|
| ϕ_1 | $-4/7 (e \langle r^{-3} \rangle_{3d})$ | } e_g |
| ϕ_2 | $+4/7 (e \langle r^{-3} \rangle_{3d})$ | |
| ϕ_3 | $-4/7 (e \langle r^{-3} \rangle_{3d})$ | } t_{2g} |
| ϕ_4 | $+2/7 (e \langle r^{-3} \rangle_{3d})$ | |
| ϕ_5 | $+2/7 (e \langle r^{-3} \rangle_{3d})$ | |

Unfortunately, this represents only half the

problem for ferrous ions, to see why, consider figure C1.

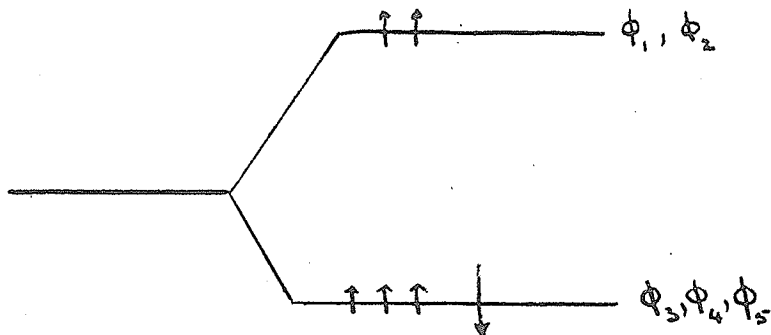


Figure C1. Illustrating the effect of orbital degeneracy.

Here, we assume a ferrous ion in an octahedral site with perfect cubic symmetry. Consequently, the ground state is triply degenerate and the sixth electron spends equal time in each of the three t_{2g} orbitals. From table C1 an equal admixture of the E.F.G. from each of the t_{2g} orbitals yields zero. A similar result holds for the e_g group. It is clear that we require a mechanism for lifting the orbital degeneracy of the ground state, to create a new ground state with one orbital at a lower energy than the rest. In this event, the sixth electron spends longer in the stabilized orbital than in the others and a non-zero E.F.G. results. This rather naturally leads to a strong temperature dependence of the E.F.G. because

of the Boltzmann population of the various possible states.

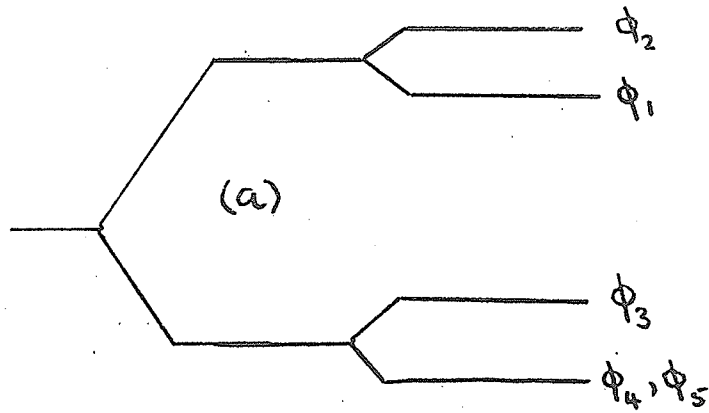
C2-3 Specific mechanisms for lifting orbital degeneracy.

Two basic mechanisms lift the orbital degeneracy:

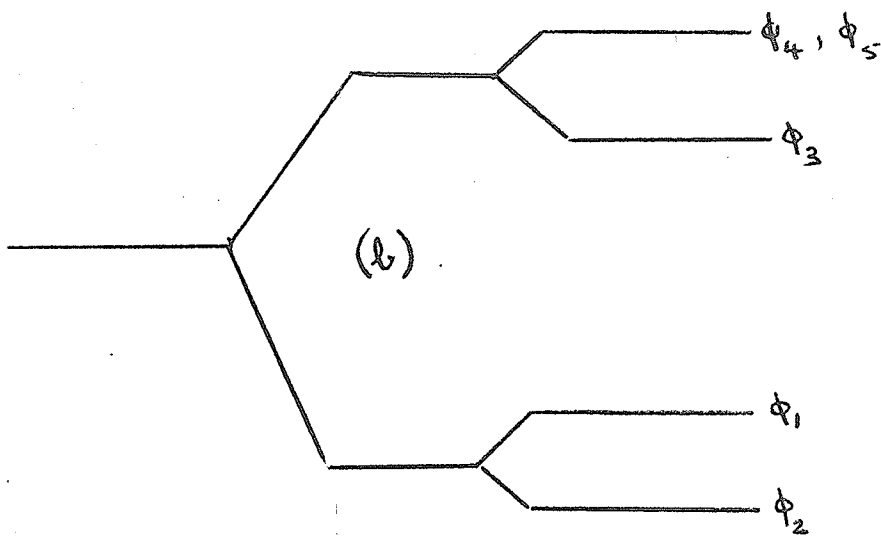
- (i) Crystallographic distortions;
- (ii) Spin orbit coupling.

Sometimes these two mechanisms combine together, for example strong spin orbit coupling may induce a crystallographic distortion. Sometimes the distortion can be spontaneous (J-T effect) sometimes a distortion occurs that does not lift the ground state degeneracy e.g. a trigonal distortion of a tetrahedral site Fe^{2+} ion, then spin orbit coupling splits the ground state orbitals.

Distortions are easier to deal with because most of the work has already been done as a result of interest in other experiments. Consider figure C2, here we show how the non-cubic part of the crystal field affects the 3d orbital functions. The particular distortion is to $c/a > 1$ via a tetragonal field (axially symmetric). Reference to table C1 reveals that the E.F.G. in C2 will be positive in both cases and $\eta = 0$ because of the axial symmetry. A tetragonal distortion that yields $c/a < 1$ clearly reverses the sign but not



free ion+cubic field+tetragonal field (axial)



free ion+cubic field+tetragonal field (axial)

Figure C2. Illustrating tetragonal distortions at
 (a) Octahedral sites;
 (b) at tetrahedral sites.

the magnitude of the E.F.G. produced which is

$$4/7e\langle r^{-3} \rangle_{3d}.$$

As an example of a spin orbit mechanism consider the question of a magnetically induced E.F.G. at a ferrous ion in a tetrahedral site. The representations chosen for this problem are:

$$t_{2g} = \begin{cases} A_1 = Y_2^1 \\ A_2 = 1/2(Y_2^2 - Y_2^{-2}) \\ A_3 = -Y_2^{-1} \end{cases} \quad e_g = \begin{cases} B_1 = Y_0^0 \\ B_2 = 1/2(Y_2^2 + Y_2^{-2}) \end{cases}$$

Here the $Y_1^{m_1}$ are the spherical harmonics which we use because we shall be involved with raising and lowering operators and there are known relationships that we can make use of. We also need some spin states, we take $S_z = 2, 1$ since $S = 2$ for all the states. The e_g orbitals behave like an $L = 0$ state, as we noted earlier. The t_{2g} orbitals behave like an $L = 2$ state. There is no spin orbit coupling in first order, the calculation is done in second order and we consider matrix elements like:

$$\langle S_z A_i | \lambda \underline{L} \cdot \underline{S} | S_z B_j \rangle \quad i=1,2,3 \quad j=1,2$$

Now $\lambda \underline{L} \cdot \underline{S} = \lambda \{ L_z S_z + \frac{1}{2}(L^+ S^- + L^- S^+) \}$ and to see how the calculation goes, we consider how $\underline{L} \cdot \underline{S}$ couples

B_1 with A_1, A_2, A_3 . There will be 12 matrix elements:

$$\begin{aligned} \langle 1, A_1 | \lambda \underline{L} \cdot \underline{S} | 1, B_1 \rangle &= 0 & \langle 2, A_1 | \lambda \underline{L} \cdot \underline{S} | 2, B_1 \rangle &= 0 \\ \langle 2, A_1 | \lambda \underline{L} \cdot \underline{S} | 1, B_1 \rangle &= 0 & \langle 1, A_1 | \lambda \underline{L} \cdot \underline{S} | 2, B_1 \rangle &= \sqrt{6} \lambda \end{aligned}$$

$$\langle 1, A_2 | \lambda \underline{L} \cdot \underline{S} | 1, B_1 \rangle = 0 \quad \langle 2, A_2 | \lambda \underline{L} \cdot \underline{S} | 2, B_1 \rangle = 0$$

$$\langle 2, A_2 | \lambda \underline{L} \cdot \underline{S} | 1, B_1 \rangle = 0 \quad \langle 1, A_2 | \lambda \underline{L} \cdot \underline{S} | 2, B_1 \rangle = 0$$

$$\langle 1, A_3 | \lambda \underline{L} \cdot \underline{S} | 1, B_1 \rangle = 0 \quad \langle 2, A_3 | \lambda \underline{L} \cdot \underline{S} | 2, B_1 \rangle = 0$$

$$\langle 2, A_3 | \lambda \underline{L} \cdot \underline{S} | 1, B_1 \rangle = 0 \quad \langle 1, A_3 | \lambda \underline{L} \cdot \underline{S} | 2, B_1 \rangle = 0$$

Second order perturbation theory then gives that the state $|2, B_1\rangle$ is lowered by an energy $6 \lambda^2 / \Delta$ via the spin orbit interaction. If we do the same exercise for the orbital B_2 , we find two non-zero matrix elements, ie.

$$\langle 1, A_3 | \lambda \underline{L} \cdot \underline{S} | 2, B_2 \rangle = -\sqrt{2} \lambda, \quad \langle 2, A_1 | \lambda \underline{L} \cdot \underline{S} | 2, B_2 \rangle = 4 \lambda$$

Second order perturbation theory then yields up the fact that the state $|2, B_2\rangle$ is lowered by an energy

$$(4\lambda)^2 / \Delta + (-\sqrt{2}\lambda)^2 / \Delta = 18\lambda^2 / \Delta$$

So that the original states $|2, B_1\rangle$ and $|2, B_2\rangle$ are split by an energy

$$18\lambda^2 / \Delta - 6\lambda^2 / \Delta = 12\lambda^2 / \Delta$$

Provided that the spin-orbit interaction does not mix in too much of the upper states, we can calculate the E.F.G. expected by assuming $|2, B_2\rangle$ remains unchanged. We take just the orbital part

$$\left(\frac{1}{2}\right) (Y_2^2 + Y_2^{-2}) \sim \phi_2 \quad \text{of table C1}$$

so the E.F.G. is $+4/7e\langle r^{-3} \rangle_{3d}$ and $\eta = 0$.

There are, of course, many other spin-orbit effects that we might consider but this example

illustrates the nature of the techniques. Implicit in this example is the assumption that:

$$\lambda^2/\Delta \ll g\mu_{Bw}^H$$

APPENDIX D COMPUTER FITTING OF MÖSSBAUER SPECTRA.

D.1 The "MONKEY" program.

This program is stored on permanent disc and may be called by means of the J.C.L. cards shown below.

```

1 //JOBNAME      'nnnn,xxx,nn,T=tt,I=ii,L=2,R=120K,' 'NAME'
2 //JOB LIB DD  UNIT=DISK,VOLUME=SER=UM1404,
3 //  DSNAME=COEY.A0830.MAR71,DISP=SHR
4 // EXEC  PGM=MONKEY,REGION=120K
5 // FT06F001 DD  SYSOUT=A
6 // FT05F001 DD  *

```

The program was given to us by the Applied Mathematics Division, Argonne National Labs. It is a least squares fitting routine in which the intensities full widths and positions of a prespecified number of Lorentzian absorption lines are varied until a best fit to the experimental spectrum is obtained. A complete listing of the program is available in the lab. together with a rather cryptic description of its main program and the various sub-routines.

D1.1 Input Data.

Card 1 Title ie. name of data to be fitted
 Format 72 H0.

Card 2 Specification of type of spectrum to be fitted
 and output required
 Format 2I1,2I2,3I6,8I1,E10.0,E6.0,2E12.0

Column 1 Choice of plotted data or not
 0=yes 1=no

Column 2 Choose format of data deck,
 0 means 6 data points per card in

the format $X_i Y_i \dots X_{i+6} Y_{i+6}$

1 means 5 data points per card
in the form $X_i Y_i \dots X_{i+4} Y_{i+4}$

2 means 10 data points per card
in the form $X_i Y_i Y_{i+1} Y_{i+2} \dots Y_{i+9}$
 $i=0 \ 10 \ 20 \ \dots$

- Column 3,4 Choice of integrated total intensity and intensity Weighted centre of gravity 1=yes 0=no. Specify
- 5,6 Specified number of peaks 14 max.
- 7-12 Specified number of data points 500 max.
- 13-18 Specified nature of base line 1=constant velocity base line assumed to be of form $Y=k_1 X$ 2=Constant acceleration base line assume to be of form $Y=k_2 X^2$
- 19,24 Number of constraints 30 max. specify
- 25 Number of random steps
- 26 Line shape = 0 for Lorentzian = 1 for Gaussian
- 27 Gradient Vector output optional = 0 for none
- 28 Errors and guesses must be imputed if = 1
- 29 Adding counts if=1 adds 10^6 counts to data, 2 adds 2×10^6 counts to data
- 30 Data table output option=1 for yes
- 31 Parameter listing after each iteration optional=0 for no, 1 for yes
- 32 Parameter listing option 0 for no = 1 for every 5 iterations
- 33-43 Minimization parameter ϵ . If 33=0 $\epsilon=1 \times 10^{-3}$ otherwise specify ϵ
- 44-49 Random step size control if=0 program calculates $\sqrt{\text{number of points}}$

50-61 0.0

62-73 Value of X_0 (this is a fixed parameter and must be imputed from a calibration spectrum)

Card 3 A guess for the number of counts, Y_0 , on the base line at the specified zero of velocity

Format 12 E 6.0 X

Card 4 A set of guesses for the percentage absorption of the Lorentzians to be fitted, one for each peak

Format 12 E 6.0 X

Card 5 A set of guesses for the full widths in channels of the peaks to be fitted, one for each peak

Format 12 E 6.0 X

Card 6 A set of guesses for the peak positions in channel numbers are for each peak

Format 12 E 6.0 X

Card 7 Guesses for the values of k_1 and k_2

Format 2 E 6.0 X

Note if column of card 2=1, k_2 0.0+00

if Column of Card 2=2 k_1 0.04+00
Since X_0 has been specified on card 2

Card 8 Estimated squared error in Y_0 , format

Format E 12.0

Card 9 Estimated squared errors in intensities

Format 12 E 6.0 X

Card 10 Estimated squared errors in full widths

Format 12 E 6.0 X

Card 11 Estimated squared errors in peak positions

Format 12 E 6.0 X

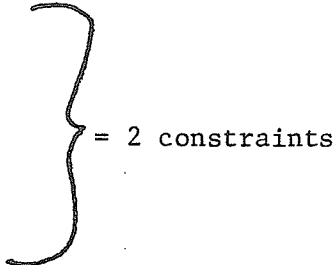
Constraint Deck

Intensities first

Card 13 1 . 0 + 0 6 - 1 . + 0 6
 Card 14 B L A N K B L A N K
 Card 15 B L A N K B L A N K

Full widths second

Card 16 B L A N K B L A N K
 Card 17 1 . 0 + 0 6 - 1 . + 0 6
 Card 18 B L A N K B L A N K



If it is required that line 1 be 4 times as intense as line 2 but of equal full width then:

| | 1 | 2 | 3 | 4 | 5 | 6 | 7 | 8 | 9 | 10 | 11 | 12 | — | — | — | — | — |
|--------|---|---|---|---|---|---|---|---|---|----|----|----|---|---|---|---|---|
| Card 4 | 8 | . | 0 | - | 0 | 2 | 2 | . | 0 | - | 0 | 2 | | | | | |
| Card 5 | 8 | . | 0 | + | 0 | 0 | 8 | . | 0 | + | 0 | 0 | | | | | |
| etc. | | | | | | | | | | | | | | | | | |

Constraint Deck

Intensities

Card 13 2 . 5 + 0 5 - 1 . + 0 6
 Card 14 B L A N K B L A N K
 Card 15 B L A N K B L A N K

Full widths

Card 16 B L A N K B L A N K
 Card 17 1 . 0 + 0 6 - 1 . + 0 6
 Card 18 B L A N K B L A N K

When the column and row vectors are multiplied out, one has:

$$(8.0-02, 2, 0-02; 8.0+00, 8.0+00; \dots) \begin{pmatrix} 2.5+05 \\ -1.+06 \\ 0 \\ 0 \\ - \\ - \\ - \\ 0 \end{pmatrix}$$

$$= 8 \times 2.5 \times 10^3 + 2 \times (-1) \times 10^3 + 0 + 0 \dots = 0$$

This process being repeated for each constraint present.

Note that the parameters must be imputed in the desired ratio. Note that the exponent on the constraint must be

large eg. 10^6 , otherwise they tend to be ignored.

D1.2 Output.

The output is up to programmer's choice. The usual output is
 A Table showing number of points $\times \sum \text{Diff}^2$ a measure of
 the goodness of fit.

Y_0 the base line counts at zero velocity

Peak intensities

Full Widths

Peak Positions

k_1 and k_2 (the base line parameter)

A Table showing

| | | | |
|---------|--------------|------------|-------------------------|
| channel | experimental | calculated | Difference ² |
| Number | Counts | Counts | |

Optional Output is:

I (a) A table showing

| | | |
|---------|------------|-----------------|
| Channel | Calculated | Calculated |
| Number | Counts | Baseline Counts |

(b) A table showing

| | |
|----------------|---|
| Channel Number | (Baseline - Calculated) counts \equiv intensity |
|----------------|---|

$$\sum \text{Intensities} = A$$

$$\sum \text{Intensity} \times \text{channel number} = B$$

and $B/A = \text{centre of gravity}$.

II A plot showing the experimental and calculated spectrum.

D1.3 The program will handle as many sets of data as desired;

there is no need to specify how many; it will run until

either the C.P.U. time or the estimated lines printed

has been exceeded or until it runs out of data to fit.

A complicated spectrum takes about 2 minutes C.P.U. time.

D2. The "POWDER" Program.

A complete description of this program is already available in the lab. but a few words concerning its practical use are in order. As we said before, it is a least squares fitting routine that utilises the complete nuclear Hamiltonian as appropriate to Mössbauer spectra viz:

$$\hat{H} = -g\beta \cdot H_{hf} + Q_I \cdot \nabla E + (2\pi ZeR^2_I e |\psi_s(0)|^2) / 5$$

Input data appropriate to a particular spectrum are specified with errors and final limits and the computer seeks an exact solution of the Hamiltonian, that best fits the experimental spectrum both from the point of view of intensities and peak positions. The parameters required are H_{hf} , θ , ϕ , η , the quadrupole and isomer shift and the approximate line width. The program is restricted to fitting equal line widths and since this rarely occurs in practice, it is essential to check the fit obtained against that found from "MONKEY". The latter can be made to reproduce the "POWDER" spectrum simply by specifying zero errors on the peak positions. MONKEY will then give the experimental intensities. One can, for example, take the product (full width x peak height) as a measure, or plot out the peak on the "Calcomp" and measure the area.

In addition, with six parameters to vary the program

will overdo the iterations and a suggested technique is to find out first what the values of ϕ and τ are. This can be done quite simply using the graphs supplied by Kundig (see reference 48 in Chapter 2). These graphs are quite accurate and enable one to specify these two parameters before going to the trouble of using "POWDER". In fact, for moderately simple spectra, the use of the graphs is more than adequate.

The "POWDER" program was written by D.C. Price and the subroutine to calculate the spectra by W. Kundig, who very kindly supplied us with a copy.

Appendix E The hydrothermal synthesis of Fe_3S_4 .

- 1 Solutions of sodium sulphide (Na_2S) and Mohr's salt ($\text{Fe}(\text{NH}_4)_2(\text{SO}_4)_2 \cdot 6\text{H}_2\text{O}$) were made using distilled deionized water.
- 2 We mixed equal quantities (5ml) of 0.20M sodium sulphide and 0.15M Mohr's salt together in a clean closed end pyrex glass tube. A black precipitate resulted.
- 3 The open end of the pyrex tube was connected to a rotary pump and the closed end was immersed in a cold bath. Under the resulting, rather modest, vacuum the pyrex tube was sealed off with an oxygen/gas torch.
- 4 The glass ampul was placed inside an aluminium reaction vessel fitted with a high pressure valve.
- 5 The reaction vessel was sealed and nitrogen was introduced into the vessel to a pressure of 90 p.s.i. The temperature of the hydrothermal reaction was to be 190°C . The nitrogen pressure would rise to 140 p.s.i. but the pressure within the glass ampul would also rise on account of the aqueous solution contained in it. According to the C.R.C. steam tables the internal pressure would be ~ 130 p.s.i. The

pressure differential across the pyrex tube would therefore, be close to zero.

- 6 The reaction vessel was placed in an oil bath at $190 \pm 2^\circ\text{C}$ for 1 hour. After this time, it was quenched into a large ice water bath.
- 7 The reaction vessel was opened and the ampul was removed, opened and the precipitate was filtered off, washed several times with distilled water and vacuum dried.